University of Alberta

The impact of tumor motion upon CT image reconstruction

by

Isabelle Marie Gagné ©

A thesis submitted to the Faculty of Graduate Studies and Research in partial
fulfillment of the requirements for the degree of Doctor of Philosophy

in

Medical Physics

Department of Physics

Edmonton, Alberta

Fall 2005

Library and
Archives Canada

Published Heritage
Branch

395 Wellington Street
Ottawa ON K1A 0N4
Canada

Bibliothèque et
Archives Canada

Direction du
Patrimoine de l'édition

395, rue Wellington
Ottawa ON K1A 0N4
Canada

0-494-08641-6

Your file Votre référence
ISBN:
Our file Notre reference
ISBN:

NOTICE:
The author has granted a non-exclusive license allowing Library and Archives Canada to reproduce, publish, archive, preserve, conserve, communicate to the public by telecommunication or on the Internet, loan, distribute and sell theses worldwide, for commercial or non-commercial purposes, in microform, paper, electronic and/or any other formats.

The author retains copyright ownership and moral rights in this thesis. Neither the thesis nor substantial extracts from it may be printed or otherwise reproduced without the author's permission.

AVIS:
L'auteur a accordé une licence non exclusive permettant à la Bibliothèque et Archives Canada de reproduire, publier, archiver, sauvegarder, conserver, transmettre au public par télécommunication ou par l'Internet, prêter, distribuer et vendre des thèses partout dans le monde, à des fins commerciales ou autres, sur support microforme, papier, électronique et/ou autres formats.

L'auteur conserve la propriété du droit d'auteur et des droits moraux qui protège cette thèse. Ni la thèse ni des extraits substantiels de celle-ci ne doivent être imprimés ou autrement reproduits sans son autorisation.

In compliance with the Canadian Privacy Act some supporting forms may have been removed from this thesis.

While these forms may be included in the document page count, their removal does not represent any loss of content from the thesis.

Conformément à la loi canadienne sur la protection de la vie privée, quelques formulaires secondaires ont été enlevés de cette thèse.

Bien que ces formulaires aient inclus dans la pagination, il n'y aura aucun contenu manquant.

Canada

ABSTRACT

In the past few years, numerous explicit and implicit methods have arisen to deal with the problem of intra-fractional, more specifically, respiration-induced lung tumor motion. Regardless of the method of choice (explicit, implicit, standard), all planning computed tomography (CT) data sets, with the exception of breath-hold acquisitions, are acquired while the target is non-stationary and are thus subject to the presence of motion artifacts. While the presence of these motion-induced aberrations is generally acknowledged, there exists a paucity of published literature concerning their quantification. In the current pursuit to achieve better treatment outcomes in conformal lung radiotherapy, a better understanding must be gained of the detrimental effects of respiration-induced tumor motion upon CT imaging. In this doctoral work, the principles of motion artifacts in CT, the functional dependence of motion artifacts associated with lung tumor motion and the impact of respiration-induced tumor motion upon CT image integrity and target delineation were investigated. A filtered backprojection (FBP) computer model developed in MATLAB and experimentally validated under both static and dynamic conditions served as the main investigational tool. Overall, it was found that respiration-induced motion projects the reconstructed object in directions displaced from its velocity vector. This is in contrast to the smearing of mobile objects in planar radiography which is always along the line of motion. It was also found that spatial extent of a mobile object is distorted from its true shape and location and does not accurately reflect the total volume occupied by the mobile object during the extent of motion captured. Finally, the presence of motion during data acquisition leads to density distributions that are altered from their true physical time-averaged density distributions. A byproduct of this research was the development of a slice-specific imaging technique which provides direct assessment of the extent of free-breathing tumor motion without recourse to gating techniques. The methodology, better known as phase sequence image, was experimentally evaluated using a three-dimensional lung tumor motion phantom and found to accurately estimate the internal target volume at a contrast threshold level of about 20 %.

TABLE OF CONTENTS

CHAPTER 1: INTRODUCTION TO THE PROBLEM OF INTRA-FRACTIONAL TUMOR MOTION IN LUNG RADIOTHERAPY 1

1.1 LUNG CANCER AND RADIOTHERAPY 1

1.2 LUNG RADIOTHERAPY PLANNING 2

1.2.1 Management of intra-fractional tumor motion *3*

1.2.1.1 Explicit techniques *4*

1.2.1.2 Implicit techniques *5*

1.3 MOTIVATION 6

1.4 ORIGINAL CONTRIBUTIONS 7

1.5 THESIS OUTLINE 8

1.6 REFERENCES 10

CHAPTER 2: BASIC PRINCIPLES OF MOTION ARTIFACT IN CT 19

2.1 INTRODUCTION 19

2.2 BACKGROUND 20

2.2.1 Historical overview of CT *20*

2.2.2 Modern CT scanners *21*

2.2.3 Basic principles of CT imaging *22*

2.2.4 Image quality *25*

2.2.4.1 Spatial resolution – resolution at high contrast 25

2.2.4.2 Contrast resolution – resolution at low contrast 26

2.2.4.3 Noise 26

2.2.4.4 Distortions 27

2.2.4.5 Artifacts 27

2.3 COMPUTER SIMULATIONS 27

2.3.1 Motivation for computer simulations *28*

2.3.2 Description of FBP algorithm *29*

2.3.3 Benchmarking of simulation program *30*

2.3.3.1 Object density 30

2.3.3.2 Unsharpness in the imaging plane 33

2.3.3.3 Partial volume effects 33

2.4 PRINCIPLES OF MOTION ARTIFACTS IN CT 35

2.4.1 Stationary object *36*

2.4.2 Linear motion *37*

2.4.2.2 Orthogonal motion 39
2.4.2.3 Combined motion 40
2.5 EXPERIMENTAL VERIFICATION 41
2.5.1 Horizontal SHM *42*
2.5.2 Orthogonal SHM *43*
2.6 SUMMARY AND CONCLUSIONS 43
2.7 REFERENCES 70

CHAPTER 3: CHARACTERIZATION OF MOTION ARTIFACTS ASSOCIATED WITH LUNG TUMOR MOTION 76

3.1 INTRODUCTION 76
3.2 BACKGROUND 77
3.2.1 Motion of lung tumors *77*
3.2.2 Verification of lung tumor motion model *79*
3.2.3 The functional parameters upon which motion artifacts are dependent *82*
3.3 METHODS AND MATERIALS 90
3.3.1 Computer simulations *90*
3.3.2 Experimental verification *92*
3.4 RESULTS AND DISCUSSION 93
3.4.1 In-plane motion *93*
3.4.1.1 Scan time to motion period ratio (alpha) 93
3.4.1.2 Amplitude, phase, orientation & asymmetry 94
3.4.1.3 Angular position of scanner at initiation 94
3.4.2 Orthogonal motion *95*
3.4.2.1 Scan time to motion period ratio (alpha) 95
3.4.2.2 Amplitude, phase & asymmetry 96
3.4.2.3 Angular position of scanner at initiation 96
3.5 SUMMARY AND CONCLUSION 97
3.6 REFERENCES 120

CHAPTER 4: THE IMPACT OF LUNG TUMOR MOTION UPON CT IMAGE INTEGRITY AND TARGET DELINEATION 122

4.1 INTRODUCTION 122
4.2 METHODS AND MATERIALS 122
4.2.1 Impact of motion upon image integrity and target delineation *124*
4.2.1.1 Image integrity 124
4.2.1.2 Target delineation 127
4.2.2 Benchmarking of computer model in high and low contrast levels *128*

4.3 RESULTS AND DISCUSSION 129
  4.3.1 Benchmarking of computer simulation *129*
    4.3.1.1 Stationary test objects 129
    4.3.1.2 Dynamic test objects 130
  4.3.2 Impact of tumor motion upon image integrity and target delineation *132*
    4.3.2.1 Static case 132
    4.3.2.2 Dynamic case 134
4.4 SUMMARY AND CONCLUSION 140
4.5 REFERENCES 195

CHAPTER 5: PHASE SEQUENCE IMAGING TO REVEAL THE TOTAL VOLUME OCCUPIED BY MOBILE LUNG TUMORS 197

5.1 INTRODUCTION 197
5.2 BACKGROUND 198
5.3 METHODS AND MATERIALS 199
  5.3.1 Phantom study *199*
  5.1.2 Clinical application *200*
5.4 RESULTS AND DISCUSSION 202
  5.4.1 Phantom Results *202*
    5.4.1.1 Cylindrical test object 202
    5.4.1.2 Spherical test object 204
  5.4.2 Clinical Application *207*
    5.4.2.1 CTV cross-section variations 207
    5.4.2.2 Geographic failures resulting from application of a single IM 207
    5.4.2.3 Minimum IM necessary to encompass CCTV contour 208
    5.4.2.4 Excess normal tissue volume in MITV 209
5.5 SUMMARY 210
5.6 REFERENCES 233

CHAPTER 6: CONCLUSION 234

6.1 THESIS SUMMARY 234
6.2 ORIGINAL CONTRIBUTIONS 236
6.3 FUTURE WORK 237
6.4 REFERENCES 239

LIST OF TABLES

Table 2.1 Measurements of mean object CT number as a function object diameter resulting from various imaging protocols. Column A – Modified oncology medium thorax, Column B – Full water calibration, and Column C – Half water calibration.................................. 46

Table 3.1 Total image intensity measured from simulation images generated using alpha values encountered in lung radiotherapy planning CT scans.. 98

Table 4.1 Target contour areas for experimental and simulation scans of a 25 mm diameter POM sphere in air and in water at $z = 0$ mm, where partial volume effects are minimal. Also included in the table are the deviations between experimental and simulation target contour centroids.. 144

Table 4.2 Target contour areas for experimental and simulation scans of a 25 mm diameter POM sphere in air and in water at $z = 9$ mm, where partial volume effects are prominent. Also included in the table are the deviations between experimental and simulation target contour centroids.. 145

Table 4.3 Target contour areas for experimental and simulation scans of a 30 mm diameter POM cylinder undergoing a SHM along the horizontal axis of the scanner in both air and water mediums. Also included in the table are the deviations between experimental and simulation target contour centroids.. 146

Table 4.4 Target contour areas for experimental and simulation scans of a 25 mm diameter POM cylinder undergoing a SHM along the z - axis of the scanner in both air and water mediums. Also included in the table are the deviations between experimental and simulation target contour centroids.. 147

Table 4.5 Fraction of CT pixels within 1, 3, 5 and 10 % of the expected time-averaged density for breath-hold scans................................ 148

Table 4.6 Comparison of image density breakdown within the TXO between the rapid and 'slow' CT scans. For each sphere diameter and motion amplitude combination, the mean and standard deviation of the percent density differences within the TXO are presented.....................149

Table 4.8 Comparison of image density breakdown outside the TXO but within a 10 mm region between the rapid and 'slow' CT scans. For each sphere diameter and motion amplitude combination, the mean and standard deviation of the percent density differences within a 10 mm region surrounding the TXO are presented.. 151

Table 4.9 Fraction of pixels within a 10 mm region surrounding the TXO that falls within 1, 3, 5 and 10 % of the expected background density of 0.25 g/cm^3.. 152

Table 4.10 Pixel statistics (mean, minimum, maximum densities) within the TXO of the rapid time-averaged and CT reconstructed images................ 153

Table 4.11 Pixel statistics (mean, minimum, maximum densities) within the TXO of the 'slow' time-averaged and CT reconstructed images............... 154

Table 4.12 CT pixel statistics (mean, minimum, maximum densities) within a 10 mm region outside the TXO.. 155

Table 4.13 Excess areas outside the TXO for both the rapid and 'slow' scans. Excess area is expressed as a percentage of the TXO area........... 156

Table 5.1 Volume external to the TVO encompassed by different iso-contrast CCTVs. All volumes expressed as a percentage of the TVO......... 212

Table 5.2 Minimum uniform margin (mm) required with iso-contrast CCTVs of 10 % to 50 % to fully encompass the TVO.. 213

Table 5.3 Number of slice locations where geographic failure would occur from the application of common uniform margins to either the smallest or largest patient CTV cross-sections.. 214

Table 5.4 ITV and excess irradiated lung volume, which would result at each slice location, from the application of an appropriate single uniform margin to either the smallest or largest CTV cross-sections. Total ITV and excess irradiated lung volumes are displayed in the last row................. 215

Table 5.5 The size of the uniform margin required to completely encompass the CCTV for both the smallest and largest CTV cross-sections at each slice location throughout the volume of interest............................. 216

LIST OF FIGURES

Figure 1.1 Planning target volume and other relevant target related volumes encountered in radiotherapy... 9

Figure 2.1 Historical development of CT scanner configurations. (a) First generation, (b) Second generation, (c) Third generation, and (d) Fourth generation.. 47

Figure 2.2 Simplified example of an iterative reconstruction. (a) Ten integral values are obtained from the object and used to correct the (b) estimated image. This process is repeated (c-g) until the estimate image converges with the image of the actual object.. 48

Figure 2.3 Simplified example of a filtered backprojection reconstruction. Ten projections (only 6 are shown) of a circular object (a) are convolved with a kernel in the spatial domain (b) prior to backprojection (c) to remove the radial blur inherent to the backprojection process (d). (e) Filtered backprojection image of the object with 400 projections............. 49

Figure 2.4 A schematic of the parallel-beam geometry adopted for CT image reconstruction. At each sampled projection angle, φ, a parallel projection is obtained by computing 512 parallel line integrals as per Equation (2.6). In total, 800 parallel projections are used to reconstruct a 512 × 512 image. For the purpose of modeling, all digital phantoms were created by superposing elliptical objects of various densities. (Shown in the above figure is a cross-sectional view of a static 25 mm diameter POM sphere centered in a 200 mm diameter water medium.)................ 50

Figure 2.5 Schematic of cylindrical step Delrin phantom used to benchmark simulation program.. 51

Figure 2.6 Three experimental images of a step-cylindrical Delrin phantom positioned (a) in air and (b) in water. (c) Image intensity values along a horizontal line passing through the center of each cross-section (diameters = 50, 30, 10 mm). These profiles are also termed central horizontal profiles in this work.. 52

Figure 2.7 Calibration curve used to derive the simulation density of POM objects embedded in an air or water medium. The errors bars represent the standard deviation within the region of interest (ROI).................. 53

Figure 2.8 Experimental and simulation central horizontal profiles for a cylindrical step phantom of various diameters: (a) 50 mm, (b) 40 mm, (c) 30 mm, (d) 20 mm, (e) 15 mm and (f) 10 mm.................................. 54

Figure 2.9 Experimental images of a 25 mm POM sphere depicting various partial volume effects. The slice location of each 3 mm CT image is indicated in the schematic. (a) $z = 0$ mm, (b) $z = 3$ mm, (c) $z = 6$ mm, (d) $z = 9$ mm, and (e) $z = 12$ mm.. 55

Figure 2.10 Slice sensitivity profile measured for a 3 mm nominal slice thickness using the impulse method.. 56

Figure 2.11 Central horizontal profiles for a 25 mm POM sphere surrounded by an air medium as measured from (a) experiment and (b) simulation using an infinitesimal slice width only.. 57

Figure 2.12 Central horizontal profiles for a 25 mm POM sphere at (c) z = 9 mm and (d) z = 12 mm. The solid line represents the experimental result while the dashed and dotted lines correspond to the simulation results achieved using a 0.5 mm and 0.25 mm SSP sampling grid........................... 58

Figure 2.13 Reconstruction illustrated for a static sphere: (a) Sinogram, (b) Locus of all line integrals passing through the centroid point of the sphere in sinogram space, (c) Projections through a specific point, (d) Simple backprojection (BP) image, (e) Filtered backprojection (FBP) image, and (f) Intensity profiles along lines B-C (dashed black line (BP), solid black line (FBP)) and E-D (dashed gray line (BP), solid gray line (FBP))... 59

Figure 2.14 Principles of motion artifacts in CT for a sphere moving within the imaging plane: (a) Sinogram, (b) Locus of all line integrals passing through the centroid point of the mobile sphere in sinogram space, (c) Projections through a specific point blurred due to motion, (d) Simple backprojection (BP) image, (e) Filtered backprojection (FBP) image with TXO contour (dashed white line), (f) Intensity profiles along line B-C (dashed black line (BP), solid black line (FBP)), (g) Intensity profiles along line E-D (dashed gray line (BP), solid gray line (FBP)), and (h) Intensity profile along TVO contour.................................... 60

Figure 2.15 Principles of motion artifacts in CT for a sphere moving perpendicular to the imaging plane: (a) Sinogram, (b) Simple backprojection (BP) image, (c) Filtered backprojection (FBP) image, (e) Intensity profiles along lines B-C (dashed black line (BP), solid black line (FBP)) and E-D (dashed gray line (BP), solid gray line (FBP)), and (f) Intensity profile along TXO contour.. 61

Figure 2.16 Principles of motion artifacts for a sphere moving both within and perpendicular to the imaging plane: (a) Sinogram, (b) Simple backprojection (BP) image, (c) Filtered backprojection (FBP) image, (e) Intensity profiles along lines B-C (dashed black line (BP), solid black line (FBP)) and E-D (dashed gray line (BP), solid gray line (FBP)), and (f) Intensity profile along TXO contour................................. 62

Figure 2.17 Graphic representation of three-dimensional motion phantom used in the investigation of motion artifacts in CT. Three cam actuated plates are used to define the motion along the horizontal (x), vertical (y) and orthogonal (z) directions. An adjustable electric motor is employed to control the motion period of a test object attached to a removable attachment arm. For clarity only the horizontal and orthogonal motion plates and their respective eccentric driver cams are shown........... 63

Figure 2.18 Experimental and simulation images of three POM cylinders undergoing a simple harmonic motion along the horizontal axis in a water background. **(a)** 10 mm diameter cylinder – 25 mm SHM, **(b)** 30 mm diameter cylinder – 15 mm SHM, and **(c)** 50 mm diameter cylinder – 5 mm SHM.. 64

Figure 2.19 Experimental and simulation images of three POM cylinders undergoing a simple harmonic motion along the horizontal axis in an air background. **(a)** 10 mm diameter cylinder – 5 mm SHM, **(b)** 30 mm diameter cylinder – 15 mm SHM, and **(c)** 50 mm diameter cylinder – 25 mm SHM.. 65

Figure 2.20 Experimental and simulation central horizontal profiles for the cylinders and horizontal SHMs shown in Figures 2.18 – 2.19................... 66

Figure 2.21 Experimental and simulation images of three POM spheres undergoing a simple harmonic motion along the *z*-axis of the scanner in a water background. **(a)** 10 mm diameter sphere – 25 mm SHM, **(b)** 30 mm diameter sphere – 15 mm SHM, and **(c)** 50 mm diameter sphere – 5 mm SHM.. 67

Figure 2.22 Experimental and simulation images of three POM spheres undergoing a simple harmonic motion along the *z*-axis of the scanner in an air background. **(a)** 10 mm diameter sphere – 5 mm SHM, **(b)** 30 mm diameter sphere – 15 mm SHM, and **(c)** 50 mm diameter sphere – 25 mm SHM.. 68

Figure 2.23 Experimental and simulation central horizontal profiles for the spheres and orthogonal SHMs shown in Figures 2.21 – 2.22.................. 69

Figure 3.1 Measured superior-inferior displacements of both tumor (solid) and diaphragm (dashed) for patient 1 99

Figure 3.2 Superior-inferior tumor displacement for patient 1 comparing experimental data (solid) with modeling (dashed) according to Equation 3.1 with $n = 2$, $\phi = 70.95^\circ$ 100

Figure 3.3 Superior-inferior diaphragm displacement for patient 1 comparing experimental data (solid) with modeling (dashed) according to Equation 3.1 with $n = 2$, $\phi = 70.95^\circ$ 101

Figure 3.4 Superior-inferior tumor displacement for patient 3 comparing experimental data (solid) with modeling (dashed) according to Equation 3.1 with $n = 2$, $\phi = 71.25^\circ$. The presence of an irregularity in the breathing pattern is indicated by the boxed area 102

Figure 3.5 Superior-inferior tumor displacement for patient 5 comparing experimental data (solid) with modeling (dashed) according to Equation 3.1 with $n = 3$, $\phi = 40.1^\circ$. The presence of a conspicuous rest or dwell phase at expiration is clearly evident 103

Figure 3.6a Stationary point like object in the CT imaging plane 104

Figure 3.6b Simple backprojection to reconstruct an image of a stationary point like object 105

Figure 3.6c Point like object moving along a strait line in the CT imaging plane 106

Figure 3.6d Simple back projection to reconstruct an image of a point like object moving along a strait line in the CT image plane. For clarity, only one half of full rotation reconstruction shown 107

Figure 3.7 Imaging and object parameters governing motion artifacts in computed tomography 108

Figure 3.8 (a) Simulation sinograms, (b) Simulation images, and (c) Experimental CT images of a 6.4 mm diameter POM cylinder moving along the horizontal axis of the scanner and imaged under various alpha conditions [0, 0.25, 0.5, 0.75, 1]. Simulation parameters: ($l_{x0} = Ax/2$, $l_{y0} = 0$, $l_{z0} = 0$, $A_x = 25$ mm, $A_y = 0$, $A_z = 0$, $n = 1$, $\phi_x = 0^\circ$, $\varphi_o = 0^\circ$) 109

Figure 3.9 (a) Simulation sinograms, and (b) Simulation images of a 6.4 mm POM cylinder moving along the horizontal axis of the scanner with various amplitudes of motion [25, 30, 35 mm]. Simulation parameters: ($l_{x0} = A_x/2$, $l_{y0} = 0$, $l_{z0} = 0$, A_x = variable, $A_y = 0$, $A_z = 0$, $\alpha = 0.5$, $n = 1$, $\phi_x = 0^\circ$, $\varphi_o = 0^\circ$)........ 110

Figure 3.10 (a) Simulation sinograms, and (b) Simulation images of a 6.4 mm diameter POM cylinder moving along the horizontal axis of the scanner with various phase of motions [0°, 45°, 90°]. Simulation parameters: ($l_{x0} = A_x/2$, $l_{y0} = 0$, $l_{z0} = 0$, $A_x = 25$ mm, $A_y = 0$, $A_z = 0$, $\alpha = 0.5$, $n = 1$, ϕ_x = variable, $\varphi_o = 0^\circ$)........ 111

Figure 3.11 (a) Simulation sinograms, and (b) Simulation images of a 6.4 mm POM cylinder moving along various angular lines, $\theta\,(\varphi_o)$, of the scanner [180°, 225°, 270°]. Simulation parameters: ($l_{x0} = A_x/2$, $l_{y0} = A_y/2$, $l_{z0} = 0$, $A_x + A_y = 25$ mm, $A_z = 0$, $\alpha = 0.5$, $n = 1$, $\phi_x = 0^\circ$, $\phi_y = 0^\circ$, $\varphi_o = 0^\circ$)........ 112

Figure 3.12 (a) Simulation sinograms, (b) Simulation images, and (c) Central horizontal profiles (CHPs) of a 6.4 mm diameter POM cylinder moving along the horizontal axis of the scanner with various asymmetry parameters [1, 2, 3]. Simulation parameters: ($l_{x0} = A_x/2$, $l_{y0} = 0$, $l_{z0} = 0$, $A_x = 25$ mm, $A_y = 0$, $A_z = 0$, $\alpha = 0.5$, n = variable, $\phi_x = 0^\circ$, $\varphi_o = 0^\circ$)........ 113

Figure 3.13 The angular dependence of motion artifact pattern upon beta (β), an angle which defines the angular difference between the orientation of motion in the imaging plane, $\theta\,(\varphi_o)$, and the initial projection angle, φ_o. (a) Simulation images for various beta values [180°, 135°, 90°] and a 25 mm motion along the horizontal axis of the scanner ($\theta\,(\varphi_o) = 0^\circ$). (b) Simulation images for various initial projection angles [0°, 45°, 90°] and a constant beta value of 180°. Simulation parameters: ($l_{x0} = A_x/2$, $l_{y0} = A_y/2$, $l_{z0} = 0$, $A_x + A_y = 25$ mm, $\alpha = 0.5$, $\phi_x = 0^\circ$, $\phi_y = 0^\circ$, $n = 1$, φ_o = variable)........ 114

Figure 3.14 (a) Simulation sinograms, (b) Simulation images using infinitesimal slice width, (c) Experimental CT images, and (d) Simulation images using finite slice width of a 25 mm POM sphere moving along the z-axis of the scanner (orthogonal to image plane) and scanned under various alpha conditions [0, 0.25, 0.5, 0.75, 1]. Simulation parameters: ($l_{x0} = 0$, $l_{y0} = 0$, $l_{z0} = A_z/2$, $A_x = 0$, $A_y = 0$, $A_z = 25$ mm, α = variable, $n = 1$, $\phi_z = 45^\circ$, $\varphi_o = 0^\circ$)........ 115

Figure 3.15 (a) Simulation sinograms, and (b) Simulation images of a 25 mm diameter POM sphere moving along the z-axis of the scanner with various amplitude of motions [20, 25, 30 mm]. Simulation parameters: ($l_{x0} = 0$, $l_{y0} = 0$, $l_{z0} = A_z/2$, $A_x = 0$, $A_y = 0$, A_z = variable, $\alpha = 0.5$, $n = 1$, $\phi_z = 45^o$; $\varphi_o = 0^o$).. 116

Figure 3.16 (a) Simulation sinograms, and (b) Simulation images of a 25 mm diameter POM sphere moving along the z-axis of the scanner with various phase of motions [45°, 67.5°, 90°]. Simulation parameters: ($l_{x0} = 0$, $l_{y0} = 0$, $l_{z0} = A_z/2$, $A_x = 0$, $A_y = 0$, $A_z = 20$ mm, $\alpha = 0.5$, $n = 1$, ϕ_z = variable, $\varphi_o = 0^o$)... 117

Figure 3.17 (a) Simulation sinograms, and (b) Simulation images of a 25 mm diameter POM sphere moving along the z-axis of the scanner with various asymmetry parameters [1, 2, 3]. Simulation parameters: ($l_{x0} = 0$, $l_{y0} = 0$, $l_{z0} = A_z/2$, $A_x = 0$, $A_y = 0$, $A_z = 20$ mm, $\alpha = 0.5$, n = variable, $\phi_z = 0^o$, $\varphi_o = 0^o$).. 118

Figure 3.18 The impact upon the motion artifact pattern of initiating the imaging sequence at various angular positions [0°, 45°, 90°]. Simulation parameters: ($l_{x0} = 0$, $l_{y0} = 0$, $l_{z0} = A_z/2$, $A_x = 0$, $A_y = 0$, $A_z = 20$ mm, $\alpha = 0.5$, $n = 1$, $\phi_z = 45^o$, φ_o = variable).. 119

Figure 4.1 Experiment (a) and simulation (b) target delineation results for a 25 mm diameter sphere scanned at z = 0 mm where partial volume effects are minimal. Three gray-level threshold contours are shown, I_{10} (dotted line), I_{50} (dashed line) and I_{90} (solid line).................................. 157

Figure 4.2 Experiment (a) and simulation (b) target delineation results for a 25 mm diameter sphere scanned at z = 9 mm where partial volume effects are observed. Three gray-level threshold contours are shown, I_{10} (dotted line), I_{50} (dashed line) and I_{90} (solid line).................................. 158

Figure 4.3 Target delineation results for a 30 mm cylinder undergoing a 15 mm SHM along horizontal axis. Contours defined using a 10 % (dotted line), 50 % (dashed line) and 90 % (solid line) threshold percentage value. (a) Experiment and (b) Simulation.. 159

Figure 4.4 Target delineation results for a 25 mm sphere undergoing a 15 mm SHM along the z-axis. Contours defined using a 10 % (dotted line), 50 % (dashed line) and 90 % (solid line) threshold percentage value. (a) Experiment and (b) Simulation.. 160

Figure 4.5 Time-averaged and CT reconstructed breath-hold images for three clinically relevant sphere sizes as well as difference density maps.. 161

Figure 4.6 Penumbra in CT images of well-defined objects. Section of central horizontal density profile illustrating the penumbral region and density difference frequency distribution within a 2 mm ring centered on TXO for the (a) large 50 mm diameter sphere, (b) intermediate 30 mm diameter sphere and (c) small 10 mm diameter sphere..................162

Figure 4.7 Target segmentation results for the (a) large, (b) intermediate and (c) small static spheres. For visualization purposes, only five target contours are displayed [I_{10}, I_{20}, I_{30}, I_{70}, I_{90}].. 163

Figure 4.8 Target cross-section to TXO ratio as a function of contrast threshold level.. 164

Figure 4.9 TXO coverage as a function of contrast threshold level.................165

Figure 4.10 Excess TXO coverage as a function of contrast threshold level...... 166

Figure 4.11 Time-averaged and CT reconstructed images for the large sphere (diameter = 50 mm) undergoing a small SHM (A_x = Az = 5 mm) and imaged with a rapid 1 second acquisition time (alpha = 0.25). Also shown are the percent density difference maps within the TXO and within a 10 mm region surrounding the TXO along with their corresponding histograms... 167

Figure 4.12 Time-averaged and CT reconstructed images for the large sphere (diameter = 50 mm) undergoing an intermediate SHM (A_x = Az = 15 mm) and imaged with a rapid 1 second acquisition time (alpha = 0.25). Also shown are the percent density difference maps within the TXO and within a 10 mm region surrounding the TXO along with their corresponding histograms... 168

Figure 4.13 Time-averaged and CT reconstructed images for the large sphere (diameter = 50 mm) undergoing a large SHM (A_x = Az = 25 mm) and imaged with a rapid 1 second acquisition time (alpha = 0.25). Also shown are the percent density difference maps within the TXO and within a 10 mm region surrounding the TXO along with their corresponding histograms...169

Figure 4.14 Time-averaged and CT reconstructed images for the medium sphere (diameter = 30 mm) undergoing a small SHM (A_x = Az = 5 mm) and imaged with a rapid 1 second acquisition time (alpha = 0.25). Also shown are the percent density difference maps within the TXO and within a 10 mm region surrounding the TXO along with their corresponding histograms.. 170

Figure 4.15 Time-averaged and CT reconstructed images for the medium sphere (diameter = 30 mm) undergoing an intermediate SHM (A_x = Az = 15 mm) and imaged with a rapid 1 second acquisition time (alpha = 0.25). Also shown are the percent density difference maps within the TXO and within a 10 mm region surrounding the TXO along with their corresponding histograms.. 171

Figure 4.16 Time-averaged and CT reconstructed images for the medium sphere (diameter = 30 mm) undergoing a large SHM (A_x = Az = 25 mm) and imaged with a rapid 1 second acquisition time (alpha = 0.25). Also shown are the percent density difference maps within the TXO and within a 10 mm region surrounding the TXO along with their corresponding histograms.. 172

Figure 4.17 Time-averaged and CT reconstructed images for the small sphere (diameter = 10 mm) undergoing a small SHM (A_x = Az = 5 mm) and imaged with a rapid 1 second acquisition time (alpha = 0.25). Also shown are the percent density difference maps within the TXO and within a 10 mm region surrounding the TXO along with their corresponding histograms.. 173

Figure 4.18 Time-averaged and CT reconstructed images for the small sphere (diameter = 10 mm) undergoing an intermediate SHM (A_x = Az = 15 mm) and imaged with a rapid 1 second acquisition time (alpha = 0.25). Also shown are the percent density difference maps within the TXO and within a 10 mm region surrounding the TXO along with their corresponding histograms.. 174

Figure 4.19 Time-averaged and CT reconstructed images for the small sphere (diameter = 10 mm) undergoing a large SHM (A_x = Az = 25 mm) and imaged with a rapid 1 second acquisition time (alpha = 0.25). Also shown are the percent density difference maps within the TXO and within a 10 mm region surrounding the TXO along with their corresponding histograms.. 175

Figure 4.20 Time-averaged and CT reconstructed images for the large sphere (diameter = 50 mm) undergoing a small SHM (A_x = Az = 5 mm) and imaged with a 'slow' 4 second acquisition time (alpha = 1). Also shown are the percent density difference maps within the TXO and within a 10 mm region surrounding the TXO along with their corresponding histograms.. 176

Figure 4.21 Time-averaged and CT reconstructed images for the large sphere (diameter = 50 mm) undergoing an intermediate SHM (A_x = Az = 15 mm) and imaged with a 'slow' 4 second acquisition time (alpha = 1). Also shown are the percent density difference maps within the TXO and within a 10 mm region surrounding the TXO along with their corresponding histograms... 177

Figure 4.22 Time-averaged and CT reconstructed images for the large sphere (diameter = 50 mm) undergoing a large SHM (A_x = Az = 25 mm) and imaged with a 'slow' 4 second acquisition time (alpha = 1). Also shown are the percent density difference maps within the TXO and within a 10 mm region surrounding the TXO along with their corresponding histograms.. 178

Figure 4.23 Time-averaged and CT reconstructed images for the medium sphere (diameter = 30 mm) undergoing a small SHM (A_x = Az = 5 mm) and imaged with a 'slow' 4 second acquisition time (alpha = 1). Also shown are the percent density difference maps within the TXO and within a 10 mm region surrounding the TXO along with their corresponding histograms.. 179

Figure 4.24 Time-averaged and CT reconstructed images for the medium sphere (diameter = 30 mm) undergoing an intermediate SHM (A_x = Az = 15 mm) and imaged with a 'slow' 4 second acquisition time (alpha = 1). Also shown are the percent density difference maps within the TXO and within a 10 mm region surrounding the TXO along with their corresponding histograms... 180

Figure 4.25 Time-averaged and CT reconstructed images for the medium sphere (diameter = 30 mm) undergoing a large SHM (A_x = Az = 25 mm) and imaged with a 'slow' 4 second acquisition time (alpha = 1). Also shown are the percent density difference maps within the TXO and within a 10 mm region surrounding the TXO along with their corresponding histograms.. 181

Figure 4.26 Time-averaged and CT reconstructed images for the small sphere (diameter = 10 mm) undergoing a small SHM (A_x = Az = 5 mm) and imaged with a 'slow' 4 second acquisition time (alpha = 1). Also shown are the percent density difference maps within the TXO and within a 10 mm region surrounding the TXO along with their corresponding histograms.. 182

Figure 4.27 Time-averaged and CT reconstructed images for the small sphere (diameter = 10 mm) undergoing an intermediate SHM (A_x = Az = 15 mm) and imaged with a 'slow' 4 second acquisition time (alpha = 1). Also shown are the percent density difference maps within the TXO and within a 10 mm region surrounding the TXO along with their corresponding histograms.. 183

Figure 4.28 Time-averaged and CT reconstructed images for the small sphere (diameter = 10 mm) undergoing a large SHM (A_x = Az = 25 mm) and imaged with a 'slow' 4 second acquisition time (alpha = 1). Also shown are the percent density difference maps within the TXO and within a 10 mm region surrounding the TXO along with their corresponding histograms.. 184

Figure 4.29 Fraction of pixels within the TXO in agreement. Agreement, in this case, is deemed to exist when CT pixel densities deviate by no more than 1 % from their corresponding time-average pixel densities................ 185

Figure 4.30 Segmentation results for the largest sphere (diameter = 10 mm) undergoing a SHM of various amplitudes during CT scanning. For visualization purposes, only five iso-intensity contours [I_{10}, I_{30}, I_{50}, I_{70}, I_{90}] are presented along with the TXO contour.......................... 186

Figure 4.31 Segmentation results for the intermediate sphere (diameter = 30 mm) undergoing a SHM of various amplitudes during CT scanning. For visualization purposes, only five iso-intensity contours [I_{10}, I_{30}, I_{50}, I_{70}, I_{90}] are presented along with the TXO contour......................... 187

Figure 4.32 Segmentation results for the small sphere (diameter = 10 mm) undergoing a SHM of various amplitudes during CT scanning. For visualization purposes, only five iso-intensity contours [I_{10}, I_{30}, I_{50}, I_{70}, I_{90}] are presented along with the TXO contour........................ 188

Figure 4.33 Percentage of TXO covered by the iso-intensity contours for the largest sphere (diameter = 50 mm) undergoing a SHM of various amplitudes during rapid and 'slow' CT scanning................................... 189

Figure 4.34 Percentage of TXO covered by the iso-intensity contours for the intermediate sphere (diameter = 30 mm) undergoing a SHM of various amplitudes during rapid and 'slow' CT scanning.......................... 190

Figure 4.35 Percentage of TXO covered by the iso-intensity contours for the smallest sphere (diameter = 10 mm) undergoing a SHM of various amplitudes during rapid and 'slow' CT scanning.................................... 191

Figure 4.36 Density along the rapid and 'slow' TXO contours for the largest sphere (diameter = 50 mm) undergoing a SHM of various amplitudes during CT scanning: (a) 5 mm, (b) 15 mm, and (c) 25 mm........................ 192

Figure 4.37 Density along the rapid and 'slow' TXO contours for the intermediate sphere (diameter = 30 mm) undergoing a SHM of various amplitudes during CT scanning: (a) 5 mm, (b) 15 mm, and (c) 25 mm............ 193

Figure 4.38 Density along the rapid and 'slow' TXO contours for the smallest sphere (diameter = 10 mm) undergoing a SHM of various amplitudes during CT scanning: (a) 5 mm, (b) 15 mm, and (c) 25 mm........................ 194

Figure 5.1 Experimental setup for cylindrical phantom.............................. 217

Figure 5.2 PSI set for 10 mm cylinder.. 218

Figure 5.3 TXO, TXO^{90} and individual iso-contrast contours..................... 219

Figure 5.4 Iso-contrast CCTV contours for lateral cylinder motion in comparison to the TXO.. 220

Figure 5.5 Experimental set-up for spherical test phantom.......................... 221

Figure 5.6b PSI set at z = 0 mm for 25 mm sphere with 5 mm motion............ 222

Figure 5.6b PSI set at z = 9 mm for 25 mm sphere with 5 mm motion.............. 222

Figure 5.7a PSI set for 25 mm sphere at z = 0 mm with 15 mm motion........... 223

Figure 5.7b PSI set for 25 mm sphere at z = 9 mm with 15 mm motion........... 223

Figure 5.8a PSI set for 25 mm sphere at z = 0 mm with 25 mm motion........... 224

Figure 5.8b PSI set for 25 mm sphere at z = 9 mm with 25 mm motion........... 224

Figure 5.9 Iso-contrast CCTV contours for 25 mm sphere with 5 mm motion at a) z = 0 mm and b) z = 9 mm.......... 225

Figure 5.10 Iso-contrast CCTV contours for 25 mm sphere with 15 mm motion at a) z = 0 mm and b) z = 9 mm.......... 226

Figure 5.11 Iso-contrast CCTV contours for 25 mm sphere with 25 mm motion at a) z = 0 mm and b) z = 9 mm.......... 227

Figure 5.12 Plot of volume of TVO encompassed by CCTVs of various iso-contrast threshold levels.......... 228

Figure 5.13 Iso-contrast contours for image #7 of the PSI set for the 25 mm sphere with 5 mm motion at a) z = 0 mm and b) z = 9 mm. TXO is denoted by the thick black contour and the ITV formed by the addition of a 5 mm uniform margin to the 50 % contour is revealed by the thick dashed line.......... 229

Figure 5.14 Iso-contrast contours for image #7 of the PSI set for the 25 mm sphere with 15 mm motion at a) z = 0 mm and b) z = 9 mm. TXO is denoted by the thick black contour and the ITV formed by the addition of a 15 mm uniform margin to the 50 % contour is revealed by the thick dashed line.......... 230

Figure 5.15 Iso-contrast contours for image #7 of the PSI set for the 25 mm sphere with 25 mm motion at a) z = 0 mm and b) z = 9 mm. TXO is denoted by the thick black contour and the ITV formed by the addition of a 25mm uniform margin to the 50 % contour is revealed by the thick dashed line.......... 231

Figure 5.16 CCTV contours generated, along with the smallest (a) and largest (b) CTV contours, at each slice location throughout the volume of interest.......... 232

LIST OF SYMBOLS

A	Major axis of ellipse, amplitude of motion
A_x	Amplitude of motion in the x-direction
A_y	Amplitude of motion in the y-direction
A_z	Amplitude of motion in the z-direction
AB	Source to detector line
α	Alpha, acquisition time to motion period ratio
B	Minor axis of ellipse
β	Orientation of the motion in the image plane
δ	Projection angle increment
δt	Time interval
ΔT	Non-imaging interval
ϕ	Phase of motion
ϕ_x	Phase of motion in the x-direction
ϕ_n	Phase of motion at i^{th} acquisition
ϕ_y	Phase of motion in the y-direction
ϕ_z	Phase of motion in the z-direction
$\Delta\phi$	Phase interval
$h_m[x,y]$	Linear system's response to mobile input delta function
I_o	Incident photon intensity
$\overline{I_o}$	Mean image intensity within region of interest after image import
$I[x, y]$	Image
$I_\varphi(x_r)$	Transmission photon intensity
φ	Projection angle
φ_o	Initial projection angle
l_0	Position of the tumor at the end of expiration
l_{x0}	x coordinate of tumor at the end of expiration
l_{y0}	y coordinate of tumor at the end of expiration

l_{z0}	z coordinate of tumor at the end of expiration
$l(t)$	Position of the tumor as a function of time t
$\lambda_{\varphi}(x_r)$	Projection
μ	Linear attenuation coefficient
μ_T	Linear attenuation coefficient of tissue
μ_{water}	Linear attenuation coefficient of water
n	Acquisition number
n	Asymmetry parameter describing the shape of the sinusoidal function
$O\,[x, y]$	Two-dimensional representation of object
$O\,[x, y, z]$	Three-dimensional representation of object
$PSF\,[x,y]$	Blurring function of the imaging system
θ	Angular position of point P
$\theta(\varphi)$	Angular position of point P at projection angle φ
$\theta(\varphi_o)$	Angular position of object at initial projection angle φ_o
r	Radial position of point P
$r(\varphi)$	Radial position of point P at projection angle φ
R	Distance from origin to the focal spot of the CT x-ray tube
R	Radius of object
ρ	Density
ρ_o	Density of object
ρ_w	Density of water
σ	Pixel noise
t	Time
t	Time
τ_m	Period of motion (breath cycle)
τ_s	Rotation period of the CT x-ray tube
ω_s	Rotational speed of the CT x-ray tube
z_{slice}	Slice location
$[x_c, y_c]$	x and y coordinates of centroid

$[x_r, y_r]$	x and y coordinates in the rotated frame
$[X^S, Y^S]$	x and y coordinates of focal spot in the stationary frame
$[X^o, Y^o]$	x and y coordinates of mobile point like object in the stationary frame

LIST OF ABBREVIATIONS

AP	Anterior-posterior
ART	Algebraic reconstructive technique
BP	Backprojection
CAD	Cumulative absolute difference
CC	Cranial-caudal
CCTV	Composite clinical target volume
CHP	Central horizontal profile
CT	Computerized tomography
CTV	Clinical target volume
FBP	Filtered backprojection
FOM	Field of measurement
FOV	Field of view
FWHM	Full width at half maximum
FWTM	Full width at tenth maximum
GTV	Gross tumor volume
HU	Hounsfield unit
ICRU	Internal Commission on Radiation Units and Measurements
IM	Internal margin
IMRT	Intensity modulated radiation therapy
ITV	Internal target volume
LR	Left-right
MITV	Minimum internal target volume
MTF	Modulated transfer function
NCIC	National Cancer Institute of Canada
NSCLC	Non-small cell lung cancer
PET	Positron emission tomography
POM	Polyoxymethylene
PSF	Point spread function

PSI	Phase sequence imaging
PTV	Planning target volume
ROI	Region of interest
RTRT	Real-time tumor tracking radiotherapy
SCLC	Small cell lung cancer
SHM	Simple harmonic motion
SI	Superior-inferior
SSP	Slice sensitivity profile
TXO	Total cross-sectional area occupied by the mobile object
TVO	Total volume occupied by the mobile object
UFCT	Ultra-fast computerized tomography

Chapter 1: Introduction to the problem of intra-fractional tumor motion in lung radiotherapy

1.1 Lung cancer and radiotherapy

Lung cancer remains the leading cause of cancer death in Canada. Roughly one-third of cancer deaths in men (29.6%) and one-quarter of cancer deaths in women (25.5%) are due to lung cancer alone. With an estimated 9,800 new cases in women and 11,900 new cases in men, lung cancer is the second leading form of cancer in Canada. On average, 417 Canadians will be diagnosed with lung cancer every week and 363 Canadians will succumb weekly from this disease [NCIC 2004].

Two histological types describe the majority of primary lung cancers, small-cell lung cancer (SCLC) and non-small-cell lung cancer (NSCLC). SCLC accounts for 20 percent of all lung cancers and is defined as a malignant transformation of the neuroendocrine cells [Mo 2001]. NSCLC, the most prominent type of lung cancer, is of epithelial origin and includes such cell types as adenocarcinoma, squamous cell carcinoma and large-cell carcincoma [Kh 1999, Mo 2001].

The prognosis for lung cancer remains dismal, with a 15 % overall five-year relative survival rate [Ke 2004a]. Surgical resection, the treatment of choice for patients with clinical Stage I and II NSCLC, yields a disappointing 30 % five-year survival rate and is limited in applicability to only 20 % of all cases [An 2000]. For those patients with medically inoperable stage I and II lung cancer, radical radiotherapy may be administered. Unfortunately, radiotherapy alone, or in combination with chemotherapy, has to date proven inadequate in curing the vast majority of lung cancer patients treated with radical intent. Local control rates with conventional radiotherapy as low as 6 – 32 % at five years have been reported in the literature [Si 1998]. Efforts at improving treatment outcome through dose escalation are currently underway. Unfortunately, tumor recurrence at the primary disease site is still observed when doses are elevated by 50 % over levels previously deemed necessary [Me 2001].

One highly plausible explanation for the current noted failure to achieve local tumor control in lung radiotherapy is inadequate coverage of the tumor with treatment portals (geometric failure). Improper management of geometrical uncertainties, such as inaccuracies in the delineation of the gross tumor volume (GTV), unknown extent of microscopic tumor involvement, variations in tumor size, shape and position due to external and internal motion and finally patient set-up disparities, can readily result in geometric failure. In cancer sites such as the lung, where tumors can move significantly during the course of radiotherapy planning and treatment [Ro 1990, Ek 1998, Ha 1999, Ba 2001, Ch 2001, Si 2003], it is strongly believed that improper management of intra-fractional tumor motion is the largest contributing factor to geographic failure [Yu 1998, Ke 2001, Ma 2001, Bo 2002, Ch 2003, Ji 2003, Bo 2004].

1.2 Lung radiotherapy planning

The standard approach to account for planning and treatment uncertainties in lung radiotherapy is to construct a planning target volume (PTV), which is to receive the prescribed dose, through the application of safety margins. The PTV is a static, geometric concept specific to radiotherapy for dose planning and specification [ICRU 1993, ICRU 1999]. Figure 1.1 illustrates the PTV and other tumor-related volumes involved in radiotherapy treatment planning: the gross tumor volume (GTV), the clinical target volume (CTV), and the internal target volume (ITV).

Generally, for CT-planned lung cancer radiotherapy, the gross tumor volume (the visible extent of the malignant disease), is outlined on a slice by slice basis. In view of the fact that microscopic involvements of the tumor are not visible in CT images, a margin is then added to the gross tumor volume (GTV) to include suspected microscopic spread, creating the clinical target volume (CTV). Using the latest International Commission on Radiation Measurements and Units (ICRU) nomenclature [ICRU 1999], to obtain the PTV requires the application of two distinct margins, an internal margin and a setup uncertainty margin. While the internal margin, used in the definition of the internal target volume (ITV), must account for variations in size, shape and position of the CTV in reference to the patient's coordinate system, the set-up margin must account for variations in patient-beam positioning in reference to the treatment machine coordinate system [ICRU 1999].

Regardless of the nomenclature used to define the PTV, the overall safety margin specified by the radiation oncologist, in consultation with the medical physicist, must be sufficient in size to account for all possible planning and treatment geometrical variations while concomitantly minimizing the volume of healthy tissues which will receive the prescribed dose.

1.2.1 Management of intra-fractional tumor motion

Many centers currently evaluate the magnitude of intra-fractional lung tumor motion present by direct observation under fluoroscopic examination using a radiotherapy simulator [Ch 2001]. At best, this method provides only a limited number of planar projections, usually just an anterior-posterior and medio-lateral, from which to assess the limits of motion. The accuracy of determining internal margins by this method is further impaired when fluoroscopy fails, as is often the case, to yield reliable tumor edge delineation. Lacking reliable direct information, one is then forced to make certain population-based assumptions about the size and shape of margins to be applied.

Even if accurate motion ranges could be determined, their correct application is problematic. The common approach to treatment planning for mobile lung tumors utilizes a single CT scan acquired during quiet respiration. Without knowledge of the specific point or phase in the trajectory captured at each slice location, one must assume that each CT image reveals in some manner the mean size, shape and position of the gross tumor. The validity of this assumption was examined by Shimizu *et al.* using sequential CT scanning at the same table position [Sh 2000a]. Their study revealed that breathing motion could cause considerable changes in the area and location of the tumor and suggested that conventional CT alone under quiet respiration was inadequate to determine the PTV in small-field treatments for lung cancer.

In the past few years, numerous explicit and implicit methods to the problem of dealing with respiration-induced tumor motion in radiotherapy have arisen in response to the shortcomings associated with the preceding standard approach.

1.2.1.1 Explicit techniques

Methods that explicitly account for respiration-induced tumor motion in radiation therapy may be broadly classified as breath-hold, forced shallow breathing, respiratory gating and real-time tumor tracking techniques. Breath-hold techniques significantly reduce respiration-induced tumor motion. In breath-hold radiotherapy, respiration is altered either voluntarily through patient coaching [Ba 1998, Ha 1999, Ma 2000, Ro 2000, Ki 2001, Ba 2001, Yo 2002, On 2003] or controlled by means of mechanical devices such as occlusion valves [Wo 1999, Da 2001, Re 2003a, Re 2003b]. Forced shallow breathing techniques employ a stereotactic frame with an attached pressure plate to limit intra-fractional tumor motion [Ne 2000]. Respiratory gating techniques limit the radiation delivery, both for imaging purposes and treatment, to a specific phase of the patient's breathing cycle. The position and width of the gate is determined by monitoring patient breathing using either external [Ku 1996, Ku 2000, Ma 2001, Ve 2003a, Ve 2003b] or internal [Sh 2000b, Sh 2000c, Sh 2001, Ha 2002, Se 2002, Sh 2003] markers. Real-time tumor tracking radiotherapy (RTRT) is an extension of gated radiotherapy currently under development. The ultimate goal of RTRT is to move the radiation beam in space so as to follow the tumor's changing position during the respiratory cycle [Ke 2004a, Ke 2004b].

For the most part, the above explicit methods require the implementation of gating equipment and software not widely available in clinical environments. Even when available, these methods are not always well tolerated by every patient. Furthermore, recent studies have suggested that some forms of gating are not effective and might even be counterproductive for some patients [Oz 2002].

1.2.1.2 Implicit techniques

In the absence of explicit methods, implicit techniques can be used to account for respiration-induced tumor motion in imaging and treatment planning. The most common implicit imaging techniques used to define the internal target volume are 'slow' CT scanning, positron emission tomography (PET) and four-dimensional CT. Long acquisition times, on the order of the respiration cycle, are employed in the 'slow' CT scanning method to capture the full extent of tumor motion during quiet respiration [La 2001, va 2001, de 2003]. Even though more reproducible tumor volumes are realized with this "slow" scan method, a greater amount of motion-induced distortions must be admitted in the images. The potential of PET to provide patient-specific internal target volumes has recently been established under ideal conditions [Ca 2003]. However, important clinical parameters such as edge detection threshold values must be investigated further before this technique can be implemented clinically [Ca 2003]. Four-dimensional computed tomography (4-D CT), employ either gated data acquisition [Ke 2004b] or the post processing of images acquired during free breathing [Ri 2003,Ve 2003a, Ke 2004a], to properly account for intra-fractional tumor motion. In 4-D CT, each image corresponds to a specific phase of motion, the entire set of which may be used to determine the mean tumor position, the range of tumor motion and its trajectory to a specified level of accuracy.

1.3 Motivation

With the exception of motion arresting (breath-hold) schemes, all planning CT images are acquired while the target is non-stationary and as such are subject to the presence of motion artifacts. The effective elimination of respiration-induced motion artifacts requires scan times much shorter than possible with current clinical scanners [Ri 1992, Mc 2000]. Correcting for the presence of motion during imaging has been investigated [Dh 2001a, Dh 2001b, Lu 2002]. These correction techniques, however, all require either specialized software, and or hardware (e.g. dual head CT), or invasive patient interventions (e.g. gold seed implants), not readily available to most centers. Hence, motion artifacts remain an integral component of all current non-motion arresting CT planning images.

While the presence of these motion-induced aberrations is generally acknowledged [Ch 2004, Mc 2000], there exists a paucity of published literature concerning their quantification. The detrimental effect of motion-induced artifacts on image quality cannot be ignored in the pursuit of improved treatment outcome [Bo 2004].

It is therefore the main goal of this doctoral work to investigate the fundamental nature of CT image artifacts associated with motion characteristic of lung tumors and the implications for target delineation. It will be shown that the net effect of these motion-induced image distortions/artifacts is threefold:

(1) *The spatial extent of a mobile object is distorted from its true shape and location and does not accurately reflect the total volume occupied (TVO) during the extent of motion captured;*

(2) *The density of the reconstructed mobile object is altered from its true physical time-averaged density; and*

(3) *The densities of the surrounding structures are also altered from their true values.*

A byproduct of this research was the development of a slice-specific imaging technique which provides direct assessment of the extent of free-breathing tumor motion without recourse to gating techniques. This methodology, called the phase sequence imaging (PSI) technique, is presented in the later portion of this thesis and is applicable in the numerous facilities which currently do not have access to methods that explicitly account for intra-fractional tumor motion during radiotherapy.

1.4 Original contributions

While motion artifacts arising from physiological functions such as respiration and cardiac contraction have long been acknowledged as a problem in CT, very little quantitative material has appeared in the literature concerning the origin, nature, and effects of these image artifacts. To the best knowledge of the author of this thesis, having conducted an extensive review of the available literature, this work presents the first in depth analysis of respiration-induced motion artifacts in CT. Specifically, the following contributions of new knowledge are presented:

- ✧ *Identification of the parameters that govern both the pattern and magnitude of artifacts associated with continuous (periodic) motion;*

- ✧ *An analysis of the functional dependence of respiration-induced motion artifact patterns;*

- ✧ *An analysis of the impact of respiration-induced motion upon CT image integrity and contour delineation of the mobile object; and*

- *A novel approach (the PSI technique) to contour delineation of mobile lung tumors*

1.5 Thesis outline

The remainder of this thesis is organized into five chapters. **Chapter 2** presents the basic principles of image artifacts generation in CT associated with continuous tumor motion. In addition, a detailed section is provided on the benchmarking of the CT simulation filtered backprojection algorithm used in Chapters 2, 3 and 4. **Chapter 3** provides an investigation of the functional dependence of motion artifacts associated with respiration-induced lung tumor motion. **Chapter 4** examines the impact of respiration-induced tumor motion on CT image integrity and target delineation. **Chapter 5** presents a slice-specific CT imaging technique to reveal the total volume occupied by mobile tumors for non-gated lung radiotherapy. Finally, **Chapter 6** provides a summary, general conclusions and future perspectives.

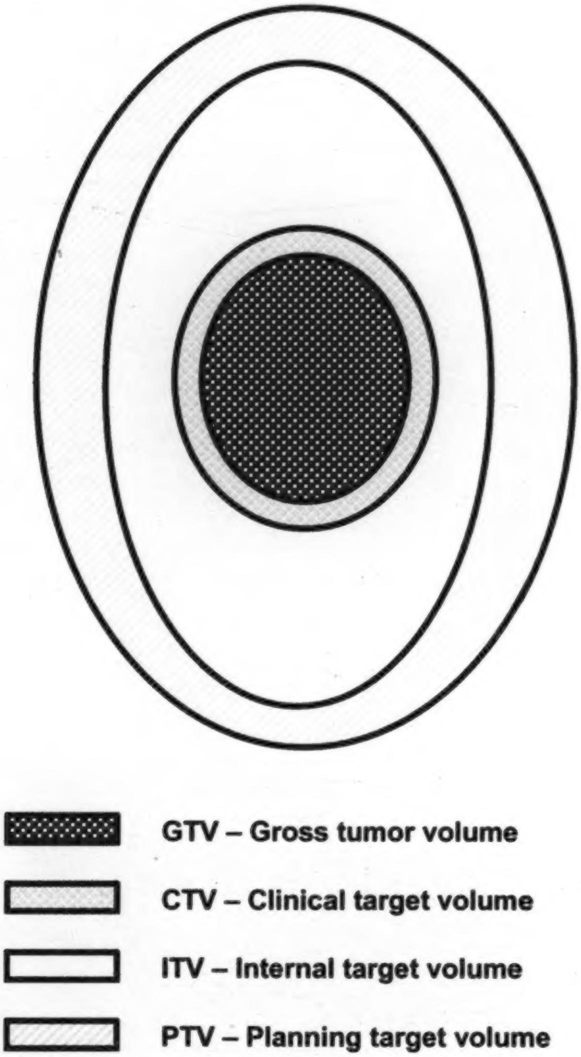
GTV – Gross tumor volume
CTV – Clinical target volume
ITV – Internal target volume
PTV – Planning target volume

Figure 1.1 Planning target volume and other relevant target related volumes encountered in radiotherapy.

1.6 References

[An 2000] W.J.A. Anderson, J.J.A McAleer, S. Stranex *et al.*, "Radical radiotherapy for inoperable non-small cell lung cancer: what factors predict prognosis?," Clinical Oncology. **12**, 48 – 52 (2000)

[Ba 2001] E.A. Barnes, B.R. Murray, D.M Robinson, *et al.*, "Dosimetric evaluation of lung tumor immobilization using breath-hold at deep inspiration," Int. J. Radiat. Oncol. Biol. Phys. **50**, 1091 – 1098 (2001)

[Ba 1998] J. Balter, K. Lam, C. McGinn, *et al.*, "Improvement of CT-based treatment-planning models of abdominal targets using static exhale imaging," Int. J. Radiat. Oncol. Biol. Phys. **41**, 939 – 943 (1998)

[Bo 2004] T. Bortfeld and G.T.Y. Chen, "Introduction: Intrafractional organ motion and its management," Semin. Radiat. Oncol. **14**, 1 (2004)

[Bo 2002] T. Bortfeld, K. Jokivarsi, M. Goitein, *et al.*, "Effects of intra-fraction motion on IMRT dose delivery: statistical analysis and simulation," Phys. Med. Biol. **47**, 2203 – 2220 (2002)

[Ca 2003] C.B. Caldwell, K. Mah, M. Skinner, *et al.*, "Can PET provide the 3D extent of tumor motion for individualized internal target volumes? A phantom study of the limitations of CT and the promise of PET," Int. J. Radiat. Oncol. Biol. Phys. **55**, 1381 – 1393 (2003)

[Ch 2001] Q.S. Chen, M.S. Weinhous, F.C. Deibel, *et al.*, "Fluoroscopic study of tumor motion due to breathing: Facilitating precise radiation therapy for lung cancer patients," Med. Phys. **28**, 1850 – 1856 (2001)

[Ch 2003] C.S. Chui, E. Yorke and L. Hong, "The effects of intra-fraction motion on the delivery if intensity-modulated field with a multileaf collimator," Med. Phys. **30**, 1736 – 1746 (2003)

[Ch 2004] G.T.Y. Chen, J.H. Kung, and K.P. Beaudette, "Artifacts in computed tomography scanning of moving objects," Semin. Radiat. Oncol. **14**, 19 – 26 (2004)

[Da 2001] L.A. Dawson, K.K. Brock, S. Kazanjian, *et al.*, "The reproducibility of organ position using active breathing control (ABC) during liver radiotherapy," Int. J. Radiat. Oncol. Biol. Phys. **51**, 1410 – 1421 (2001)

[de 2003] J.R. de Koste, F.J. Lagerwaard, H.C. de Boer, *et al.*, "Are multiple CT scans required for planning curative radiotherapy in lung tumors of the lower lobe?," Int. J. Radiat. Oncol. Biol. Phys. **55**, 1394 – 1399 (2003)

[Dh 2001a] A.C. Dhanantwari, S. Stergiopoulos, and I. Iakovidis, "Correcting organ motion artifacts in x-ray CT medical imaging systems by adaptive processing. I. Theory," Med. Phys. **28**, 1562 – 1576 (2001)

[Dh 2001b] A.C. Dhanantwari, S. Stergiopoulos, N. Zamboglou, *et al.*, "Correcting organ motion artifacts in x-ray CT based on tracking of motion phase by the spatial overlap correlator. II. Experimental study," Med. Phys. **28**, 1577 – 1596 (2001)

[Ek 1998] L. Ekberg, O. Holmberg, L. Wittgren, *et al.*, "What margins should be added to the clinical target volume in radiotherapy treatment planning for lung cancer?," Radiother. Oncol. **48**, 71 – 77 (1998)

[Ha 1999] J. Hanley, M.M. Debois, D. Mah *et al.*, "Deep inspiration breath-hold technique for lung tumors: the potential value of target immobilization and reduced lung density in dose escalation," Int. J. Radiat. Oncol. Biol. Phys. **45**, 603 – 611 (1999)

[Ha 2002] T. Harada, H. Shirato, S. Ogura, *et al.*, "Real-time tumor-tracking radiation therapy for lung carcinoma by the aid of insertion of a gold marker using bronchofiberscopy," Cancer **95**, 1720 – 1727 (2002)

[ICRU 1993] International Commission on Radiation Units and Measurements, "Prescribing, recording and reporting photon beam therapy," ICRU Report **50**, ICRU Publications, Bethesda, Maryland (1993).

[ICRU 1999] International Commission on Radiation Units and Measurements, "Prescribing, recording and reporting photon beam therapy (Supplement to ICRU Report 50)," ICRU Report **62**, ICRU Publications, Bethesda, Maryland (1999).

[Ji 2003] S.B. Jiang, C. Pope, K. Al Jarrah, *et al.*, "An experimental investigation of intra-fractional organ motion effects in lung IMRT treatments," Phys. Med. Biol. **48**, 1773 – 1784 (2003)

[Ke 2001] P.J. Keall, V.R. Kini, S.S. Vedam, *et al.*, "Motion adaptive x-ray therapy: A feasibility study," Phys. Med. Biol. **46**, 1 – 10 (2001)

[Ke 2004a] P. Keall, “4-dimensional computed tomography imaging and treatment planning,” Semin. Radiat. Oncol. **14**, 81 – 90 (2004)

[Ke 2004b] P.J. Keall., “Acquiring 4D thoracic CT scans using a multislice helical method,” Phys. Med. Biol. **49**, 2053 – 2067 (2004)

[Kh 1999] F.R. Khuri, S.M. Keller, and H. Wagner Jr., “Non-small-cell lung cancer and mesothelioma,” in *Cancer management: A multidisciplinary approach* edited by R. Pazdur and W.J. Hoskins, Research and Representation, Melville, NY (1999)

[Ki 2001] D.J. Kim, B.R. Murray, R. Halperin *et al.*, “Held-breath self-gating technique for radiotherapy of non-small-cell lung cancer: A feasibility study,” Int. J. Radiat. Oncol. Biol. Phys. **49**, 43 – 49 (2001)

[Ku 1996] H.D. Kubo and B.C. Hill, “Respiration gated radiotherapy treatment: a technical study,” Phys. Med. Biol. **41**, 83 – 91 (1996)

[Ku 2000] H. Kubo, P. Len, S. Minohara, *et al.*, “Breathing-synchronized radiotherapy program at the University of California Davis Cancer Center,” Med. Phys. **27**, 346 – 353 (2000)

[La 2001] F.J. Lagerwaard, J.R. Van Sornsen de Koste, M.R. Nijssen-Visser, *et al.*, “Multiple “slow” CT scans for incorporating lung tumor mobility in radiotherapy planning,” Int. J. Radiat. Oncol. Biol. Phys. **51**, 932 – 937 (2001)

[Lu 2002] W. Lu and T. R. Mackie, "Tomographic motion detection and correction directly in sinogram space," Phys. Med. Biol. **47**, 1267 – 1284 (2002)

[Ma 2000] D. Mah, J. Hanley, K. Rosenzwig, *et al.*, "Technical aspects of the deep inspiration breath hold technique in the treatment of thoracic cancer," Int. J. Radiat. Oncol. Biol. Phys. **48**, 1175 – 1185 (2000)

[Ma 2001] G.S. Mageras, E. Yorke, K. Rosenzweig, *et al.*, "Fluoroscopic evaluation of diaphragmatic motion reduction with a respiratory gated radiotherapy system," J. Appl. Clin. Med. Phys. **2**, 191 – 200 (2001)

[Mc 2000] C.H. McCollough, M.R. Bruesewithz, T.R. Daly, *et al.*, "Motion artifacts in subsecond conventional CT and electron-beam CT: pictorial demonstration of temporal resolution," Radiographics **20**, 1675 – 1681 (2000)

[Me 2001] M. Mehta, R. Scimger, R. Mackie, *et al.*, "A new approach to dose escalation in non-small cell lung cancer," Int. J. Radiat. Oncol. Biol. Phys. **49**, 23 – 33 (2001)

[Mo 2001] G. Moore-Higgs, R.A. Sthohl, and M. Suntharalingam, "Lung Cancer" in *Outcomes in Radiation Therapy: Multidisciplinary management*, edited by D. Watkins-Burner, G. Moore-Higgs, and M. Haas, Jones and Bartlett Publishers, Sudbury (2001)

[NCIC 2004] National Cancer Institute of Canada: Canadian Cancer Statistics 2004, Toronto, Canada. (2004)

[Ne 2000] Y. Negoro, Y. Nagat, T. Aoki, *et al.*, "The effectiveness of an immobilization device in conformal radiotherapy for lung tumor: reduction of respiratory tumor movement and evaluation of the daily setup accuracy," Int. J. Radiat. Oncol. Biol. Phys. **50**, 889 – 898 (2000)

[On 2003] H. Onishi, K. Kuriyama, T. Komiyama, *et al.*, " A new irradiation system for lung cancer combining linear accelerator, computed tomography, patient self-breath-holding, and patient-directed beam-control without respiratory monitoring devices," Int. J. Radiat. Oncol. Biol. Phys. **56**, 14 – 20 (2003)

[Oz 2002] C. Ozhasoglu and M.J. Murphy, "Issues in respiratory motion compensation during external-beam radiotherapy," Int. J. Radiat. Oncol. Biol. Phys. **52**, 1389 – 99 (2002)

[Re 2003a] V. M. Remouchamps, F. A. Vicini, M. B. Sharpe, *et* al., "Significant reductions in heart and lung doses using deep inspiration breath hold with active breathing control and intensity-modulated radiation therapy for patients with locoregional breast irradiation," Int. J. Radiat. Oncol. Biol. Phys. **55**, 392 – 406 (2003)

[Re 2003b] V. M. Remouchamps, N. Letts, F. A. Vicini, *et al.*, "Initial clinical experience with moderate breath hold using an active breathing control device in the treatment of patients with left-sided breast cancer using external beam radiation therapy," Int. J. Radiat. Oncol. Biol. Phys. **56**, 704 – 715 (2003)

[Ri 1992] C. J. Ritchie, J. D. Godwin, C. R. Crawford, *et al.*, "Minimum scan speeds for suppression of motion artifacts in CT," Radiology **185**, 37 – 42 (1992)

[Ri 2003] E. Rietzel, G. T. Chen, K. P. Doppke, *et al.*, "4D computed tomography for treatment planning," Int. J. Radiat. Oncol. Biol. Phys. **57**, Supplement 1 S232-S233 (2003)

[Ro 1990] C.S. Ross, D.H. Hussey, E.C. Pennington, *et al.*, "Analysis of movement of intrathoracic neoplasms using ultrafast computerized tomography," Int. J. Radiat. Oncol. Biol. Phys. **18**, 671 – 677 (1990)

[Ro 2000] K.E. Rosenzweig, J. Hanley, D. Mah, *et al.*, "The deep inspiration breath hold technique in the treatment of inoperable non-small cell lung cancer," Int. J. Radiat. Oncol. Biol. Phys. **48**, 81 – 87 (2000)

[Se 2002] Y. Seppendwoole, H. Shirato, K. Kitamura, *et al.*, "Precise and real-time measurement of 3D tumor motion in lung due to breathing and heartbeat, measured during radiotherapy," Int. J. Radiat. Oncol. Biol. Phys. **53**, 822 – 834 (2002)

[Sh 2000a] S. Shimizu, H. Shirato, K. Kagei, *et al.*, "Impact of respiratory movement on the computed tomographic images of small lung tumors in three-dimensional (3D) radiotherapy," Int. J. Radiat. Oncol. Biol. Phys. **46**, 1127 – 1133 (2000)

[Sh 2000b] H. Shirato, S. Shimizu, K. Kitamura, *et al.*, "Four-dimensional treatment planning and fluoroscopic real-time tumor tracking radiotherapy for moving tumor," Int. J. Radiat. Oncol. Biol. Phys. **48**, 435 – 442 (2000)

[Sh 2000c] H. Shirato, S. Shimizu, T. Kunieda, *et al.*, "Physical aspects of a real-time tumor-tracking system for gated radiotherapy," Int. J. Radiat. Oncol. Biol. Phys. **48**, 1187 – 1195 (2000)

[Sh 2001] S. Shimizu, H. Shirato, S. Ogura, *et al.*, "Detection of lung tumor movement in real-time tumor-tracking radiotherapy," Int. J. Radiat. Oncol. Biol. Phys. **51**, 304 – 310 (2001)

[Sh 2003] H. Shirato, T. Harada, T. Harabayashi, *et al.*, "Feasibility of insertion/implantation of 2.0-mm-diameter gold internal fiducial markers for precise set-up and real-time tumor tracking in radiotherapy," Int. J. Radiat. Oncol. Biol. Phys. **56**, 240 – 247 (2003)

[Si 1998] G.S. Sibley, "Radiotherapy for patients with medically inoperable stage I non-small cell lung carcinoma: Smaller volumes and higher doses – a review," Cancer. **82**, 433 – 438 (1998)

[Si 2003] K.E. Sixel, M. Ruschin, R. Tirona, *et al.*, "Digital fluoroscopy to quantify lung tumor motion: potential for patient-specific planning target volumes," Int. J. Radiat. Oncol. Biol. Phys. **57**, 717 – 723 (2003)

[Un 2004] R.W.M. Underberg, F.J. Lagerwaard, J.P. Cuijpers, *et al.*, "Four-dimensional CT scans for treament planning in stereotactic radiotherapy for stage I lung cancer," Int. J. Radiat. Oncol. Biol. Phys. **60**, 1283 – 1290 (2004)

[va 2001] J.R. van Sornsen de Koste, F. J. Lagerwaard, R. H. Schuchhard-Schipper, *et al.*, "Dosimetric consequences of tumor mobility in radiotherapy of stage I non-small cell lung cancer -- an analysis of data generated using 'slow' CT scans," Radiat. Oncol. **61**, 93 – 99 (2001)

[Ve 2003a] S.S. Vedam, P.J. Keall, V.R. Kini, *et al.*, "Acquiring a four-dimensional computed tomography dataset using an external respiratory signal," Phys. Med. Biol. **48**, 45 – 62 (2003)

[Ve 2003b] S.S. Vedam, V.R. Kini, P.J. Keall, *et al.*, "Quantifying the predictability of diaphragm motion during respiration with a noninvasive external marker," Med. Phys. **30**, 505 – 513 (2003)

[Wo 1999] J.W. Wong, M.B. Sharpe, D.A. Jaffray, *et al.*, "The use of active breathing control (ABC) to reduce margin for breathing motion," Int. J. Radiat. Oncol. Biol. Phys. **44**, 911 – 919 (1999)

[Yo 2002] E.D. Yorke, L. Wang, K.E. Rosenzweig, *et al.*, "Evaluation of deep inspiration breath-hold lung treatment plans with Monte Carlo dose calculation," Int. J. Radiat. Oncol. Biol. Phys. **53**, 1058 – 1070 (2002)

[Yu 1998] C.X. Yu. D.A. Jaffray, and J.W. Wong, "The effects of intra-fraction organ motion on the delivery of dynamic intensity modulation," Phys. Med. Biol. **43**, 91 – 104 (1998)

Chapter 2: Basic principles of motion artifact in CT

2.1 Introduction

Three-dimensional conformal radiotherapy (CRT) techniques, such as conventional 3D-CRT and intensity modulated radiotherapy (IMRT), rely heavily upon the anatomical information provided by computed tomography for target volume delineation and dose calculations. One implicit assumption in current CT image reconstruction algorithms is the spatial invariance of objects during data acquisition. When movement is present during data acquisition, motion artifacts arise.

There are numerous sources of motion that can be encountered during CT scanning, each with its own detrimental effect. One such source of motion is patient movement, often referred to in radiotherapy planning as external motion. Numerous approaches are commonly employed during CT scanning to reduce patient motion, including rapid scan times, immobilization techniques and patient education [Bo 2000]. Another source of motion is respiration and cardiac function. Unfortunately, even with the relatively fast acquisition times possible with today's scanners, internal tumor motion associated with these physiological events can still be problematic [Bu 1994]. As indicated in the previous chapter, numerous investigators have examined the problem of internal tumor motion associated with respiration in CT imaging. As a result, new CT imaging techniques have been developed, including breath-hold, 'slow' spiral, gated and very recently four-dimensional CT scanning [Ku 1996, Ba 1998, Ha 1999, Wo 1999, Ku 2000, Ba 2001, Da 2001, Se 2002, La 2001, va 2001, Sh 2003, On 2003, Ri 2003, Ke 2004a, Ke 2004b].

With the exception of breath-hold imaging schemes, all current approaches acquire images while the target is non-stationary and, as such, are subject to the presence of motion artifacts. Because the outcome of modern radiotherapy is highly governed by the accuracy of target volume delineation, it is important to understand how these motion artifacts arise in CT imaging and their effects on the images produced. It is thus the main objective of this chapter to describe the basic principles which govern the artifacts that arise in CT images due to continuous internal tumor motion of the form associated with free-breathing respiration.

2.2 Background

2.2.1 Historical overview of CT

Even though computed tomography (CT) surfaced in the early 1970s, the mathematical ideas on which it is based were developed by Radon in 1917 [Ka 1988, Bu 1994]. Radon revealed that the distribution of a material property in an object layer could be derived if the integral values along any number of lines passing through that layer were known [Bu 1994]. Radon's central slice theorem, which is the key to tomographic imaging, wasn't exploited for medical purposes until 1963 [Ka 2000]. In an effort to improve radiotherapy planning, A.M. Cormack, a physicist at Tufts University, developed, without knowledge of Radon's work, a method of determining linear absorption coefficient distributions based on transmission measurements [Co 1963a, Co 1963b, Ka 2000]. Cormack carried out experiments using gamma-rays and reported his results but never carried them any further [Bu 1981].

It took roughly another ten years before tomographic imaging became available clinically. In 1971, G.N. Hounsfield, an engineer at EMI Ltd, built a prototype machine (EMI Mark I scanner) after successfully reconstructing images of a phantom using a well-collimated gamma source and a sodium iodide scintillation detector [Bu 1981, Ka 2000]. The above experimental set-up used by Hounsfield is commonly known today as "first generation" CT scanner geometry. In this geometry, parallel transmission measurements are acquired by first translating a well-collimated source-detector pair across the field of measurement and then rotating to a new angular position before repeating the above measurement procedure (see Figure 2.1a). Because of its simplicity, this scanning configuration is often adopted for computer simulations [Ka 1988].

Similar to his experimental set-up, the CT prototype machine built by Hounsfield acquired transmission measurements by means of a translation/rotation sequence. However to speed the acquisition process, the single detector and pencil beam arrangement was replaced by a linear array of detectors and a small fan beam as illustrated in Figure 2.1b [Bu 1994, Ka 2000]. Even though it took several minutes to acquire the transmission data with this "second generation" scanner geometry, the potential of computed tomography to provide high contrast soft-tissue images was clearly established and enthusiastically welcomed by the medical community [Bu 1981, Mc 1998].

At this point in time, only brain imaging was possible. Whole body scanning became feasible with the advent of fan beam scanning in the mid-seventies. In 1976, the first whole body scanner with a rotating fan beam and detector arc assembly emerged on the market (see Figure 2.1c) [Bu 1994, Ka 2000]. Because translation was completely eliminated in these so-called "third geometry" scanners, scan times were reduced to about 20 seconds. In 1978, 'fourth-generation" CT scanners, with a ring of stationary detectors fully encircling the patient, surfaced, leaving only the source to rotate (see Figure 2.1d) [Ka 2000].

2.2.2 Modern CT scanners

Most modern CT scanners are based on either third or fourth generation scanner geometry [Ka 2000]. Compared to early models, however, today's machines are capable of much shorter acquisition times due, in part, to the development of continuous rotation and data acquisition systems based on slip ring technology [Ka 2000]. The introduction of slip ring technology in the late eighties also provided a platform for the development of spiral CT in 1990 [Ka 1990, Ka 1991]. In comparison to conventional axial CT systems where the x-ray tube and detector assembly rotates completely around the patient before shifting the table to a new position, attenuation measurements in spiral CT are performed in non-planar geometry and then converted to planar geometry via interpolation [Ka 1990, Ka 1991]. Spiral scanning offers many advantages over conventional scanning including shorter overall scan times and the flexibility of reconstructing transverse images at any point along the patient's longitudinal axis [Ka 2000].

Further reductions in volume scanning time were made possible with the introduction of multi-row detector systems in 1994. In its infancy stage, multi-slice scanners could acquire 2 tomographic slices in a single rotation [Ka 2000]. Nowadays, multi-slice CT scanners can reconstruct up to 40 images per second [Philips]. Most CT scanners available on the market today offer multi-slice imaging capabilities and are based on "third generation" geometry [Ka 2000].

2.2.3 Basic principles of CT imaging

The fundamental principles of image reconstruction in CT can be readily understood by considering a first generation CT scanner geometry where multiple parallel-beam x-ray transmission measurements are obtained by first translating a well collimated source-detector pair across the object, and then rotating it about the scanner isocenter by small angular increments, and repeating this procedure until all transmission measurements are acquired (see Figure 2.1a). Assuming, for simplicity, that one has a very narrow pencil beam of mono-energetic photons and that no scatter radiation reaches the detector, then the transmission intensity, $I_\varphi(x_r)$, is given by the following extension of Beer's law [Ka 2000, We 1990]

$$I_\varphi(x_r) = I_o e^{-\int_{AB} \mu[x,y]dy_r} \tag{2.1}$$

where φ is the angular position of the rotated frame $[x_r, y_r]$ with respect to the stationary frame $[x, y]$, also known as the projection angle, I_o is the incident photon intensity, μ $[x, y]$ is the two-dimensional distribution of the linear attenuation coefficient and *AB* is the source to detector line. If we further assume that Compton scattering is the only interaction, the linear attenuation coefficient distribution may be identified with the density distribution ρ $[x, y]$ of the medium [We 1990]. Mathematically, a single projection of the object, $\lambda_\varphi(x_r)$, can be defined as

$$\lambda_\varphi(x_r) = \ln\left(\frac{I_o}{I_\varphi(x_r)}\right) = \int_{AB} u[x,y]dy_r \tag{2.2}$$

or

$$\lambda_\varphi(x_r) = \ln\left(\frac{I_o}{I_\varphi(x_r)}\right) \cong k \int_{AB} \rho[x,y]dy_r \tag{2.3}$$

where k is a proportionality constant. For parallel beam geometry, the projection is simply a collection of numerous parallel line integrals measured at a given projection angle. The task of image reconstruction is to recover the linear attenuation coefficient or density distribution from a set of projection measurements, $\lambda(x_r, \varphi)$ [Ka 2000].

There are two major categories of CT image reconstruction algorithms, namely filtered backprojection (or corresponding Fourier) and iterative reconstruction. The algebraic reconstruction technique (ART), one of a variety of iterative reconstruction algorithms, is an intuitive approach to image reconstruction that was used in the first commercial EMI scanner [Ka 2000]. In essence, ART is a mathematical "trial and error" process in which an estimated image is iteratively corrected to approach the "correct" image using measured transmission data [Za 1981]. Figure 2.2 illustrates the basic principles of ART. The object in the simplified example is a 2 x 2 non-uniform density distribution (see Figure 2.2b). The initial estimated image is a 2 x 2 uniform density distribution (see Figure 2.2c). In the first pass of the reconstruction process, the horizontal projection values (6, 6) of the estimated image are compared to those obtained from the real object (8, 8) and the differences are equally distributed between the corresponding pixels to generate a new estimated image (see Figure 2.2d). The process is repeated at other projection angles until the estimated image yields the correct projection values. Iterative techniques require that all transmission data be collected before image reconstruction can begin and are vulnerable to noise [Za 1981].

Filtered backprojection is the reconstruction method adopted by most of the current CT scanners as it is comparatively less susceptible to noise and is inherently faster [Ka 2000, Za 1981]. In filtered backprojection, each measured projection is first convolved with a kernel and then back projected along the lines of the original projection paths (see Figure 2.3) [Ka 2000]. The type of convolution kernel used to remove the radial blurring inherent in the simple backprojection (e.g. smoothing, standard or edge enhancement) depends on the image characteristics sought.

Computed tomography images are displayed using CT numbers which are related to attenuation coefficients according to the following linear scale [Ka 2000]:

$$\text{CT value} = \frac{(\mu_T - \mu_{water})}{\mu_{water}} \times 1000 \ HU \tag{2.4}$$

where μ_T and μ_{water} are the linear attenuation coefficients of tissues and water, respectively. In honor of the inventor of computed tomography, CT numbers are specified in Hounsfield units (HU). On the Hounsfield scale, water has a CT number of 0 HU, air a value of – 1000 HU and soft-tissue values between roughly 20 HU and 70 HU.

The attenuation information collected during the scanning process can be represented in a Cartesian coordinate system, better known as sinogram space [We

1990], where the axes are given by x_r and φ, respectively. In this coordinate system, each point corresponds to a distinct line integral in the object space [We 1990]. Conversely, the locus of all line integrals passing through a point, P, of a stationary object traces out a cosine curve in the sinogram space [We 1990].

2.2.4 Image quality

The ability to visualize and outline internal anatomic structures in computed tomography depends on the overall quality of the image [Bu 1994, Sp 1994]. Image quality, however, is an intricate feature which is shaped by five main factors: spatial resolution, contrast resolution, noise, distortions and artifacts [Sp 1994]. Here, a brief description of each will be presented.

2.2.4.1 Spatial resolution – resolution at high contrast

Conceptually, spatial resolution describes the capability of an imaging system to differentiate small objects that are adjacent to one another [Ha 1991]. Spatial resolution can be measured directly with hole patterns and bar tests or indirectly from the point spread function (PSF) and modulation transfer function (MTF) [Mc 2003]. In a perfect imaging system, every point in the object would correspond to a point in the image [Sp 1994]. However, in real systems, image blur is an unavoidable reality. Numerous factors contribute to the blurring process in computed tomography systems, including focal spot size, detector width, ray sampling, pixel size and choice of convolution kernel [Mo 1983].

Since computed tomography can, to some extent, be modeled as a space-invariant, linear imaging system, any image, $I\,[x, y]$, at a given slice location $[z = z_{slice}]$ can, to a first approximation, be mathematically computed in advance according to [Ka 2000]:

$$I[x,y] = O[x,y] \otimes PSF[x,y] \qquad (2.5)$$

where $O[x,y]$ is the object's two-dimensional density distribution and $PSF[x,y]$ is the blurring function of the imaging system.

2.2.4.2 Contrast resolution – resolution at low contrast

Contrast resolution describes the system's ability to distinguish detail at low contrast [Ka 2000, Ha 1991]. Numerous factors, including object size, contrast between object and background, image noise and the system's MTF [Wa 1997] influence the low-contrast resolution of a computed tomography imaging system. Low-contrast resolution can be determined subjectively using specialized low-contrast phantoms. However, a more quantitative descriptor of contrast resolution is the contrast-detail curve, which reveals the impact of the system's quantum noise and spatial resolution on the detectability of object detail [Ka 2000].

2.2.4.3 Noise

Pixel noise in computed tomography results chiefly from statistical variations in the primary and attenuated intensity measurements due to quantum noise in the detected number of x-ray quanta [Ka 2000]. Other sources of noise, such as electronic noise, contribute to the overall CT image noise but their input is generally minimal in today's modern CT scanners [Ka 2000]. Pixel noise, σ, is determined by computing the standard deviation of image intensities from their mean value within a uniform region of interest. Measurements for pixel noise determination are often performed using cylindrical water phantoms.

2.2.4.4 Distortions

Geometric image distortions present as inaccurate representations of an object's size, shape and location and can occur in CT as a result of mechanical misalignment of the scanner unit during image acquisition [Ke 1991]. The most common sources of geometric distortions are related to improper recording of gantry tilt angles and CT couch velocity vectors, both of which lead to shearing distortions [Zy 1996]. Table speed inaccuracies as well as errors in the enlargement or reduction of the field of view (FOV) also lead to geometric distortions, referred to as scaling distortions [Zy 1996]. The magnitude of geometrical distortions that result during a specific image acquisition can be assessed through the use of specialized calibration devices [Zy 1996].

2.2.4.5 Artifacts

Artifacts are simply distortions or errors in the image that are unrelated to the object being imaged [Mo 1983]. The most common sources of artifacts are motion, the presence of metallic objects, beam hardening, scattered radiation, partial volume effects, sampling errors and out-of field measurements [Ka 2000, Lu 2003]. Artifacts can appear in the image as geometrical inconsistencies, blurring, streaks or inaccurate CT numbers [Lu 2003]. In order to improve image quality, many schemes aimed at eliminating or minimizing these artifacts have been devised [Hs 1995, Ka 2000]. As far as motion artifacts are concerned, many techniques have been proposed to reduce the corresponding streaking or blurring which results. Most are, however, either limited in their applicability or require sophisticated software/hardware not readily available in most centers [Lu 2002, Dh 2001a, Dh 2001b, Li 2001, Cr 1996].

2.3 Computer simulations

This investigation into the effects of lung tumor motion upon CT imaging for radiotherapy application was conducted using both experimental and computer modeling techniques. While experimental measurement remains the final arbiter, computer simulations provide a powerful investigational tool with which to explore this subject.

2.3.1 Motivation for computer simulations

Computer modeling was employed as an integral component of this investigation because it allows better control over motion and scanning parameters which dictate the image reconstruction process. Furthermore, since experimental CT reconstruction is a mathematical process carried out by a computerized system, computer modeling provides a natural avenue with which to investigate the impact of motion upon this imaging modality. In addition, experimental images entail the superposition of numerous processes which can confound the identification of individual effects. For example, an object of variable cross-section moving in directions perpendicular to the image plane may produce experimental images which contain both orthogonal motion artifacts and partial volume effects. A method by which one might experimentally separate these two distinct contributions is not known. Computer modeling, on the other hand, allows the reproduction of each of these processes separately or in combination so that the proper contribution of each may be evaluated. Finally and most importantly, it was not possible to construct a physical phantom replicating all the essential features of tumors in lung tissue. While lung tumors exhibit densities typical of soft tissue (0.9 – 1.0 g/cm^3), and thus can easily be constructed from tissue-equivalent materials such as wax and polystyrene [Na 2002, Mi 2001], lung tissues, on the other hand, have a typical density range of approximately 0.2 to 0.35 g/cm^3 [Kh 2000]. Construction of a physical lung tumor phantom with which to study motion artifacts requires the free movement of the mass representing the tumor within the "lung tissue" material. Practically speaking, this requires the use of either a gaseous or liquid medium to serve as lung tissue equivalent material. Employing a gaseous medium requires the use of a pressure vessel in order to achieve the physical densities required which, in turn, raises numerous engineering difficulties with regard to ease and safety of use. With regards the use of a liquid medium, none could be identified with a density falling within the required range. The only common liquid which even approaches these physical requirements is hexane with a density of 0.66 g/cm^3. The generally volatile nature of low density liquids rules out this approach. Finding an adequate physical medium within the correct density range and which also allows free movement of macroscopic objects within it is thus highly problematic, and hence the utility of computer modeling which is unbound by these practical constraints.

The ability of computer simulation to accurately reproduce experimental results under both static and dynamic conditions was assessed using high and low contrast geometries. High contrast arrangements were provided by imaging solid test objects, machined from Polyoxymethylene or POM material (ρ = 1.41 g/cm^3) [Dupont product information data sheet, DuPont Company], in air ($\rho \approx$ 0.001 g/cm^3). Low contrast geometries were achieved using the same test objects in a 20 cm diameter cylindrical water phantom (ρ = 1.0 g/cm^3). Application to the intermediate contrast dynamic situation more representative of real lung tumors was achieved by extrapolation between these two bounding conditions. It is reasonable to assume that the accuracy achieved in both the high and low contrast geometries extends to the intermediate tumor-lung tissue contrast situation as well.

2.3.2 Description of FBP algorithm

A parallel-beam filtered backprojection (FBP) algorithm was developed in MATLAB [Version 6.5, Release 13, Mathworks Inc., June 2002] to compute infinitesimally thin transverse images of static and mobile three-dimensional digital phantoms. FBP was used throughout this research as it is the predominant reconstruction method used in clinical settings and is the only algorithm available experimentally for this investigation. For the purpose of modeling, all digital phantoms were created by the superposition of circular objects of various uniform densities [Ka 1988]. Figure 2.4 depicts a cross-sectional view of one digital phantom used in the investigation (static 25 mm diameter POM sphere centered in a 200 mm diameter water medium) and some of the important imaging parameters.

To reconstruct transverse CT images at a given slice location, 800 evenly spaced parallel projections were acquired over 360° of rotation by summing the parallel projection of each individual ellipse present in the infinitesimally thin slice. The parallel projections were determined by computing 512 line integral values within a circular field of measurement (FOM) using the following analytical expression [Ka 1988]

$$\lambda_{\varphi}(x_r) = \frac{2\rho r^2}{a^2(\varphi)}\sqrt{a^2(\varphi) - x_r^2(\varphi)} \tag{2.6}$$

where ρ is the density of the circular cross-section, r is the radius of the circle, $a^2(\varphi) = r^2\cos^2(\varphi) + r^2\sin^2(\varphi)$ and $x_r(\varphi) = x\cos(\varphi) + y\sin(\varphi)$. Before being backprojected onto a 512 × 512 image matrix using a linear interpolation scheme, each parallel projection was convolved with a digital Shepp-Logan reconstruction kernel (modified ramp filter) to minimize the radial blurring inherent to the backprojection process [Ka 2000, Ka 1988].

2.3.3 Benchmarking of simulation program

2.3.3.1 Object density

Figure 2.5 illustrates the cylindrical step phantom, machined from a single piece of POM, used to benchmark the simulation program. Figure 2.6 illustrates a subset (diameters = 50, 30, 10 mm) of experimental images of this phantom acquired in air and in water using a modified oncology medium thorax axial technique (120 kVp, 200 mA, 3 mm slice thickness, 300 mm FOV) and their corresponding central horizontal profiles (i.e. profile along the horizontal midline of the images). Two distinctive features are characteristic of the experimental results. Overall, the water images and their corresponding central horizontal profiles exhibit a greater degree of noise than do their in air counterparts due to a significant decrease in x-ray quanta reaching the detectors. Second, image statistics (mean intensity within a circular region of interest and standard deviation) vary with object diameter. The latter is small for objects scanned in a water background but substantial for objects imaged in air. The observed variations in mean intensity and standard deviation with object diameter are deemed to arise as a result of an improper application of beam hardening software corrections during image reconstruction when small phantoms are imaged using full body protocols. To test this hypothesis, the cylindrical step phantom was scanned in air using full and half water calibration protocols. A greater degree of variation in reconstructed density as a function of cylinder diameter was observed with the full water calibration protocol as compared to the half water protocol. Results of these measurements, shown in Table 2.1, are consistent with the above inference. The exact nature of the reconstruction algorithms employed by the Picker 5000 CT scanner are, however, proprietary, and without a complete description of the scanner's reconstruction algorithms, this hypothesis can not be validated with absolute certainty. The proprietary nature of the reconstruction algorithms employed by the Picker 5000 CT scanner thus dictates that experimental image intensities must be used to calibrate the simulation model. Density calibration data was measured using the cylindrical step phantom with static in air and in water scans. Results obtained with the investigational modified oncology medium thorax axial technique, used for all experimental imaging throughout this thesis, are shown in Figure 2.7 along with their polynomial fits. Good correlation exists as demonstrated by the resultant R^2 values of 0.9942 (water) and 0.9968 (air), respectively. [Note: The DICOMREAD program used in MATLAB to import and read CT data results in the rescaling of all pixel intensities (CT numbers) within the experimental images to values between 0 and 4096. On this new scale, water corresponds to 1000 HU while air has a value of 0 HU].

Simulation images were generated using uniform object density values derived from experimental CT values, as detailed above, under the general assumption that object physical density, ρ_o, is linearly related to CT number

$$\rho_o = \frac{CT\,number * \rho_w}{1000} + \rho_w \tag{2.7}$$

where ρ_w is the water density (1 g/cm^3). Again, because DICOMREAD was used to import experimental CT data into MATLAB, object densities for the simulations were defined using the following modified equation

$$\rho_o = \frac{\left(\bar{I}_o - 1000\right)}{1000} + 1 \tag{2.8}$$

where $\bar{I}_o$ is the mean image intensity within the selected region of interest (ROI) after image import.

Simulation images of the cylindrical step phantom were generated using densities derived from the above calibration curves. The accuracy of the simulation code to reproduce experimental image detail was evaluated by comparing the simulation central horizontal profiles with their experimental counterparts. The normalized profiles (normalized with respect to $\bar{I}_o$) for the in air scans are depicted in Figure 2.8. Overall, good agreement between experiment and simulation exists. A small gradual lateral shift between experimental and simulation profiles was noticed indicating that the cylindrical step phantom was slightly misaligned with respect to the z-axis.

2.3.3.2 Unsharpness in the imaging plane

In physical CT imaging systems, many factors influence in-plane spatial resolution, including focus size, detector size, and element spacing [Ka 2000]. However, as illustrated in Figure 2.8, the blurring contribution from these geometrical variables is minimal. Since no significant differences are observed between the normalized experimental and simulated profiles of cylindrical objects ranging in diameter from a maximum of 50 mm to a minimum of 10 mm, no attempts were made to incorporate this type of unsharpness in the computer modeling.

2.3.3.3 Partial volume effects

Experimental images of static objects whose cross-sections vary in the z-dimension exhibit partial volume effects due to scanner finite slice data acquisition widths. The magnitude of these effects depends upon both object geometry and the slice sensitivity profile (SSP) of the CT scanner. Figure 2.9 presents experimental images of a 25 mm diameter POM sphere which was imaged at various distances from its center (z = 0 mm) using the modified oncology medium thorax axial technique (slice width = 3 mm) with a bed index of 3 mm. Greater partial volume effects are observed towards the periphery of the sphere where large variations in cross-section occur. This phenomenon is readily visualized by examining profiles (see Figure 2.11a) through the center of each image which reveal increased edge broadening as slice location approaches the radius of the sphere.

In order to incorporate partial volume effects into the simulation model, the SSP was measured for the 3 mm nominal slice width used throughout for experimental investigations. SSP measurements were obtained according to the impulse method [Da 1995] using a 0.5 mm diameter steel ball bearing fastened to a styrofoam block and scanned every 0.5 millimeters in both forward (+ z) and reverse (– z) directions. Maximum CT numbers within the ROI immediately surrounding the steel ball were summed from both scan directions and averaged to account for positioning errors. The experimental SSP for the 3 mm nominal slice thickness is presented in Figure 2.10. It can be observed that the full width at half maximum (FWHM) is 3 mm while the full width at tenth maximum (FWTM) is 5 mm.

When no attempt is made to incorporate partial volume effects in the computer simulation, various degrees of deviation between simulation and experiment result, as shown in Figure 2.11b for a 25 mm diameter POM sphere in air. At slice locations, where minimal changes in cross-sectional areas occur ($z = 0$), there are no distinguishable discrepancies between the simulation and experimental central horizontal profiles. However, at slice locations near the edge of the sphere where large variations in cross-section take place ($z = 9$ and $z = 12$ mm), deviations between simulation and experiment are readily evident.

In order to model partial volume effects, simulation images are generated at every 0.5 mm within the experimental SSP FWTM range ($z = -2.5$ to $z = +2.5$ mm). The measured SSP is used to properly weight each individual image prior to summation and renormalization. The central horizontal profiles depicted in Figures 2.12a-b indicate the utility of this approach. Good agreement between experiment and simulation is observed at $z = 9$ mm as a result of the partial volume modeling. Small deviations are still observed at $z = 12$ mm in association with the 0.5 mm sampling scheme. Much improved agreement is observed when a 0.25 mm sampling distance is adopted. In this thesis, however, a 0.5 mm sampling width is used to model partial volume effects.

The proprietary nature of the experimental reconstruction algorithm sets a fundamental limit with regard to the accuracy expected with the computer modeling. Subtle differences between experiment and simulation can be expected with regards to beam compensation, reconstruction filter, partial volume effects, etc… Despite these limitations, the agreement between experiment and simulation is very good, therefore, allowing this computer model to be used with confidence as an investigational tool in future sections.

2.4 Principles of motion artifacts in CT

CT imaging presumes the temporal invariance of the object or objects under investigation during data acquisition. When this requirement is not met, the projections obtained form an inconsistent data set upon which to base image reconstruction and motion artifacts result. Regarding the nature of these artifacts, a distinction may be identified between the effects of in-plane and orthogonal motion. A rigid object, for example, constrained solely to motion in the image plane presents the same physical cross-section but displaced in spatial location as a function of projection angle. By contrast, a rigid object constrained solely to motion orthogonal to the image plane will, in general, present a cross-section which varies not only in spatial location but also in size, shape and density distribution as a function of projection angle. The impact of orthogonal motion upon image reconstruction is thus inherently more complicated that that arising from in-plane motion. If deformability of objects is allowed, the complexity of the impact of motion upon image reconstruction is further increased. Realistic physiological motions are, of course, composed of both in-plane and orthogonal elements and apply to deformable objects of heterogeneous construction. For clarity and simplicity, the confounding effects of deformability and heterogeneity will be eliminated by limiting this investigation to the consideration of rigid homogeneous objects. As dynamics constrained to the imaging plane represent the simplest form of motion in terms of their impact upon image reconstruction, they will be considered separately from orthogonal movement. Finally, the effects of motion consisting of both in-plane and orthogonal components will be examined.

The formation of motion artifacts in tomographic imaging are examined in this section by means of computer simulation and mathematical analysis. This approach is taken here for clarity of presentation. The validity of modeling to reproduce the essential features of motion artifacts in experimentally generated images will be demonstrated later in this chapter and also in chapters 3 and 4 of this thesis. In order to comprehend how motion artifacts arise in CT, the investigation begins by reviewing the FBP reconstruction process of a stationary spherical object. The manner in which motion perturbs this process is then examined. In order to clearly elucidate the physics behind the formation of motion artifacts, the confounding presence of partial volume effects is eliminated by using simulation images of infinitesimal slice thickness.

2.4.1 Stationary object

Let the object to be imaged be a unit density spherical object, O[x,y,z] of radius R, centered at [$x_c = x$, $y_c = 0$, $z_c = z_{slice}$] in the imaging plane and surrounded by air (density ~ 0 g/cm^3). Numerous projections, each consisting of 512 line integrals, are obtained of this static object during image acquisition. This data may be represented graphically in sinogram format as shown in Figure 2.13a. Since the object in question is spherical, each projection in the sinogram is identical. Furthermore, the locus of all line integrals passing through a specific point within the object's cross-section (see Figure 2.13b for the centroid point [x_c, y_c]) traces out the fundamental cosine curve in sinogram space given by:

$$x_r(\varphi) = r \cdot \cos(\theta - \varphi) \tag{2.9}$$

where r is the radial position of the point from the origin, θ represents the angular position and φ is the projection angle. In image space, the backprojections for this spherical object all intersect at [x, y] (see Figure 2.13c). Because simple backprojection (BP) is a linear process that results in a (1/r) blurred image (see Figures 2.13d & 2.13f), a specialized kernel (e.g. Shepp-Logan, as is used throughout this work) must be convolved with each individual projection prior to reconstruction to correct for this effect. The net result of filtered backprojection (FBP) is an image that preserves the object's attenuation and geometric properties (see Figures 2.13e-f).

Under these conditions the cross-section of the imaged sphere exhibits a uniform unit density while the surrounding area displays a corresponding constant density of zero. Profiles along lines C-D and E-F through the centroid of the reconstructed sphere with (solid lines) and without filtering (dashed lines) are shown in Figure 2.13f. These profiles exhibit radial symmetry as expected.

2.4.2 Linear motion

For the purpose of this investigation, the following constant linear motion will be imparted to the above unit density spherical object:

$$\left[x(t)=\frac{A_x}{2}-\frac{A_x}{\pi}\left|\varphi-\varphi_o\right|, y(t)=0, z(t)=z_{slice}+\frac{A_z}{2\pi}\left|\varphi-\varphi_o\right|\right] \tag{2.10}$$

where φ is the projection angle, φ_o is the initial projection angle and A_x and A_z are the amplitudes of in-plane and orthogonal motions, respectively. These rather simplified motions serve to demonstrate, in a highly visible manner, the inconsistencies which arise in motion-impacted projection data sets. An examination of the individual impacts of in-plane and orthogonal motion upon CT image reconstruction precedes a treatment of more general motion consisting of both components.

2.4.2.1 In-plane

Let the above unit density sphere now move from $\frac{A_x}{2}$ to $-\frac{A_x}{2}$ in a linear fashion along the horizontal axis of the imaging plane during data acquisition. Here A_x is greater than R in order to provide better visualization of the effect of in-plane motion upon the reconstruction process. Because motion is constrained to the imaging plane, each projection in sinogram space retains its original profile but is now shifted in position (compared to the static case) as the object projects to different detector positions (see Figure 2.14a). Furthermore, the locus of all line integrals passing through a specific point within the object's cross-section no longer corresponds to the fundamental cosine curve characteristic of the static object (see Figure 2.14b for centroid point [x_c,y_c]). For this solitary moving object, the observed departure from the fundamental cosine curve characteristic of the static situation renders the motion-induced inconsistency in the projection data set readily visible. In general the shape of the resultant curve is dependent upon both the form and extent of motion captured during acquisition. For in-plane motion, the locus of all line integrals passing through a point within the object's cross-section may be described as follows:

$$x_r(\varphi) = r(\varphi) \cdot \cos\big(\theta(\varphi) - \varphi\big) \tag{2.11}$$

where $r(\varphi)$ and $\theta(\varphi)$ are the radial and angular positions of the mobile point at projection angle φ. The inconsistencies in the projection data set, as evidenced by the positional shifts observed in the sinogram, lead to multiple intersection points during backprojection (see Figure 2.14c), the spatial distribution which dictates the essential shape or pattern of the motion artifact. Significant deviations from the true path of motion are indicated. In particular, positions displaced from to the true path of motion are created. The (1/*r*) blurred image density associated with a static object is now redistributed over a larger area of the image matrix in a pattern which no longer preserves radial symmetry (see Figures 2.14d & 2.14f-g). Due to the linear nature of this BP process, the resultant image may be mathematically described as a convolution between the object O[x,y] and the linear system's response h_m[x,y] to a mobile input delta function according to:

$$I[x,y] = O[x,y] \otimes \otimes h_m[x,y] \tag{2.12}$$

where

$$h_m[x,y] = \int_0^{2\pi} \int_{-\infty}^{\infty} \frac{1}{2\pi} \delta\big(x_r(\varphi)\big) \delta\big(y_r(\varphi)\big) dy_r \, d\varphi \tag{2.13}$$

The impact of filtering the motion-encoded projection data upon the reconstructed image is illustrated in Figure 2.14e. Because in-plane motion leads to a redistribution of the blur pattern, it also results in a redistribution of the filter. The overall effect of filtering when in-plane motion is present during acquisition is an incomplete reduction of radial blurring and a partial sharpening of the resultant motion artifact pattern (see Figures 2.14f and 2.14g). The reconstruction pattern, which emerges at this slice location, deviates markedly from the corresponding TXO contour depicted by the white line in Figure 2.14e. The TXO contour delineates the total cross-sectional area occupied by the mobile object at this specific slice location during the imaging process. Significant density variations, ranging from – 0.75 g/cm^3 to 0.56 g/cm^3 (mean = 0.17 g/cm^3) characterize the cross-sectional area encompassed by the TXO contour. Image densities which occur along the line defining the TXO contour, beginning at $\varphi = 0^o$ (3 o'clock position) and proceeding counterclockwise to $\varphi = 360^o$, are shown in Figure 2.14h. Clearly, no single density value characterizes the TXO contour or any other physically meaningful area associated with this mobile object. Density values within a 10 mm radial area surrounding the TXO contour also deviate from that under static conditions ranging, in this case, from – 0.75 g/cm^3 to 0.37 g/cm^3.

2.4.2.2 Orthogonal motion

The consequences of orthogonal motion upon the CT image reconstruction process may be examined by letting the unit density sphere now move perpendicularly through the infinitesimal imaging plane during data acquisition in a linear fashion from its initial position centered on the imaging plane at $[x_c = x, y_c = y, z = z_{slice}]$ to a final location at $[x_c = x, y_c = 0, z = z_{slice} + R]$. Because the object's cross-section present in the imaging plane varies during image acquisition, both the width and intensity of the sinogram projections change accordingly (see Figure 2.15a) but follow a similar curve to that associated with a stationary object centered at $[x_c = x, y_c = 0, z = z_{slice}]$ as a result of the object's geometric properties. In this case the motion-induced inconsistencies in the projection data set are manifested in terms of the width and intensity variations observed in the sinogram rather than a departure from the fundamental cosine shape as seen with the in-plane motion above. It is these variations in the width and intensity of the projections that are responsible for the motion artifacts observed in the unfiltered image shown in Figure 2.15b. In clinical situations, however, where tumor geometry is more complex, orthogonal motion will, in general, result in variations in both the width and intensity of projections as well as in positional shifts leading to more complex motion artifacts. As with in-plane motion, the blur pattern of the reconstructed object no longer displays radial symmetry. Similarly, filtering the motion-encoded projection data, results in an incomplete reduction of radial blur and a partial sharpening of the pattern of distortion (see Figures 2.15c and 2.15d). As with in-plane motion, profiles (lines B-C and D-E) through the mean position of the object in the imaging plane no longer retain the radial symmetry associated with the static object (see Figure 2.15d). While the true TXO contour associated with this motion coincides with that of the static sphere, once again no single density value can be identified with this contour (see Figure 2.15e). Overall, the density heterogeneities observed are much less severe than seen with in-plane motion, but nevertheless they are sufficient to confound TXO delineation. Densities within the TXO contour range, in this case, from – 0.08 g/cm^3 to 1.00 g/cm^3 (mean = 0.66 g/cm^3) while outside this contour (within 10 mm radial area) the density heterogeneity extends from – 0.19 g/cm^3 to 0.22 g/cm^3.

2.4.2.3 Combined motion

Combining the preceding in-plane and orthogonal motions yields the sinogram of Figure 2.16a. Inconsistencies in this motion impacted projection data set are now evidenced by the positional shifts observed in this sinogram, which arise due to the in-plane component of motion, in combination with the width and intensity variations resulting from the orthogonal component. Figures 2.16b-c demonstrate the resulting unfiltered and filtered reconstructions which now lack the pattern symmetry observed with the individual components of motion. The TXO associated with this motion is indicated by the white contour in Figure 2.16c. The edge enhancement that emerges from filter application may be seen by comparing profiles (lines B-C and D-E) through the mean position of mobile object in the imaging plane [$x = 0$, $y = 0$] as shown in Figure 2.16d. As with the individual motion components, significant density heterogeneity is observed throughout the image. Within the TXO contour, image densities range from – 0.49 g/cm^3 to 0.54 g/cm^3 (mean = 0.16 g/cm^3) while external to this contour (within 10 mm radius)the density heterogeneity extends from – 0.72 g/cm^3 to 0.38 g/cm^3. As with the individual motion components, isodensity contours do not correspond to physically meaningful quantities (see Figure 2.16e).

2.5 Experimental verification

The results presented in section 2.4.2 above were generated by computer simulation for the purpose of demonstrating the basic principles which give rise to motion-induced artifacts and were offered without supporting experimental validation. In order to verify the accuracy of simulation to reproduce experimental results when motion is introduced during the imaging process, a motion phantom was constructed. As illustrated in Figure 2.17, the phantom contains three independent motion plates defining horizontal, vertical and orthogonal motions. A separate cam and cam follower apparatus provides each plate with periodic motion. All three plates are coupled to a common variable speed electric motor. The phase of motion imparted to any one plate in relation to that of the others is dictated by the relative orientation of the cams. For the purpose of validating the simulation software, only the horizontal (x) and orthogonal (z) axis of motion were utilized.

Experiments were performed using simple harmonic motion (SHM) of the form

$$\lfloor x(t) = -A_x \cos\left(\alpha\left(\varphi - \varphi_o\right) - \phi_x\right),\; y(t) = 0,\; z(t) = -A_z \cos\left(\alpha\left(\varphi - \varphi_o\right) - \phi_z\right)\rfloor \qquad (2.14)$$

where α depicts the acquisition time to motion period ratio, and ϕ_x and ϕ_z are the x and z components of the phase of motion. Cam sets defining various amplitudes of motion ($A_x = A_z = 2.5, 7.5, 12.5$ mm) were machined and used to impart SHM to various cylindrical (diameters = 10, 30, 50 mm) and spherical (diameters = 10, 25, 50 mm) POM test objects. For each orthogonal and horizontal SHM, experimental images were acquired, in air and water, using a modified oncology medium thorax axial technique (120 kVp, 200 mA, 3 mm slice thickness, 300 mm FOV). Since the extent of motion captured during a single scan depends upon the initial phase of motion (as will be demonstrated in the following chapter), a trigger apparatus was developed and temporarily installed on the CT scanner to gate the motion at a constant phase ($\phi_x = \phi_z = 0^o$). Furthermore, to eliminate possible scanner angular dependence, the initial projection angle was set to zero. Simulation images were then generated for each motion and compared with their experimental counterparts.

2.5.1 Horizontal SHM

Figures 2.18 – 2.19 show experimental and simulation images obtained for three POM cylinders (diameters = 10, 30, 50 mm) undergoing a specific simple horizontal harmonic motion ($A_x = 5, 7.5, 12.5$ mm) in air and water mediums. Since a trigger system was used to gate motion at $\phi_x = 0 \pm 5^o$, each experimental image displays the same motion artifact pattern. Simulation images were generated for these experimental conditions ($\phi_x = 0^o$, $\varphi_o = 0^o$) using physical densities derived from the appropriate experimental calibration curves. Good agreement is seen between experimental and simulated motion impacted images. Figure 2.20 illustrates the normalized image intensity profiles measured along the horizontal midline of both experimental and simulated images. Normalization was performed with respect to the mean intensity measured under static conditions. Good agreement is seen to exist between experiment and simulation, further validating the accuracy of the simulation technique. The slight discrepancies discernable between experiment and simulation in some of the images and profiles are attributable to experimental gating uncertainties.

An analysis of image intensity profiles from repeated measurements of the same motion revealed the accuracy of the gating system to be ± 5°.

2.5.2 Orthogonal SHM

Experimental and simulation images obtained for three spherical POM spheres (diameters = 10, 25, 50 mm) initially centered in the scanner at mid-trajectory position and then scanned while undergoing SHM (A_z = 5, 7.5, 12.5 mm) orthogonal to the imaging plane in both air and water are depicted in Figures 2.21 – 2.22. In view of the fact that partial volume effects can not be ignored when spherical test objects are imaged using a finite slice thickness, they were included in the orthogonal SHM simulations for comparison to experimental images. Good agreement is seen between experimental and simulated motion-impacted images. Figure 2.23 shows the central horizontal profiles measured from both the experimental and simulated finite slice width images. Again, good agreement between experiment and simulation is observed validating the accuracy of the computer model to properly incorporate partial volume effects in the reconstructed CT images.

2.6 Summary and Conclusions

A filtered backprojection (FBP) algorithm, based on parallel-beam geometry, was developed in MATLAB to reconstruct axial CT images of stationary and dynamic objects. The ability of the computer model to reproduce experimental results under static conditions was evaluated using stationary POM cylinders and spheres. Based upon these evaluations, modifications were made to the main program to account for partial voluming effects and the dependence of CT number upon object diameter observed experimentally. Good agreement between computer model and experimental results was observed with the modified FBP algorithm.

The motion of objects during image acquisition produces inconsistencies in the projection data set which, upon reconstruction, result in the generation of artifacts. The formation of these motion artifacts was investigated, through the use of computer simulation, by examining a uniform density sphere subject to three forms of linear motion and comparing the results to that obtained under static conditions. Imaging of the sphere under static conditions produces a sinogram which presents with the fundamental cosine curve characteristic of a consistent projection data set. Filtered and unfiltered CT reconstructions, along with their respective intensity profiles, derived from this projection data were examined for comparison with motion-impacted images. The same sphere was then imaged while it underwent a linear in-plane motion along the horizontal axis. The inconsistencies in the projection data set which result due to the presence of this form of motion were clearly evident in the departure from the fundamental cosine curve observed in sinogram space. CT image reconstructions formed from this motion impacted data set were compared to those of the static case. Here the inconsistencies introduced into the projection data set resulted in multiple intersection points which dictate the essential shape of the resultant image artifact. CT reconstruction based on this motion-encoded projection data set yielded images and intensity profiles which were significantly divergent from those of the static case. The large density variations associated with regions both within and surrounding the TXO render contour delineation highly problematic.

The impact of linear motion orthogonal to the image plane was examined next and found to produce an artifact pattern quite distinct from that associated with in-plane movement. Unlike the alterations observed with in-plane movement, this motion impacted data set retained the fundamental cosine shape associated with static objects. Here the inconsistencies introduced into the projection data set due to the presence of this form of motion were evident as variations in both the size and intensity of the object curve in sinogram space. As with in-plane motion, the substantial density variations both within and surrounding the TXO render contour delineation highly problematic.

When the preceding linear motions were combined, the resultant object curve in sinogram space clearly demonstrated both in-plane and orthogonal components with a departure from the fundamental cosine shape and the inclusion of size and intensity variations. As with the individual component motions, substantive density variations both within and external to the TXO were produced in the reconstructed image which again were of sufficient a magnitude to render contour delineation highly problematic.

Finally, the validity of computer simulation as a tool with which to investigate the impact of motion upon CT image reconstruction was evaluated by comparison with experimental data. The ability of simulation to accurately reproduce experimental results associated with in-plane and orthogonal simple harmonic motion was established using uniform POM density cylinders and spheres respectively. Good agreement, as established by comparing both reconstructed images and intensity profiles, was obtained for all cases examined, lending confidence to the use of computer modeling as a valid investigational tool into the effects of motion on the reconstruction of CT images.

Table 2.1

Measurements of mean object CT number as a function of object diameter resulting from various imaging protocols. Column A – Modified oncology medium thorax, Column B – Full water calibration, and Column C – Half water calibration.

	Mean CT number (Standard deviation)		
Object diameter (mm)	Column A Modified oncology medium thorax	Column B Full water scan	Column C Half water scan
50	318.5 (18.1)	326.0 (15.8)	338.6 (1.4)
40	309.1 (17.6)	317.1 (16.7)	337.8 (3.2)
30	295.3 (10.0)	301.7 (9.7)	336.1 (5.2)
20	271.6 (3.5)	275.1 (3.2)	327.0 (5.7)
15	259.0 (3.3)	261.0 (1.9)	318.1 (6.7)
10	249.3 (2.3)	253.1 (2.2)	300.0 (7.6)

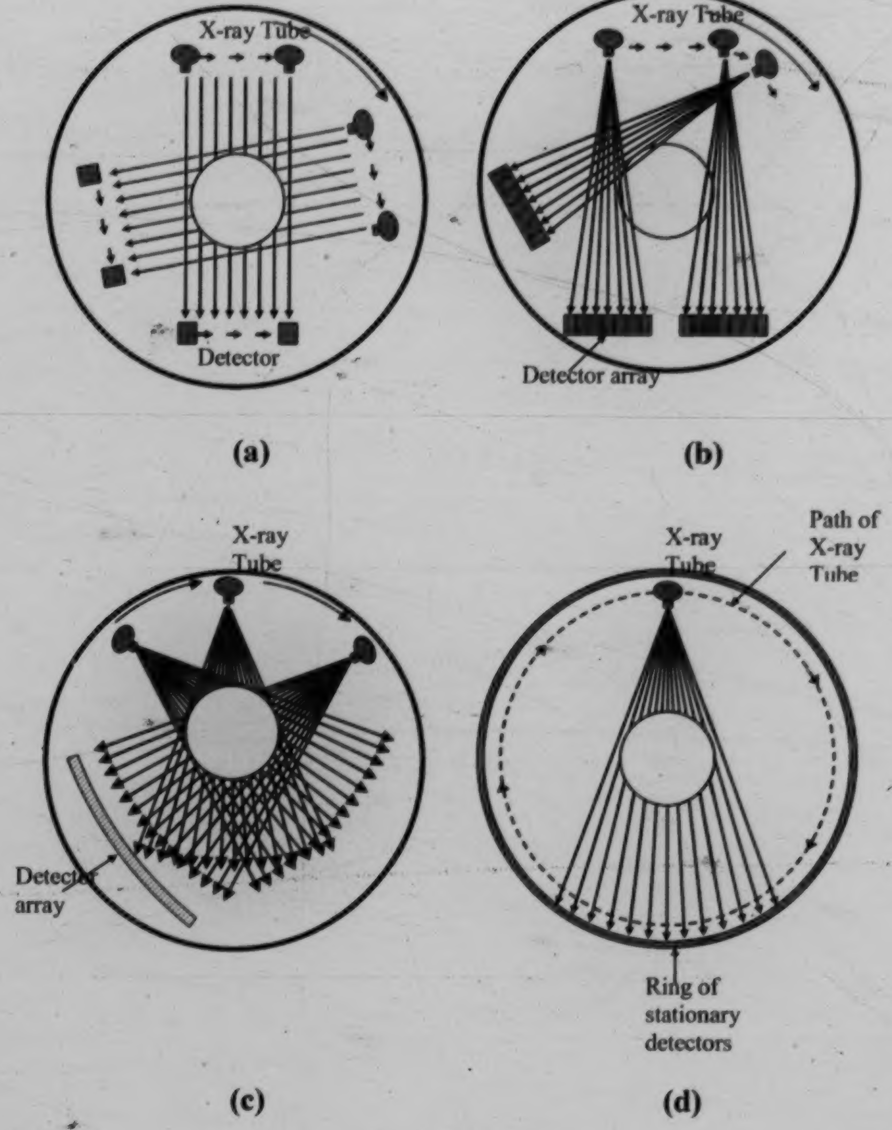
X-ray Tube
Detector
(a)
X-ray Tube
Detector array
(b)
X-ray Tube
Detector array
(c)
X-ray Tube
Path of X-ray Tube
Ring of stationary detectors
(d)

Figure 2.1 Historical development of CT scanner configurations. (a) First generation, (b) Second generation, (c) Third generation and (d) Fourth generation.

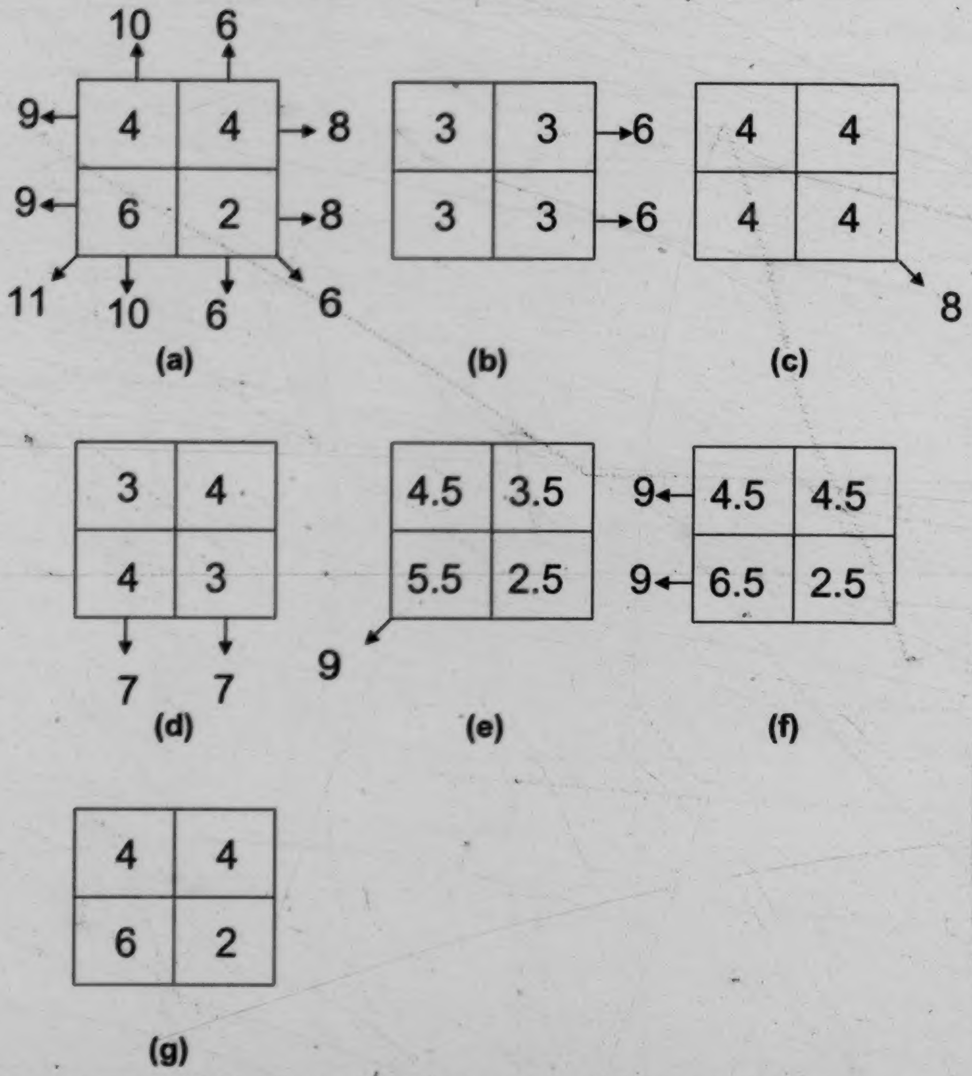
10
6
9
4
4
8
9
6
2
8
11
10
6
6
(a)
3
3
6
3
3
6
(b)
4
4
4
4
8
(c)
3
4
4
3
7
7
(d)
4.5
3.5
5.5
2.5
9
(e)
9
4.5
4.5
9
6.5
2.5
(f)
4
4
6
2
(g)

Figure 2.2 Simplified example of an iterative reconstruction. (a) Ten integral values are obtained from the object and used to correct the (b) estimated image. For the purpose of illustration, a non-zero matrix is used as the first estimate. The number three was chosen arbitrarily. This process is repeated (c-g) until the estimate image converges with the image of the actual object.

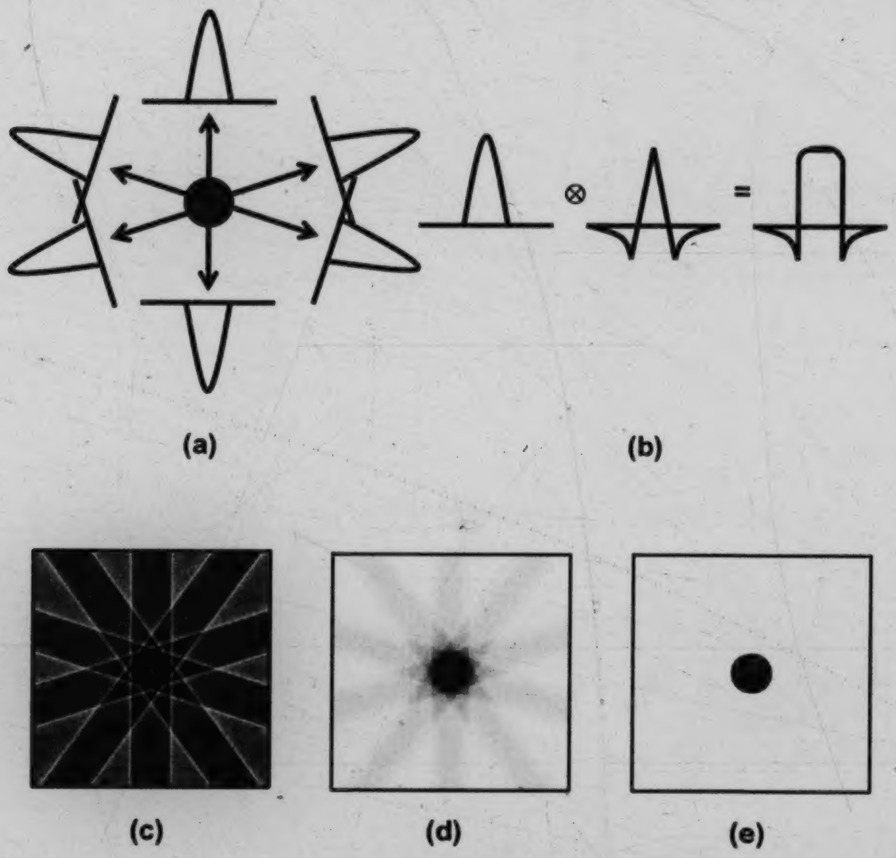

Figure 2.3 Simplified example of a filtered backprojection reconstruction. Ten projections (**only 6 are shown**) of a circular object (a) are convolved with a kernel in the spatial domain (b) prior to backprojection (c) to remove the radial blur inherent to the backprojection process (d). (e) Filtered backprojection image of the object with 400 projections.

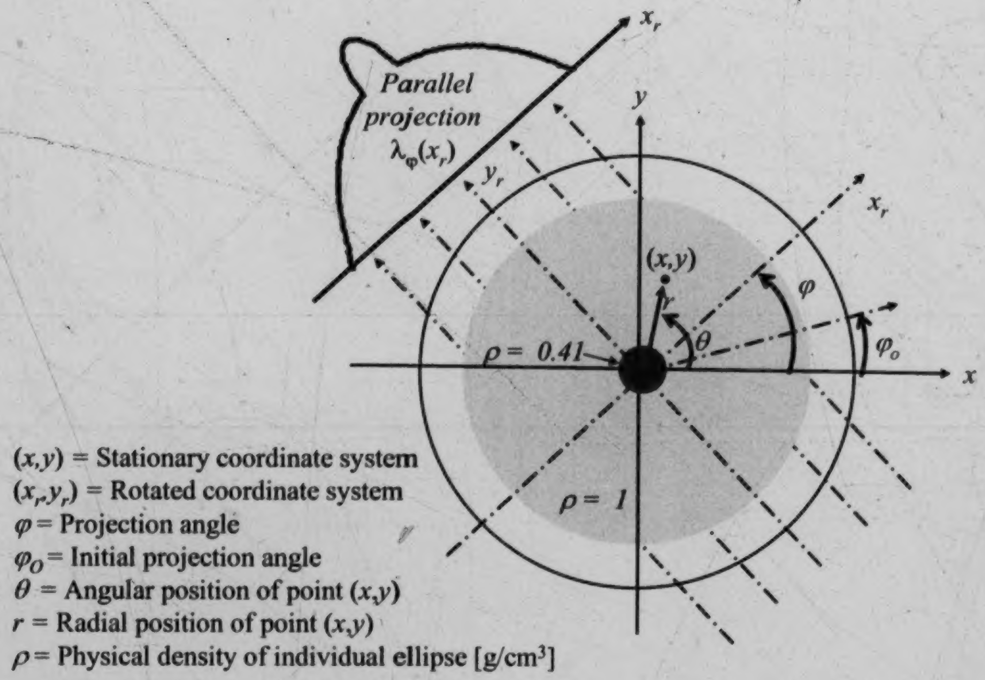

(x,y) = Stationary coordinate system
(x_r,y_r) = Rotated coordinate system
φ = Projection angle
φ_O = Initial projection angle
θ = Angular position of point (x,y)
r = Radial position of point (x,y)
ρ = Physical density of individual ellipse [g/cm^3]

Figure 2.4 A schematic of the parallel-beam geometry adopted for CT image reconstruction. At each sampled projection angle, φ, a parallel projection is obtained by computing 512 parallel line integrals as per Equation (2.6). In total, 800 parallel projections are used to reconstruct a 512 × 512 image. For the purpose of modeling, all digital phantoms were created by superposing elliptical objects of various densities. (Shown in the above figure is a cross-sectional view of a static 25 mm diameter POM sphere centered in a 200 mm diameter water medium.)

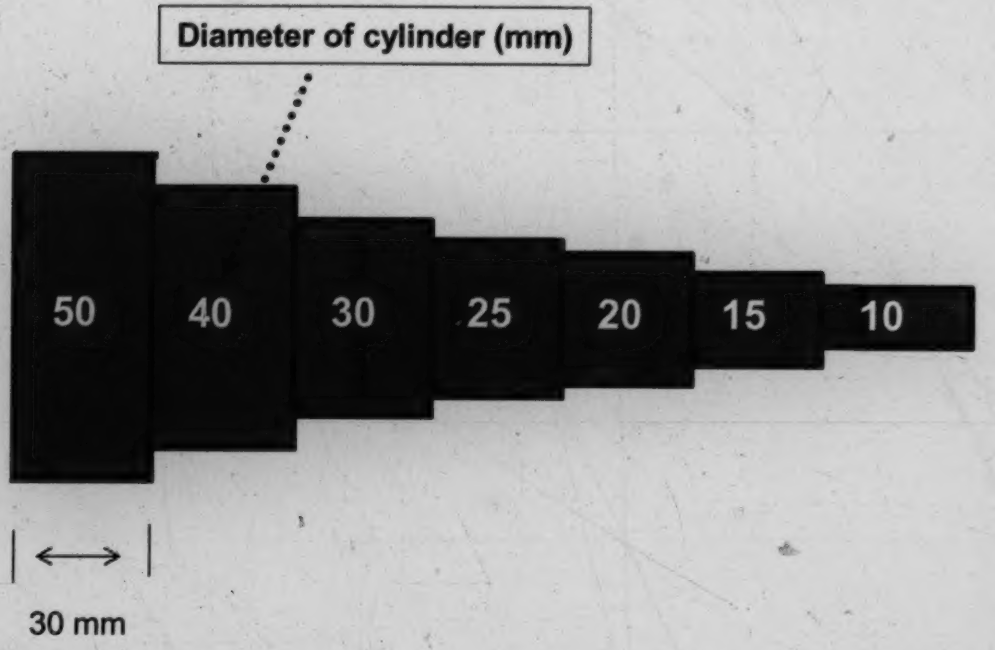
Diameter of cylinder (mm)
50
40
30
25
20
15
10
30 mm

Figure 2.5 Schematic of cylindrical step Delrin phantom used to benchmark simulation program.

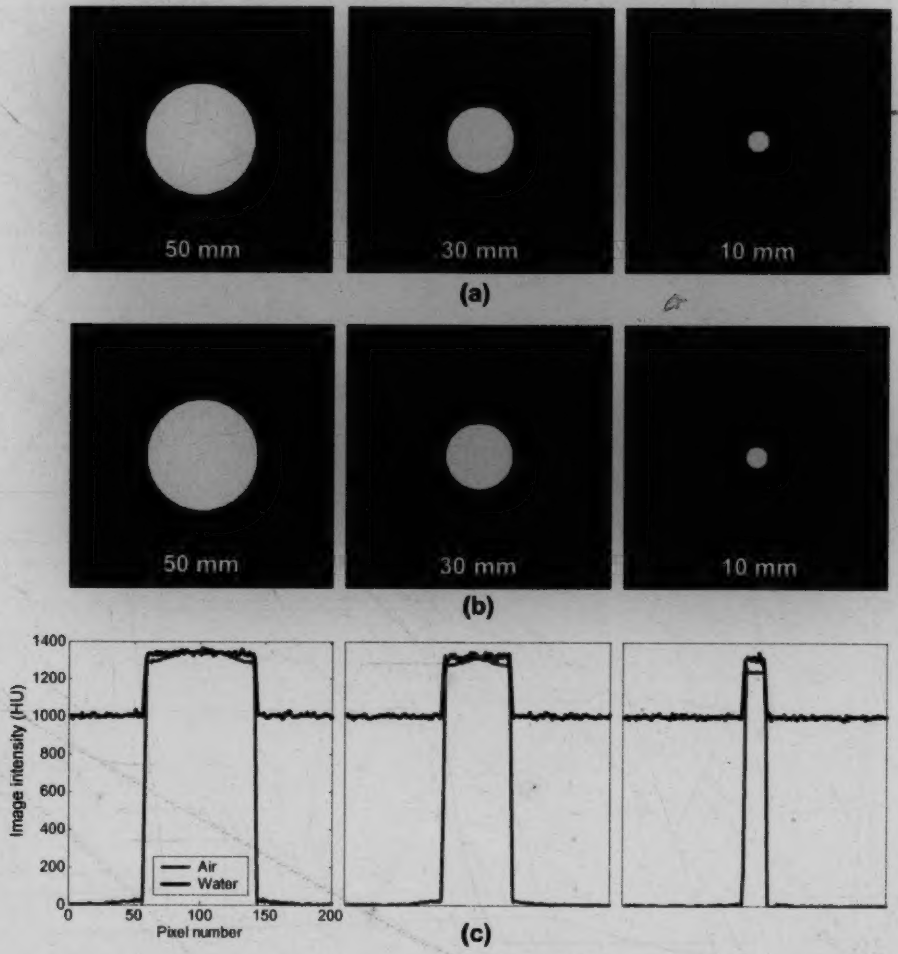

Figure 2.6 Three experimental images of a step-cylindrical Delrin phantom positioned (a) in air and (b) in water. (c) Image intensity values along a horizontal line passing through the center of each cross-section (diameters = 50, 30, 10 mm). These profiles are also termed central horizontal profiles in this work.

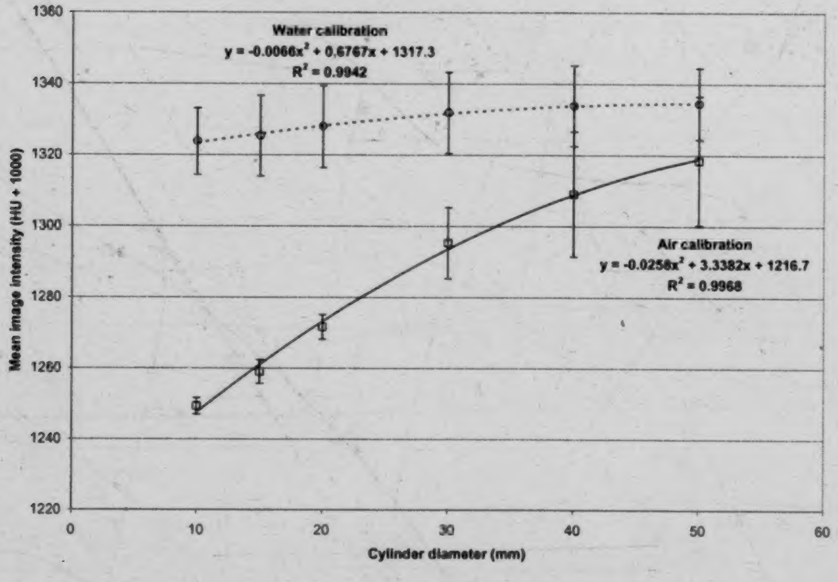

Figure 2.7 Calibration curve used to derive the simulation density of POM objects embedded in an air or water medium. The errors bars represent the standard deviation within the region of interest (ROI).

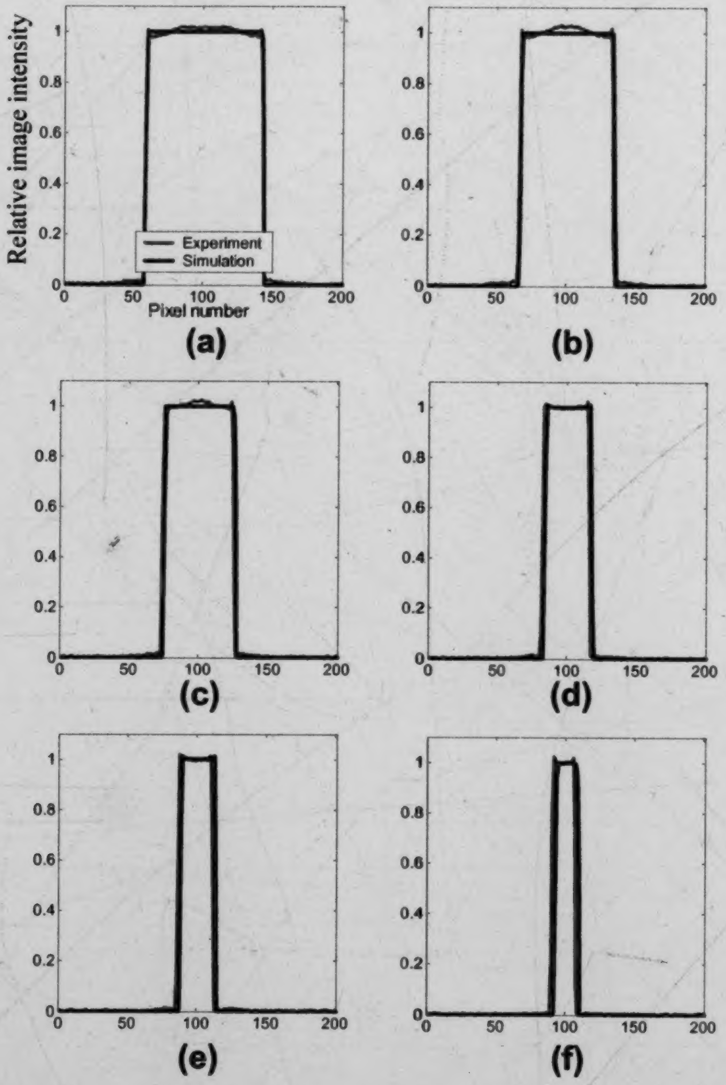

Figure 2.8 Experimental and simulation central horizontal profiles for a cylindrical step phantom of various diameters: (a) 50 mm, (b) 40 mm, (c) 30 mm, (d) 20 mm, (e) 15 mm and (f) 10 mm.

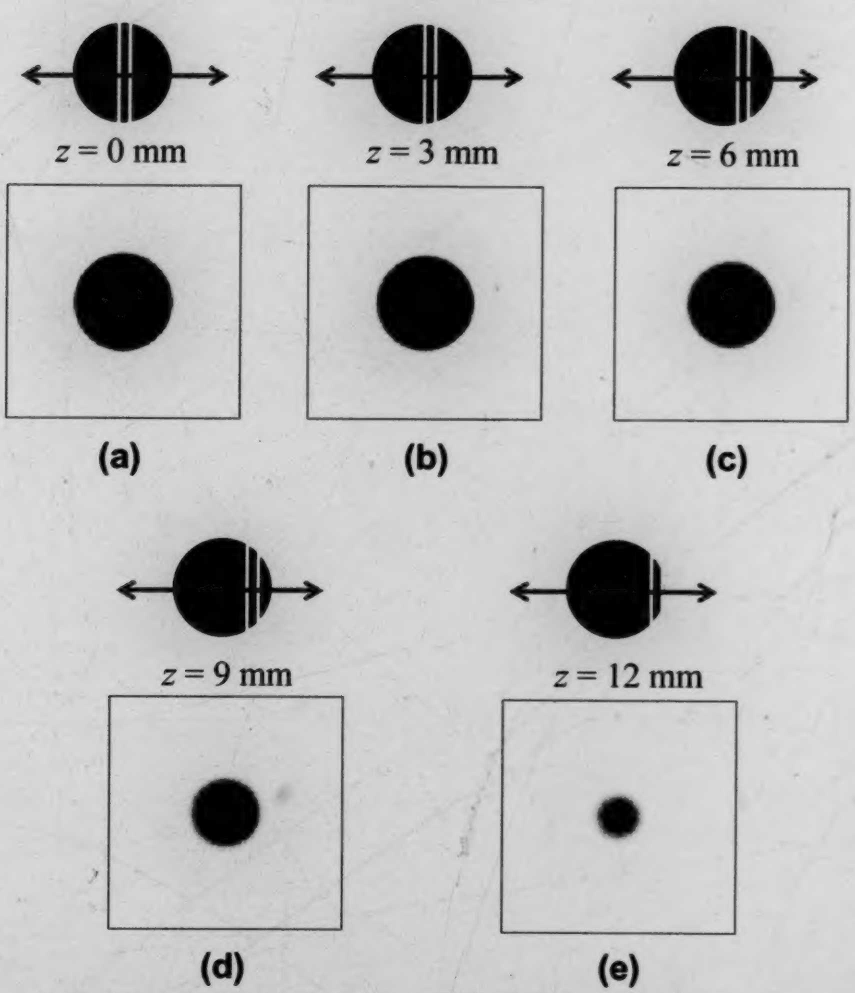
$z = 0$ mm
$z = 3$ mm
$z = 6$ mm
(a)
(b)
(c)
$z = 9$ mm
$z = 12$ mm
(d)
(e)

Figure 2.9 Experimental images of a 25 mm POM sphere depicting various partial volume effects. The slice location of each 3 mm CT image is indicated in the schematic. (a) $z = 0$ mm, (b) $z = 3$ mm, (c) $z = 6$ mm, (d) $z = 9$ mm, and (e) $z = 12$ mm.

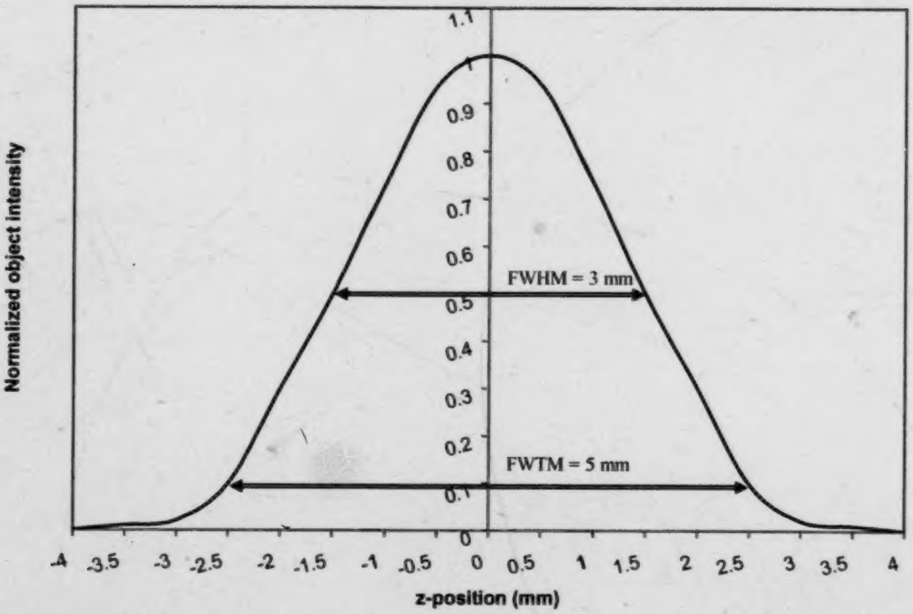

Figure 2.10 Slice sensitivity profile measured for a 3 mm nominal slice thickness using the impulse method.

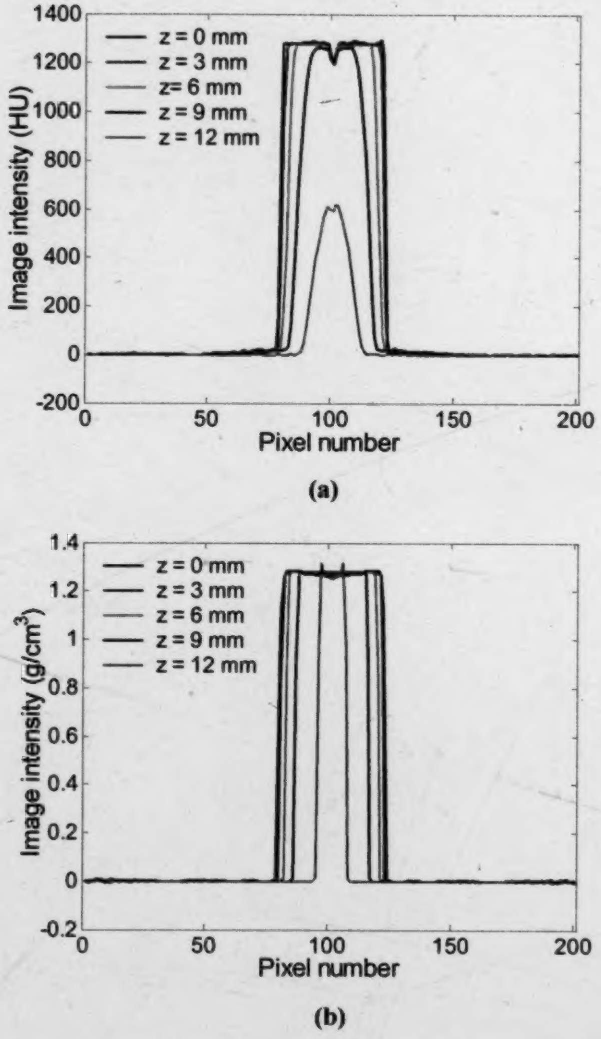

(a)

(b)

Figure 2.11 Central horizontal profiles for a 25 mm POM sphere surrounded by an air medium as measured from (a) experiment and (b) simulation using an infinitesimal slice width only. The slight drop in the middle of the experimental profiles results from the small air cavity present in the center of the POM sphere.

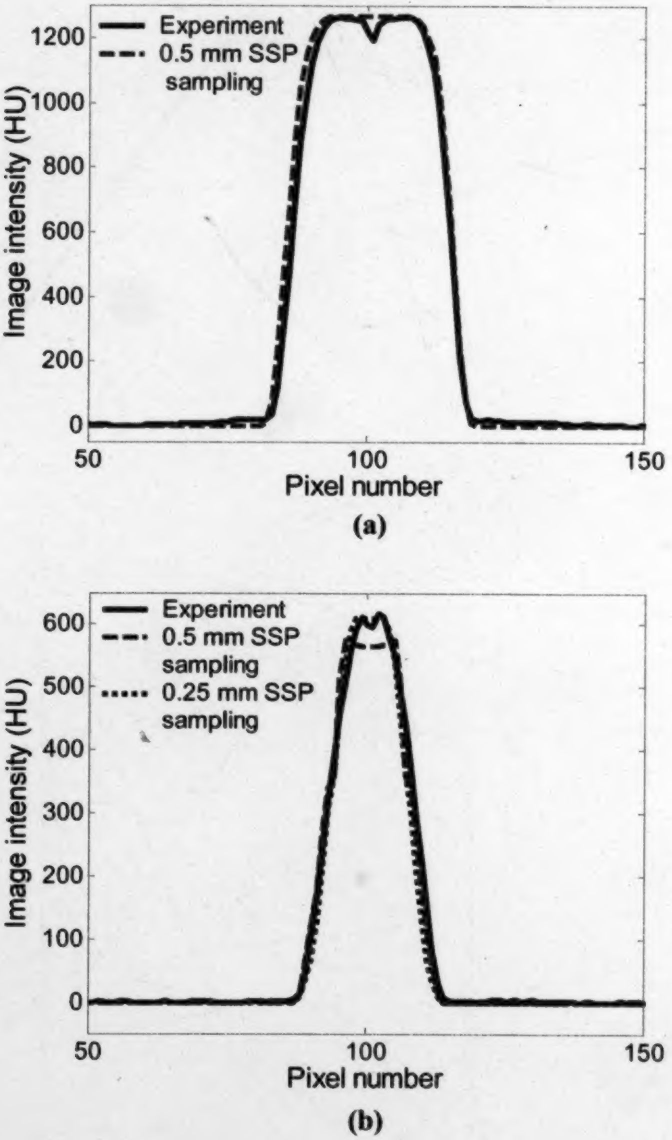

Figure 2.12 Central horizontal profiles for a 25 mm POM sphere at (a) z = 9 mm and (b) z = 12 mm. The solid line represents the experimental result while the dashed and dotted lines correspond to the simulation results achieved using a 0.5 mm and 0.25 mm SSP sampling distance.

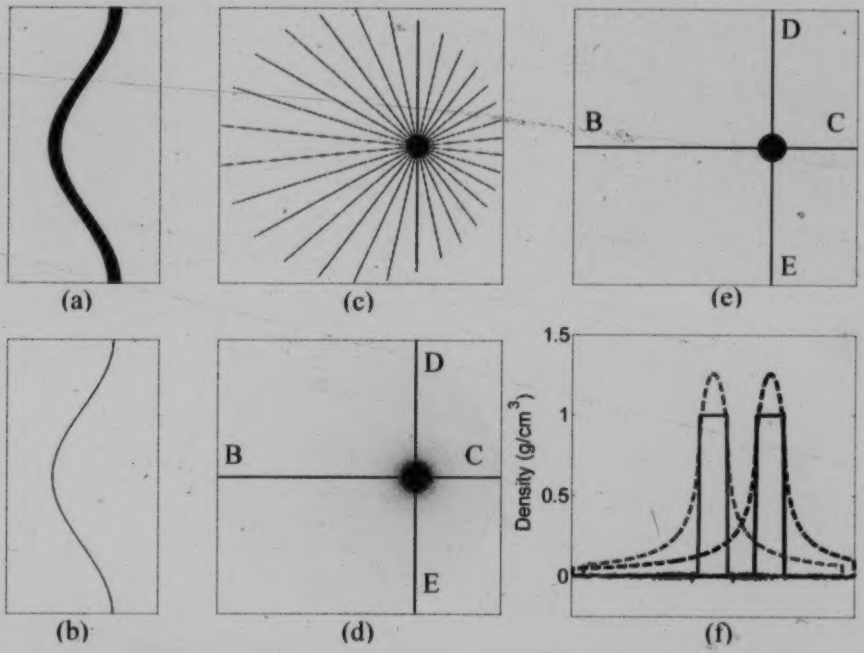

(a) (c) (e)

(b) (d) (f)

Figure 2.13 Reconstruction illustrated for a static sphere: (a) Sinogram, (b) Locus of all line integrals passing through the centroid point of the sphere in sinogram space, (c) Projections through a specific point, (d) Simple backprojection (BP) image, (e) Filtered backprojection (FBP) image, and (f) Intensity profiles along lines B-C (dashed black line (BP), solid black line (FBP)) and E-D (dashed gray line (BP), solid gray line (FBP)).

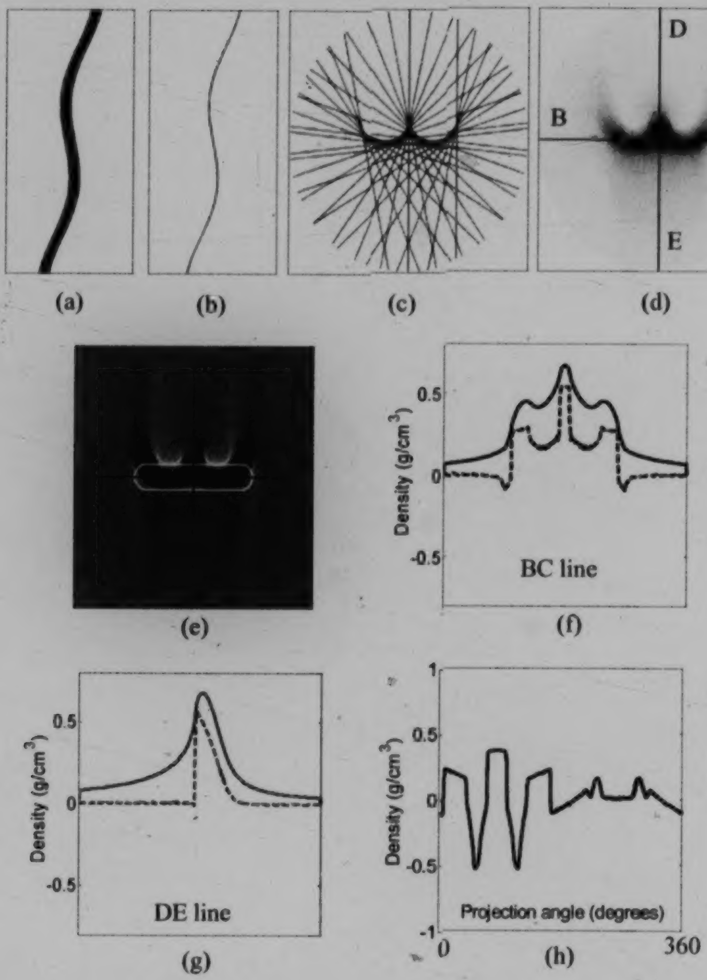

Figure 2.14 Principles of motion artifacts in CT for a sphere moving within the imaging plane: (a) Sinogram, (b) Locus of all line integrals passing through the centroid point of the mobile sphere in sinogram space, (c) Projections through a specific point blurred due to motion, (d) Simple backprojection (BP) image, (e) Filtered backprojection (FBP) image with TXO contour (dashed white line), (f) Intensity profiles along line B-C (dashed black line (BP), solid black line (FBP)), (g) Intensity profiles along line E-D (dashed gray line (BP), solid gray line (FBP)), and (h) Intensity profile along TVO contour.

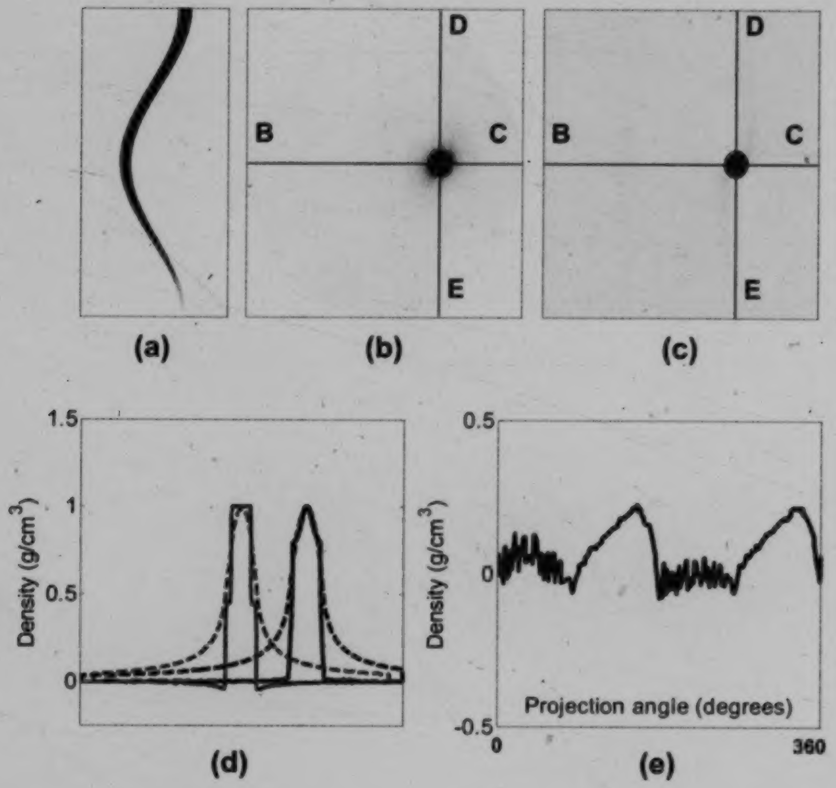

Figure 2.15 Principles of motion artifacts in CT for a sphere moving perpendicular to the imaging plane: (a) Sinogram, (b) Simple backprojection (BP) image, (c) Filtered backprojection (FBP) image with TXO contour (dashed white line), (d) Intensity profiles along lines B-C (dashed black line (BP), solid black line (FBP)) and E-D (dashed gray line (BP), solid gray line (FBP)), and (e) Intensity profile along TXO contour.

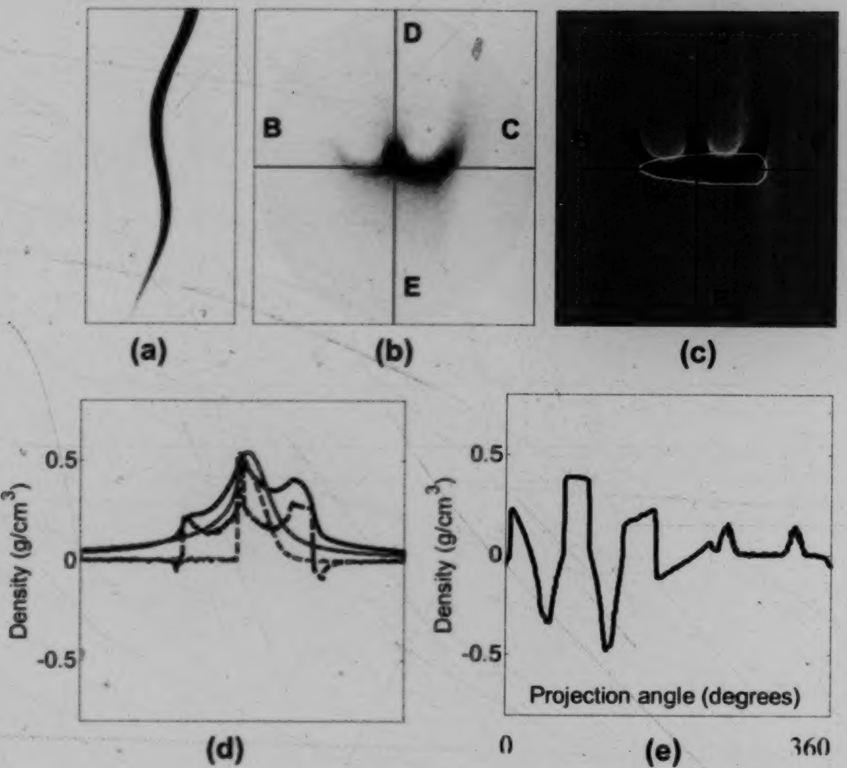

Figure 2.16 Principles of motion artifacts for a sphere moving both within and perpendicular to the imaging plane: (a) Sinogram, (b) Simple backprojection (BP) image, (c) Filtered backprojection (FBP) image with TXO contour (dashed white line), (d) Intensity profiles along lines B-C (dashed black line (BP), solid black line (FBP)) and E-D (dashed gray line (BP), solid gray line (FBP)), and (e) Intensity profile along TXO contour.

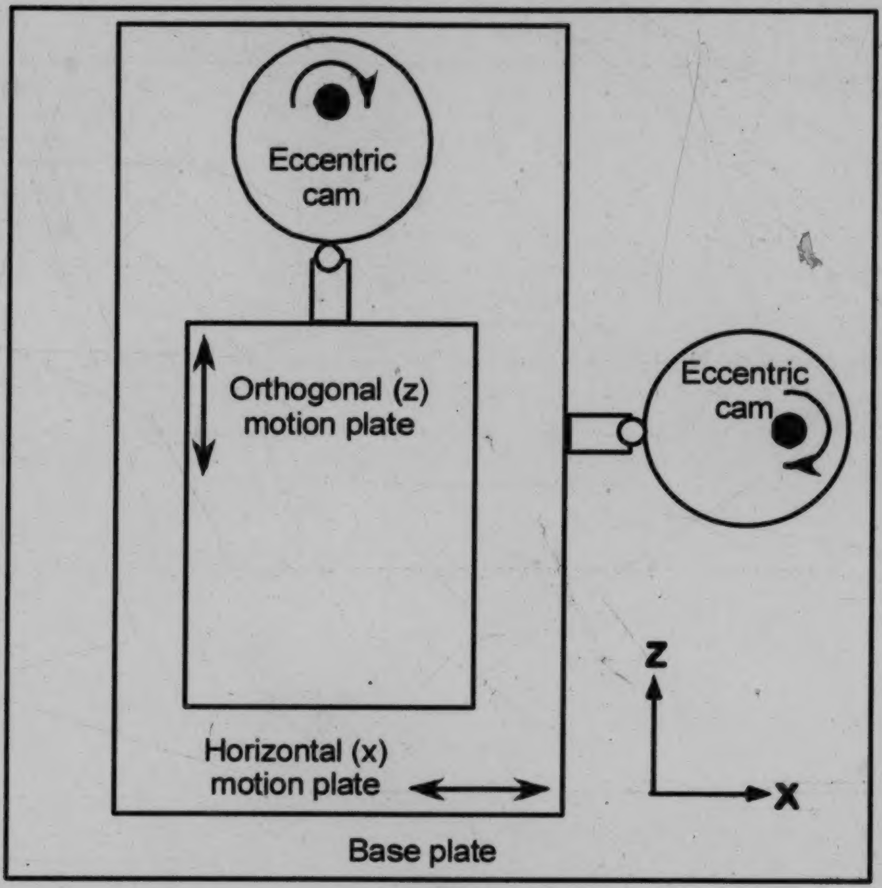
Eccentric cam
Orthogonal (z) motion plate
Eccentric cam
z
Horizontal (x) motion plate
x
Base plate

Figure 2.17 Graphic representation of three-dimensional motion phantom used in the investigation of motion artifacts in CT. Three cam actuated plates are used to define the motion along the horizontal (*x*), vertical (*y*) and orthogonal (*z*) directions. An adjustable electric motor is employed to control the motion period of a test object attached to a removable attachment arm. For clarity only the horizontal and orthogonal motion plates and their respective eccentric driver cams are shown.

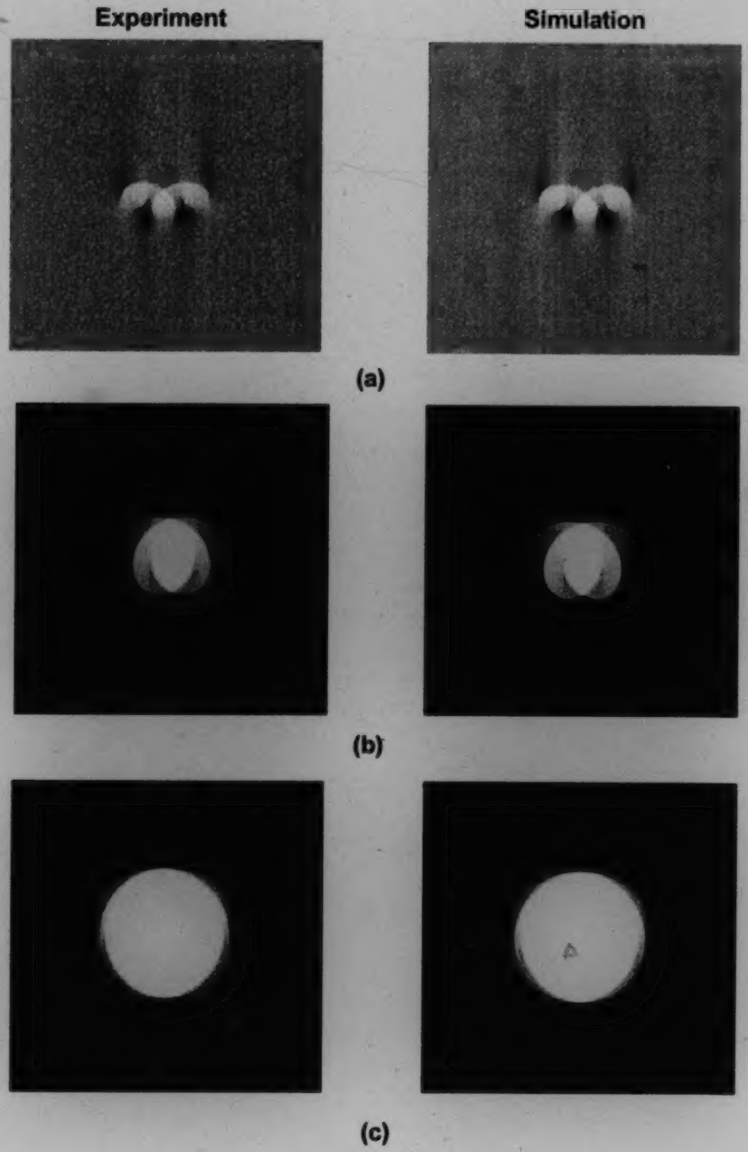

Figure 2.18 Experimental and simulation images of three POM cylinders undergoing a simple harmonic motion along the horizontal axis in a water background. **(a)** 10 mm diameter cylinder – 25 mm SHM, **(b)** 30 mm diameter cylinder – 15 mm SHM, and **(c)** 50 mm diameter cylinder – 5 mm SHM.

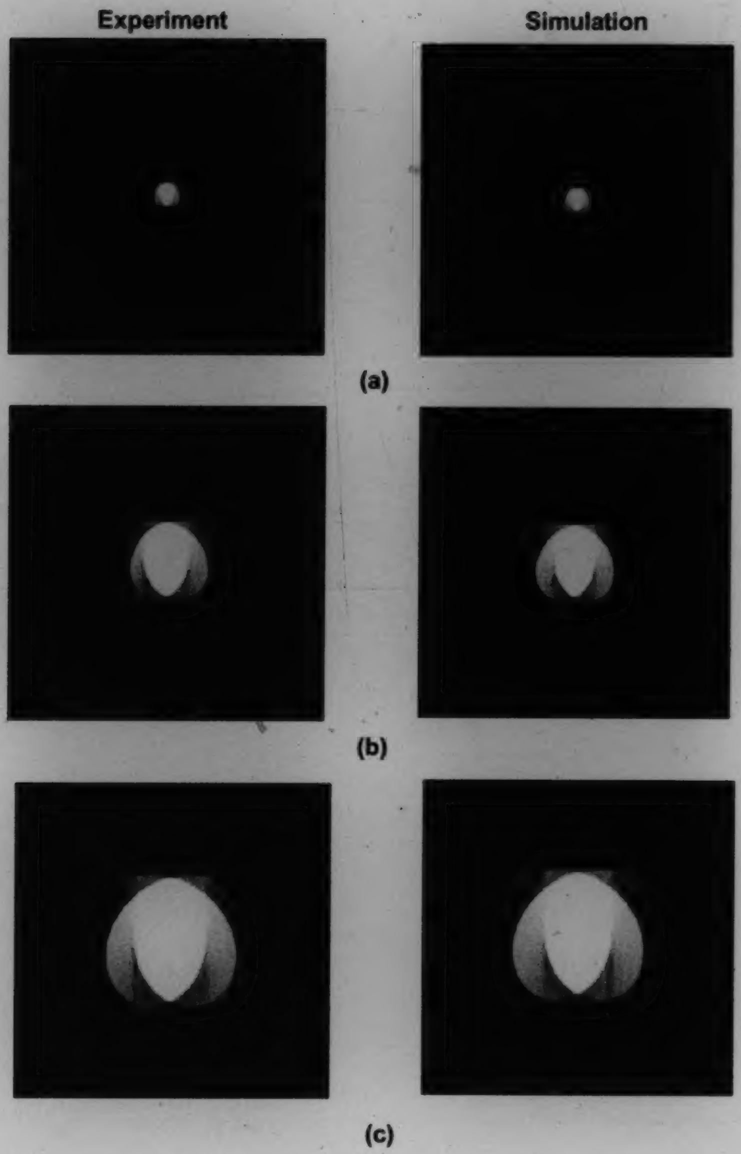

Figure 2.19 Experimental and simulation images of three POM cylinders undergoing a simple harmonic motion along the horizontal axis in an air background. **(a)** 10 mm diameter cylinder – 5 mm SHM, **(b)** 30 mm diameter cylinder – 15 mm SHM, and **(c)** 50 mm diameter cylinder – 25 mm SHM.

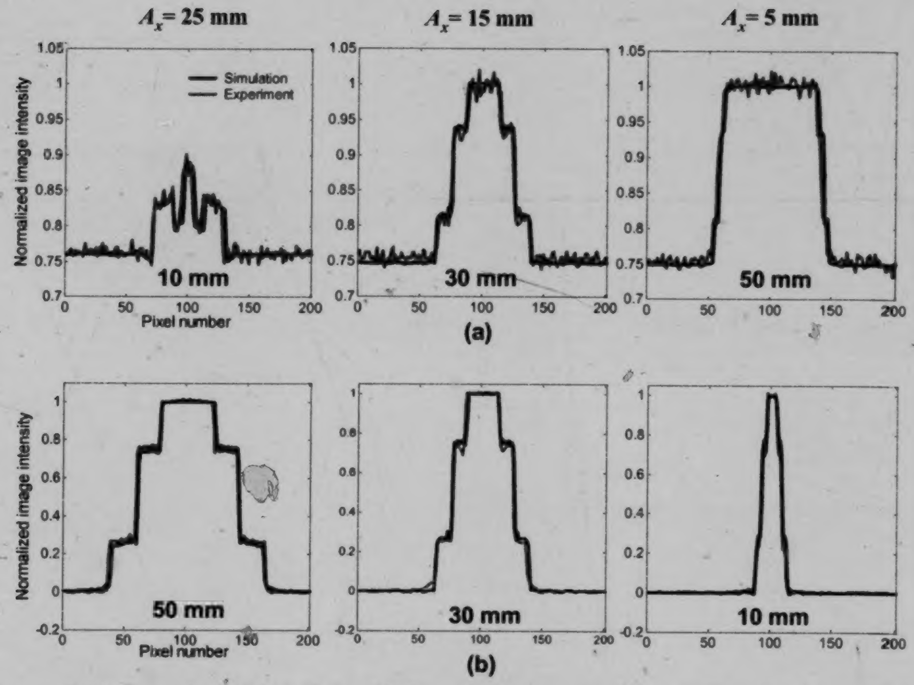

Figure 2.20 Experimental and simulation central horizontal profiles for the cylinders and horizontal SHMs shown in Figures 2.18 – 2.19.

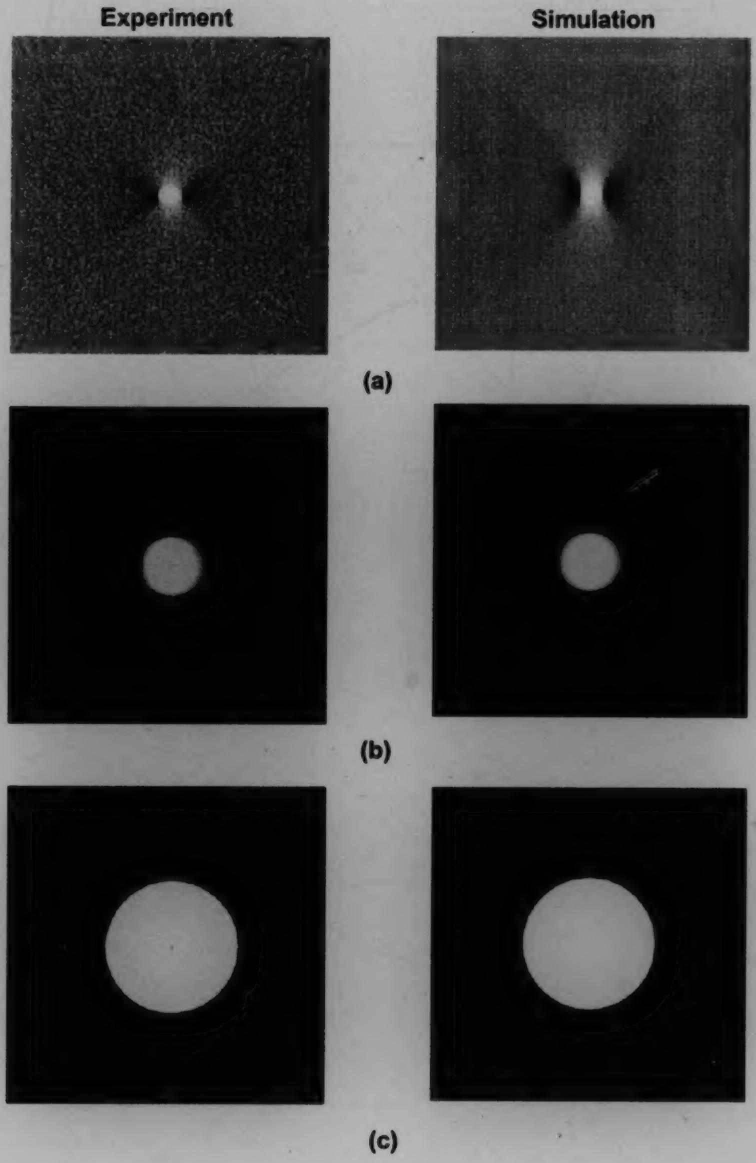

Figure 2.21 Experimental and simulation images of three POM spheres undergoing a simple harmonic motion along the *z*-axis of the scanner in a water background. **(a)** 10 mm diameter sphere – 25 mm SHM, **(b)** 25 mm diameter sphere – 15 mm SHM, and **(c)** 50 mm diameter sphere – 5 mm SHM.

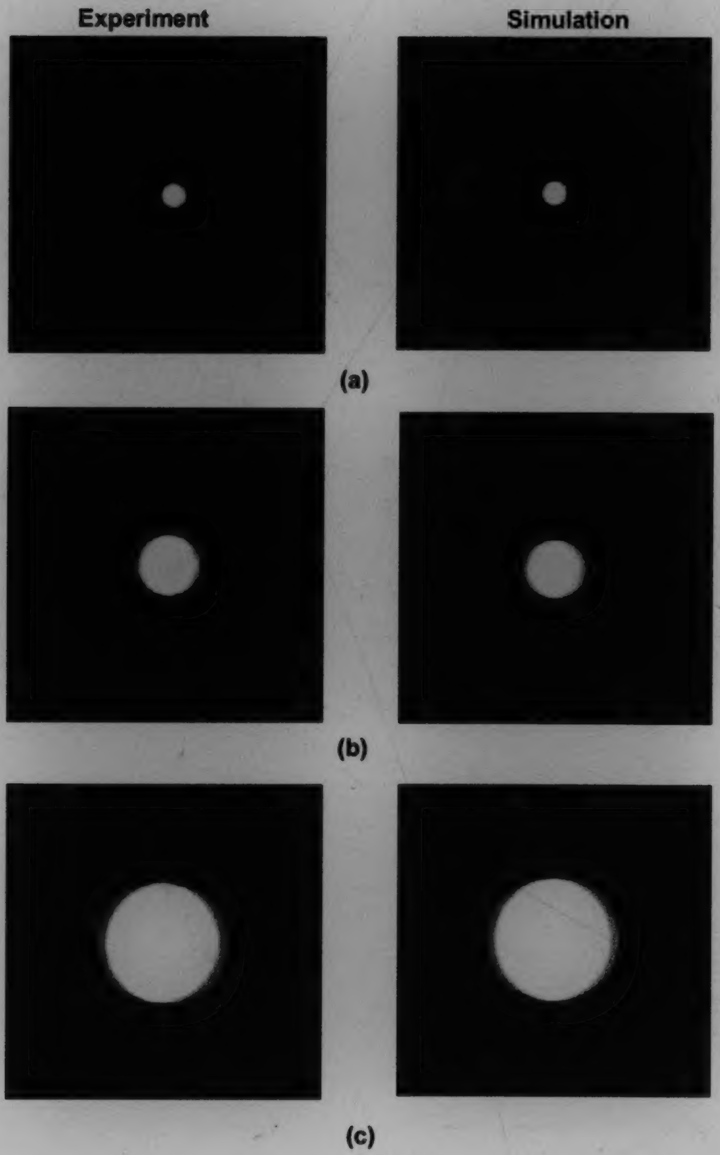

Figure 2.22 Experimental and simulation images of three POM spheres undergoing a simple harmonic motion along the *z*-axis of the scanner in an air background. **(a)** 10 mm diameter sphere – 5 mm SHM, **(b)** 25 mm diameter sphere – 15 mm SHM, and **(c)** 50 mm diameter sphere – 25 mm SHM.

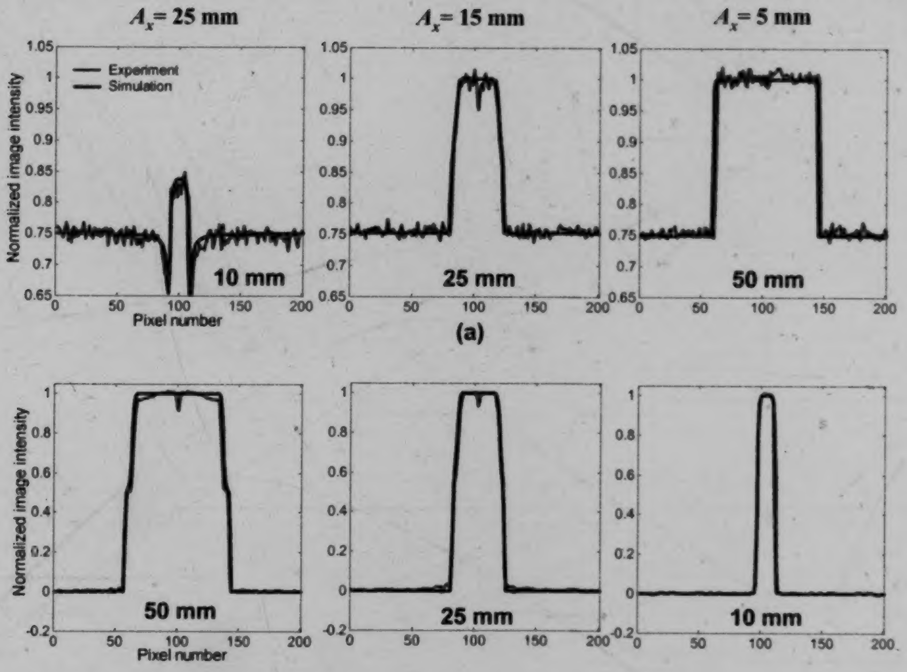

Figure 2.23 Experimental and simulation central horizontal profiles for the spheres and orthogonal SHMs shown in Figures 2.21 – 2.22.

2.7 References

[Ba 2001] E.A. Barnes, B.R. Murray, D.M Robinson, *et al.*, "Dosimetric evaluation of lung tumor immobilization using breath-hold at deep inspiration," Int. J. Radiat. Oncol. Biol. Phys. **50**, 1091 – 1098 (2001)

[Ba 1998] J. Balter, K. Lam, C. McGinn, *et al.*, "Improvement of CT-based treatment-planning models of abdominal targets using static exhale imaging," Int. J. Radiat. Oncol. Biol. Phys. **41**, 939 – 943 (1998)

[Bu 1981] J. Bull, "History of computed tomography," in *Radiology of the skull and brain: Technical aspects of computed tomography*, edited by T.H. Newton and D.G. Potts, The C.V. Mosby Company, London (1981) pp. 3835 – 3849

[Bu 1994] J.T. Bushberg, J.A. Anthony, E.M. Leidholdt *et al.*, *The Essential Physics of Medical Imaging*. Williams and Wilkins, Baltimore (1994)

[Co 1963a] A.M. Cormack, "Representation of a function by its line integrals, with some radiological applications," J. Appl. Physics **34**, 2722 – 2727 (1963)

[Co 1963b] A.M. Cormack, "Representation of a function by its line integrals, with some radiological applications. II," J. Appl. Physics **35**, 2908 – 2913 (1963)

[Cr 1996] C.R. Crawford, K.F. King, C.J. Ritchie, "Respiratory compensation in projection imaging using a magnification and displacement model," IEEE Trans. on Med. Imag. **Vol. 15**, no.3 (1996)

[Da 1995] W.J. Davros, B.R. Herts, J.J. Walmsley, *et al.* "Determination of spiral CT slice sensitivity profiles using a point response phantom," J. Comp. Assist. Tomogr. **Vol. 19**, no. 5, 838 – 843 (1995)

[Da 2001] L.A. Dawson, K.K. Brock, S. Kazanjian, *et al.*, "The reproducibility of organ position using active breathing control (ABC) during liver radiotherapy," Int. J. Radiat. Oncol. Biol. Phys. **51**, 1410 – 1421 (2001)

[Dh 2001a] A.C. Dhanantwari, *et al.* "Correcting organ motion artifacts in x-ray CT medical imaging systems by adaptive processing. I. Theory," Med. Phys. **28**, 1562 – 1576 (2001)

[Dh 2001b] A.C. Dhanantwari, *et al.* "Correcting organ motion artifacts in x-ray CT based on tracking of motion phase by the spatial overlap correlator. II. Experimental study," Med. Phys. **28**, 1577 – 1596 (2001)

[Ha 1999] J. Hanley, M.M. Debois, D. Mah *et al.*, "Deep inspiration breath-hold technique for lung tumors: the potential value of target immobilization and reduced lung density in dose escalation," Int. J. Radiat. Oncol. Biol. Phys. **45**, 603 – 611 (1999)

[Ha 1991] B.H. Hasegawa, *The physics of medical x-ray imaging*, 2nd Edition, Medical Physics Publishing, Madison, Wisconsin (1991)

[Hs 1995] J. Hsieh, "Image artifacts, causes and corrections," in *Medical CT and Ultrasound: Current Technology and Applications*, edited by L.W. Goldman and J.B. Fowles, Advanced Medical Publishing, Madison (1995) pp. 487-518

[Ka 1988] A.C. Kak and Malcolm Slaney, *Principles of Computerized Tomographic Imaging*, IEEE Press (1988)

[Ka 2000] W.A. Kalender, *Computed tomography: fundamentals, system technology, image quality, applications*, Publicis MCD Werbeagentur GmbH, Munich (2000)

[Ka 1990] W.A. Kalender, W. Seissler, E. Vock et al., "Spiral volumetric CT with single-breathold technique, continuous transport, and continuous scanner rotation," Radiology **176**, 181-183 (1990)

[Ke 2004a] P. Keall, "4-dimensional computed tomography imaging and treatment planning," Semin. Radiat. Oncol. **14**, 81 – 90 (2004)

[Ke 2004b] P.J. Keall., "Acquiring 4D thoracic CT scans using a multislice helical method," Phys. Med. Biol. **49**, 2053 – 2067 (2004)

[Ke 1991] P.J. Kelly. *Tumor Stereotaxis*, W.B. Saunders, Philadelphia (1991)

[Kh 2000] F.M. Khan and R.A. Polish, *Treatment planning in Radiation Onocology*, Lippincott, Williams & Wilkins (2000)

[Ku 2000] H. Kubo, P. Len, S. Minohara, *et al.*, "Breathing-synchronized radiotherapy program at the University of California Davis Cancer Center," Med. Phys. **27**, 346 – 353 (2000)

[Ku 1996] H.D. Kubo and B.C. Hill, "Respiration gated radiotherapy treatment: a technical study," Phys. Med. Biol. **41**, 83 – 91 (1996)

[La 2001] F.J. Lagerwaard, J.R. Van Sornsen de Koste, M.R. Nijssen-Visser, *et al.*, "Multiple "slow" CT scans for incorporating lung tumor mobility in radiotherapy planning," Int. J. Radiat. Oncol. Biol. Phys. **51**, 932 – 937 (2001)

[Li 2001] N.C. Linney, P.H. Gergson, "Organ motion detection in CT images using opposite rays in fan-beam projection systems," IEEE Trans. on Med. Imag. **Vol. 20**, no. 11 (2001)

[Lu 2002] W. Lu and T.R. Mackie, "Tomographic motion detection and correction directly in sinogram space," Phys. Med. Biol. **47**, 1267 – 1284 (2002)

[Lu 2003] Q. Luo, "Artifacts in X-ray CT," http://ric.uthscsa.edu/personalpages/lancaste/DI2_Projects_2003/XrayCT_artifacts.pdf (2003)

[Mc 1998] C.H. McCollough and F.E. Zink, "CT Numbers and Electron Density," AAPM Monogr. **No. 24**, 135-162 (1998)

[Mc 2003] M.F. McNitt-Gray, "Tradeoffs in CT image quality and dose," Proceedings of the American Association of Physics in Medicine 45th Annual Meeting, San Diego CA 9794-13379.pdf (2003)

[Mi 2001] M. Miften, M. Winsmeyer, A. Kapur, *et al.*, "Comparison of RTP dose distributions in heterogeneous phantoms with BEAM Monte Carlo simulation system," J. Appl. Clin. Med. Phys. **2**, 21 – 31 (2001).

[Mo 1983] C.L. Morgan, *Basic Principles of Computed Tomography*, University Park Press, Baltimore (1983)

[Na 2002] D. Narla, M.C. Schell, R.L. Ruo, *et al.*, "Pertubation of dose distribution at the lung-tumor tissue interface by changes in density," http://radonc.urmc.rochester.edu/~wodell/abstracts/rubi_dir/RubiNarla2002Poster.pdf (2002)

[On 2003] H. Onishi, K. Kuriyama, T. Komiyama, *et al.*, "A new irradiation system for lung cancer combining linear accelerator, computed tomography, patient self-breath-holding, and patient-directed beam-control without respiratory monitoring devices," Int. J. Radiat. Oncol. Biol. Phys. **56**, 14 – 20 (2003)

[Philips] www.medical.philips.com

[Ri 2003] E. Rietzel, G. T. Chen, K. P. Doppke, *et al.*, "4D computed tomography for treatment planning," Int. J. Radiat. Oncol. Biol. Phys. **57**, Supplement 0 (2003)

[Sh 2003] H. Shirato, T. Harada, T. Harabayashi, *et al.*, "Feasibility of insertion/implantation of 2.0-mm-diameter gold internal fiducial markers for precise set-up and real-time tumor tracking in radiotherapy," Int. J. Radiat. Oncol. Biol. Phys. **56**, 240 – 247 (2003)

[Se 2002] Y. Seppendwoole, H. Shirato, K. Kitamura, *et al.*, "Precise and real-time measurement of 3D tumor motion in lung due to breathing and heartbeat, measured during radiotherapy," Int. J. Radiat. Oncol. Biol. Phys. **53**, 822 – 834 (2002)

[Sp 1994] P. Sprawls, "X-ray imaging concepts: Basic considerations," AAPM Monogr. **No. 20**, 41-74 (1994) [va 2001] J.R. van Sornsen de Koste, F. J. Lagerwaard, R. H. Schuchhard-Schipper, *et al.*, “Dosimetric consequences of tumor mobility in radiotherapy of stage I non-small cell lung cancer -- an analysis of data generated using ‘slow’ CT scans,” Radiat. Oncol. **61**, 93 – 99 (2001)

[Wa 1997] G. Wang and M.W. Vannier, “Low-contrast resolution in volumetric x-ray CT - Analytical comparison between conventional and spiral CT,” Med. Phys. **24**, 373 – 376 (1997)

[We 1990] S. Webb, *The Physics of Medical Imaging*, Adam Hilger, New York (1990)

[Wo 1999] J.W. Wong, M.B. Sharpe, D.A. Jaffray, et al., “The use of active breathing control (ABC) to reduce margin for breathing motion,” Int. J. Radiat. Oncol. Biol. Phys. **44**, 911 – 919 (1999)

[Za 1981] L.M. Zatz, “Basic principles of computed tomography scanning,” in *Radiology of the skull and brain: Technical aspects of computed tomography*, edited by T.H. Newton and D.G. Potts, The C.V. Mosby Company, London (1981) pp. 3853 – 3876

[Zy 1996] W. Zylka and H.A. Wishmann. “On Geometric Distortions in CT images,” Proc. 18th Int. Conference IEEE Eng. Med. & Biol. Society EMBS, Amsterdam (1996)

Chapter 3: Characterization of motion artifacts associated with lung tumor motion

3.1 Introduction

In Chapter 2, the basic principles of motion-induced image artifact formation were presented. The investigation was carried out using a FBP algorithm developed in MATLAB and experimentally validated for both static and dynamic imaging conditions. In this chapter, the same simulation program is used to characterize respiration-induced motion artifacts associated with lung tumor motion. The respiration-induced lung tumor motion model used for these simulations and experimental verifications is described in Section 3.2.1 and is validated in Section 3.2.2 with clinical data.

In an attempt to better account for tumor motion in lung radiotherapy planning, findings are presented of an investigation into the functional nature of motion artifacts associated with axial scanning of mobile lung tumors. The understanding of these effects is crucial to any detailed analysis of planning CT images acquired of structures in motion. This is especially pertinent to the CT image artifacts that result from respiratory and cardiac motions which can contribute to inaccurate gross tumor volume delineation. It will be shown that the image artifacts produced by tumor motion are dependent not only upon the trajectory, scan time and relative size of the tumor with respect to its displacement, but also on the direction of the imaging beam at the time of acquisition initiation.

3.2 Background

3.2.1 Motion of lung tumors

In the past few years, several investigators have characterized lung tumor movements using a real-time tumor-tracking (RTRT) system [Sh 2001, Se 2002]. They reveal that the position of a lung lesion as a function of time during free-breathing in supine position may be described by the following sinusoidal function:

$$l(t) = l_0 - A\cos^{2n}\left(\frac{\pi t}{\tau_m} - \phi\right) \tag{3.1}$$

where n is a positive integer describing the shape of the sinusoidal function, l_0 is the position of the tumor at the end of expiration, A is the amplitude of motion, τ_m is the period of motion (breath cycle) and ϕ is the initial phase of motion [Lu 1999].

In the above studies [Sh 2001, Se 2002], the lung tumor movements were tracked using what is considered the most precise method currently available [Sh 2004]. Prior to initial treatment, a small 2 mm gold marker was inserted in or near the tumor. The x, y, z coordinates of the marker were recorded using the RTRT system 30 times a second over at least 10 minutes. For the majority of patients in the Seppendwoole *et al.* study (17/21), the general shape of the average breathing cycle could be well fitted with an asymmetry parameter, n, of either 1 (9/21) or 2 (8/21) [Se 2002]. Furthermore, inter-patient breathing cycles varied from 2.7 to 6.6 seconds and averaged 3.6 ± 0.8 seconds [Se 2002]. The amplitude of motion was reasonably constant over the course of the treatment although small intra-fractional variations were observed [Se 2002]. The mean amplitude of motion was the greatest in the cranial-caudal (CC) direction with a median of 12 ± 2 mm (range, 0.2 – 24.6 mm) [Se 2002]. Mean amplitudes in the left-right (LR) and anterior-posterior (AP) directions ranged from 0.2 – 2.8 mm and 0.2 – 8.2 mm, respectively [Se 2002]. In general, the mean amplitude of motion in the CC direction was larger for tumors in the lower lobes and not attached to the chest wall (12 ± 6 mm) than for tumors in the upper lobes and fixed to rigid structures (2 ± 2 mm). Four lung cancer patients were tracked using the RTRT system by Shimuzu *et al.* during both treatment beam-on and beam-off periods [Sh 2001]. The range of marker movement observed by this group during beam-off (i.e. normal tidal breathing) was 5.5 – 10.0 mm in the LR direction, 6.9 – 15.9 mm in the CC direction and 8.1 – 14.6 mm in the AP direction [Sh 2001].

The magnitude of lung tumor motion due to respiration has also been widely investigated using computed tomography and fluoroscopy [Ro 1990, Ek 1998, Sh 2000, Ba 2001, Ch 2001]. Ross *et al.* analyzed the intrathoracic movement of lung lesions using an ultrafast computerized tomography (UFCT) scanner and found that unrestricted lower lobe lung tumors can move an average of 10.5 mm (range, 5 – 22 mm) in the LR direction and 9.8 mm anteroposteriorly (5 – 19 mm) due to respiration and cardiac function [Ro 1990]. They attributed, however, most of the apparent LR and AP movements seen in the transverse images to cranial-caudal motion [Ro 1990]. Shimizu *et al.* also studied the impact of respiration on CT images of small lung tumors [Sh 2000]. Their study revealed tumor displacement ranges of 5.5 – 10.0 mm in the LR direction, 6.8 – 15.9 mm in the CC direction and 8.1 – 14.6 mm in the AP direction [Sh 2000]. Consecutive sequential CT images recently acquired at the same table position during quiet respiration for several patients with peripheral NSCLC lesions at this institute revealed intra-slice GTV centroid displacement due to internal motions as high as 13.2 mm. Ebkerg *et al.* used fluoroscopy to determine the extent of clinical target volume (CTV) motion in lung cancer patients [Ek 1998]. In their study, twenty tumors were observed via fluoroscopy and found to move an average of 2.4 mm, 2.4 mm and 3.9 mm in the LR, AP and CC directions. Maximum displacements of 5 mm, 5 mm and 12 mm were also reported in these directions. Barnes *et al.* found that tumor motion in the CC direction under free-breathing could be as large as 31.9 mm [Ba 2001]. Finally, *Chen et al.* reported in their paper that lung lesions can move as much as 50 millimeters due to breathing [Ch 2001].

In general, lateral displacements are greatest for tumors near the heart or aorta and the largest craniocaudal movements are related to the action of the diaphragm [Ro 1990, Gi 2001]. Overall mean displacements on the order of 5 mm in all directions characterize tumors of the upper lobe while 12 mm and 15 mm are typical of average anterior-posterior and lateral average movements respectively in the middle and lower lobes [Gi 2001].

3.2.2 Verification of lung tumor motion model

Prior to this research a study was conducted at this institute in which a number of patients (5) slated to receive radical 3-D conformal radiotherapy for non-small cell lung cancer (NSCLC) consented to fluoroscopic examination during which the movements of their lung tumors were observed and video recorded. Currently, most radiotherapy centers use conventional fluoroscopy, provided by a radiotherapy simulator, to assess the physiologic extent of tumor motion for treatment planning purposes. The aim of this particular study was to examine the accuracy of fluoroscopy in identifying the superior and inferior extremes of GTV physiologic motion. Eligibility was restricted to patients with intraparenchymal tumors fully circumscribed by lung. All five patients presented with parenchymal lung tumors below the level of the top of the aortic arch. According to current institute clinical practice, each patient was initially examined using fluoroscopy in treatment position while undergoing quiet respiration in order to estimate the superior-inferior (SI) boundaries of tumor motion. The location of these boundaries, as indicated by fluoroscopy, was marked on the patient's skin using external markers. Definitive superior-inferior tumor motion boundaries were then identified by first acquiring ten axial CT images in rapid succession (Picker PQ5000, 2 mm slice thickness, 1 sec/rotation) at each boundary location as indicated by the skin markers. If any of the images acquired revealed evidence of tumor, additional sets of 10 sequential images were acquired every 2 mm, moving outward from tumor center, until tumor was absent in all 10 scans. In cases where tumor was absent in the initial set of CT images, the above procedure was carried out in an inward moving fashion.

The results of this study revealed a distance from fluoroscopy marker to CT determined gross tumor edge ranging from 0 to 8 mm. In 4 of the five patients, at least one of the motion limits determined through fluoroscopy proved incorrect. Both superior and inferior limits were incorrectly identified in two of these five patients. From this limited study it was concluded that conventional fluoroscopic evaluation of the physiological motion associated with respiration was inadequate to accurately determine superior and inferior tumor extents. Radiotherapy fields designed using fluoroscopic data would most likely provide inadequate tumor coverage, thus compromising curative intent.

During the course of this investigation the large degree of tumor motion observed between consecutive CT images at the same physical location was noted. This observation served in large part as the motivation behind the research undertaken in this thesis. While not specifically a part of this research, the data gathered from this previous investigation serves to revalidate the utility of characterizing lung tumor motion according to the approximation of harmonic motion as specified by Equation 3.1 above. Unfortunately the accuracy of the data gathered was limited as implantation of marker seeds was not possible. Observations were limited to a single anterior-posterior view and thus revealed only the superior-inferior and lateral projections of motion. Lacking definitive marker seeds, measurements relied upon tracking the location of an identifiable radio-opaque feature of the imaged tumor mass during the course of motion captured. While such a limited number of measurements of do not yield statistics sufficient to draw conclusions with regard to the frequency of the values of *n* in Equation 3.1, they do provide a window into the degree of accuracy (and/or the lack thereof) to which Equation 3.1 models real clinical data.

For brevity sake only the superior-inferior tumor motions for patients 1, 3 and 5 will be presented here. Goodness of fit of Equation 3.1 to clinical data was determined by minimizing the cumulative absolute difference (CAD) between clinical data and Equation 3.1 according to

$$CAD(n,\phi) = \sum_{t=0}^{t=t_{\max}} \left| \text{measured displacement}(t) - \left[l_o - A\cos^{2n}\left(\frac{\pi t}{\tau_m} - \phi \right) \right] \right| \tag{3.2}$$

The motion captured for patient 1 is presented in Figure 1. Here the motions of both the tumor and diaphragm are shown. Tumor and diaphragm motions are clearly seen to be correlated, but disproportionately so. Each exhibits roughly the same variable periodicity but with markedly different patterns and scaling factors over successive repetitive segments. Both motion trajectories may be best classified as a quasi-periodic irregular cyclical series and are reasonably well, but not exactly, synchronized with one another. Amplitudes of displacement in the superior-inferior direction for the diaphragm and tumor range from 35 to 62 mm and from 19 to 25 mm respectively. Over the data span captured, the period of motion varies from 2.2 to 3.6 (mean = 3.0) seconds corresponding to respirations rates of 27.3 to 16.7 (mean = 20.1) breaths per minute respectively. The best fit of Equation 3.1 to the clinical data for this patient was achieved for $n = 2$ and $\phi = 70.95^\circ$as shown in Figures 3.2 and 3.3.

The tumor displacement measured for patient 3 is presented in Figure 3.4 along with the best fit by Equation 3.1 for $n = 2$ and $\phi = 71.25^\circ$. The most significant feature of this patient's data (and the reason for presentation here) is the breathing irregularity captured at the beginning of data acquisition which is highlighted by the box in Figure 3.4. This anomaly clearly illustrates the limitations of modeling this form of clinical data by a simple function such as Equation 3.1. Over the data span captured the amplitude of displacement for this tumor ranges from 6.8 to 25.4 mm and the period of motion varies from 2.9 to 4.6 (mean = 3.7) seconds corresponding to respirations rates from 20.7 to 13.0 (mean = 16.2) breaths per minute.

Finally, the data from patient 5 is presented in Figure 3.5 and is representative of breathing-induced motion with a pronounced rest or dwell phase at expiration. Here the best fit by Equation 3.1 is provided by $n = 3$ and $\phi = 40.1^{\circ}$. For this patient the amplitude of tumor displacement ranged from 8.2 to 8.6 mm and the period of motion varied from 2.3 to 3.1 (mean = 2.7) seconds, corresponding to respirations rates from 26.1 to 19.4 (mean = 22.2) breaths per minute over the data span captured.

The motions for all five patients were clearly seen to be distinct from one another. From the data presented here it is immediately obvious that Equation 3.1 provides a good first order approximation of the gross features of motion but fails to represent the finer details of tumor dynamics (on a time scale less than the breath period). Equation 3.1 is thus an adequate model of tumor dynamics for this thesis work as it is the large scale structure of motion-induced distortions that is the focus of this investigation. The finer scale details of tumor motion are clearly patient specific and beyond the scope of this work.

3.2.3 The functional parameters upon which motion artifacts are dependent

Due to CT scanner geometry, a natural division exists between motions which are constrained to the imaging plane (in-plane motions) and those orthogonal to it (orthogonal motions). Realistic motions including the natural dynamics associated with respiration and cardiac function, as well as other physiologic processes, exhibit components of varying magnitude of both in-plane and orthogonal motions. The functional parameters upon which motion artifacts are dependent may be readily deduced by considering dynamics constrained to the imaging plane and imaged with an infinitesimal slice width. It will be shown in Section 3.4.2 that the functional parameters identified for in-plane motion also apply to orthogonal movement. In reality, finite slice width adds partial volume effects to further compound these motion-induced image artifacts. The presence of partial volume effects due to finite slice width will be dealt with in future sections as required. For the time being, infinitesimal slice width will be assumed as this allows for a simplification of analysis without a loss in generality. Proceeding in this manner, the functional parameters which govern the form of motion-induced artifact patterns may be identified by considering a point like object moving with a constant velocity along a line in the imaging plane.

Consider first a point like object embedded within a uniform density background (see Figure 3.6a). Under static conditions all back projections intersect at a single point forming a reconstruction of the original point like object (see Figure 3.6b). Now let this same object move with a constant velocity V along a line in the imaging plane at an angle β to the *x*-axis as shown in Figure 3.6c. The form of the motion artifact produced will be dominated by the intersections of consecutive back projections. Thus consider the intersection of back projections from projection angles φ and $\varphi + \delta$, where δ is the angular increment between consecutive projection angles (see Figure 3.6d). If the distance from the center of reconstruction to the focal spot of the CT *x*-ray tube is **R** then the *x* and *y* coordinates of the focal spot (X^S, Y^S) as a function of projection angle are

$$\begin{aligned} X^S &= R\cos(\varphi) \\ Y^S &= R\sin(\varphi) \end{aligned} \tag{3.3}$$

If the rotational speed of the CT is ω_s, then the projection angle φ at time t is given by

$$\varphi = \varphi_o + \omega_s t \tag{3.4}$$

where φ_o is the projection angle at t = 0.

Thus one may write

$$t = \frac{\varphi - \varphi_o}{\omega_s} \tag{3.5}$$

where

$$\omega_s = \frac{2\pi}{\tau_s} \tag{3.6}$$

and τ_s is the rotation period of the CT. Here a full rotation acquisition, and thus an image acquisition time equal to τ_s will be assumed.

Now if the object displaces a distance 2A in time ΔT then its speed V is given by

$$V = \frac{2A}{\Delta T} \tag{3.7}$$

and the position of the mobile point like object along the line of motion is

$$l = l_o + Vt = l_o + V\left(\frac{\varphi - \varphi_o}{\omega_s}\right) = \frac{A}{\pi}\alpha(\varphi - \varphi_o + \phi) \tag{3.8}$$

where α is the ratio of image acquisition time (τ_s) to the time which characterizes the motion of the object (ΔT) and ϕ is the phase of motion.

The *x* and *y* coordinates (X^o, Y^o) of the mobile object are given by

$$\begin{aligned} X^o &= x_o + l\cos(\beta) = \frac{A}{\pi}\alpha(\varphi - \varphi_o + \phi)\cos(\beta) \\ Y^o &= y_o + l\sin(\beta) = \frac{A}{\pi}\alpha(\varphi - \varphi_o + \phi)\sin(\beta). \end{aligned} \tag{3.9}$$

If the following identifications are made

$$\begin{aligned} g &= \frac{A}{\pi}\alpha\cos(\beta) \\ h &= \frac{A}{\pi}\alpha(\phi - \varphi_o)\cos(\beta) \\ j &= \frac{A}{\pi}\alpha\sin(\beta) \\ k &= \frac{A}{\pi}\alpha(\phi - \varphi_o)\sin(\beta) \end{aligned} \tag{3.10}$$

then one may write

$$\begin{aligned} X^o &= g\varphi + h \\ Y^o &= j\varphi + k \end{aligned} \tag{3.11}$$

The line describing the back projection from *x*-ray focal spot to object at projection angle φ is given in its standard form of

$$y = m_1 x + b_1 \tag{3.12}$$

where m_1 is the slope of the projection line and b_1 is the y-intercept.

Here,

$$m_1 = \frac{Y^o - Y^S}{X^o - X^S} = \frac{j\varphi + k - R\sin(\varphi)}{g\varphi + h - R\cos(\varphi)} \tag{3.13}$$

and

$$\begin{aligned} b_1 = Y^o - m_1 X^o &= j\varphi + k - \frac{j\varphi + k - R\sin(\varphi)}{g\varphi + h - R\cos(\varphi)}(g\varphi + h) \\ &= j\varphi + k - m_1(g\varphi + h) \\ &= (j - m_1 g)\varphi + k - m_1 h \end{aligned} \tag{3.14}$$

or

$$b_1 = \frac{\varphi[gR\sin(\varphi) - jR\cos(\varphi)] + R[h\sin(\varphi) - kR\cos(\varphi)]}{g\varphi + h - R\cos(\varphi)}. \tag{3.15}$$

Now if the next projection is acquired at a projection angle of $\varphi + \delta$, then the slope and y-intercept of this line from focal spot to object is

$$m_2 = \frac{Y^o - Y^S}{X^o - X^S} = \frac{j(\varphi + \delta) + k - R\sin(\varphi + \delta)}{g(\varphi + \delta) + h - R\cos(\varphi + \delta)} \tag{3.16}$$

and

$$b_2 = (j - m_2 g)(\varphi + \delta) + k - m_2 h \tag{3.17}$$

or

$$b_2 = \frac{\varphi[gR\sin(\varphi+\delta) - jR\cos(\varphi+\delta)] + R[h\sin(\varphi+\delta) - kR\cos(\varphi+\delta)]}{g(\varphi+\delta) + h - R\cos(\varphi+\delta)}. \tag{3.18}$$

The intersection between these two consecutive projection lines occurs at

$$y = m_1 x_{int} + b_1 = m_2 x_{int} + b_2$$

$$x_{int} = \frac{b_2 - b_1}{m_1 - m_2} \quad . \tag{3.19}$$

$$y_{int} = m_1 x_{int} + b_1$$

More specifically,

$$x_{int} = \frac{[(j - m_2 g)(\varphi + \delta) + k - m_2 h] - [(j - m_1 g)\varphi + k - m_1 h]}{\left[\dfrac{j\varphi + k - R\sin(\varphi)}{g\varphi + h - R\cos(\varphi)}\right] - \left[\dfrac{j(\varphi+\delta) + k - R\sin(\varphi+\delta)}{g(\varphi+\delta) + h - R\cos(\varphi+\delta)}\right]}$$

$$y_{int} = \frac{j\varphi + k - R\sin(\varphi)}{g\varphi + h - R\cos(\varphi)} \frac{[(j - m_2 g)(\varphi + \delta) + k - m_2 h] - [(j - m_1 g)\varphi + k - m_1 h]}{\left[\dfrac{j\varphi + k - R\sin(\varphi)}{g\varphi + h - R\cos(\varphi)}\right] - \left[\dfrac{j(\varphi+\delta) + k - R\sin(\varphi+\delta)}{g(\varphi+\delta) + h - R\cos(\varphi+\delta)}\right]}. \tag{3.20}$$

$$+ (j - m_1 g)\varphi + k - m_1 h$$

These rather lengthy expressions reveal the functional parameters which determine the essential form of the artifact patterns produced by objects in motion in the image plane during CT image acquisition. For a single scanner the distance R from x-ray focal spot to rotation center is fixed. Thus the functional parameters which define the form of the artifact pattern are

α the ratio of image acquisition time to the time which characterizes the motion of the object ($\alpha = \tau_s / \Delta \mathrm{T}$),

φ_o the initial projection angle,

A the amplitude of object motion,

ϕ the phase of object motion, and

β the orientation of the motion in the image plane.

It is instructive to constrain the line of object motion to the positive *x*-axis ($\beta = 0^{\circ}$). In this case one has

$$\begin{gathered}
g = \frac{A}{\pi} \alpha \cos(\beta = 0) = \frac{A}{\pi} \alpha \\
h = \frac{A}{\pi} \alpha (\phi - \varphi_o) \cos(\beta = 0) = -\frac{A}{\pi} \alpha (\phi - \varphi_o) \\
j = \frac{A}{\pi} \alpha \sin(\beta = 0) = 0 \\
k = \frac{A}{\pi} \alpha (\phi - \varphi_o) \sin(\beta = 0) = 0
\end{gathered} \tag{3.21}$$

and Equation (3.20) above reduces to

$$x_{int} = \frac{\left[(m_1 g)\varphi + m_1 h\right] - \left[(m_2 g)(\varphi + \delta) + m_2 h\right]}{\left[\frac{R\sin(\varphi)}{R\cos(\varphi) - g\varphi - h}\right] - \left[\frac{R\sin(\varphi + \delta)}{R\cos(\varphi + \delta) - g(\varphi + \delta) - h}\right]}$$

$$y_{int} = \frac{R\sin(\varphi)}{R\cos(\varphi) - g\varphi - h} \cdot \frac{\left[(m_1 g)\varphi + m_1 h\right] - \left[(m_2 g)(\varphi + \delta) + m_2 h\right]}{\left[\frac{R\sin(\varphi)}{R\cos(\varphi) - g\varphi - h}\right] - \left[\frac{R\sin(\varphi + \delta)}{R\cos(\varphi + \delta) - g(\varphi + \delta) - h}\right]} \\ - (m_1 g)\varphi - m_1 h \qquad (3.22)$$

where

$$g = \frac{A}{\pi}\alpha$$

$$h = -\frac{A}{\pi}\alpha(\phi - \varphi_o)$$

$$m_1 = \frac{R\sin(\varphi)}{R\cos(\varphi) - g\varphi - h} \qquad (3.23)$$

$$m_2 = \frac{R\sin(\varphi + \delta)}{R\cos(\varphi + \delta) - g(\varphi + \delta) - h}$$

From the above one can see that even though object motion is, in this case, restricted to the *x*-axis, the motion artifact pattern has non-zero components in the *y* dimension. Thus motion during CT acquisition projects the reconstructed object in directions displaced from its velocity vector. This is in contrast to the smearing of mobile objects in planar radiography which is always along the line of motion. That the reconstructed object is displaced from its in-plane trajectory path is perhaps the most striking feature of motion- induced CT artifacts.

3.3 Methods and Materials

3.3.1 Computer simulations

The filtered backprojection (FBP) computer simulation program, described in Chapter 2, is used to investigate the functional dependence of lung tumor motion artifacts associated with respiration. Since the CT projection angle is a function of time, the time-dependent lung tumor motion function described in Equation (3.1) may be parameterized in terms of projection angle

$$l(\varphi) = l_0 - A \cdot \cos^{2n}\left(\frac{\tau_s}{2 \cdot \tau_m}(\varphi - \varphi_0) - \phi\right) \tag{3.24}$$

where φ is the projection angle, τ_s the scanner rotation time, and φ_o the initial projection angle. An investigation into the essential nature of motion artifacts associated with the dynamics of mobile lung tumors should entail an analysis of objects undergoing motion of the following form:

$$l_x(\varphi) = l_{x0} - A_x \cdot \cos^{2n}\left(\frac{\alpha}{2}(\varphi - \varphi_0) - \phi_x\right) \tag{3.25}$$

$$l_y(\varphi) = l_{y0} - A_y \cdot \cos^{2n}\left(\frac{\alpha}{2}(\varphi - \varphi_0) - \phi_y\right) \tag{3.26}$$

$$l_z(\varphi) = l_{z0} - A_z \cdot \cos^{2n}\left(\frac{\alpha}{2}(\varphi - \varphi_0) - \phi_z\right). \tag{3.27}$$

where α is the ratio τ_s/τ_m of the acquisition time to the motion period, A_x, A_y, A_z are the amplitudes of motion in the medio-lateral (LR), antero-posterior (AP), and cranio-caudal (CC) directions, l_{x0}, l_{y0}; l_{z0} are the three-dimensional coordinates of the tumor at the end of expiration, and ϕ_x, ϕ_y, ϕ_z are the initial LR, AP, and CC phases of motion.

In view of the fact that a natural division exists in CT between in-plane and orthogonal motions, all investigations regarding the functional dependence of respiration-induced motion artifacts were carried out by restricting the object movement to either one of these planes. Most investigations were conducted with computer simulations using a 300 mm FOM, an infinitesimal slice thickness and a digital phantom consisting of either a 6.4 mm diameter POM cylinder (in-plane motion) or a 25 mm diameter POM sphere (orthogonal motion) situated inside a 200 mm diameter cylinder filled with water.

Since motion-induced artifacts patterns are most readily discerned when motion amplitudes are large in relation to the object size, the degree of motion imparted to the above-mentioned cylindrical and spherical objects was chosen near the upper limit of clinical experience. All objects were modeled to move according to Equations 3.25 – 3.27. The functional dependence of the respiration-induced artifact patterns was explored by individually varying alpha α (note: kept period of motion to 4 seconds and varied the rotation time from 1 to 4 seconds), the amplitude A, the initial phase ϕ, the asymmetry value n, and the initial projection angle φ_o. The impact of varying the orientation of motion within the imaging plane was also addressed. For the purpose of investigation, orientation of motion in the scan plane was defined as the angular position of the object at image initiation, $\beta = \theta(\varphi_o)$ (see Figure 3.7).

The functional dependence of the motion artifacts associated with lung tumor motion is illustrated using both reconstruction images and sinograms. For visualization purposes, only the central 201 × 201 pixels of the reconstructed images and the central portion [$- 75 \text{ mm} \leq x_r(\varphi) \geq 75 \text{ mm}$] of the sinograms are presented.

Finally, all images and sinograms are displayed using a gray colormap defined according to the minimum and maximum pixel intensities.

3.3.2 Experimental verification

Measurements for experimental verification were carried out on a Picker 5000 CT scanner. Images were reconstructed from projection data acquired using a full 360° tube rotation. All axial scans were acquired at 120 kVp, with a tube current of 200 mA using a nominal slice thickness of 3 mm and a 300 mm FOV. For consistency, all data sets were reconstructed using a vendor designated "standard filter" and a 512 × 512 image matrix. As the vendor regards as proprietary a great many details regarding the exact working of the scanner, a detailed description of the algorithms of reconstruction (including filter design) cannot be supplied. The phantom used to evaluate the functional dependence of motion artifacts was constructed in-house and designed to reproduce the essential motions of real lung tumors according to Equations 3.25 – 3.27. For a detailed description of the phantom, please refer to Chapter 2, Section 2.5. Spherical (diameter = 25 mm) and cylindrical (diameter = 6.4 mm) objects made out of POM were used as imaging targets. All experiments were carried out in a water filled cylinder, 200 mm in diameter.

All experimental images were imported into MATLAB for analysis and direct comparison with modeling results. In order to properly demonstrate the functional dependence of respiration-induced motion artifacts, only the central 201 × 201 pixels of the experimental images are presented. For visualization purposes, all experimental images are displayed using a gray colormap defined according to the minimum and maximum pixel intensities.

3.4 Results and Discussion

3.4.1 In-plane motion

3.4.1.1 Scan time to motion period ratio (alpha)

Simulation sinograms for various values of alpha (ranging from 0 to 1) typical of radiotherapy planning scans (both current and proposed) are shown in Figure 3.8a. An alpha value of 1, for example, corresponds to a 4 second image acquisition and a motion period of 4 second. The motion imparted to the cylindrical object was a 25 mm sinusoidal motion along the horizontal axis of the imaging plane as per Equation 3.25. As alpha increases from a minimum of 0 to a maximum of 1, the sinogram deviates further and further from the fundamental cosine curve associated with a static object and more complex image reconstruction artifacts result accordingly. The impact of these deviations upon image reconstruction is illustrated in Figure 3.8b. Positions of both the mobile object and CT *x*-ray tube become synchronized when acquisition times are integer multiples of the motion period and closed reconstruction patterns occur. Furthermore, it is noted that the spatial distribution of the motion artifact, and thus the spread of the object's contrast, is always beyond the spatial extent of the motion captured during data acquisition. Since image artifacts associated with in-plane motion are the result of a convolution between the object and the mobile blur functions, h_m, the sum intensity of the full (512 × 512) image must remain the same. Table 3.1 summarizes the sum of all pixel values for each alpha value simulated. It can be observed from the statistics and the overall standard deviation (± 0.06 HU) that image contrast is conserved when motion is restricted to the imaging plane. The validity of the simulated reconstructions presented is confirmed by the experimental images shown in Figure 3.8c.

3.4.1.2 Amplitude, phase, orientation & asymmetry

The simulation sinograms and images in Figures 3.9 – 3.12 illustrate how changes in the amplitude, phase, orientation and asymmetry affect the spatial extent, intensity, and orientation of the motion artifact. It can be seen from Figure 3.9 that as the amplitude of motion increases, the spatial extent of the motion artifact expands accordingly, but the shape of the pattern remains unaffected. Moreover, it was found that the reconstructed densities decreased with increasing amplitude. Variations in the amplitude of motion correspond directly to changes in the radial position, r (φ), of the object in sinogram space. Variations in the initial phase of motion at the start of acquisition from 0° to 90°, however, result in changes to both the radial, r (φ), and angular, θ (φ), positions of the object in sinogram space and thus create distinct motion artifacts (see Figure 3.10). Similarly, alterations to the orientation of motion from 180° to 270° also lead to different motion artifact patterns (see Figure 3.11). It is observed that the shape of the motion artifact is less affected by a change in orientation than by a change in phase. Figures 3.12a – b illustrate the impact of varying the asymmetry parameter, n, upon both the sinogram and image spaces. As n increases, a more accurate representation of the object at the end of expiration results due to the increased number of projections acquired while the object is quasi-stationary. Since, however, a portion of the sinogram space still contains motion-encoded information, motion artifacts remain as n increases but their intensity is reduced (see Figure 3.12c).

3.4.1.3 Angular position of scanner at initiation

The simulation images in Figure 3.13 demonstrate the dependence of the motion artifact pattern upon beta (β), an angle which defines the angular difference between orientation of motion in the imaging plane, θ (φ_o), and the initial projection angle, φ_o. It can be seen from Figure 3.13a, that as beta decreases from 180° to 90° for a motion along the horizontal axis (θ (φ_o) = 180°), the shape of the motion artifact varies from a bow tie to a hypercycloid pattern. On the other hand, when beta is maintained, indicating a synchronization between the initial scanner and the object angular positions, the shape of the motion artifact remains unaltered from one acquisition to the next but its orientation varies according to the difference between initial scanner positions (see Figure 3.13b).

3.4.2 Orthogonal motion

3.4.2.1 Scan time to motion period ratio (alpha)

The simulation sinograms which result for a 25 mm diameter spherical test object undergoing a 25 mm orthogonal SHM along the *z*-axis of the scanner are shown in Figure 3.14a for alpha values ranging from 0 to 1. As alpha increases, the sinogram departs by ever greater amounts from that of the static sphere as a result of alterations to both the intensity and width of the projections. The impact of these alterations upon image reconstruction is illustrated in Figure 3.14b. As alpha increases, the severity of the motion artifact increases accordingly. Experimental reconstructions for the same motions are shown in Figure 3.13c and are seen to agree well with the results generated by simulation. Slight differences between the simulation and experimental images are observed. Experimental images incorporate the effects of partial voluming and thus appear more blurred than the simulation images which are based upon infinitesimal slice width analysis. The rotational differences observed arise due to experimental setup errors as well as uncertainties in the phase synchronization between object and scanner motions. As discussed in Chapter 2, partial volume effects can be integrated in the computer modeling process using experimental slice sensitivity profiles. Figure 3.14d illustrates the corresponding simulation results generated using a finite slice width of 3 mm. As expected, blurring is observed in these finite slice width CT simulation images which better agree with their experimental counterparts.

3.4.2.2 Amplitude, phase & asymmetry

Figures 3.15 – 3.17 illustrate the effects of varying the amplitude, phase and asymmetry parameter upon the sinogram and its corresponding simulation image. It can be seen from the sinograms in Figure 3.15a that as the amplitude of the orthogonal motion increases from 20 to 30 mm, the number of projections containing information about the mobile object decreases. The resultant images are shown in Figure 3.15b. For motions where a cross-section of the object is always present in the imaging plane, the motion artifact appears as two identical circles separated in space. The dimension of the circles and the spatial distance between them are dependant upon the amplitude of motion. The sinograms of Figure 3.16a illustrate the impact of increasing the initial phase of motion for a 20 mm orthogonal SHM from an initial value of 45^o to 90^o by an increment of 22.5^o. It can be observed from these sinograms that as the initial phase of motion is increased by 22.5^o, the projection data are displaced by 90^o. In image space, this shift results in an equivalent rotation of the motion artifact pattern (see Figure 3.16b). Finally, it can be discerned from the sinograms in Figure 3.17a that as the asymmetry parameter n, of the orthogonal motion increases, from 1 to 3, a greater amount of motion is captured during data acquisition. In image space, the increased amount of motion captured with increasing asymmetry parameter results in motion artifacts that are present more distally in the image matrix (see Figure 3.17b).

3.4.2.3 Angular position of scanner at initiation

Figure 3.18 illustrates the impact of initiating the imaging sequence at various angular positions. It can be seen from the reconstructed images, that as the initial projection angle, φ_o, is increased from 0^o to 90^o for a 20 mm orthogonal SHM, the shape of the motion artifact pattern remains invariant but its orientation changes according to the difference between the two initial projection angles.

3.5 Summary and Conclusion

Numerous studies have reported on the magnitude of tumor motion associated with free breathing and cardiac function. While displacements as large as 50 mm have been reported, typical values of 5 mm in all directions characterize tumors of the upper lobe while 12 mm anterior-posterior and 15 mm laterally are associated with middle and lower lobe lesions. The functional dependence of the image artifacts which arise due to target dynamics were investigated using simple geometric objects undergoing well defined trajectories approximating real lung tumor motions. The ability of computer modeling to accurately reproduce experimental results was demonstrated. While artifact patterns associated with movement constrained to either the imaging plane or orthogonal to it are quite distinctive from one another, the parameters upon which they depend are the same. These functional parameters are the ratio α of scan time to motion period, the amplitude, phase and asymmetry of motion and the angular position of the x-ray tube at the initiation of image acquisition.

With the exception of breath-hold techniques, all current CT scans for lung radiotherapy are acquired while the tumor is non-stationary and as such are subject to the presence of motion artifacts. From an imaging standpoint the mobile object is subject to a wide ranging degree of distortion from its true shape depending on object size, extent of motion, and scan time. Mild and even barely detectable distensions are associated with rapid scans of objects whose range of motion is small in comparison to their physical size. In contrast, highly contorted images can result when object size is small in comparison to the extent of motion. These effects are exacerbated by long scan times in comparison to more rapid image acquisition schemes. These contortions can be so severe as to render the reconstructed image unrecognizable in relation to its static counterpart.

TABLE 3.1

Sum of all pixel values from simulation images generated using alpha values encountered in lung radiotherapy planning CT scans

Alpha value	Sum intensity (HU)
0	44.9310
0.25	44.9230
0.50	44.8956
0.75	45.0327
1	44.8844
Mean ± SD	**44.93 ± 0.06**

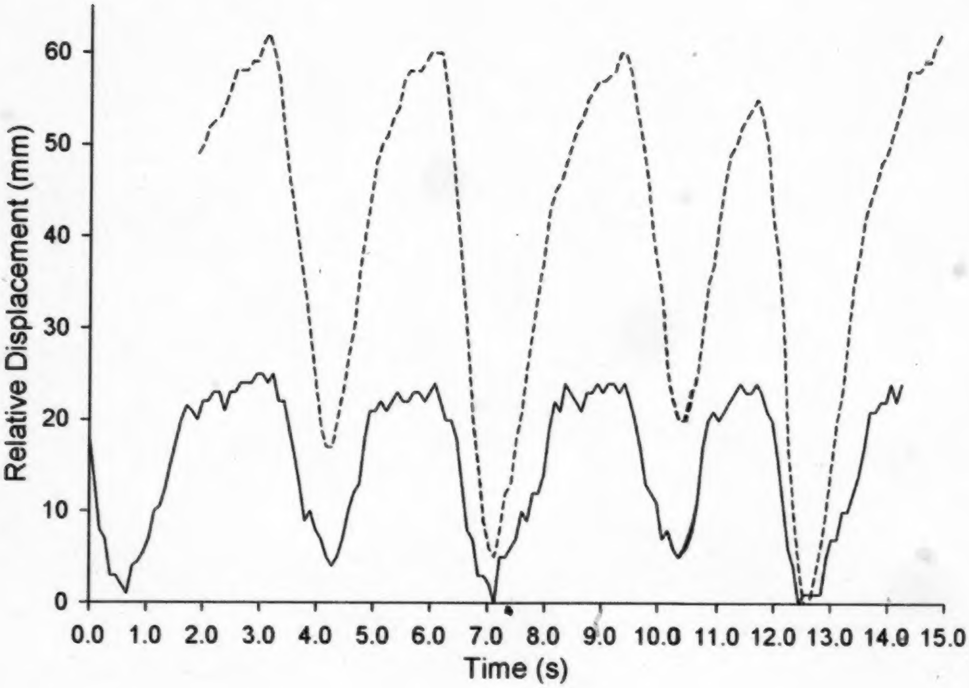

Figure 3.1 Measured superior-inferior displacements of both tumor (solid) and diaphragm (dashed) for patient 1.

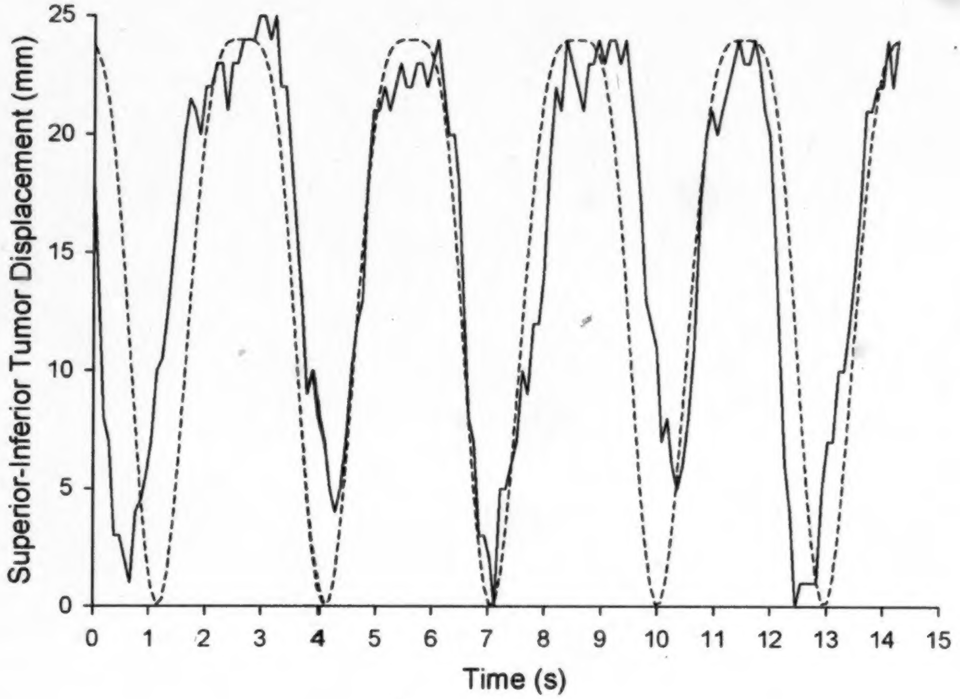

Figure 3.2 Superior-inferior tumor displacement for patient 1 comparing experimental data (solid) with modeling (dashed) according to Equation 3.1 with $n = 2$, $\phi = 70.95^{\circ}$.

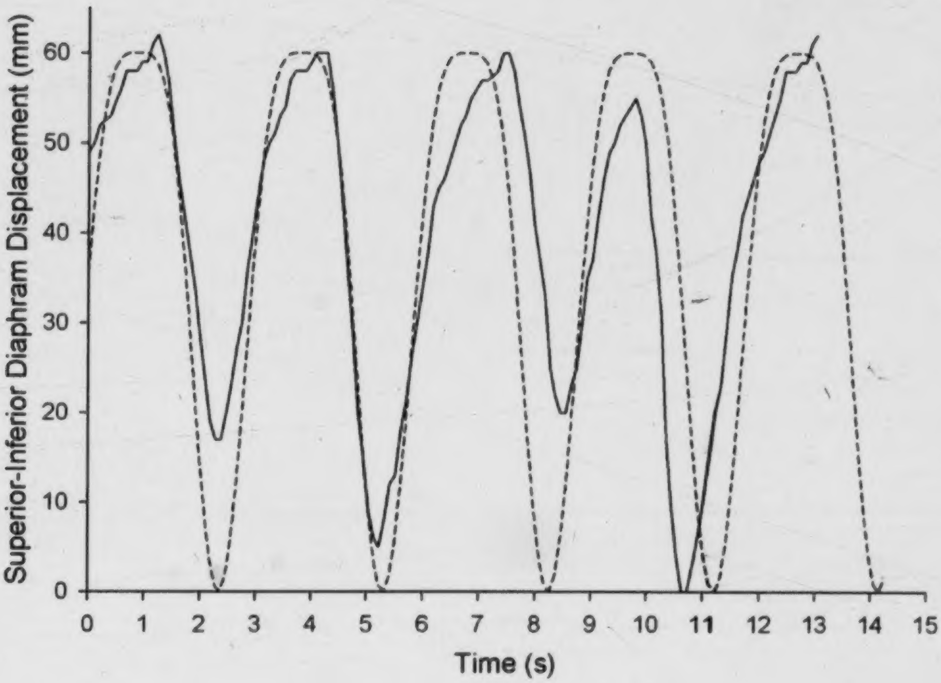

Figure 3.3 Superior-inferior diaphragm displacement for patient 1 comparing experimental data (solid) with modeling (dashed) according to Equation 3.1 with $n = 2$, $\phi = 70.95^{\circ}$.

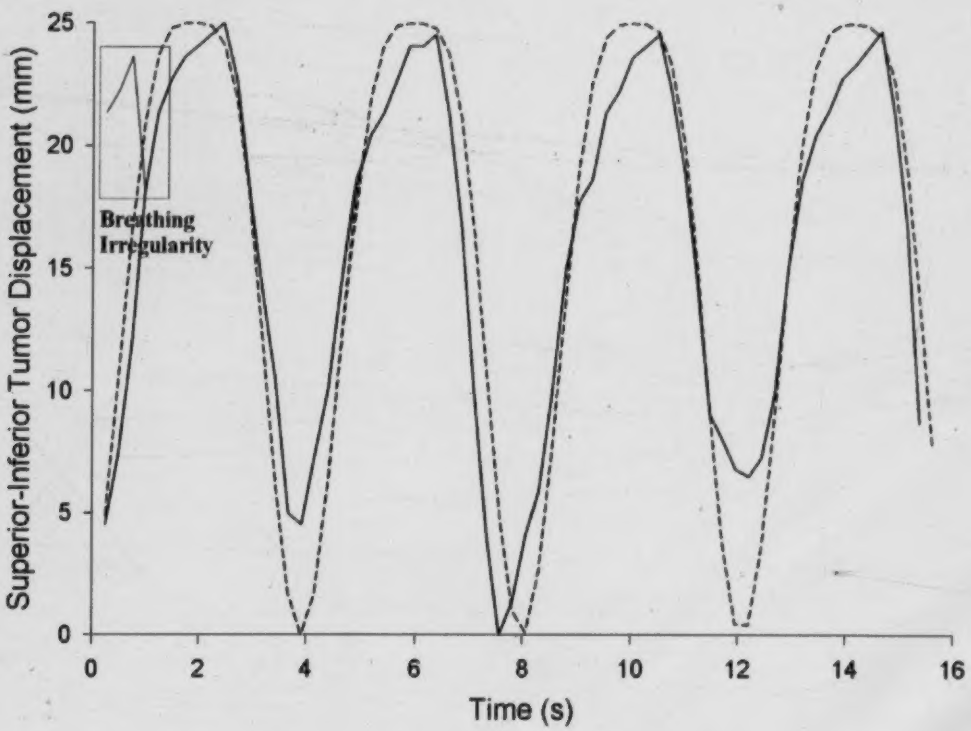

Figure 3.4 Superior-inferior tumor displacement for patient 3 comparing experimental data (solid) with modeling (dashed) according to Equation 3.1 with n = 2, $\phi = 71.25^\circ$. The presence of an irregularity in the breathing pattern is indicated by the boxed area.

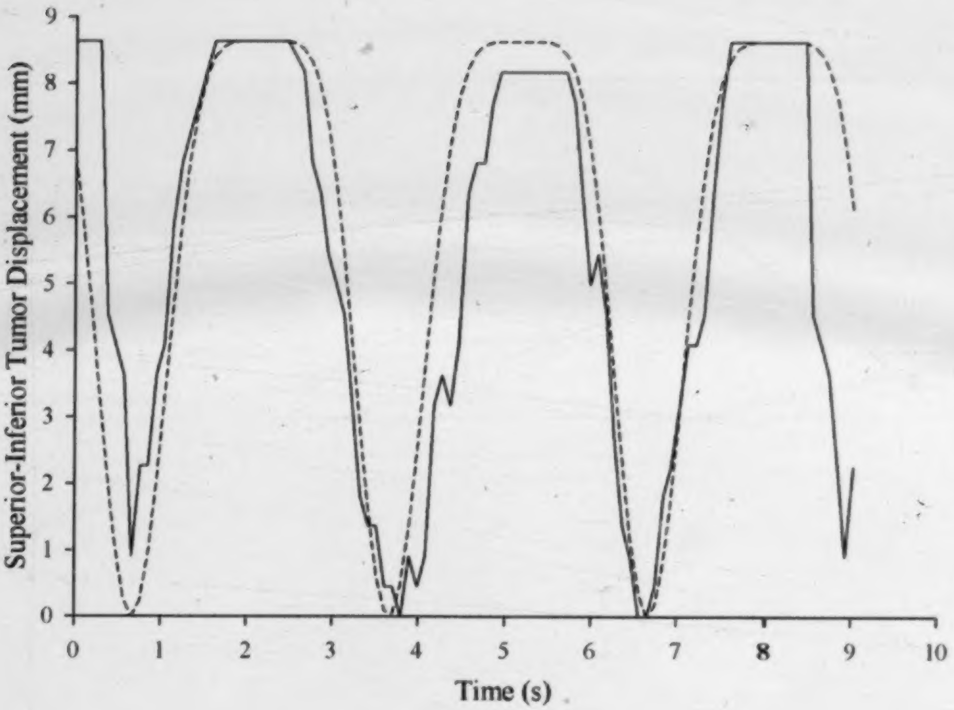

Figure 3.5 Superior-inferior tumor displacement for patient 5 comparing experimental data (solid) with modeling (dashed) according to Equation 3.1 with $n = 3$, $\phi = 40.1^{\circ}$. The presence of a conspicuous rest or dwell phase at expiration is clearly evident.

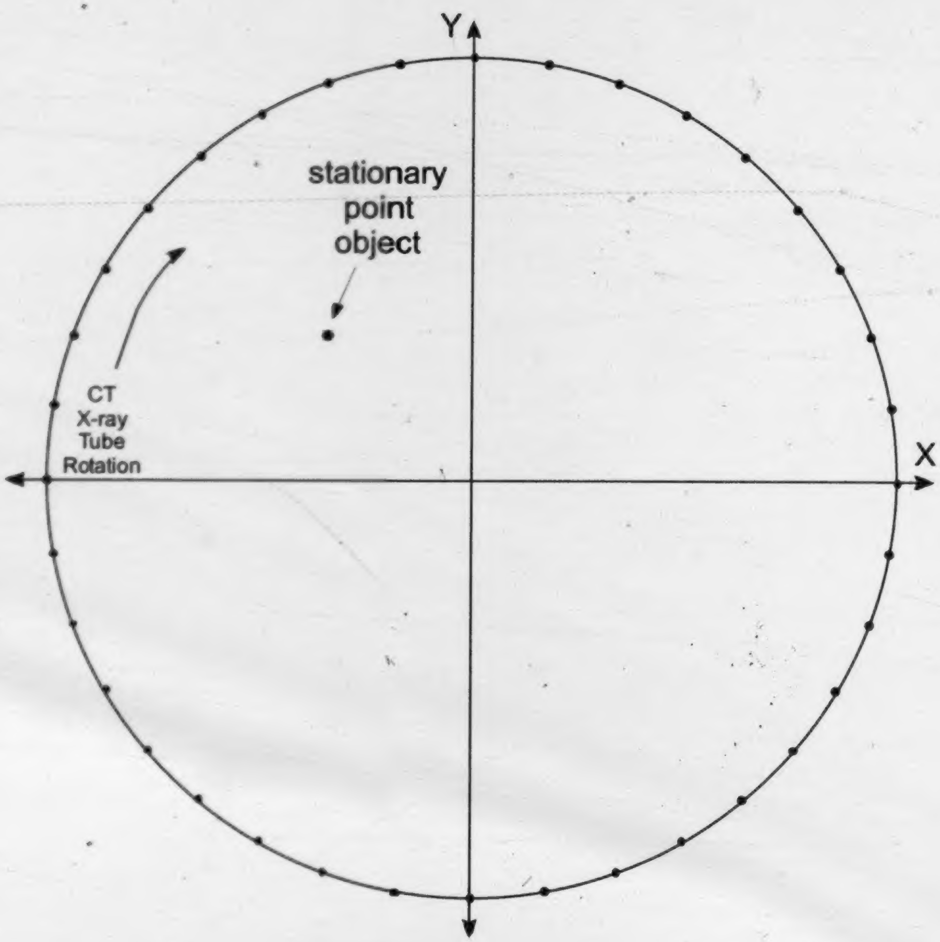
Y
X
stationary point object
CT X-ray Tube Rotation

Figure 3.6a Stationary point like object in the CT imaging plane.

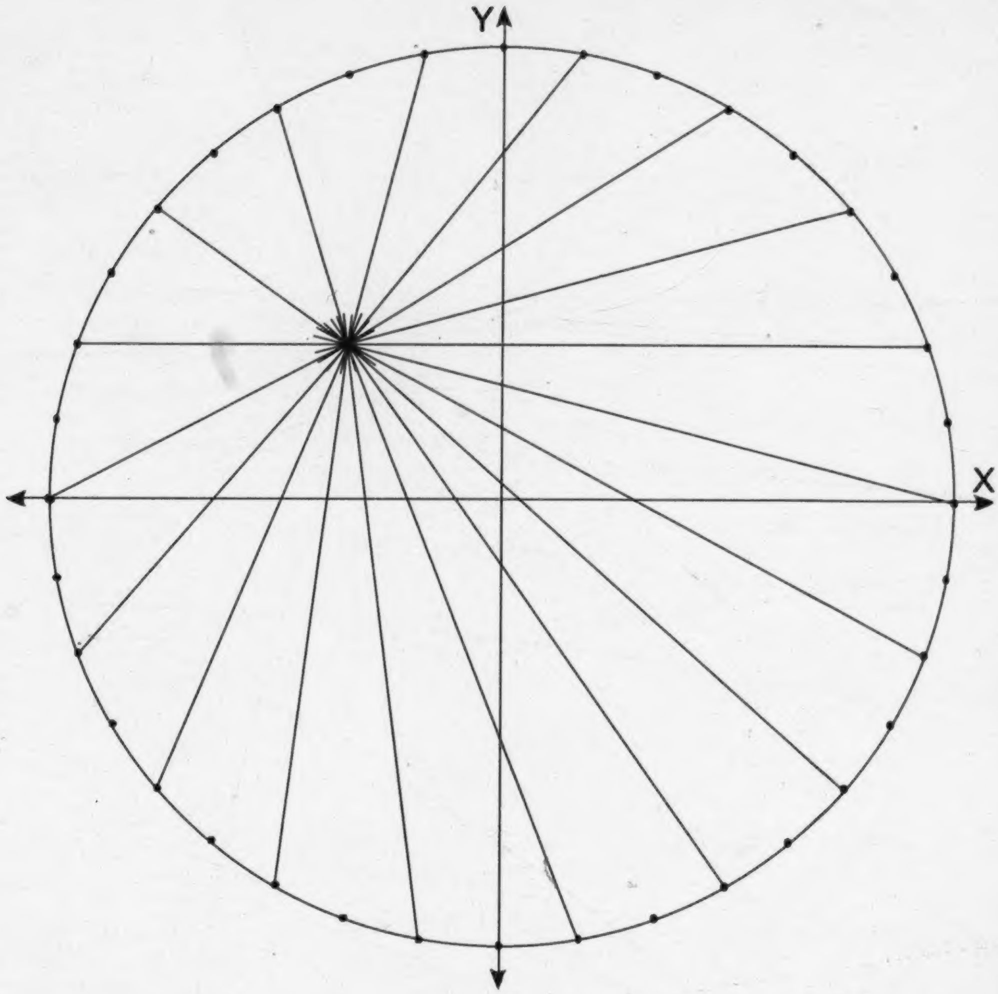

Figure 3.6b Simple backprojection to reconstruct an image of a stationary point like object.

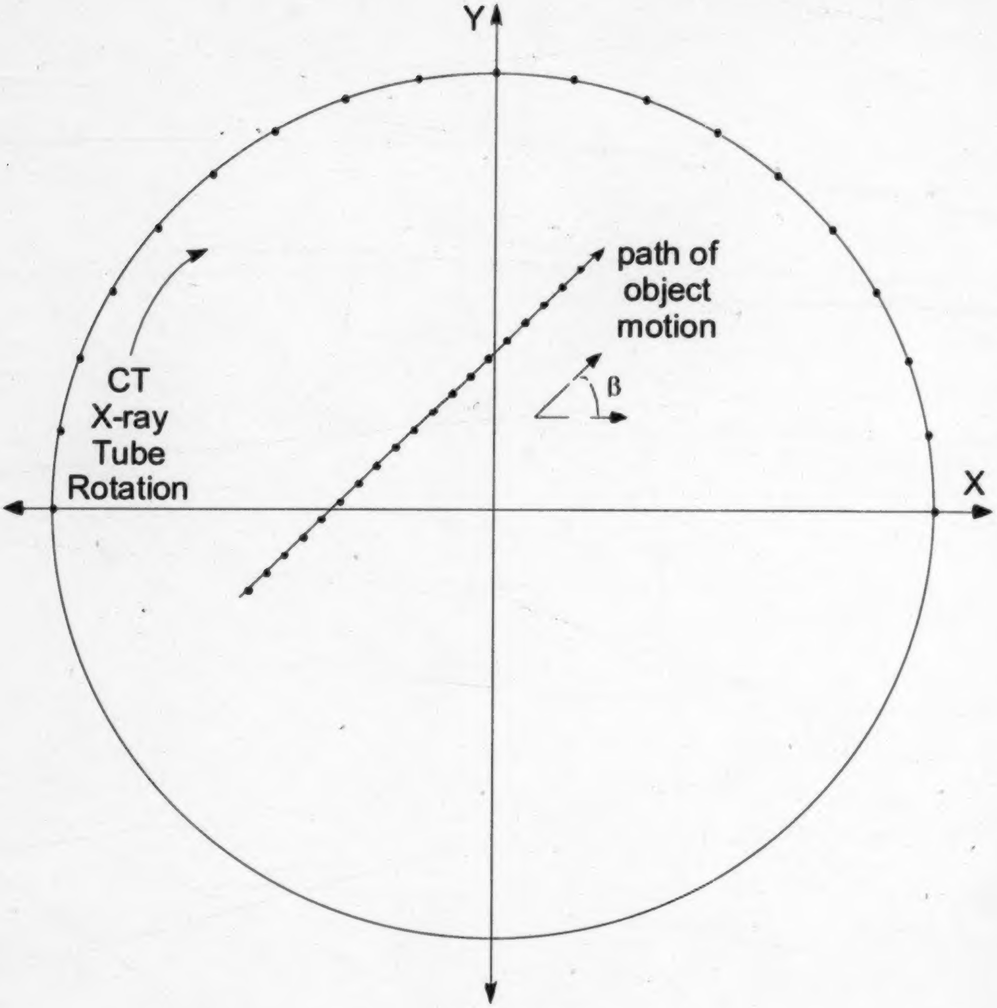
Y
X
path of
object
motion
β
CT
X-ray
Tube
Rotation

Figure 3.6c Point like object moving along a strait line in the CT imaging plane.

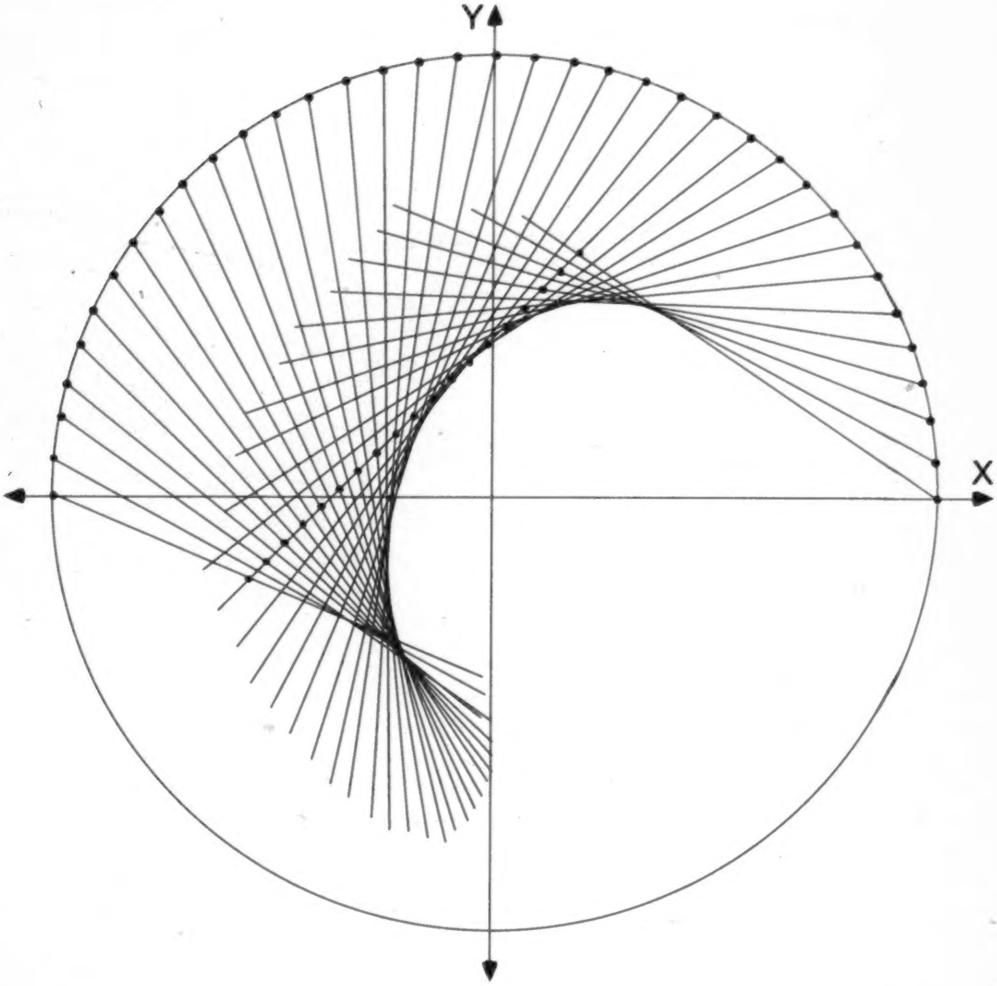

Figure 3.6d Simple back projection to reconstruct an image of a point like object moving along a straight line in the CT image plane. For clarity, only one half of full rotation reconstruction shown.

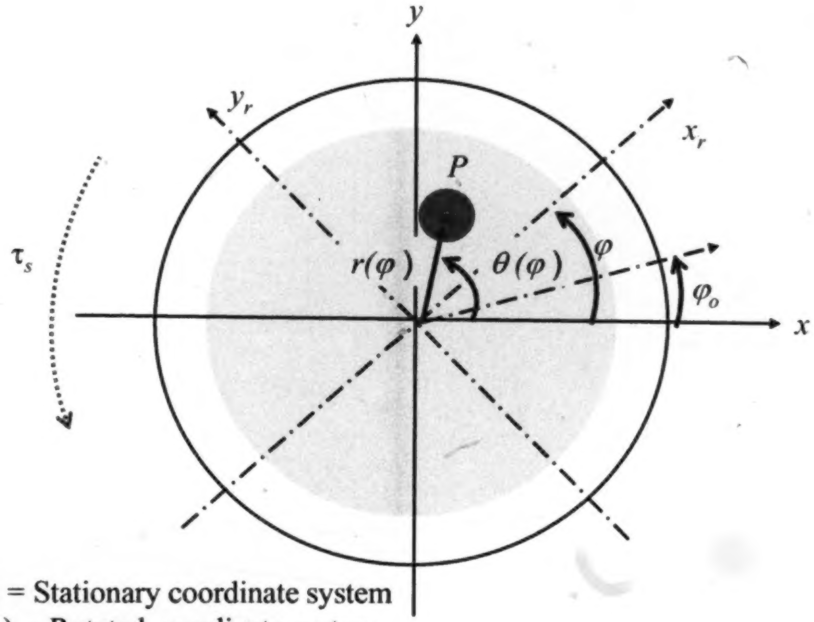
y
y_r
x_r
P
τ_s
$r(\varphi)$
$\theta(\varphi)$
φ
φ_o
x

(x,y) = Stationary coordinate system
(x_r,y_r) = Rotated coordinate system
φ = Projection angle
φ_o = Initial projection angle
$\theta(\varphi)$ = Angular position of point P at projection angle φ
$r(\varphi)$ = Radial position of point P at projection angle φ
τ_s = Rotation time

Figure 3.7 Imaging and object parameters governing motion artifacts in computed tomography.

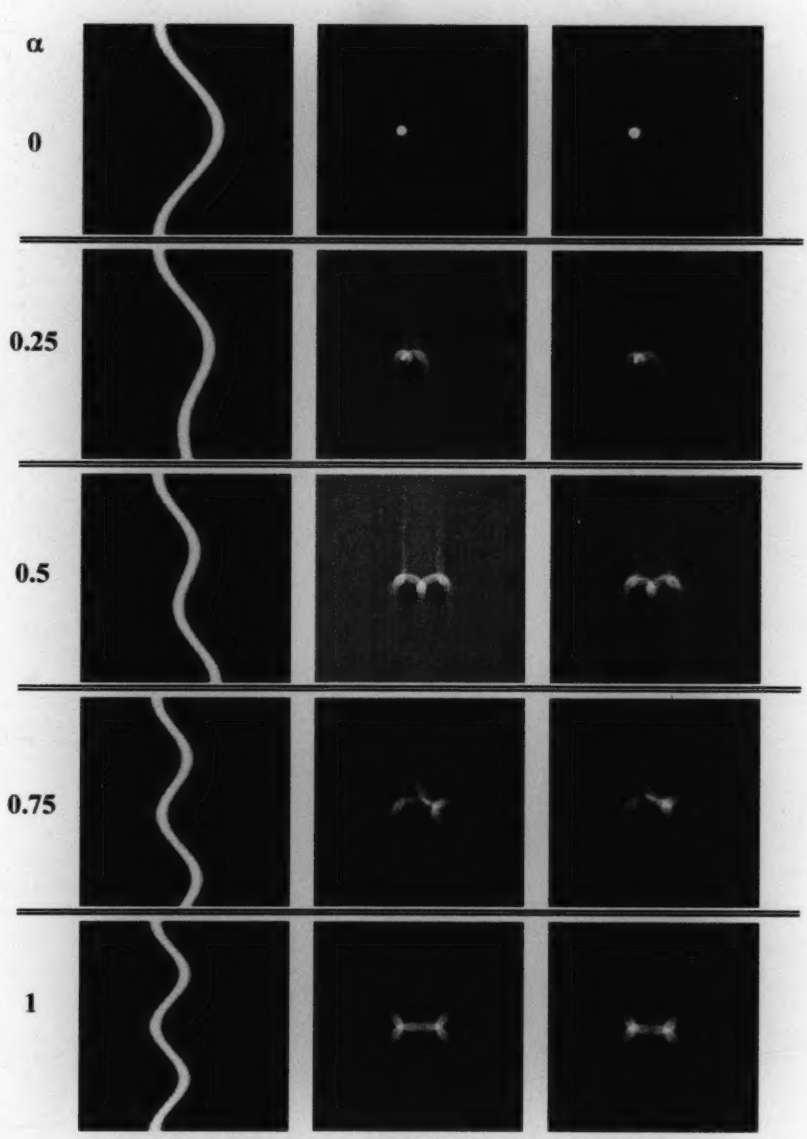

(a) (b) (c)

Figure 3.8 **(a)** Simulation sinograms, **(b)** Simulation images, and **(c)** Experimental CT images of a 6.4 mm diameter POM cylinder moving along the horizontal axis of the scanner and imaged under various alpha conditions [0, 0.25, 0.5, 0.75, 1]. Simulation parameters: ($l_{x0} = Ax/2$, $l_{y0} = 0$, $l_{z0} = 0$, $A_x = 25$ mm, $A_y = 0$, $A_z = 0$, $n = 1$, $\phi_x = 0^o$, $\varphi_o = 0^o$).

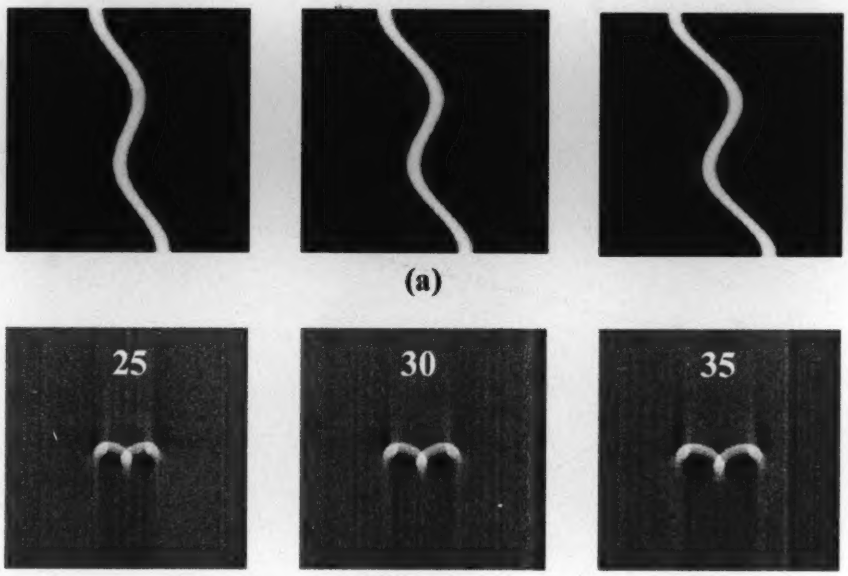

(a)

(b)

Figure 3.9 (a) Simulation sinograms, and **(b)** Simulation images of a 6.4 mm POM cylinder moving along the horizontal axis of the scanner with various amplitudes of motion [25, 30, 35 mm]. Simulation parameters: ($l_{x0} = A_x/2$, $l_{y0} = 0$, $l_{z0} = 0$, A_x = variable, $A_y = 0$, $A_z = 0$, $\alpha = 0.5$, $n = 1$, $\phi_x = 0^{\circ}$, $\varphi_o = 0^{\circ}$).

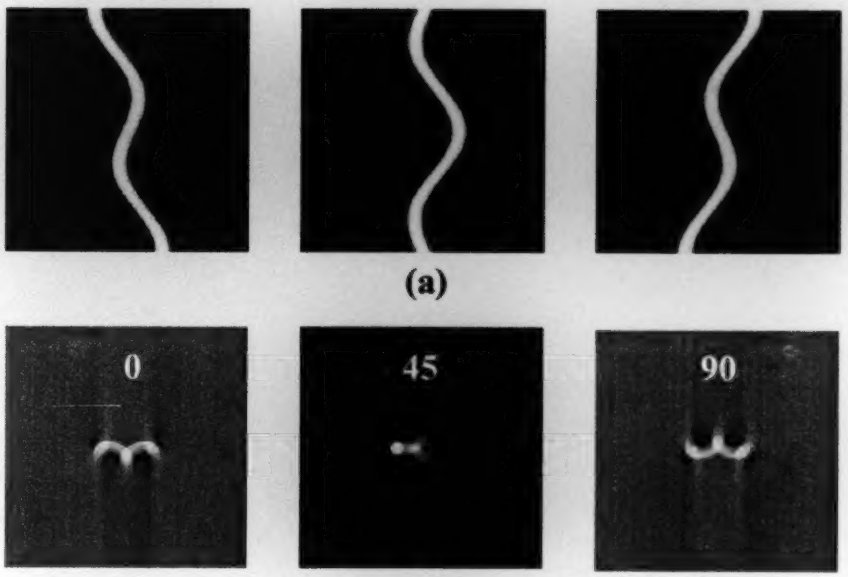

(a)

(b)

Figure 3.10 **(a)** Simulation sinograms, and **(b)** Simulation images of a 6.4 mm diameter POM cylinder moving along the horizontal axis of the scanner with various phase of motions [0°, 45°, 90°]. Simulation parameters: ($l_{x0} = A_x/2$, $l_{y0} = 0$, $l_{z0} = 0$, $A_x = 25$ mm, $A_y = 0$, $A_z = 0$, $\alpha = 0.5$, $n = 1$, ϕ_x = variable, $\varphi_o = 0^\circ$).

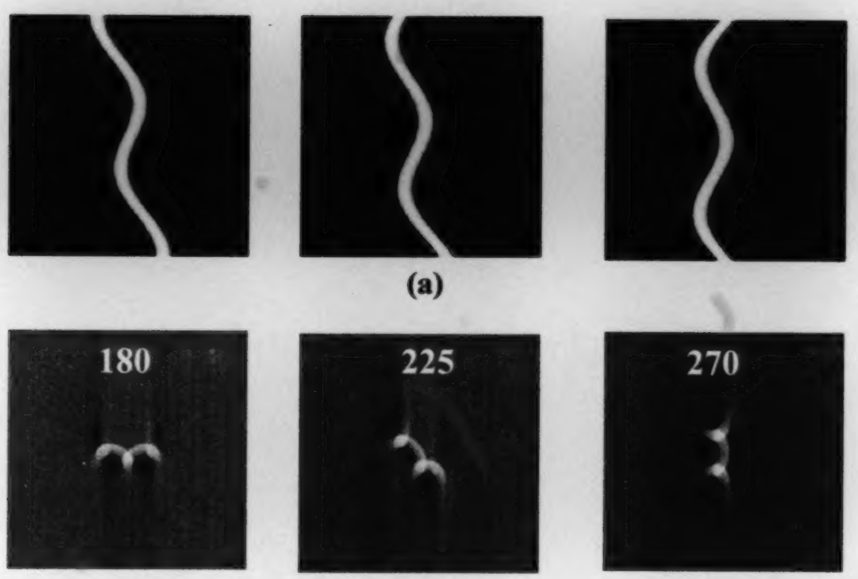

(a)

(b)

Figure 3.11 **(a)** Simulation sinograms, and **(b)** Simulation images of a 6.4 mm POM cylinder moving along various angular lines, θ (φ_o), of the scanner [180°, 225°, 270°]. Simulation parameters: ($l_{x0} = A_x/2$, $l_{y0} = A_y/2$, $l_{z0} = 0$, $A_x + A_y = 25$ mm, $A_z = 0$, $\alpha = 0.5$, $n = 1$, $\phi_x = 0^\circ$, $\phi_y = 0^\circ$, $\varphi_o = 0^\circ$).

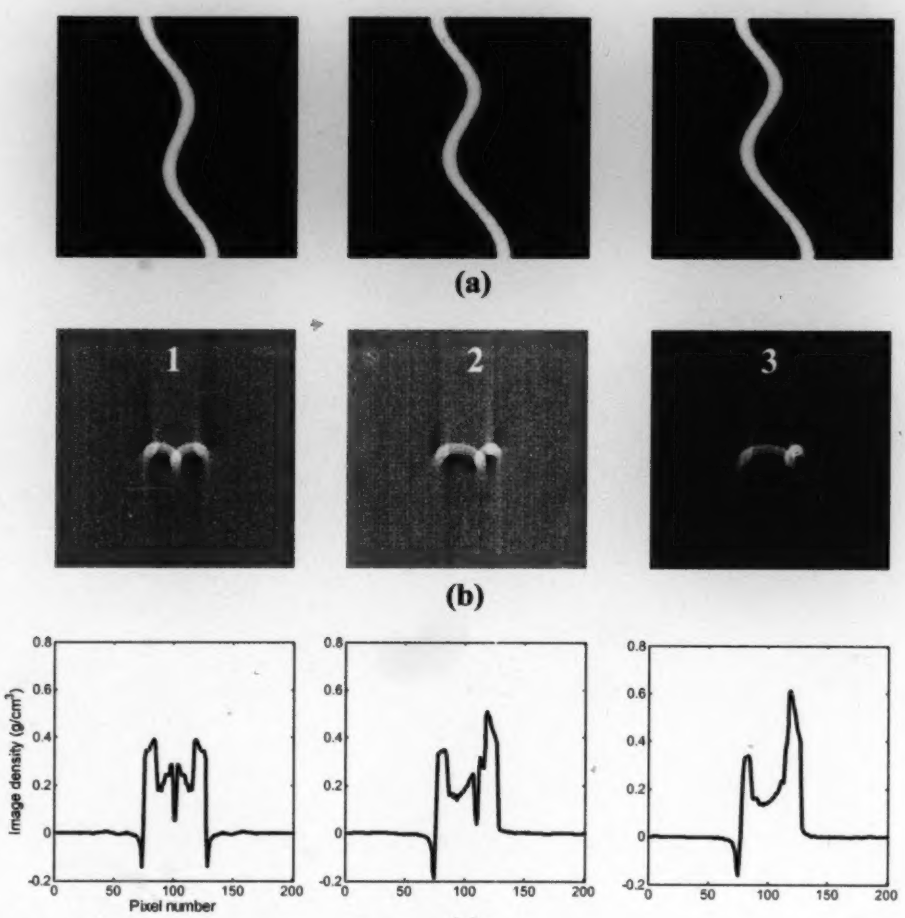

(a)

(b)

(c)

Figure 3.12 **(a)** Simulation sinograms, **(b)** Simulation images, and **(c)** Central horizontal profiles (CHPs) of a 6.4 mm diameter POM cylinder moving along the horizontal axis of the scanner with various asymmetry parameters [1, 2, 3]. Simulation parameters: ($l_{x0} = A_x/2$, $l_{y0} = 0$, $l_{z0} = 0$, $A_x = 25$ mm, $A_y = 0$, $A_z = 0$, $\alpha = 0.5$, n = variable, $\phi_x = 0^{\circ}$, $\varphi_o = 0^{\circ}$).

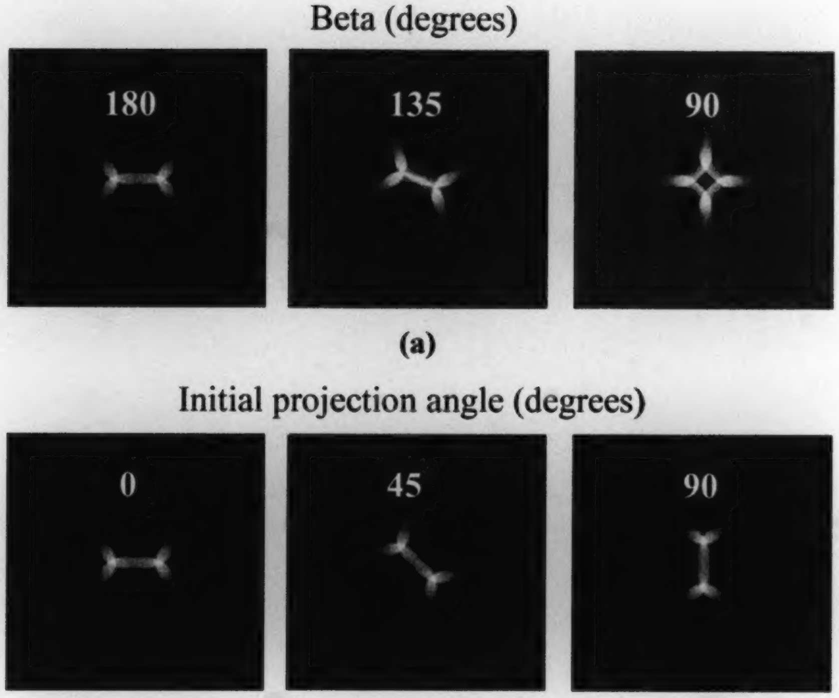
Beta (degrees)
180
135
90
Initial projection angle (degrees)
0
45
90

(a)

(b)

Figure 3.13 The angular dependence of motion artifact pattern upon beta (β), an angle which defines the angular difference between the orientation of motion in the imaging plane, $\theta(\varphi_o)$, and the initial projection angle, φ_o. **(a)** Simulation images for various beta values [180°, 135°, 90°] and a 25 mm motion along the horizontal axis of the scanner ($\theta(\varphi_o) = 0°$). **(b)** Simulation images for various initial projection angles [0°, 45°, 90°] and a constant beta value of 180°. Simulation parameters: ($l_{x0} = A_x/2$, $l_{y0} = A_y/2$, $l_{z0} = 0$, $A_x + A_y = 25$ mm, $\alpha = 0.5$, $\phi_x = 0°$, $\phi_y = 0°$, $n = 1$, φ_o = variable).

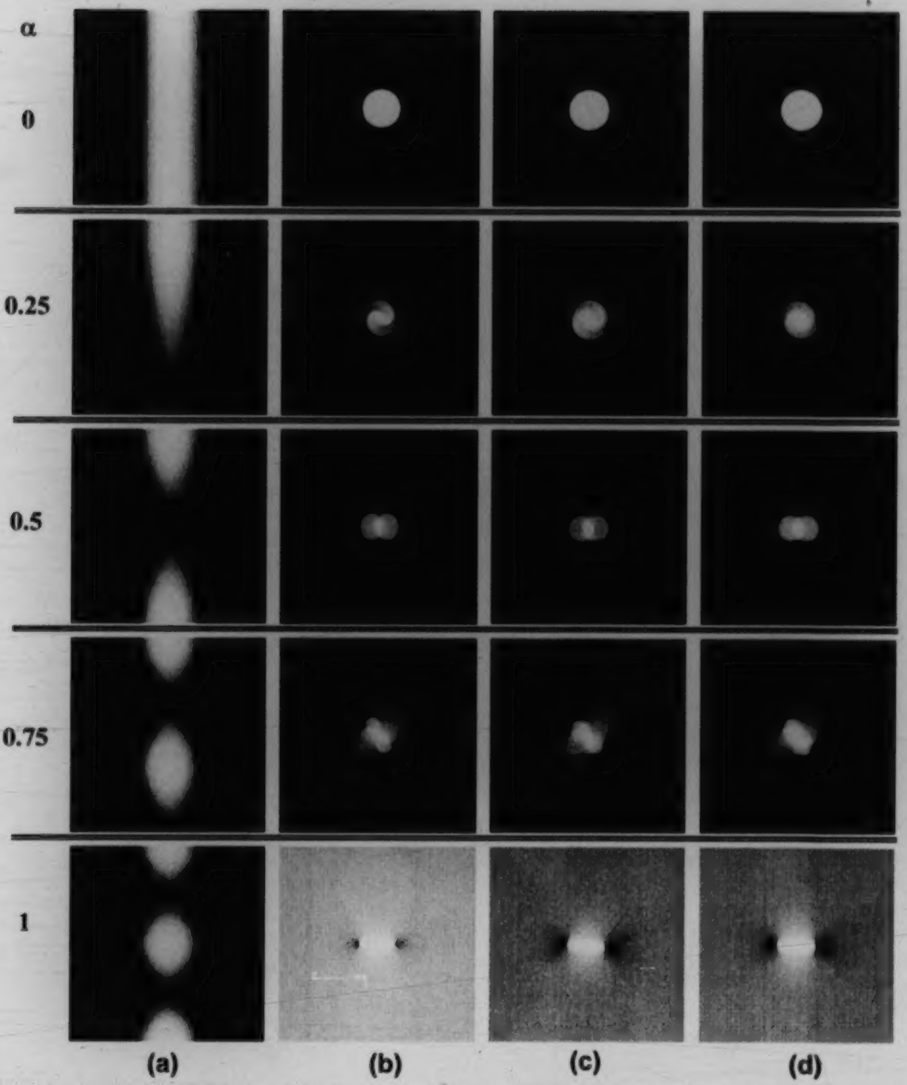

Figure 3.14 (**a**) Simulation sinograms, (**b**) Simulation images using infinitesimal slice width, (**c**) Experimental CT images, and (**d**) Simulation images using finite slice width of a 25 mm POM sphere moving along the z-axis of the scanner (orthogonal to image plane) and scanned under various alpha conditions [0, 0.25, 0.5, 0.75, 1]. Simulation parameters: ($l_{x0} = 0$, $l_{y0} = 0$, $l_{z0} = A_z/2$, $A_x = 0$, $A_y = 0$, $A_z =$ 25 mm, α = variable, $n = 1$, $\phi_z = 45^{\circ}$, $\varphi_o = 0^{\circ}$).

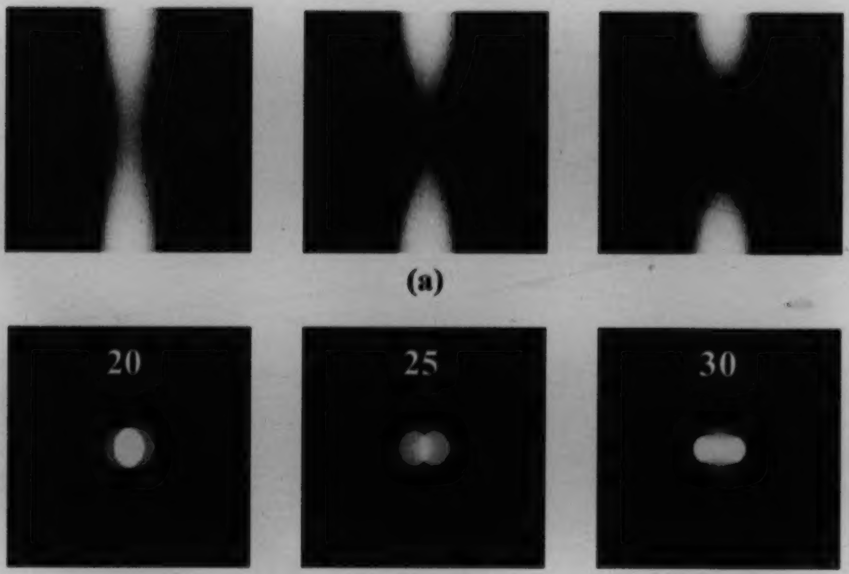

(a)

(b)

Figure 3.15 **(a)** Simulation sinograms, and **(b)** Simulation images of a 25 mm diameter POM sphere moving along the *z*-axis of the scanner with various amplitude of motions [20, 25, 30 mm]. Simulation parameters: ($l_{x0} = 0$, $l_{y0} = 0$, $l_{z0} = A_z/2$, $A_x = 0$, $A_y = 0$, $A_z =$ variable, $\alpha = 0.5$, $n = 1$, $\phi_z = 45^\circ$, $\varphi_o = 0^\circ$).

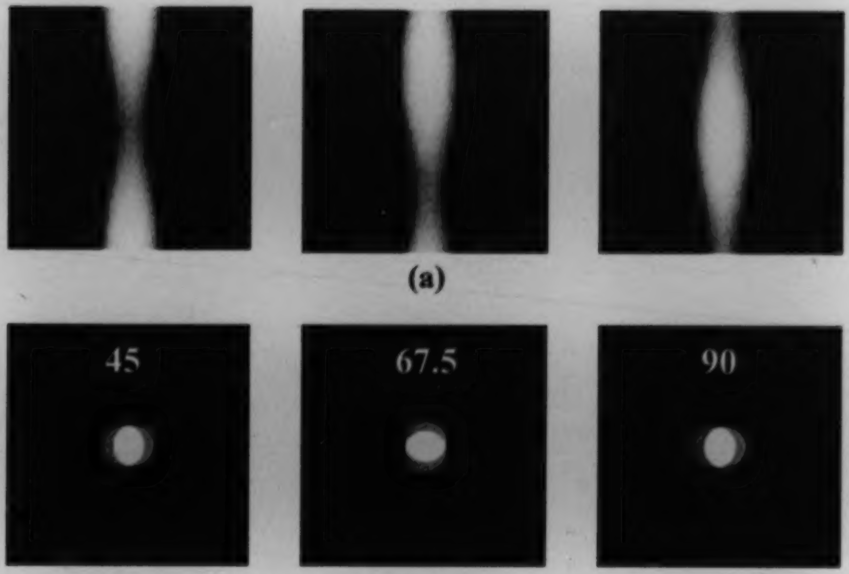

(a)

(b)

Figure 3.16 (a) Simulation sinograms, and **(b)** Simulation images of a 25 mm diameter POM sphere moving along the *z*-axis of the scanner with various phase of motions [45°, 67.5°, 90°]. Simulation parameters: ($l_{x0} = 0$, $l_{y0} = 0$, $l_{z0} = A_z/2$, $A_x = 0$, $A_y = 0$, $A_z = 20$ mm, $\alpha = 0.5$, $n = 1$, ϕ_z = variable, $\varphi_o = 0^{\circ}$).

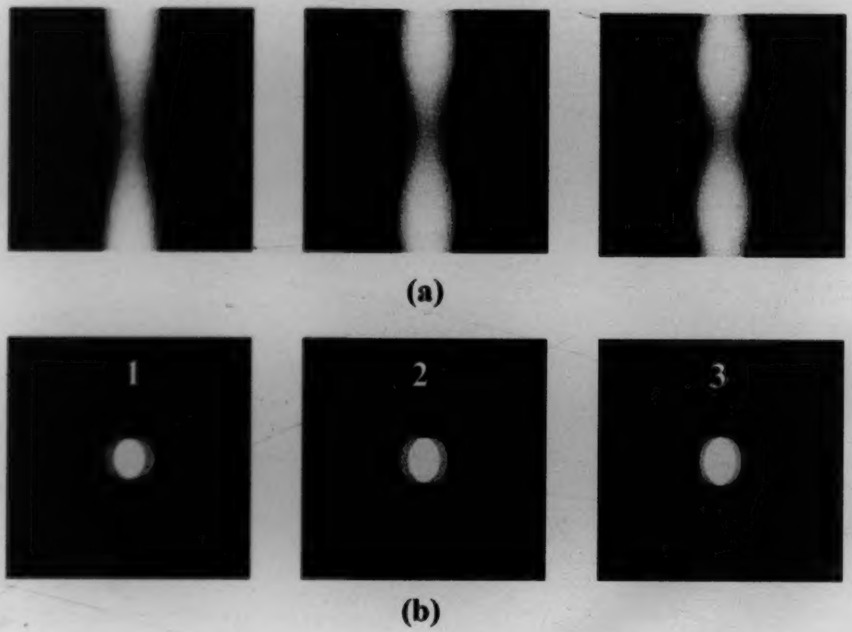

Figure 3.17 **(a)** Simulation sinograms, and **(b)** Simulation images of a 25 mm diameter POM sphere moving along the *z*-axis of the scanner with various asymmetry parameters [1, 2, 3]. Simulation parameters: ($l_{x0} = 0$, $l_{y0} = 0$, $l_{z0} = A_z/2$, $A_x = 0$, $A_y = 0$, $A_z = 20$ mm, $\alpha = 0.5$, n = variable, $\phi_z = 0^\circ$, $\varphi_o = 0^\circ$).

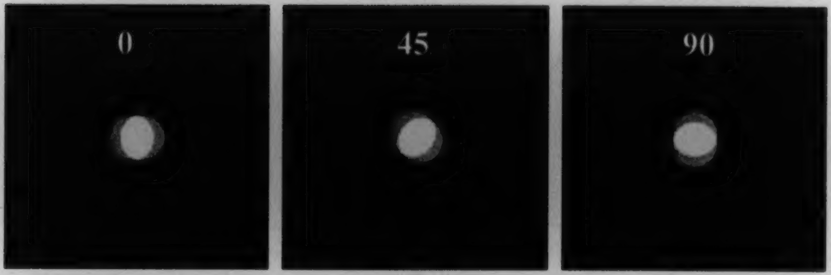

Figure 3.18 The impact upon the motion artifact pattern of initiating the imaging sequence at various angular positions [0°, 45°, 90°]. Simulation parameters: ($l_{x0} = 0$, $l_{y0} = 0$, $l_{z0} = A_z/2$, $A_x = 0$, $A_y = 0$, $A_z = 20$ mm, $\alpha = 0.5$, $n = 1$, $\phi_z = 45^{\circ}$, φ_o = variable).

3.6 References

[Ba 2001] E.A. Barnes, B.R. Murray, D.M. Robinson *et al.*, "Dosimetric evaluation of lung tumor immobilization using breath hold at deep inspiration," Int. J. Radiat. Oncol. Biol. Phys. **50**, 1091 – 1098 (2001)

[Ch 2001] Q.S. Chen, M.S. Weinhous, F.C. Deibel *et al.*, "Fluoroscopic study of tumor motion due to breathing: Facilitating precise radiation therapy for lung cancer patients," Med. Phys. **28**, 1850 –1856 (2001)

[Ek 1998] L. Ekberg, O. Holmberg, L. Wittgren, *et al.*, "What margins should be added to the clinical target volume in radiotherapy treatment for lung cancer?," Radiother. Oncol. **48**, 71 –77 (1998)

[Gi 2001] P. Giraud, Y. de Rycke, B. Dubray *et al.*, "Conformal radiotherapy (CRT) planning for lung cancer: Analysis of intrathoracic organ motion during extreme phases of breathing," Int. J. Radiat. Oncol. Biol. Phys. **51**, 1081 – 1092 (2001)

[La 2001] F.J. Lagerwaard, J.R. Van Sornsen de Koste, M.R.J. Nussen-Visser *et al.*, "Multiple "slow" CT scans for incorporating lung tumor mobility in radiotherapy planning," Int. J. Radiat. Oncol. Biol. Phys. **51**, 932 – 937 (2001)

[Lu 1999] A.E. Lujan, E.W. Larsen, J.M. Balter, *et al.*, "A method for incorporating organ motion due to breathing and heartbeat, measured during radiotherapy," Med. Phys. **26**, 715 – 720 (1999)

[Ro 1990] C.S. Ross, D.H. Hussey, E.C. Pennington, *et al.*, "Analysis of movement of intrathoracic neoplasms using ultrafast computerized tomography," Int. J. Radiat. Oncol. Biol. Phys. **18**, 671 – 677 (1990)

[Se 2002] Y. Seppenwoolde, H. Shirato, K. Kitamura, *et al.*, "Precise and real-time measurements of 3D tumor motion in lung due to breathing and heartbeat, measured during radiotherapy," Int. J. Radiat. Oncol. Biol. Phys. **53**, 822 – 834 (2002)

[Sh 2001] S. Shimizu, H. Shirato, S. Ogura, J. Akita-Dosaka, *et al.*, "Detection of lung tumor movement in real-time tumor-tracking radiotherapy," Int. J. Radiat. Oncol. Biol. Phys. **51**, 304 – 310 (2001)

[Sh 2000] S. Shimizu, H. Shirato, K. Kagei, T. Nishioka, *et al.*, "Impact of respiratory movement on the computed tomographic images of small lung tumor in three-dimensional (3D) radiotherapy," Int. J. Radiat. Oncol. Biol. Phys. **46**, 1127 – 1133 (2000)

[Oz 2002] C. Ozhasoglu and M.J. Murphy, "Issues in respiratory motion compensation during external-beam radiotherapy," Int. J. Radiat. Oncol. Biol. Phys. **52**, 1389 – 1399 (2002)

Chapter 4: The impact of lung tumor motion upon CT image integrity and target delineation

4.1 Introduction

In Chapter 2 the principles behind the generation of motion-induced CT image artifacts were presented. The presence of motion was clearly seen to cause the reconstructed image to deviate from that which might be intuitively expected from the dynamics involved. The properties of the artifacts associated with motion characteristic of respiration were explored in Chapter 3. In this chapter, the impact of motion upon image integrity in terms of the ability of CT reconstruction to accurately reproduce the physical density distributions which result under dynamic conditions is investigated. The implications of motion for target delineation are also examined. Target volume delineation is a crucial step in conformal radiotherapy. Any uncertainties introduced at this early stage of planning will lead to improper selection of beam portals and thus result in one of two undesirable consequences, both of which jeopardize the curative outcome of the treatment. The first, and most serious of these two, is an under dosage of the tumor as a consequence of geometric failure. The second is the irradiation of an unnecessary volume of healthy tissue bringing about excessive normal tissue complication probabilities.

4.2 Methods and Materials

As previously demonstrated in Chapter 3, experimental CT images incorporate a superposition of the individual effects arising solely from motion and also those which result from finite slice width. While it is not readily possible to separate these two contributions experimentally, this feat may be easily accomplished with computer simulation. Thus, the computer reconstruction model developed and presented in Chapter 2 is used extensively in this chapter to explore the effects of respiration-induced tumor motion upon CT image integrity and target delineation.

This investigation into the effects of motion upon image integrity and target delineation is conducted with geometries representative of the intermediate densities associated with real lung tumors. Spheres with diameters of 10, 30 and 50 mm (all with a uniform density of 0.90 g/cm^3) representing small, medium and large size lung tumors are simulated to move in a homogeneous lung tissue background (density = 0.25 g/cm^3) during image acquisition according to the respiration-induced lung tumor motion model described in the previous chapter. For the purpose of investigation, only one specific motion is imparted to the spheres, namely a simple harmonic motion (SHM) with medio-lateral (LR) and superior-inferior (SI) components:

$$l_x(\varphi) = l_{x0} - A_x \cdot \cos^{2n}\left(\frac{\alpha}{2}(\varphi - \varphi_0) - \phi_x\right) \tag{4.1}$$

$$l_z(\varphi) = l_{z0} - A_z \cdot \cos^{2n}\left(\frac{\alpha}{2}(\varphi - \varphi_0) - \phi_z\right) \tag{4.2}$$

where $l_{x0} = \frac{A_x}{2}$, $l_{z0} = \frac{A_z}{2}$, $n = 1$, $\varphi_0 = 0^\circ$ and $\phi_x = \phi_z = 45^\circ$. Three clinically relevant motion amplitudes are investigated, a small upper lobe motion ($A_x = A_z = 5$ mm), an intermediate motion ($A_x = A_z = 15$ mm) and a large lower lobe motion ($A_x = A_z = 25$ mm). As mentioned in earlier chapters, many scanning techniques are currently available for lung radiotherapy planning. These techniques result in a wide range of alpha values. For the purpose of investigation, alpha values of 0, 0.25 and 1 are contemplated. These alpha values are representative of breath-hold, fast (1 second image acquisition with 4 second period of motion) and 'slow' (4 second image acquisition with 4 second period of motion) CT scans, respectively. To clearly elucidate the effects associated purely with motion without the obscuring contributions due to the presence of finite slice width, all simulated CT image reconstructions are carried out using an infinitesimal slice thickness.

4.2.1 Impact of motion upon image integrity and target delineation

4.2.1.1 Image integrity

In CT, a determination of image quality usually involves an evaluation of a number of quantities (including spatial resolution, contrast resolution, noise, distortions and artifacts) which have been identified and expounded upon by numerous authors [Bl 1981, Mo 1983, Ha 1991, Ke 1991, Sp 1994, Ka 2000, Lu 2003]. Clearly, quantities such as high and low contrast resolution will be degraded within the TXO in direct relation to the magnitude of motion. The inconsistencies introduced by the presence of motion into the projection data set will clearly affect the entire reconstructed image as well. For example, in Chapters 2 and 3 of this thesis, it was shown that motion during CT image acquisition projects the reconstructed object in directions displaced from its velocity vector. This particular feature of motion-induced CT artifacts results in errors in the reconstructed image over regions which extend not only within but also beyond the physical area traced out by the mobile object during the course of image acquisition. Thus, both the image of the mobile object and its surrounding background are altered in the CT reconstruction process. The breakdown in overall image integrity which results has significant implications for target identification and delineation.

The presence of motion in combination with finite image acquisition time dictates an assessment of image integrity based upon time-averaged quantities which physically result due to the dynamics involved. A full investigation of the effects of motion on image quantities such as high and low contrast resolution, and image noise is beyond the scope of this thesis. The evaluation of image integrity presented here will be based on the ability of CT image reconstruction to faithfully reproduce the time-averaged density distributions which physically result due the presence of motion. This investigation will be carried out using simulated reconstruction images for which the presence of noise is not a factor. The standard measurement of quantities, such as low contrast resolution and CT number uniformity, are conducted under static conditions and thus do not strictly apply to the dynamic case. Never the less, the general expectations of that which such tests should yield under static conditions serve to provide reasonable benchmarks for an evaluation of the detrimental effects of motion on image integrity. Cross-field uniformity, for example, as measured with a static homogeneous water phantom is expected to yield a maximum deviation in mean CT number of no larger than ± 4 HU [Ka 2000]. A deviation of 4 HU translates into a density difference of 0.4 %. A standard deviation in CT number for water of between 3 to 10 (0.3 % to 1.0 % density variations) is typically expected for measurements derived from a homogeneous 20 cm phantom reconstructed using a standard convolution kernel [Ka 2000]. The expected CT number for air is – 1000 ± 5 HU which corresponds to a 0.5 % variance in density. Contrast resolution can be expressed in terms of the ability to resolve small objects (of the order of 2 to 3 mm in diameter) that vary slightly in density from their surrounding background. A modern well calibrated CT scanner is expected to resolve density differences in the order of 0.25 % to 0.5 %. The contrast resolution of the PQ 5000 CT scanner used experimentally in this thesis work is quoted by the manufacturer as being able to resolve tissue differences as small as 2 mm at 0.3 % contrast [Picker PQ 5000 CT specifications sheet]. From such quantitative evaluations obtained under static conditions it would seem reasonable to expect that a good reconstruction should reproduce the physical densities resultant under dynamic conditions to within at least 1 % of their true values, and in what follows this will serve as a benchmark against which to gauge the fidelity of CT reconstruction when motion is involved.

Physically, a uniform density distribution equal to that of the background is to be expected external to the TXO, the total cross-section occupied by the mobile object during image acquisition, due to the absence of motion in this region. Within the TXO, the combination of finite image acquisition time and target motion results in the generation of time-averaged density distributions. Consider motion which produces, at a given (x, y) location, densities of ρ_1 and ρ_2 in 60 % and 40 % of the total number of projection acquisitions respectively. The physical time-averaged density $\overline{\rho_{phys}}(x,y)$ over the entire image acquisition at this location will be

$$\bar{\rho}_{phys}(x,y) = 0.6\rho_1 + 0.4\rho_2 . \tag{4.3}$$

Extension to the general case in which density may assume a different value for each projection angle yields the physical time-averaged density distribution, $\bar{\rho}_{phys}(x,y)$, at location (x, y) in the image plane according to

$$\bar{\rho}_{phys}(x,y) = \frac{1}{n}\sum_{i=1}^{n}\rho_i(x,y) \tag{4.4}$$

where $\rho_i(x,y)$ is the density at point (x, y) at the time of the projection acquisition at the i^{th} projection angle and n is the total number of projections. Subtraction of CT reconstructed densities $\rho_{recon}(x,y)$ from time-averaged densities $\bar{\rho}_{phys}(x,y)$ results in the generation of a density difference distribution which may also be referred to as a density difference image or map. Density difference images reveal both the magnitude and location of discrepancies between physically expected and CT reconstructed densities. The ability of image reconstruction to faithfully reproduce the physical time-averaged density distribution associated with the motion captured will serve as a measure of image integrity. Histograms and image statistics such as the mean, minimum and maximum densities within the TXO and within a 10 mm margin surrounding the TXO will be employed to evaluate the breakdown of image integrity associated with CT scanning of mobile objects. Density difference maps are calculated as percentage differences according to

$$\mathrm{diff}(x,y) = \frac{\bar{\rho}_{recon}(x,y) - \bar{\rho}_{phys}(x,y)}{\bar{\rho}_{phys}(x,y)} \times 100\,\% . \tag{4.5}$$

4.2.1.2 Target delineation

The process of defining an object (or objects) of interest within an image is generally referred to as segmentation or delineation. While numerous image segmentation techniques for lung radiotherapy planning abound [Go 1985, Ch 1992, Pe 1992, Tr 1994, Ch 1998], it is not the purpose of this thesis to explore their various virtues and short comings. This investigation into the effects of motion upon image integrity and the consequences for object delineation is conducted using a simple gray-level threshold image segmentation technique, in which any portion of the image with intensities greater than or equal to a predefined value, I, is deemed to be associated with the object and those of lesser value define the background. Individual target contours (I_{xx}) are defined according to static contrast threshold levels, *xx*

$$I_{xx} = \frac{\left\lfloor \overline{I_o^s} - \overline{I_b^s} \right\rfloor}{100} xx + \overline{I_b^s} \tag{4.6}$$

where $\overline{I_o^s}$ is the mean object intensity/density measured under static conditions at the widest target cross-section and $\overline{I_b^s}$ is the mean background intensity/density. A contrast threshold level of 100 % corresponds to the static lung tumor density (0.90 g/cm^3) while a contrast level of 0 % corresponds to the surrounding lung medium density (0.25 g/cm^3).

It is well known that CT scanning of mobile objects results in distorted volumes [Ba 1996, Ba 1998, Ch 2004, Ke 2004]. What has not yet appeared in the literature is a quantitative assessment of the effect of motion on target contour delineation. In this section, the ability of iso-intensity target contours to properly represent the total cross-section occupied by a mobile target, TXO, during image acquisition is assessed. Two quantities are used to evaluate the impact of respiration-induced tumor motion on target delineation. The first of these is the TXO coverage which is the ratio (expressed in percent) of the common overlapping area to that of the TXO. The common overlapping area is defined as the intersection between the area delineated by the iso-intensity contour and that of the TXO. The second evaluation quantity is the unnecessary coverage, defined as the area delineated by the iso-intensity contour which extends beyond the bounds of the TXO and is also expressed as a percentage of the TXO.

4.2.2 Benchmarking of computer model in high and low contrast levels

Implicit in the ability of computer modeling to reproduce both static and dynamic experimental results, as established in Chapters 2 and 3, is its ability to faithfully generate image contours. Nevertheless, this capability is explicitly demonstrated in this chapter.

Experimental and simulation CT data (images) previously collected, many of which were presented in Chapters 2 and 3 are used to benchmark the computer model. For the sake of brevity, only two static and two dynamic scenarios are contemplated:

1. A static 25 mm diameter POM sphere scanned in air and in water at $z = 0$ mm, where partial volume effects are minimal.

2. A static 25 mm diameter POM sphere scanned in air and in water at $z = 9$ mm, where partial volume effects are more substantive.

3. A 30 mm diameter POM cylinder scanned in air and in water at $z = 0$ mm, while undergoing SHM along the horizontal axis of the scanner.

4. A 25 mm diameter POM sphere scanned in air and in water at $z = 0$ mm, while undergoing SHM along the z-axis of the scanner.

The ability of computer modeling to reproduce experimental segmentation results in both high (air) and low (water) contrast levels is confirmed by comparing cross-sectional areas and evaluating the deviation (distance) between simulation and experiment target contour centroids. Nine equidistant target contours [I_{10}, I_{20}, I_{30}, I_{40}, I_{50}, I_{60}, I_{70}, I_{80}, I_{90}] are used for the analysis.

4.3 Results and Discussion

4.3.1 *Benchmarking of computer simulation*

4.3.1.1 Stationary test objects

Figures 4.1 and 4.2 show a partial set of experimental and simulation target segmentation contours (I_{10}, I_{50}, I_{90}) which result for the 25 mm diameter static POM sphere at slice locations $z = 0$ mm and $z = 9$ mm. Upon visual inspection, good agreement is seen to exist between computer modeling and experimental segmentation results at both slice locations. Deviations less than ± 1 mm between experiment and modeling contours are measured. In general, target contours obtained for the experimental scans conducted in water (low contrast level) are noisier than their in air (high contrast level) counterparts due to the lower number of quanta available for image reconstruction. Target contours obtained for the simulation scans are all smooth and circular as computer modeling is devoid of experimental noise.

Tables 4.1 ($z = 0$ mm) and 4.2 ($z = 9$ mm) list the experimental and simulation target contour areas corresponding to all nine contrast threshold levels investigated [10, 20, 30, 40, 50, 60, 70, 80, 90 %]. Also included in these tables are the deviations between the experiment and simulation target contour centroids. In general, only small discrepancies between simulation and experimental contour areas are observed, confirming the ability of the computer model to reproduce experimental results under static conditions with reasonable accuracy. At $z = 0$ mm, where partial volume effects are minimal, the mean percentage discrepancy between the simulation and experiment cross-sectional areas is 1.3 ± 0.5 % for the high contrast (air) scans and 1.3 ± 0.2 % for the low contrast (water) scans. At z = 9 mm, where partial volume effects are more pronounced, the mean percentage discrepancy between simulation and experimental cross-sectional areas is 2.7 ± 1.1 % for the in-air scans and 3.1 ± 2.1 % for the in-water scans. For each slice location, the ratios of cross-sectional areas A, between low (I_{10}) and high (I_{90}) iso-intensity target contours [A_{10}/A_{90}] are comparable. Finally, the deviations between simulation and experimental target contour centroid positions are, in all instances, less than 0.5 mm.

No significant differences are observed in the segmentation results between the high (air) and low (water) contrast experimental results. The mean of the absolute difference between the static experimental target contour areas obtained in air and in water is 1.9 ± 3.0 mm^2 at z = 0 mm and 1.7 ± 1.6 mm^2 at z = 9 mm, respectively. These correspond to differences of 0.4 % and 0.9 % respectively. Moreover, the mean deviation between centroid positions derived from high and low experimental contrast situations is 0.63 ± 0.01 mm (0.6 %) at z = 0 mm and 0.64 ± 0.05 mm (0.6 %) at z = 9 mm.

4.3.1.2 Dynamic test objects

Figure 4.3 depicts a partial set of experimental and simulation target segmentation contours (I_{10}, I_{50}, I_{90}) which result for the 30 mm diameter POM cylinder undergoing in-plane SHM (A_x = 15 mm, α = 0.5, $\varphi_o = 0^\circ$, $\phi_x = 0^\circ$) along the horizontal axis of the scanner. Figure 4.4 illustrates target segmentation results at the same contrast threshold levels (10, 50, 90 %) for the 25 mm diameter static POM sphere undergoing orthogonal SHM (A_z = 15 mm, α = 0.5, $\varphi_o = 0^\circ$, $\phi_z = 0^\circ$) along the z-axis of the scanner. Upon visual inspection, no significant differences (apart from noise) are discerned between the computer simulation and experimental target contours. The maximum deviations recorded between these experimental and simulation contours are less than ± 1mm.

Table 4.3 and 4.4 summarize the target contour areas [experimental and simulation] and centroid deviations corresponding to at all nine contrast threshold levels for the above dynamic scans conducted in air and water mediums. Slightly larger disagreements are observed for the dynamic case (overall mean percentage discrepancy = 3.1 ± 2.1 %) between simulation and experimental target contour areas as compared to the static situation (overall mean percentage discrepancy = 2.7 ± 1.1 %). Furthermore, larger deviations between computer simulation and experimental target contour centroid positions are also recorded in the dynamic case as (overall mean deviation = 0.81 ± 0.46 mm) compared to the static situation (overall mean deviation = 0.33 ± 0.08 mm). These larger discrepancies are reasonable given the highly contorted shapes of these contours.

Once again, no significant differences are observed between the high (in-air) and low (in-water) contrast experimental segmentation results. The mean absolute difference between the dynamic experimental target contour areas obtained in air and in water is 6.6 ± 4.4 mm^2 (mobile cylinder) and 5.7 ± 4.1 mm^2 (mobile sphere), respectively. These correspond to differences of 1.1 % and 1.5 % respectively. Moreover, the mean deviation between centroid positions derived from high and low experimental contrast situations is 2.00 ± 0.59 mm (2.0 %) for the mobile cylinder and 0.78 ± 0.14 mm (0.8 %) for the mobile sphere.

On the whole, only small discrepancies are observed between the simulation and experimental static and dynamic target contours, confirming the ability of the computer model to accurately reproduce experimental results. Interestingly, no significant differences were observed between the segmentation results obtained in high (air) and low (water) contrast situations, entailing that the above threshold segmentation technique should yield comparably accurate results in simulated intermediate density situations which more closely related to lung tumors.

4.3.2 Impact of tumor motion upon image integrity and target delineation

In the previous section, the ability of computer modeling to correctly reproduce experimental results was demonstrated. In this section, the impact of respiration-induced tumor motion upon CT image integrity and target delineation is assessed using the computer model presented in Chapter 2 with densities more representative of lung tumors (lung density = 0.25 g/cm^3, tumor density = 0.90 g/cm^3). To single out the effects associated purely with motion, all image reconstructions are carried out using an infinitesimal slice thickness.

Throughout this section, time-averaged and density difference distributions (CT – time-averaged) are used to assess the breakdown of CT image integrity that results when mobile targets are imaged. To determine the effects of motion on target delineation, quantities such as the TXO coverage and excess TXO coverage are evaluated. Two alpha values are examined and compared, ($\alpha = 0.25$) corresponding to a typical rapid CT scan and ($\alpha = 1$) representing a 'slow' CT scan. Sphere diameters and motion amplitudes typical of those which may be clinically observed in lung cancer radiotherapy are chosen for this analysis. A static or breath-hold ($\alpha = 0$) scanning scenario is also presented to expose the limitations of CT in ideal (non-dynamic) imaging conditions.

4.3.2.1 Static case

As stated in Chapter 2, an infinite number of continuous projections are necessary for perfectly accurate reconstruction of the density distribution of a static object. However, because a finite number of discrete projections are used in practical CT to reconstruct the object density distribution, exact object representation is not feasible. The limitations of CT to yield accurate densities in ideal conditions ($\alpha = 0$) are assessed for three clinically relevant lung tumor sizes (diameters = 50, 30, 10 mm) by comparing the reconstructed CT densities to the true physical object density distributions. For comparison purposes, all object density distributions were defined using the CT simulation image matrix [512 × 512]. Figure 4.5 illustrates the object, CT reconstructed and percent density difference (CT reconstructed – true physical) images of the static spheres at $z = 0$ mm. For maximum visualization, all images are scaled according to the minimum and maximum pixel intensities within the cropped 201 × 201 image matrix. Moreover, all images pertaining to the 10 mm diameter sphere are magnified by a factor of two. Significant deviations between the true object and CT reconstructed densities are observed in the percent density difference image. These deviations are, however, mostly concentrated in the vicinity of the TXO boundary, which, in this specific imaging condition ($\alpha = 0$), corresponds to the edge of the spherical cross-section imaged.

Figure 4.6 depicts a section of the central horizontal density profiles (CHPs) through the object and CT reconstructed images. Also displayed are the density difference (CT reconstructed – true object) frequency distributions within a 2 mm ring centered on the TXO contour. Unlike the true physical object density profiles, the CT reconstructed profiles exhibit a penumbral region. The width of the penumbra and the magnitude of discrepancies between object and CT reconstructed densities are found to increase with decreasing object diameter. The presence of a penumbra in CT reconstruction of static objects affects the integrity of the image both within and outside the TXO. Statistics for 1, 3, 5 and 10 % levels of agreement within the TXO and within a 10 mm region surrounding the TXO for the small, medium and large static spheres are summarized in Table 4.5. Within the TXO of the 50 mm diameter sphere almost 5 % of all reconstructed pixel report density values differ by more than 1 % from their true time-averaged values. This figure increases to approximately 10 % within the 10 mm margin immediately surrounding the TXO. Seven and a half percent (7.5 %) of all pixels within both the TXO and the surrounding 10 mm margin region of the 30 mm diameter sphere disagree by more that 1 % from their physical time-averaged density values. Within the TXO of the 10 mm diameter sphere, the fraction of pixels in agreement with their physical time-averaged density values drops to only

62 % while within the 10 mm margin region the level of agreement raises to more than 95 %. Excluding the penumbral regions, however, CT reconstruction faithfully reproduces physical density values to within 1 %.

Even though the width of the penumbra was found to be relatively small (< 2 mm in all cases), its presence must nonetheless impact target delineation accuracy. To assess this impact, target contours were defined at the following contrast threshold levels [10, 20, 30, 40, 50, 60, 70, 80, 90 %]. As implied in Section 4.2.1, a contrast level of 100 % corresponds to the static lung tumor density (0.90 g/cm^3) while a contrast level of 0 % corresponds to the surrounding lung medium density (0.25 g/cm^3). Furthermore, three quantities were measured at each individual contrast threshold level: (1) ratio of target cross-section to TXO, (2) TXO coverage, and (3) unnecessary TXO coverage. Figure 4.7 illustrates the segmentation results for the static spheres along with the TXO contour, which defines the edge of the physical spherical cross-section. For visualization purposes, only five of the nine target contours are presented [I_{10}, I_{20}, I_{30}, I_{70}, I_{90}]. Figures 4.8 – 4.10 depict the target contour to TXO area ratios, TXO coverage and excess TXO coverage at each individual contrast threshold level. On the whole, larger delineation uncertainties are observed with decreasing object size as a result of increasing penumbra in the reconstructed CT images. However, for the full range of contrast threshold levels and sphere sizes investigated, the spatial deviation between physical and CT reconstructed contours are less than 1 mm. Consequently, it is safe to conclude that CT reconstruction of well-defined, stationary objects yields reliable target contour delineation.

4.3.2.2 Dynamic case

So far it has been shown that respiration leads to a multitude of motion artifacts in CT images. How severely these motion artifacts affect image integrity and the subsequent effect this has on target delineation have not yet been addressed. Consequently, the impact of respiration-induced tumor motion upon CT image integrity and target delineation is presented in this section. As mentioned earlier, two imaging protocols for lung radiotherapy planning are examined and compared, a typical rapid CT scan ($\alpha = 0.25$) and a 'slow' CT scan ($\alpha = 1$).

Figures 4.11 – 4.28 illustrate the physical time-averaged and CT reconstructed images at $z = 0$ mm (a slice corresponding to the mid-orthogonal trajectory position) for the complete set of sphere diameter and motion amplitude combinations scanned with rapid ($\alpha = 0.25$) and 'slow' ($\alpha = 1.0$) acquisition times. Also shown are the percent density difference maps within the TXO and within a 10 mm region surrounding the TXO and their respective frequency histograms. The TXO for each motion is delineated by the dashed contour line in both the time-averaged and CT reconstructed images. For small motions, both time-averaged and CT reconstructed images appear visually similar. As the magnitude of motion increases the degree of similarity between time-averaged and CT reconstructed images diverges with respect to their respective morphologies. In general, the divergence between the time-averaged and CT reconstructed images increases as the sphere diameter to motion amplitude ratio (identified in the remainder of this chapter by the Greek letter kappa, κ) decreases and is greater for the 'slow' scans ($\alpha = 1$) as compared to the rapid scans ($\alpha = 0.25$). As expected, similar patterns are observed for sphere size and motion amplitude combinations that yield equal κ values. As with the static cases, density differences between the CT reconstructed and time-averaged images are seen in the dynamic cases, but the spatial extent of these deviations is, however, much more complex. Whereas density variations occur in the immediate vicinity of the TXO boundary in the static cases, they arise over a much larger area in the dynamic cases.

Table 4.6 summarizes, for all sphere-motion combinations, the mean and standard deviation of the percent differences observed within the TXO between CT reconstructed and time-averaged densities. In all cases, the reconstructed density distributions exhibit mean densities greater than their true physical time-averaged values. Mean differences range from a minimum of 0.5 % to a maximum of 9.6 %.

The standard deviation of the percent density difference values is greater than 1 % in all cases, ranging from a minimum of 7.1 % to a maximum of 23.8 %. These large standard deviations are indicative of the widespread discrepancy between reconstructed and true time-averaged density values. Examination of the histograms presented in Figures 4.11 – 4.28 reveals that even when the mean difference values are less than 1 % they are not the outcome of prevalent agreement between reconstructed and true physical time-averaged density distributions but rather the product of a relatively equivalent spread of reconstructed densities both above and below their true time-averaged values. Pixel statistics for deviations within the TXO of greater than or equal to 1, 3, 5 and 10 % are summarized in Table 4.7. In the best case (50 mm diameter sphere, 5 mm motion, rapid scan) more than 13 % of all reconstructed pixel densities deviate from their true time-averaged values by more than 1 %. Indeed, for the same situation 11 % of all pixels deviate from their physical time averaged values by more than 3 % and almost 7 % by more than 10 %. For the intermediate case of the 30 mm diameter sphere with 15 mm motion and imaged with a rapid scan, almost one half of all reconstructed pixels deviate by more than 1 % from their true time-averaged density values while a deviation of 5 % is seen in 38.5 % of all pixels and almost one quarter of all pixels deviate by more than 10 %. In the worst case scenario, almost 99 % of all CT reconstructed pixels deviate from their true physical time-averaged density values by more than 1 % (10 mm diameter sphere, 15 mm motion, 'slow' scan) and deviations of greater than 10 % are seen in 63.6 % of all pixels for the 30 mm sphere, 25 mm motion, slow scan combination.

Within the 10 mm margin external to the TXO, where a physical uniform background density of 0.25 g/cm^3 exists, the discrepancies observed between reconstructed and true physical density distributions are even more dramatic. The mean and standard deviation of the percent differences observed between CT reconstructed and time-averaged densities within the 10 mm region surrounding the TXO are listed for all sphere-motion combinations in Table 4.8. In all cases, the mean difference is less than 2 %. However, the standard deviation of the percent density difference values is greater than 1 % in all cases, ranging from a minimum of 4.5 % to a maximum of 38.6 %. These large standard deviations are indicative of the magnitude of image integrity breakdown that results outside the TXO in CT scanning of mobile targets. Pixel statistics for deviations within the 10 mm margin external to the TXO of greater than or equal to 1, 3, 5 and 10 % are summarized in Table 4.9. Within this region the number of pixels which agree to within 1 % of their physical time-averaged values never exceeds 40 % (50 mm sphere, 5 mm motion, 'slow' scan). Here, deviations of 3 % and 5 % are observed in more than 18 % and 9 % of all reconstructed pixels respectively. For the 30 mm diameter sphere with 15 mm motion, the number of reconstructed pixels which agree to within 1 % of their physical time-averaged density values is less than 6 % for both the rapid, and 3 % for the 'slow' scan scenarios. For this sphere size and motion amplitude combination the number of reconstructed pixels which agree to within 10 % of their true time-averaged density values drops to less than 45 % for the rapid scan and less than 58 % for the 'slow' scan acquisitions. In the worst case (30 mm diameter sphere, 25mm motion, 'slow' scan) more than 99 % of all reconstructed pixels deviate from their true physical time-averaged density values by more than 1 %. In this case, almost 98 % of all reconstructed pixels deviate by more than 3 %, about 97.5 % differ by more than 5 %, and nearly 93 % are in error by more than 10 % from their physical time-averaged values. Clearly evident both within the TXO and the 10 mm surrounding margin is the wide spread departure from true time-averaged density values in these motion-impacted CT reconstructed images.

Tables 4.10 – 4.11 summarize the time-averaged and CT reconstructed absolute density statistics (minimum, maximum, mean) within the TXO for all rapid and 'slow' scans. The most striking feature revealed by this data is the generation of reconstructed densities below that of the surrounding background. The existence of CT densities below background density in the TXO is a direct result of the application of the filter designed for static reconstruction but applied under dynamic conditions. Here, the negative portions of the filter, which are intended to mitigate the radial blur characteristic of static images, are misapplied. This misapplication results in a limited or partial reduction of radial blur in some regions and the erroneous decrease in reconstructed densities in other areas. Indeed, in all dynamic cases, the minimum CT reconstructed density within the TXO was always less than the physical background density of 0.25 g/cm^3 and in one instance (30 mm sphere, 15 mm motion, 'slow' scan) the generation of negative densities occurred.

While the improper application of the filter accounts for some of the observed discrepancies between time-averaged and CT reconstructed densities (densities below background and below time-averaged densities), it does not account for all density deviations observed within the TXO. The largest portion of deviations between the CT reconstructed and time-averaged densities results from the projection of object density away from the path of motion as seen in both Chapters 2 and 3. The net effect of this projection is the displacement of density from one region of the image to another, thus artificially lowering values in one area while elevating them in others. Figure 4.29 summarizes, for all dynamic cases explored, the fraction of CT pixels within the TXO that are in agreement with the time-averaged pixels. Agreement, in these dynamic situations, is deemed to exist when CT pixel densities fall within 1.0 % of their corresponding time-averaged pixel densities. As expected, the loss of density integrity within the TXO is greatest for the smallest sphere undergoing the largest motion (κ = 0.4) and scanned with the longest acquisition time (α = 1) and least for the largest sphere undergoing the smallest motion (κ = 10) and scanned with the shortest acquisition time (α = 0.25).

External to the TXO, where partial volume effects are physically non-existent, accurate CT reconstruction should yield densities equal to the uniform background value of 0.25 g/cm^3. Tables 4.12 summarizes the CT reconstructed image absolute density statistics (minimum, maximum, mean) outside the TXO contour but within a 10 mm margin for both rapid and 'slow' scans at z = 0 mm. The minimum, maximum and mean densities outside the TXO in the time-averaged images were, as expected, 0.25 g/cm^3 for all sphere diameter and motion amplitude combinations. Even though the mean reconstructed image density outside the TXO is found to be in the vicinity of 0.25 g/cm^3 for all sphere size and motion amplitude combinations, values as low as –0.341 g/cm^3 and as high as 0.762 g/cm^3 are recorded. Densities in excess of the expected background value result from the distension of the reconstructed object in directions displaced from the path of motion while their unphysical suppression below background is solely due to inappropriate filter application.

Since motion disturbs the integrity of the CT images, it must also impact target delineation. Figures 4.30 through 4.32 depict the rapid and 'slow' CT scans object segmentation results at $z = 0$ mm for all sphere diameter and motion amplitude combinations. For visualization purposes, only five intensity levels [I_{10}, I_{30}, I_{50}, I_{70}, I_{90}] are presented corresponding to 10, 30, 50, 70, and 90 percent of the static image contrast above background. Also shown in these figures are the corresponding TXO contours. Compared to the breath-hold target contours (see Figure 4.7), which are virtually indistinguishable from one another and congruent with the surface of each immobile sphere (TXO), the dynamic target contours are clearly divergent, by varying degrees, from one another and from physically meaningful volumes which might be associated with these mobile objects. As expected, the divergence is greatest for the smallest sphere undergoing the largest motion and scanned with the longest acquisition time ($\alpha = 1$), and least for the largest sphere undergoing the smallest motion and scanned using the shortest acquisition time ($\alpha = 0.25$). In all cases presented, none of the dynamic iso-intensity contours fully encompass the entire TXO contour. The percent TXO coverage achieved by these contours, as well as all other omitted iso-contours [I_{20}, I_{40}, I_{60}, I_{80}], for the rapid and 'slow' scans are shown in Figures 4.33 – 4.35. In all cases the rapid scan yielded better TXO coverage than did the 'slow' scan for the same sphere diameter and motion amplitude combinations at each threshold level. This result is to be expected with the increased magnitude of motion artifacts associated with the 'slow' scan technique due to the larger degree of object movement incorporated. Furthermore, the 'slow' scan TXO coverage decreases in a rather discontinuous manner as a function of iso-contrast level in comparison to that associated with the rapid scan data. With both techniques the decrease in TXO coverage is particularly dramatic for the small sphere where large motion amplitudes can completely remove the target from the scan plane a significant portion of the time

In addition to the inability to fully encompass the TXO, areas external to the TXO may also be incorporated by iso-contrast level defined cross-sections. The most significant excursions beyond the bounds of the TXO occur with the 10 % and 20 % iso-contrast contours. The excess areas external to the TXO are listed for these two iso-contrast levels for all sphere size and motion amplitude combinations investigated. These excess areas are in general greater for larger motions in combination with the 'slow' scan technique and can be seen to range from as little as 0.1 % to as large as 153 %.

The density variations along the TXO contour at the $z = 0$ slice location for all sphere diameter and motion amplitude combinations are shown in Figures 4.36 – 4.39. In all dynamic cases, significant density variations occur along these contour lines. The degree of heterogeneity observed along each of these contours clearly indicates the inability to define this or any other physically meaningful cross-sectional area without knowledge additional to that provided by the images themselves.

4.4 Summary and Conclusion

With the exception of breath-hold techniques, all current CT scans for lung radiotherapy are acquired while the tumor is non-stationary and as such are subject to the presence of motion artifacts. From an imaging standpoint, the mobile object is subject to a wide ranging degree of distortion from its true shape depending on object size, extent of motion, and scan time. Mild and even barely detectable distensions are associated with rapid scans of objects whose range of motion is small in comparison to their physical size. In contrast, highly contorted images can result when object size is small in comparison to the extent of motion. These effects are exacerbated by long scan times in comparison to more rapid image acquisition schemes. These distortions can be so severe as to render the reconstructed image unrecognizable in relation to its static counterpart.

For the static case, CT image reconstruction is seen to faithfully reproduce the physical densities of objects to within 1% accuracy in all regions excluding narrow regions in the immediate vicinity of density discontinuities. Within the penumbral regions which result, the integrity of CT reconstruction to accurately reproduce physical densities is compromised. The departure in image fidelity observed within these density discontinuity penumbral regions reflects fundamental practical limitations of CT reconstruction.

The presence of motion during acquisition, on the other hand, produces inconsistent projection data sets which, upon CT reconstruction, negatively impact image integrity on a global basis. The degradation in image integrity which results is due to the combination of improper filter application and the distension of object density away from the path of motion. The degree to which motion impacts image integrity was investigated in terms of the ability to reproduce the physical time-averaged density distributions resultant from the dynamics involved. Two specific regions within these motion impacted images were investigated with regard to their adherence to the true distribution of densities. These two areas were the TXO, where the presence of motion produces time-averaged density distributions divergent from the static case, and a 10 mm margin immediately surrounding the TXO where static conditions physically exist. Over the range of all sphere diameter and motion amplitude combinations investigated, mean differences between physical and reconstructed densities within the TXO were seen to range from as little as 0.5 % to as much as 9.6 %. Standard deviations in percent density difference values for the TXO region were in all cases greater than 1 %, ranging from a minimum of 7.1 % to a maximum of 23.8 %. Mean density differences of less than 2 % were observed in all margin regions. The standard deviations in percentage density difference values were, as within the TXO, all larger than 1 % and ranged from a minimum of 4.5 % to a maximum of 38.6 %. In all cases, and in both regions, a wide spread departure in reconstructed densities from their true physical values was observed as indicated by the large standard deviations in percentage density difference. In the worst case observed (30 mm sphere, 25 mm motion, 'slow' scan), densities deviations within the TXO of more than 10 % occurred for almost 63 % of all reconstructed pixels. For this same case, density deviations of greater than 10 % were observed in nearly 93 % of all reconstructed pixels within the 10 mm margin region. Even in regions where mean differences of less than 1 % were observed, the data clearly reveals that this is not the result of widespread agreement but instead is the product of a rather fortuitous relatively equivalent spread in reconstructed densities both above and below their true time- averaged values.

Not surprisingly, the widespread negative impact of motion on CT reconstructed image integrity has significant concomitant consequences for object delineation. Simple threshold based contouring proves readily able to locate and delineate the physical extent of static objects. When applied to motion-impacted images the same technique is seen to yield results which range from reasonable to dismal. As is to be expected, the best results are obtained with small motions in combination with large target sizes while the worst results derive from large motions coupled with small targets. In all of the dynamic cases investigated, this simple delineation scheme failed to yield contours which fully encompassed the TXO. Furthermore, those contours which best enveloped the TXO could, in the case of large motions and small target sizes, include significant areas external to the TXO. The widespread failure to accurately identify the TXO is clearly the result of the large degree of image degradation resultant from the presence of motion-induced image artifacts and not the simplicity of the delineation technique employed. This is perhaps most readily seen by examining the density variations which characterize the contour of the TXO in all dynamic cases. The magnitude of heterogeneity observed along these contour lines, and within these motion-impacted images as a whole, clearly indicates the inability of any simple strait forward delineation scheme to define this or any other physically meaningful cross-sectional area associated with mobile objects without knowledge additional to that provided by the images themselves.

TABLE 4.1

Target contour areas for experimental and simulation scans of a 25 mm diameter POM sphere in air and in water at $z = 0$ mm, where partial volume effects are minimal. Also included in the table are the deviations between experimental and simulation target contour centroids.

Gray-threshold level (%)	Air			Water		
	Area experiment (mm^2)	Area simulation (mm^2)	Centroid deviation (mm)	Area experiment (mm^2)	Area simulation (mm^2)	Centroid deviation (mm)
10	520.5	528.3	0.24	521.2	528.2	0.40
20	506.4	514.4	0.24	507.3	514.2	0.41
30	495.3	503.9	0.25	495.8	503.6	0.42
40	485.7	494.2	0.25	486.2	493.7	0.42
50	477.1	484.6	0.26	477.6	484.2	0.42
60	468.3	475.5	0.25	469.0	474.9	0.42
70	463.8	465.5	0.25	459.9	465.0	0.42
80	458.8	455.2	0.25	449.3	454.6	0.42
90	435.3	439.5	0.24	435.1	438.5	0.42

Note: Actual area of POM sphere at this slice location is 490. 9 mm^2.

TABLE 4.2

Target contour areas for experimental and simulation scans of a 25 mm diameter POM sphere in air and in water at $z = 9$ mm, where partial volume effects are prominent. Also included in the table are the deviations between experimental and simulation target contour centroids.

Gray-threshold level (%)	Air			Water		
	Area experiment (mm^2)	Area simulation (mm^2)	Centroid deviation (mm)	Area experiment (mm^2)	Area simulation (mm^2)	Centroid deviation (mm)
10	312.2	316.2	0.26	308.1	316.2	0.38
20	283.8	289.3	0.26	283.0	289.0	0.40
30	262.0	267.3	0.25	261.8	267.1	0.40
40	242.8	247.6	0.26	243.4	247.2	0.38
50	224.1	229.8	0.26	225.5	229.0	0.34
60	205.8	211.5	0.25	207.1	211.1	0.37
70	186.2	192.2	0.25	186.4	192.2	0.47
80	163.3	170.1	0.25	161.3	169.7	0.47
90	132.0	137.8	0.25	127.3	137.1	0.36

Note: Actual area of POM sphere at this slice location is 236.4 mm^2.

TABLE 4.3

Target contour areas for experimental and simulation scans of a 30 mm diameter POM cylinder undergoing a SHM along the horizontal axis of the scanner in both air and water mediums. Also included in the table are the deviations between experimental and simulation target contour centroids.

Gray-threshold level (%)	Air			Water		
	Area experiment (mm^2)	Area simulation (mm^2)	Centroid deviation (mm)	Area experiment (mm^2)	Area simulation (mm^2)	Centroid deviation (mm)
10	1268.0	1314.6	1.36	1277.0	1315.1	0.48
20	987.2	1037.3	0.95	997.5	1037.5	0.69
30	874.9	910.6	1.41	874.7	910.7	0.81
40	757.6	777.6	1.74	758.8	777.8	0.62
50	680.7	664.7	1.70	668.6	665.0	0.62
60	575.3	581.3	1.94	569.1	581.7	0.83
70	490.9	479.7	1.85	480.9	480.0	1.18
80	411.1	382.7	1.03	409.0	383.1	1.07
90	369.1	327.3	0.71	360.5	327.6	0.89

TABLE 4.4

Target contour areas for experimental and simulation scans of a 25 mm diameter POM cylinder undergoing a SHM along the *z* - axis of the scanner in both air and water mediums. Also included in the table are the deviations between experimental and simulation target contour centroids.

Gray-threshold level (%)	Air			Water		
	Area experiment (mm^2)	Area simulation (mm^2)	Centroid deviation (mm)	Area experiment (mm^2)	Area simulation (mm^2)	Centroid deviation (mm)
10	482.3	483.8	0.34	483.3	483.9	0.84
20	461.9	463.7	0.35	460.9	463.7	0.79
30	456.7	447.3	0.35	443.5	447.3	0.78
40	432.3	431.7	0.34	427.1	431.7	0.75
50	416.9	410.5	0.36	407.3	410.7	0.68
60	383.8	376.5	0.37	379.9	376.5	0.57
70	359.5	349.5	0.36	353.6	349.8	0.53
80	335.4	322.3	0.39	326.9	322.5	0.51
90	295.5	287.2	0.41	292.3	288.1	0.54

TABLE 4.5

Fraction of CT pixels within 1, 3, 5 and 10 % of the expected time-averaged density for breath-hold scans.

Sphere diameter	Within TXO				Within 10 mm region outside TXO			
	1 %	3 %	5 %	10 %	1 %	3 %	5 %	10 %
50 mm	95.1	97.1	98.0	99.1	90.2	91.2	91.4	92.4
30 mm	92.5	92.9	94.9	97.5	92.5	93.1	93.4	94.0
10 mm	62.0	71.8	77.4	87.2	95.1	95.5	95.8	96.4

TABLE 4.6

Comparison of image density breakdown within the TXO between the rapid and 'slow' CT scans. For each sphere diameter and motion amplitude combination, the mean and standard deviation of the percent density differences within the TXO are presented.

		Rapid scan		'Slow' scan	
Combination	Kappa value	Mean (%)	Standard deviation (%)	Mean (%)	Standard deviation (%)
50 mm sphere – 5 mm motion	10.0	1.4	7.4	1.8	9.8
50 mm sphere – 15 mm motion	3.3	1.7	10.3	3.4	16.6
50 mm sphere – 25 mm motion	2.0	1.5	12.7	5.2	18.6
30 mm sphere – 5 mm motion	6.0	1.1	7.1	1.7	10.7
30 mm sphere – 15 mm motion	2.0	1.6	11.7	4.9	17.3
30 mm sphere – 25 mm motion	1.2	2.0	16.3	7.5	23.8
10 mm sphere – 5 mm motion	2.0	0.5	8.2	1.9	13.9
10 mm sphere – 15 mm motion	0.7	2.9	16.6	9.6	12.8
10 mm sphere – 25 mm motion	0.4	0.2	20.4	7.8	13.1

TABLE 4.7

Fraction of pixels within the TXO that falls within 1, 3, 5 and 10 % of the true time-averaged density values.

Combination	Kappa value	Rapid scan				'Slow' scan			
		1 %	3 %	5 %	10 %	1 %	3 %	5 %	10 %
50 mm sphere–5 mm motion	10.0	86.9	89.0	90.3	93.2	77.2	79.9	82.7	89.3
30 mm sphere–5 mm motion	6.0	79.1	83.0	85.4	90.7	64.0	68.4	71.8	83.0
50 mm sphere–15 mm motion	3.3	68.3	72.1	75.4	83.5	44.2	49.1	53.4	67.0
30 mm sphere–15 mm motion	2.0	50.3	56.3	61.5	75.8	19.1	26.8	34.2	56.9
30 mm sphere–25 mm motion	1.2	19.3	26.7	34.0	54.6	5.8	14.3	22.2	37.4
10 mm sphere–15 mm motion	0.7	7.7	19.7	28.4	49.9	1.1	6.9	17.6	59.9
10 mm sphere–25 mm motion	0.4	4.6	15.0	23.4	47.4	2.2	7.1	14.4	56.5

TABLE 4.8

Comparison of image density breakdown outside the TXO but within a 10 mm region between the rapid and 'slow' CT scans. For each sphere diameter and motion amplitude combination, the mean and standard deviation of the percent density differences within a 10 mm region surrounding the TXO are presented.

		Rapid scan		'Slow' scan	
Combination	Kappa value	Mean (%)	Standard deviation (%)	Mean (%)	Standard deviation (%)
50 mm sphere – 5 mm motion	10.0	0.6	8.7	0.4	4.5
50 mm sphere – 15 mm motion	3.3	0.3	14.7	-0.2	11.1
50 mm sphere – 25 mm motion	2.0	0.8	18.3	0.9	28.4
30 mm sphere – 5 mm motion	6.0	1.6	11.2	1.7	11.2
30 mm sphere – 15 mm motion	2.0	1.0	16.3	0.7	24.2
30 mm sphere – 25 mm motion	1.2	0.7	19.1	1.3	38.6
10 mm sphere – 5 mm motion	2.0	0.8	9.7	0.7	11.8
10 mm sphere – 15 mm motion	0.7	0.0	14.2	0.2	24.9
10 mm sphere – 25 mm motion	0.4	0.1	14.9	0.3	20.9

TABLE 4.9

Fraction of pixels within a 10 mm region surrounding the TXO that falls within 1, 3, 5 and 10 % of the expected background density of 0.25 g/cm^3.

Combination	Kappa value	Rapid scan				'Slow' scan			
		1 %	3 %	5 %	10 %	1 %	3 %	5 %	10 %
50 mm sphere–5 mm motion	10.0	9.8	41.0	67.5	83.9	40.0	81.6	90.2	95.2
30 mm sphere–5 mm motion	6.0	8.7	27.6	55.3	83.7	29.8	71.1	84.4	94.7
50 mm sphere–15 mm motion	3.3	3.1	10.1	18.0	59.3	9.9	26.4	40.0	75.8
30 mm sphere–15 mm motion	2.0	5.9	15.8	24.0	44.9	2.9	11.4	24.8	57.8
30 mm sphere–25 mm motion	1.2	11.8	26.9	34.9	52.4	0.4	1.5	2.5	6.3
10 mm sphere–15 mm motion	0.7	10.2	36.1	52.9	76.2	0.7	1.8	3.0	24.1
10 mm sphere–25 mm motion	0.4	4.5	15.2	35.0	67.9	0.6	2.2	15.2	38.2

TABLE 4.10

Pixel statistics (mean, minimum, maximum densities) within the TXO of the rapid time-averaged and CT reconstructed images.

Combination	Kappa value	Time-averaged image Mean density (g/cm^3)	Time-averaged image Minimum density (g/cm^3)	Time-averaged image Maximum density (g/cm^3)	CT reconstructed image Mean density (g/cm^3)	CT reconstructed image Minimum density (g/cm^3)	CT reconstructed image Maximum density (g/cm^3)
50 mm sphere–5 mm motion	10.0	0.863	0.263	0.900	0.870	0.211	0.908
30 mm sphere–5 mm motion	6.0	0.841	0.263	0.900	0.846	0.202	0.906
50 mm sphere–15 mm motion	3.3	0.796	0.263	0.900	0.803	0.209	0.904
30 mm sphere–15 mm motion	2.0	0.732	0.263	0.900	0.738	0.144	0.901
30 mm sphere–25 mm motion	1.2	0.606	0.263	0.900	0.612	0.146	0.901
10 mm sphere–15 mm motion	0.7	0.413	0.263	0.546	0.421	0.172	0.550
10 mm sphere–25 mm motion	0.4	0.351	0.263	0.417	0.354	0.117	0.420

* The minimum density within the TXO should be just above 0.250 g/cm^3. However, due to pixel averaging, the minimum density recorded is 0.263 g/cm^3.

TABLE 4.11

Pixel statistics (mean, minimum, maximum densities) within the TXO of the 'slow' time-averaged and CT reconstructed images.

		Time-averaged image			CT reconstructed image		
Combination	Kappa value	Mean density (g/cm^3)	Minimum density (g/cm^3)	Maximum density (g/cm^3)	Mean density (g/cm^3)	Minimum density (g/cm^3)	Maximum density (g/cm^3)
50 mm sphere–5 mm motion	10.0	0.830	0.263	0.900	0.836	0.232	0.910
30 mm sphere–5 mm motion	6.0	0.794	0.263	0.900	0.798	0.243	0.908
50 mm sphere–15 mm motion	3.3	0.731	0.263	0.900	0.746	0.237	0.905
30 mm sphere–15 mm motion	2.0	0.660	0.263	0.900	0.674	-0.228	0.901
30 mm sphere–25 mm motion	1.2	0.551	0.263	0.726	0.577	0.105	0.768
10 mm sphere–15 mm motion	0.7	0.388	0.263	0.458	0.425	0.097	0.472
10 mm sphere–25 mm motion	0.4	0.331	0.263	0.367	0.358	0.113	0.398

* The minimum density within the TXO should be just above 0.250 g/cm^3. However, due to pixel averaging, the minimum density recorded is 0.263 g/cm^3.

TABLE 4.12

CT pixel statistics (mean, minimum, maximum densities) within a 10 mm region outside the TXO.

		Rapid CT scan			'Slow' CT scan		
Combination	Kappa value	Mean density (g/cm^3)	Minimum density (g/cm^3)	Maximum density (g/cm^3)	Mean density (g/cm^3)	Minimum density (g/cm^3)	Maximum density (g/cm^3)
50 mm sphere–5 mm motion	10.0	0.257	0.155	0.762	0.256	0.226	0.718
30 mm sphere–5 mm motion	6.0	0.255	0.149	0.693	0.255	0.194	0.736
50 mm sphere–15 mm motion	3.3	0.254	0.130	0.653	0.253	0.091	0.625
30 mm sphere–15 mm motion	2.0	0.253	0.117	0.510	0.252	0.018	0.437
30 mm sphere–25 mm motion	1.2	0.252	0.116	0.621	0.253	-0.341	0.563
10 mm sphere–15 mm motion	0.7	0.250	-0.115	0.402	0.251	-0.153	0.588
10 mm sphere–25 mm motion	0.4	0.250	0.036	0.397	0.251	0.095	0.381

* Note: Time-averaged minimum, maximum and mean are all equal to 0.250 g/cm^3.

TABLE 4.13

Excess areas outside the TXO for both the rapid and 'slow' scans. Excess area is expressed as a percentage of the TXO area.

Sphere diameter (mm)	Gray-level threshold	Rapid scan 5 mm motion	Rapid scan 15 mm motion	Rapid scan 25 mm motion	'Slow' scan 5 mm motion	'Slow' scan 15 mm motion	'Slow' scan 25 mm motion
50	I_{10}	1.8 %	4.8 %	7.6 %	0.6 %	0.7 %	18.9 %
	I_{20}	0.2 %	0.1 %	0.2 %	0.1 %	0.0 %	0.0 %
30	I_{10}	3.3 %	8.0 %	13.6 %	1.2 %	18.7 %	71.9 %
	I_{20}	0.5 %	0.2 %	0.8 %	0.1 %	0.0 %	23.5 %
10	I_{10}	10.0 %	22.1 %	29.2 %	13.6 %	139 %	153 %
	I_{20}	0.9 %	1.6 %	0.0 %	0.1 %	43.7 %	0.0 %

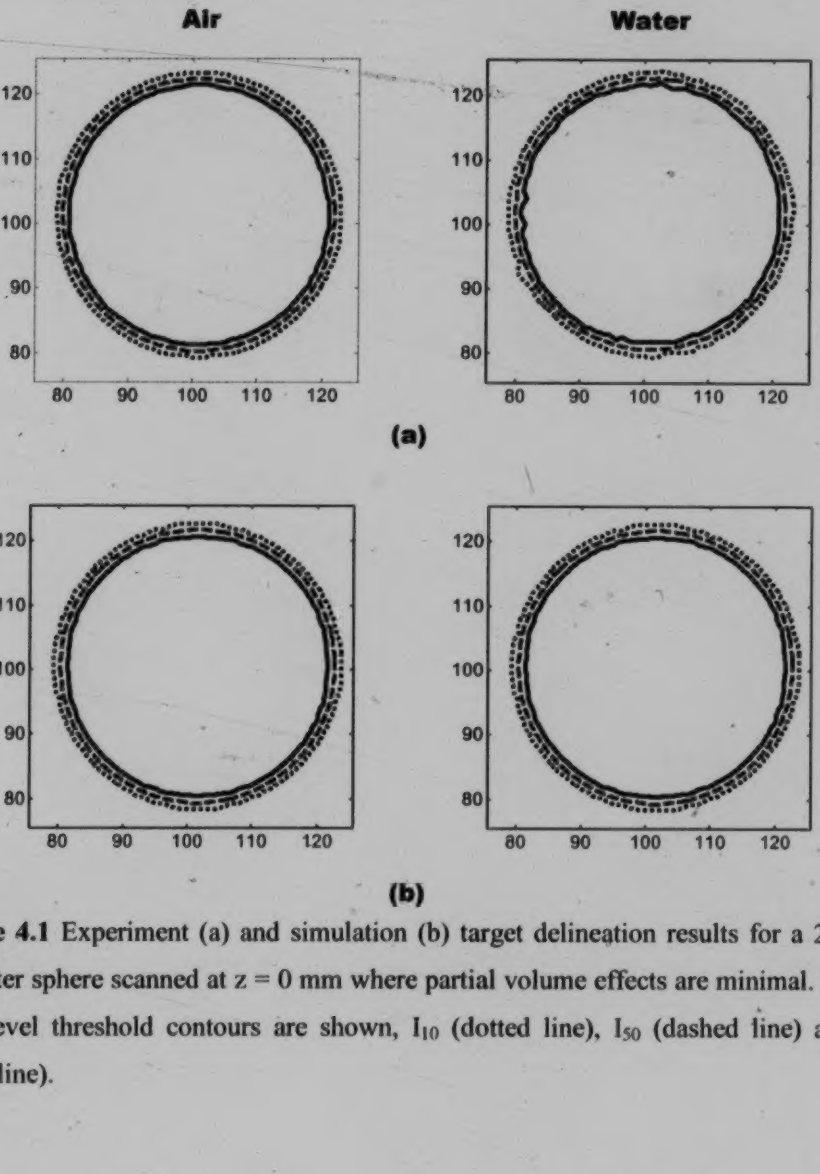

Figure 4.1 Experiment (a) and simulation (b) target delineation results for a 25 mm diameter sphere scanned at z = 0 mm where partial volume effects are minimal. Three gray-level threshold contours are shown, I_{10} (dotted line), I_{50} (dashed line) and I_{90} (solid line).

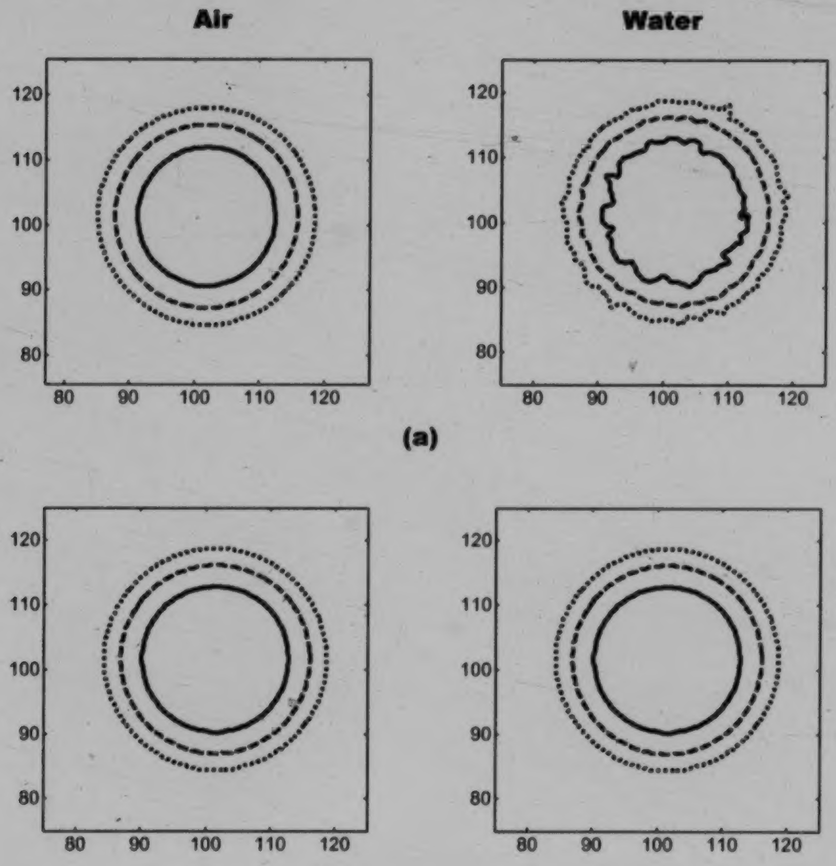

(a)

(b)

Figure 4.2 Experiment (a) and simulation (b) target delineation results for a 25 mm diameter sphere scanned at $z = 9$ mm where partial volume effects are observed. Three gray-level threshold contours are shown, I_{10} (dotted line), I_{50} (dashed line) and I_{90} (solid line).

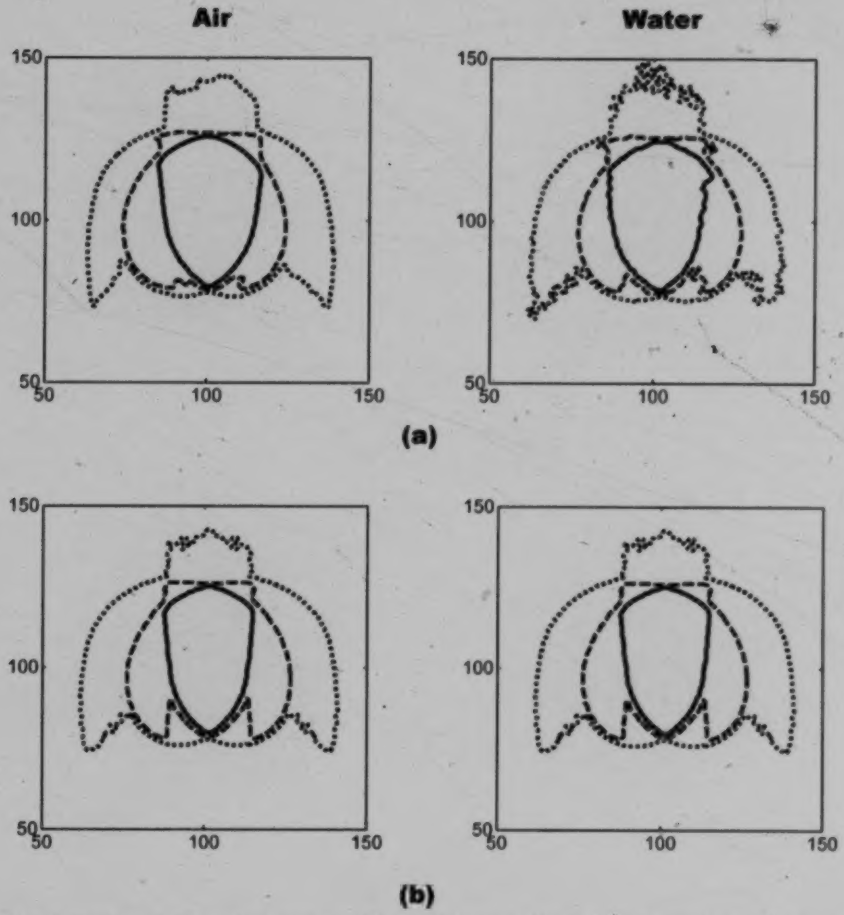

Figure 4.3 Target delineation results for a 30 mm cylinder undergoing a 15 mm SHM along horizontal axis. Contours defined using a 10 % (dotted line), 50 % (dashed line) and 90 % (solid line) threshold percentage value. (a) Experiment and (b) Simulation.

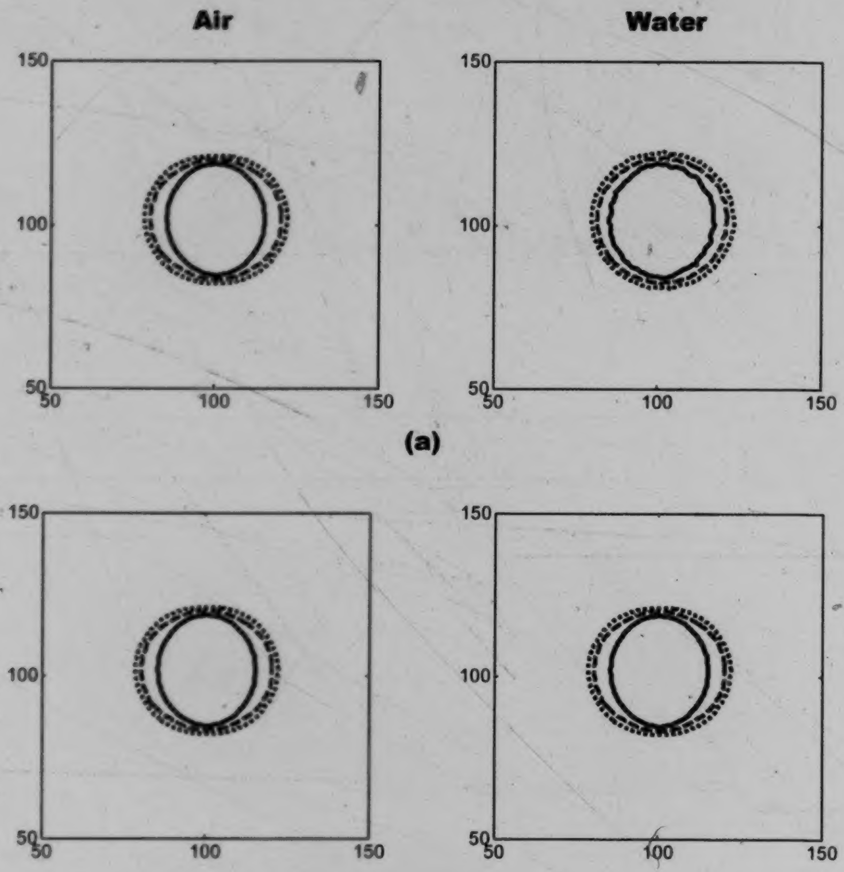

(a)

(b)

Figure 4.4 Target delineation results for a 25 mm sphere undergoing a 15 mm SHM along the *z*-axis. Contours defined using a 10 % (dotted line), 50 % (dashed line) and 90 % (solid line) threshold percentage value. (a) Experiment and (b) Simulation.

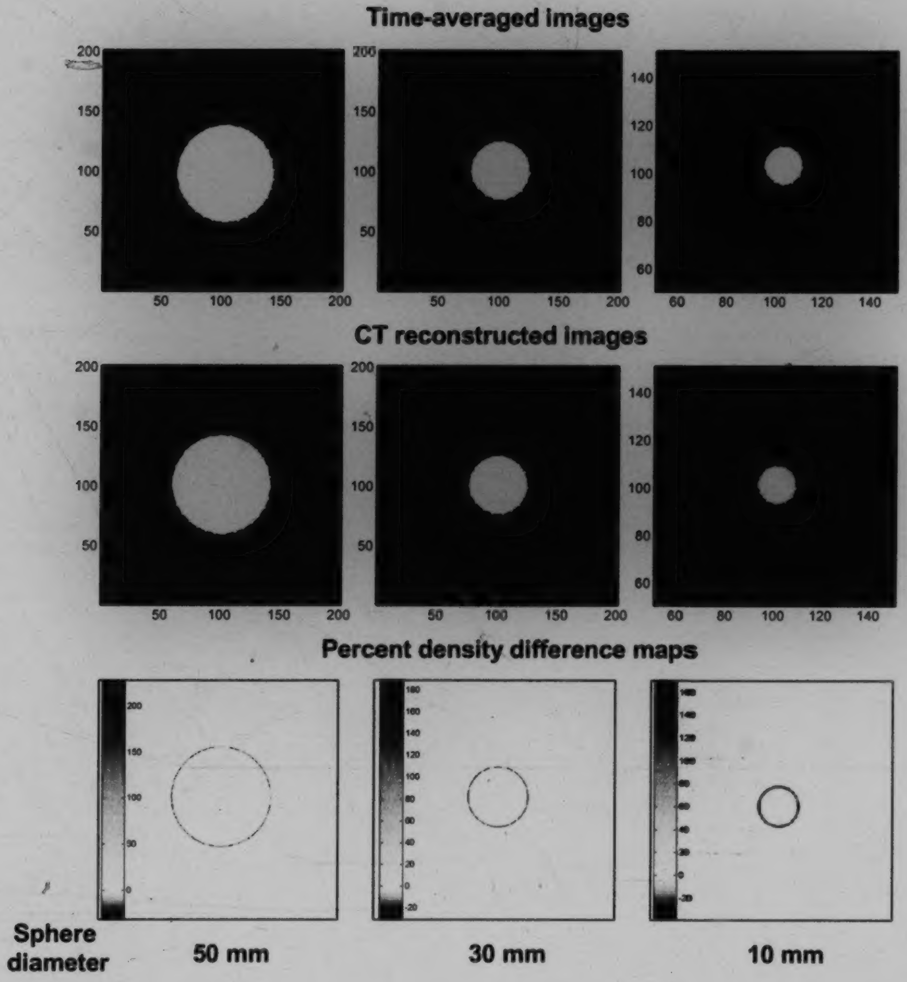

Figure 4.5 Time-averaged and CT reconstructed breath-hold images for three clinically relevant sphere sizes as well as difference density maps.

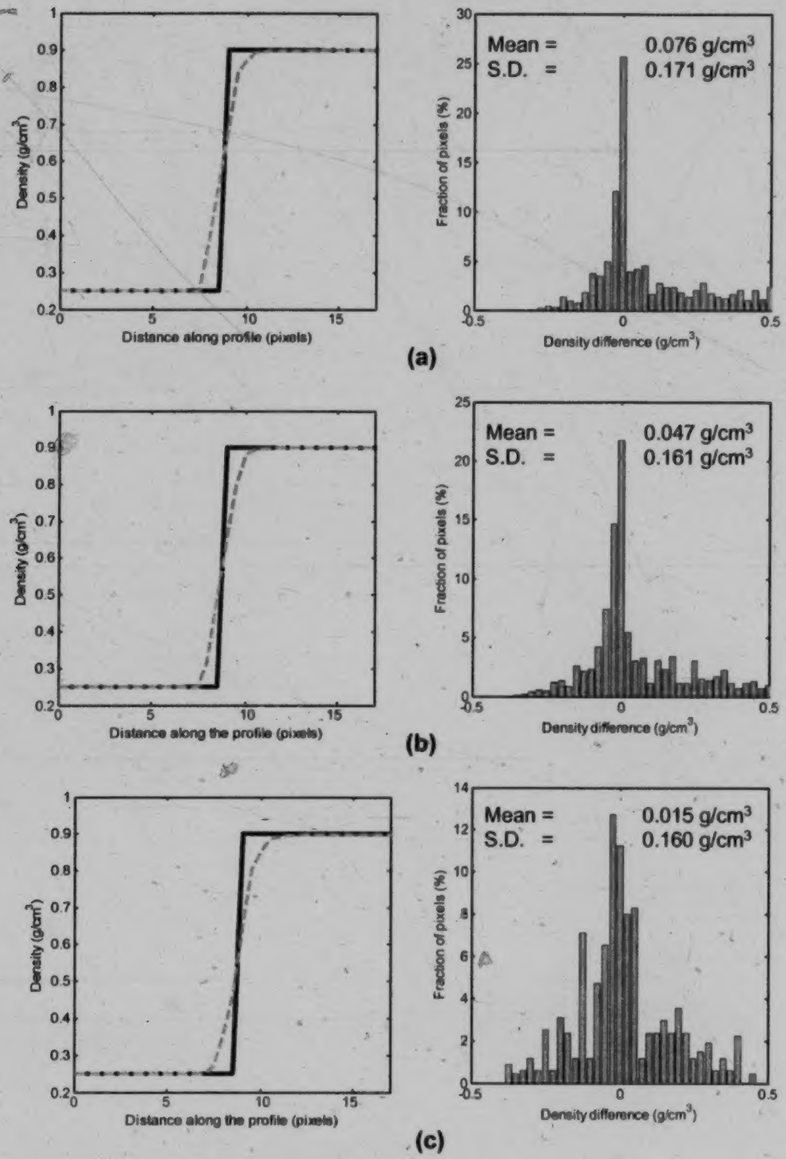

Figure 4.6 Penumbra in CT images of well-defined objects. Section of central horizontal density profile illustrating the penumbral region and density difference frequency distribution within a 2 mm ring centered on TXO for the (a) large 50 mm diameter sphere, (b) intermediate 30 mm diameter sphere and (c) small 10 mm diameter sphere.

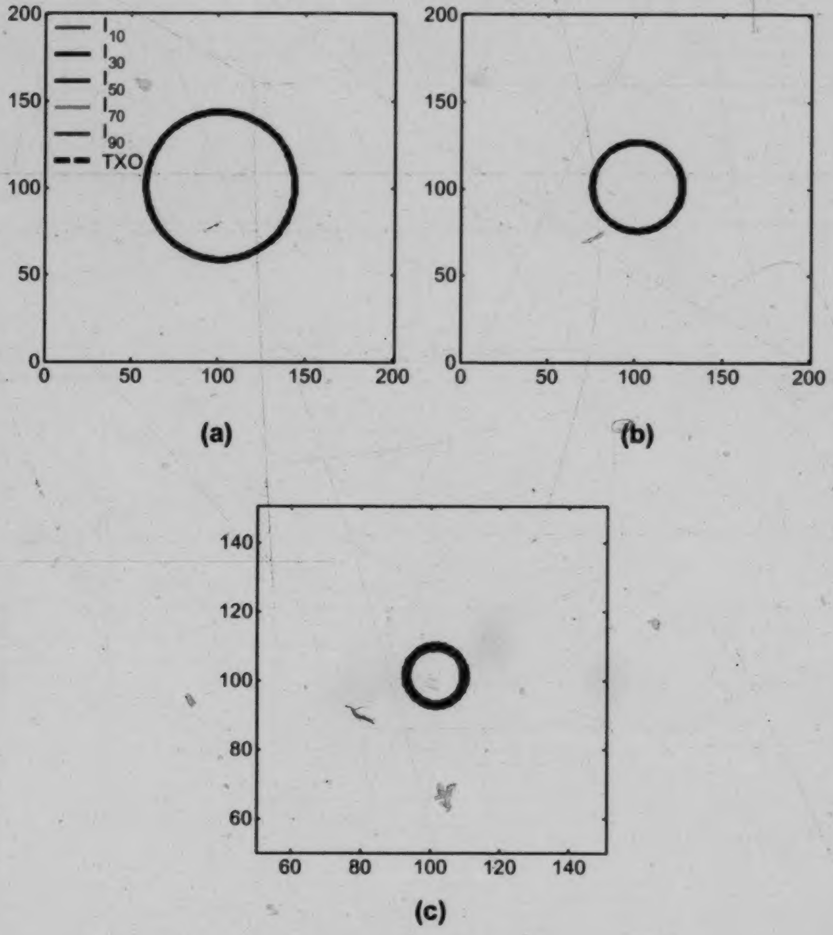

(a)

(b)

(c)

Figure 4.7 Target segmentation results for the (a) large, (b) intermediate and (c) small static spheres. For visualization purposes, only five target contours are displayed [I_{10}, I_{20}, I_{30}, I_{70}, I_{90}]. (Note: I_{100} corresponds to the static lung tumor density (0.90 g/cm^3) while I_0 corresponds to the background density (0.25 g/cm^3)).

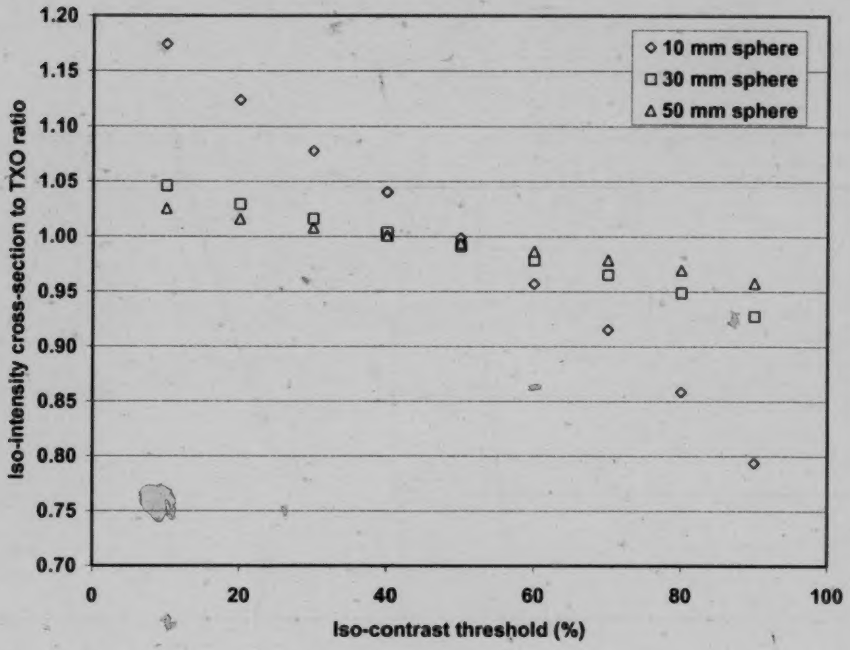

Figure 4.8 Target cross-section to TXO ratio as a function of contrast threshold level.

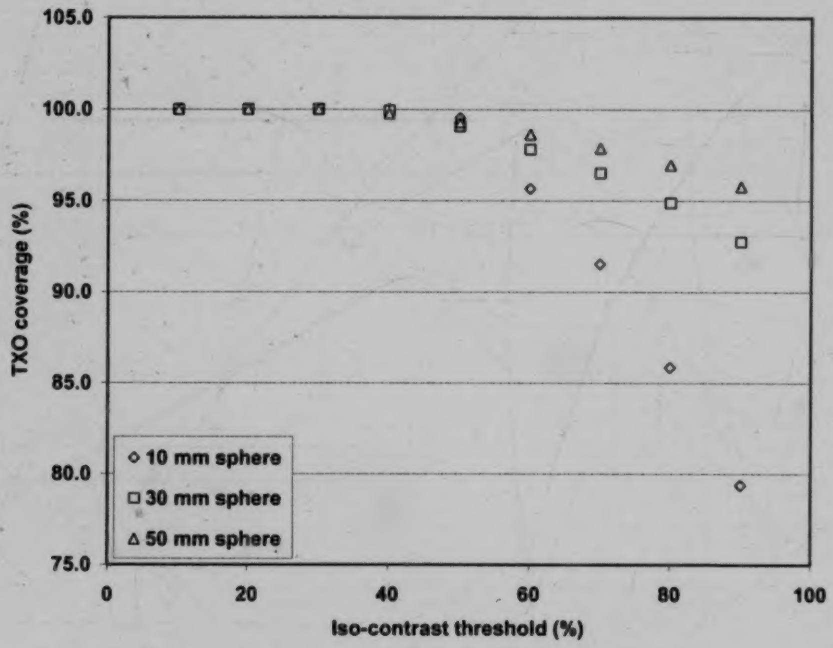

Figure 4.9 TXO coverage as a function of contrast threshold level.

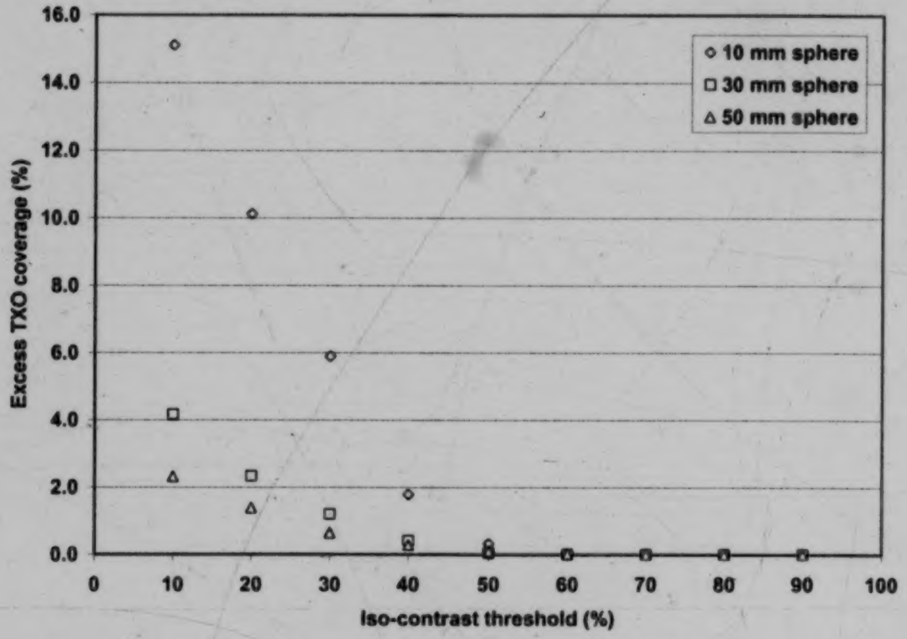

Figure 4.10 Excess TXO coverage as a function of contrast threshold level.

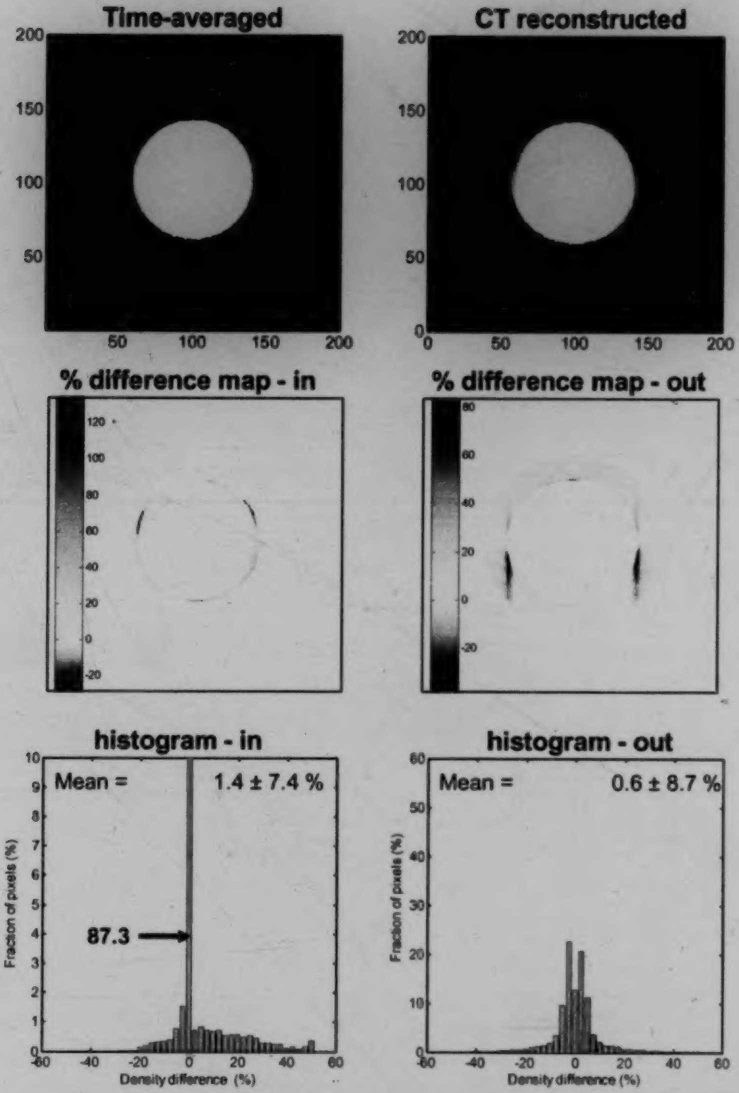

Figure 4.11 Time-averaged and CT reconstructed images along with TXO contours (dashed lines) for the large sphere (diameter = 50 mm) undergoing a small SHM (A_x = Az = 5 mm) and imaged with a rapid 1 second acquisition time (alpha = 0.25). Also shown are the percent density difference maps within the TXO (% difference map – in) and within a 10 mm region surrounding the TXO (% difference map – out) along with their corresponding histograms (histogram – in, histogram – out).

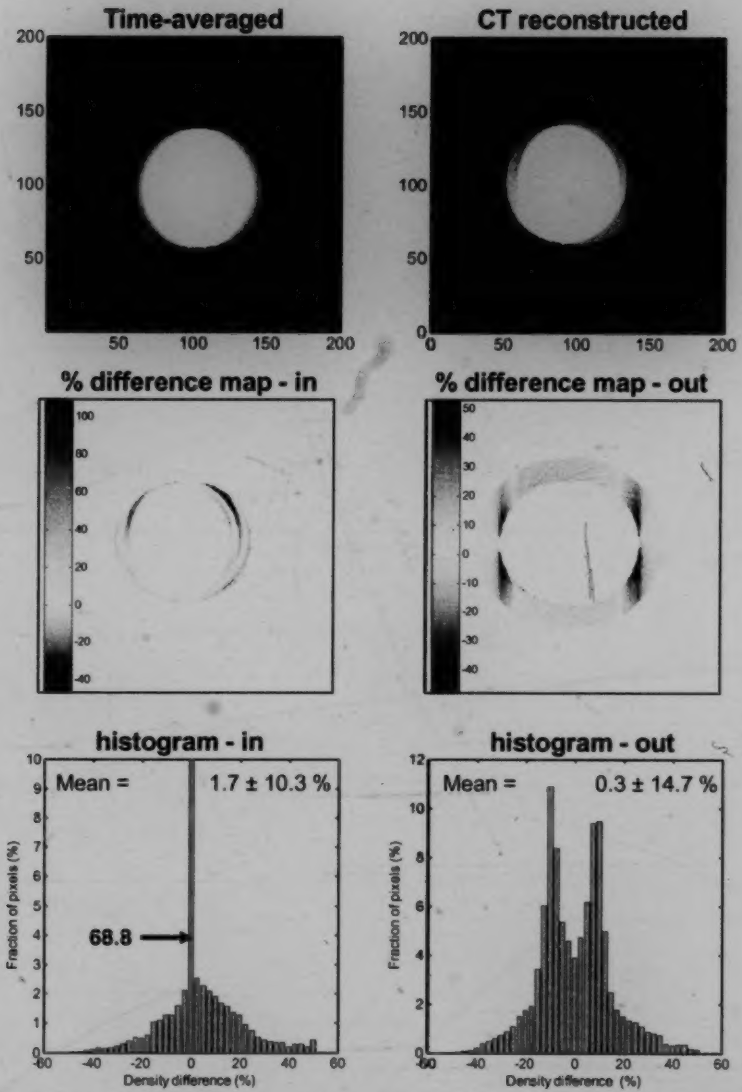

Figure 4.12 Time-averaged and CT reconstructed images along with TXO contours (dashed lines) for the large sphere (diameter = 50 mm) undergoing an intermediate SHM ($A_x = Az = 15$ mm) and imaged with a rapid 1 second acquisition time (alpha = 0.25). Also shown are the percent density difference maps within the TXO (% difference map – in) and within a 10 mm region surrounding the TXO (% difference map – out) along with their corresponding histograms (histogram – in, histogram – out).

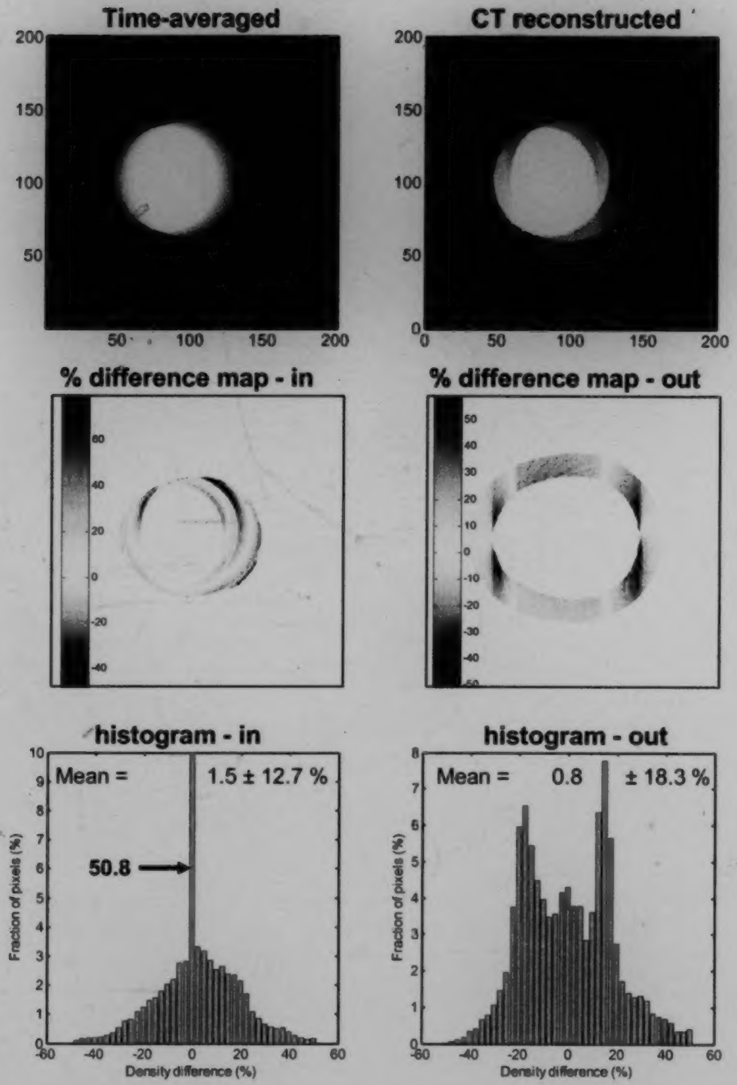

Figure 4.13 Time-averaged and CT reconstructed images along with TXO contours (dashed lines) for the large sphere (diameter = 50 mm) undergoing a large SHM (A_x = Az = 25 mm) and imaged with a rapid 1 second acquisition time (alpha = 0.25). Also shown are the percent density difference maps within the TXO (% difference map – in) and within a 10 mm region surrounding the TXO (% difference map – out) along with their corresponding histograms (histogram – in, histogram – out).

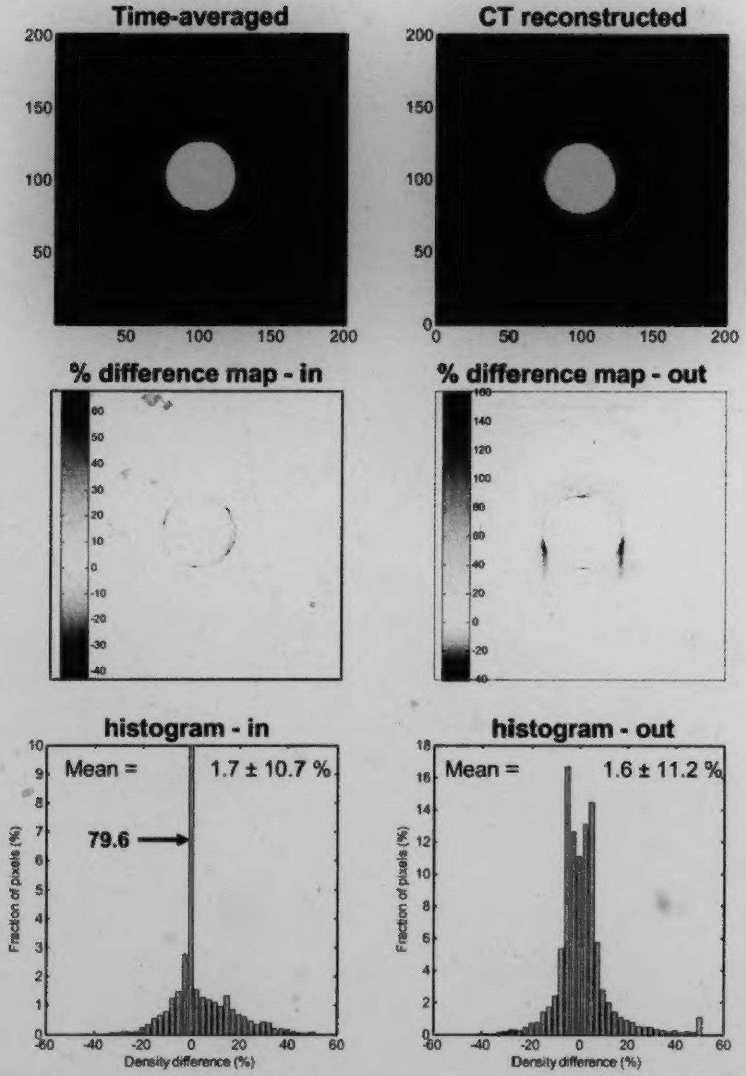

Figure 4.14 Time-averaged and CT reconstructed images along with TXO contours (dashed lines) for the medium sphere (diameter = 30 mm) undergoing a small SHM (A_x = Az = 5 mm) and imaged with a rapid 1 second acquisition time (alpha = 0.25). Also shown are the percent density difference maps within the TXO (% difference map – in) and within a 10 mm region surrounding the TXO (% difference map – out) along with their corresponding histograms (histogram – in, histogram – out).

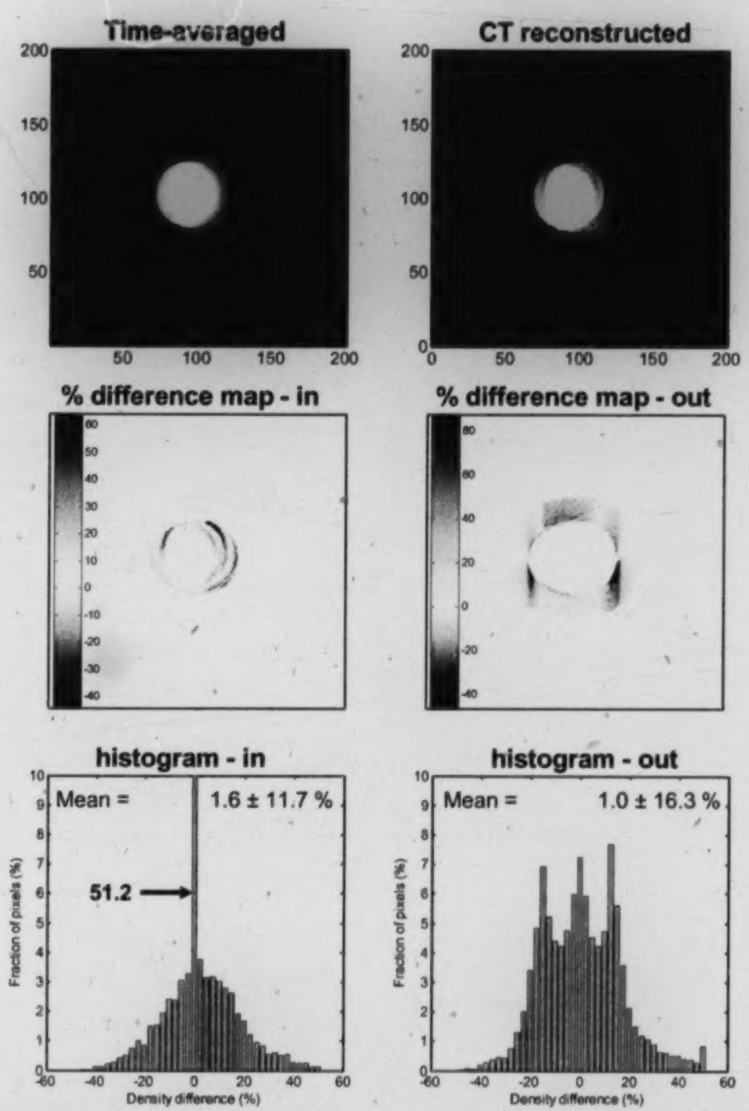

Figure 4.15 Time-averaged and CT reconstructed images along with TXO contours (dashed lines) for the medium sphere (diameter = 30 mm) undergoing an intermediate SHM ($A_x = Az = 15$ mm) and imaged with a rapid 1 second acquisition time (alpha = 0.25). Also shown are the percent density difference maps within the TXO (% difference map – in) and within a 10 mm region surrounding the TXO (% difference map – out) along with their corresponding histograms (histogram – in, histogram – out).

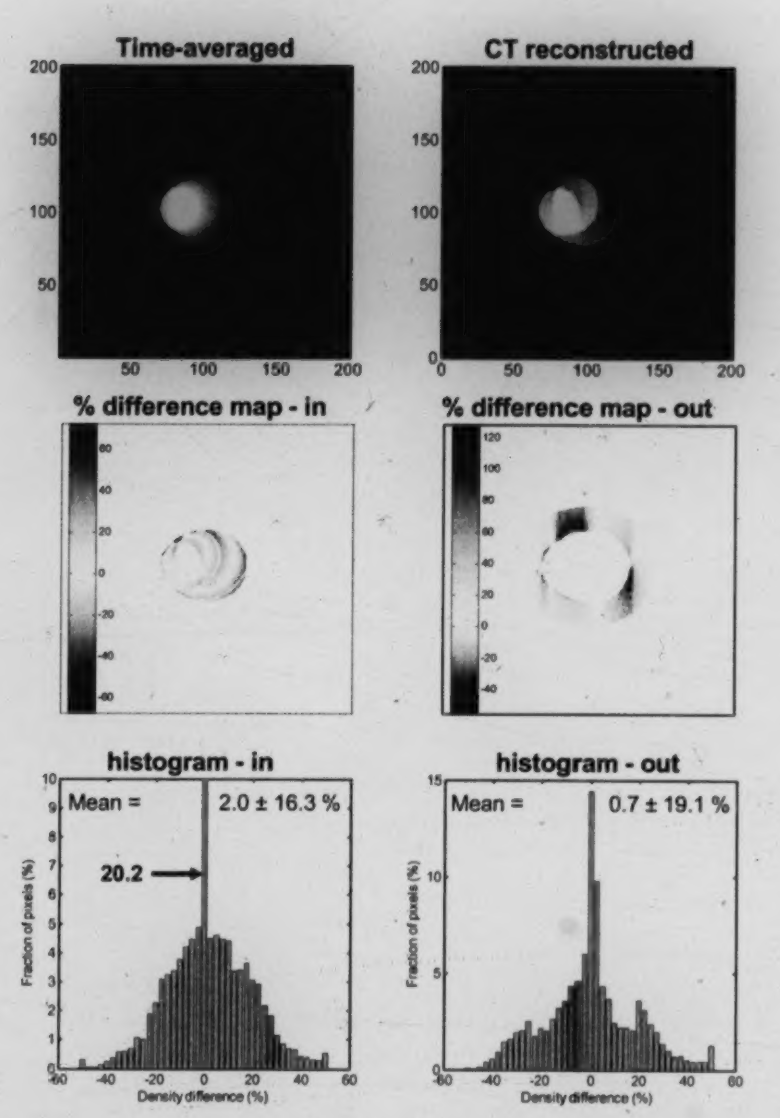

Figure 4.16 Time-averaged and CT reconstructed images along with TXO contours (dashed lines) for the medium sphere (diameter = 30 mm) undergoing a large SHM (A_x = Az = 25 mm) and imaged with a rapid 1 second acquisition time (alpha = 0.25). Also shown are the percent density difference maps within the TXO (% difference map – in) and within a 10 mm region surrounding the TXO (% difference map – out) along with their corresponding histograms (histogram – in, histogram – out).

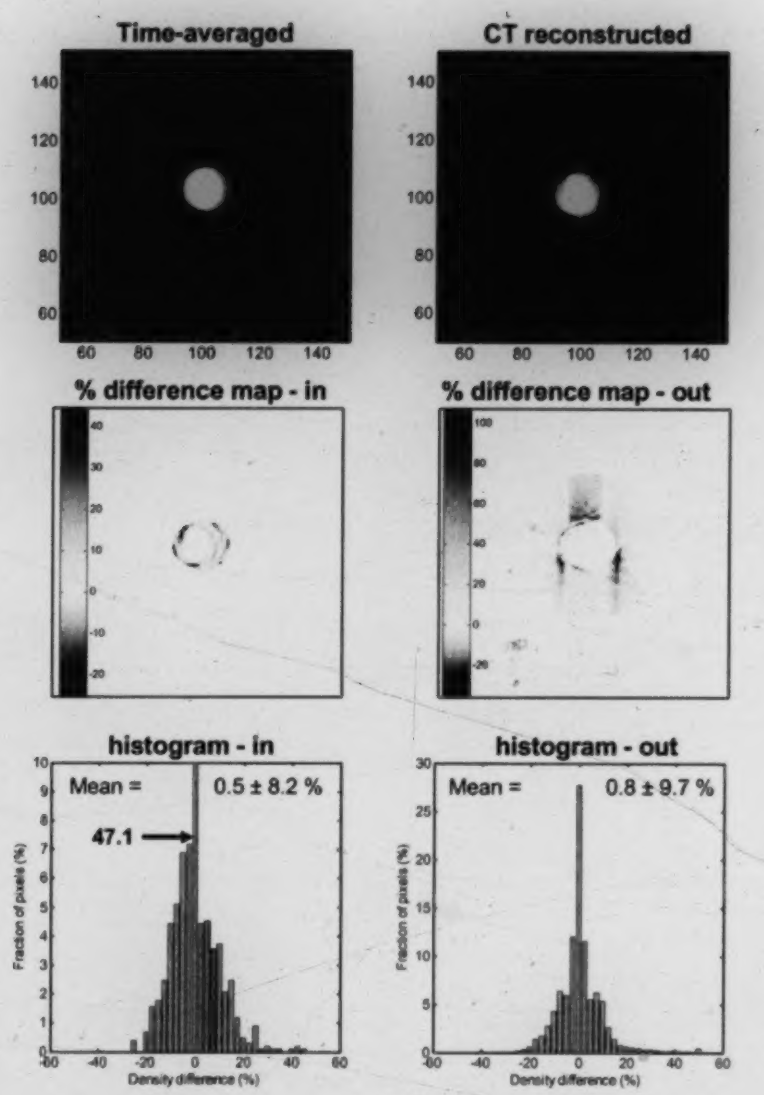

Figure 4.17 Time-averaged and CT reconstructed images along with TXO contours (dashed lines) for the small sphere (diameter = 10 mm) undergoing a small SHM (A_x = Az = 5 mm) and imaged with a rapid 1 second acquisition time (alpha = 0.25). Also shown are the percent density difference maps within the TXO (% difference map – in) and within a 10 mm region surrounding the TXO (% difference map – out) along with their corresponding histograms (histogram – in, histogram – out).

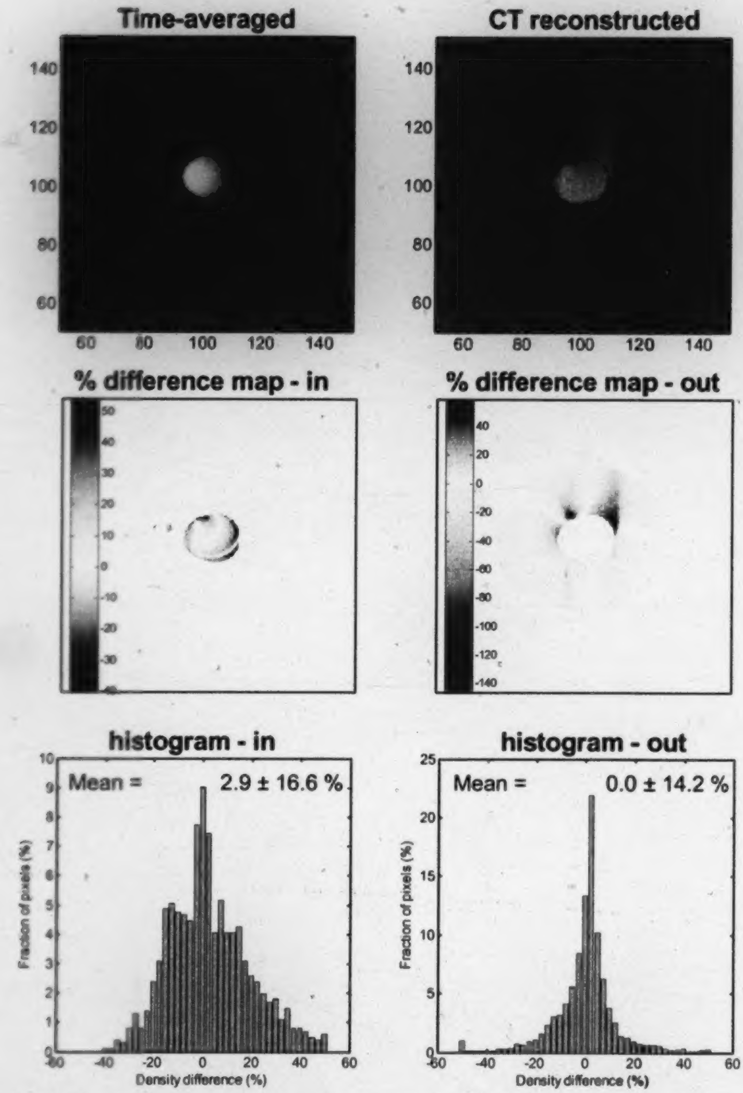

Figure 4.18 Time-averaged and CT reconstructed images along with TXO contours (dashed lines) for the small sphere (diameter = 10 mm) undergoing an intermediate SHM ($A_x = Az = 15$ mm) and imaged with a rapid 1 second acquisition time (alpha = 0.25). Also shown are the percent density difference maps within the TXO (% difference map – in) and within a 10 mm region surrounding the TXO (% difference map – out) along with their corresponding histograms (histogram – in, histogram – out).

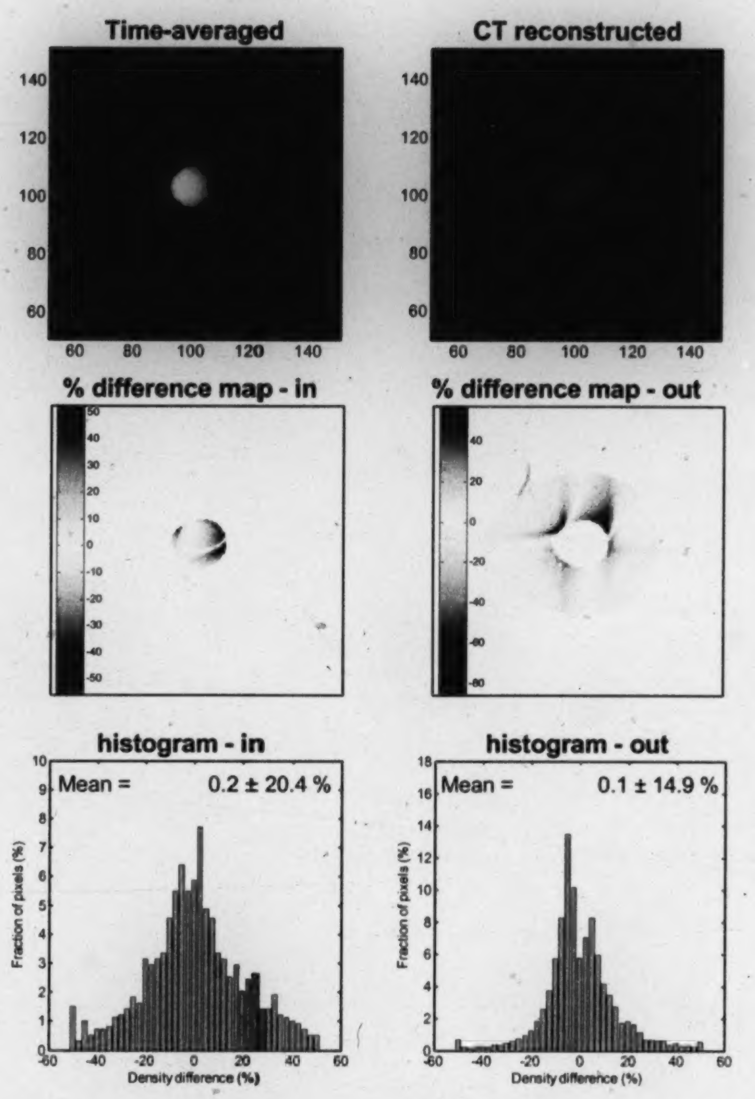

Figure 4.19 Time-averaged and CT reconstructed images along with TXO contours (dashed lines) for the small sphere (diameter = 10 mm) undergoing a large SHM (A_x = Az = 25 mm) and imaged with a rapid 1 second acquisition time (alpha = 0.25). Also shown are the percent density difference maps within the TXO (% difference map – in) and within a 10 mm region surrounding the TXO (% difference map – out) along with their corresponding histograms (histogram – in, histogram – out).

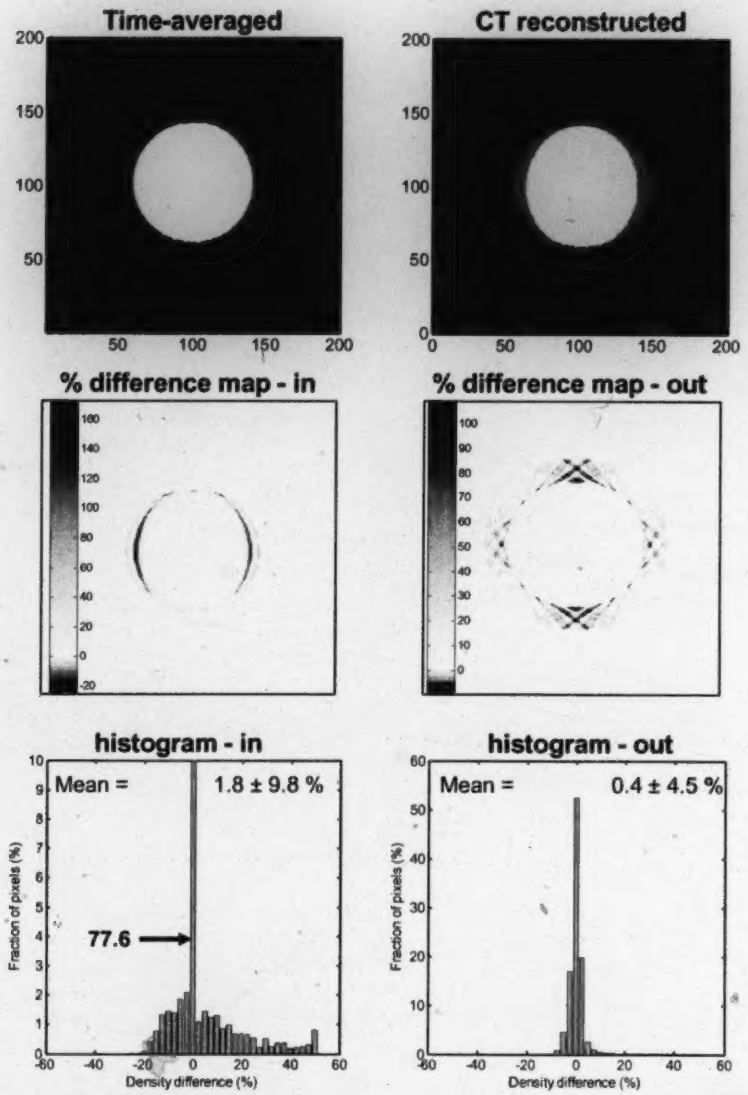

Figure 4.20 Time-averaged and CT reconstructed images along with TXO contours (dashed lines) for the large sphere (diameter = 50 mm) undergoing a small SHM (A_x = Az = 5 mm) and imaged with a 'slow' 4 second acquisition time (alpha = 1). Also shown are the percent density difference maps within the TXO (% difference map – in) and within a 10 mm region surrounding the TXO (% difference map – out) along with their corresponding histograms (histogram – in, histogram – out).

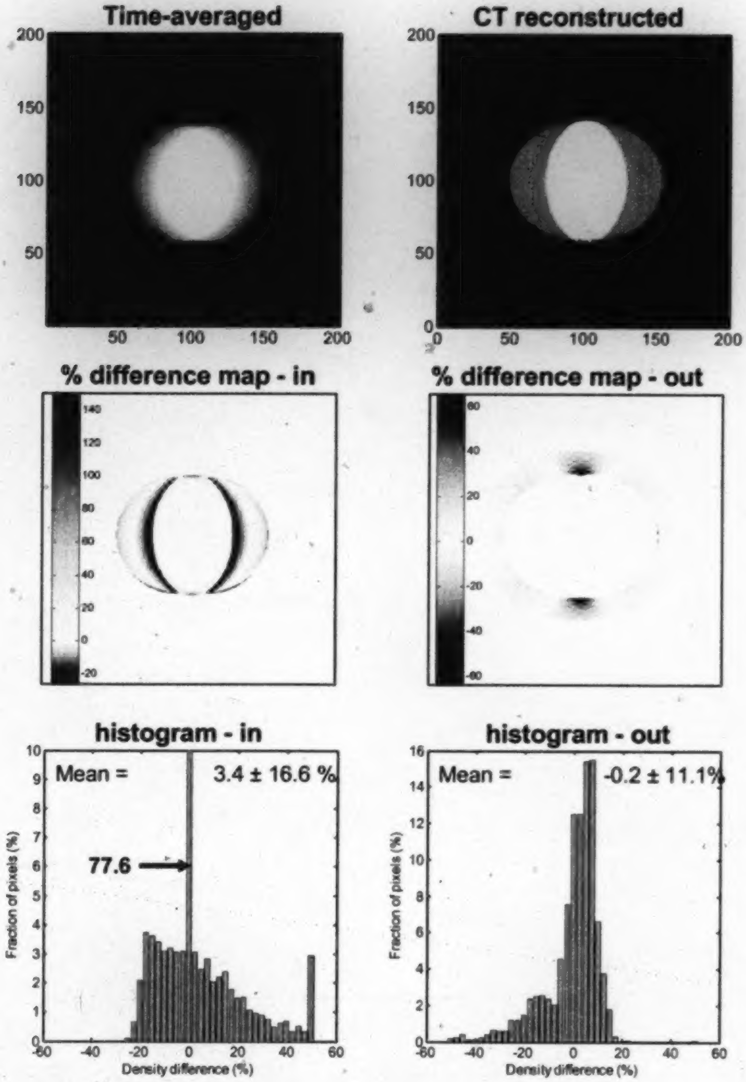

Figure 4.21 Time-averaged and CT reconstructed images along with TXO contours (dashed lines) for the large sphere (diameter = 50 mm) undergoing an intermediate SHM ($A_x = Az = 15$ mm) and imaged with a 'slow' 4 second acquisition time (alpha = 1). Also shown are the percent density difference maps within the TXO (% difference map – in) and within a 10 mm region surrounding the TXO (% difference map – out) along with their corresponding histograms (histogram – in, histogram – out).

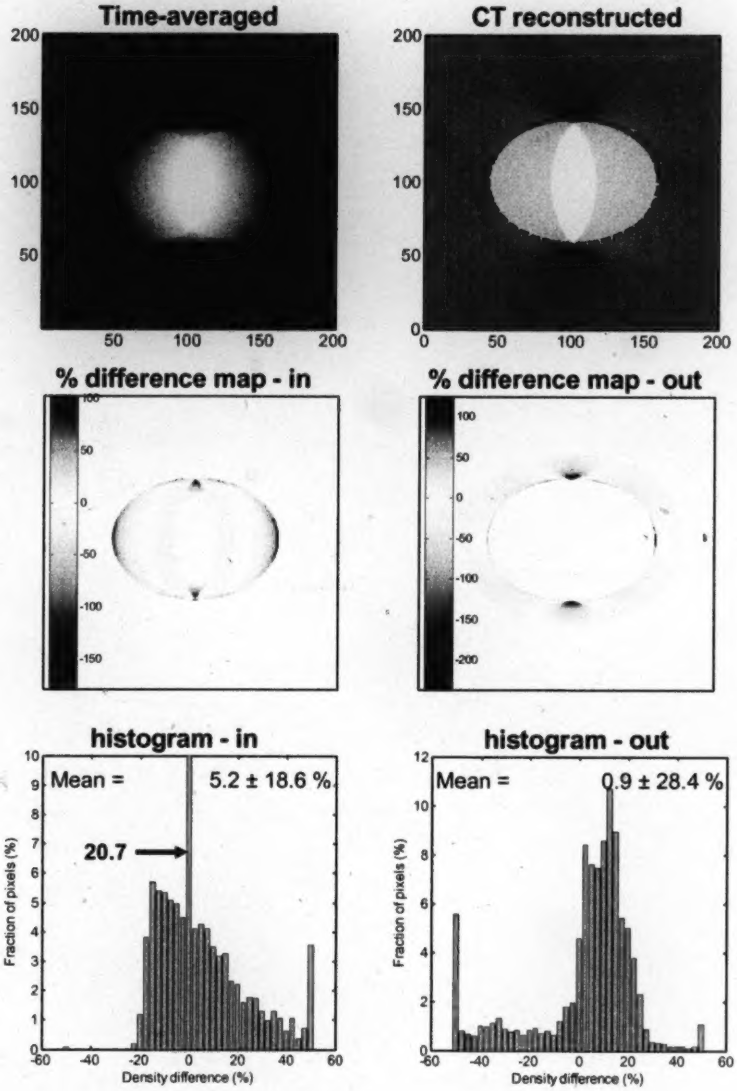

Figure 4.22 Time-averaged and CT reconstructed images along with TXO contours (dashed lines) for the large sphere (diameter = 50 mm) undergoing a large SHM (A_x = Az = 25 mm) and imaged with a 'slow' 4 second acquisition time (alpha = 1). Also shown are the percent density difference maps within the TXO (% difference map – in) and within a 10 mm region surrounding the TXO (% difference map – out) along with their corresponding histograms (histogram – in, histogram – out).

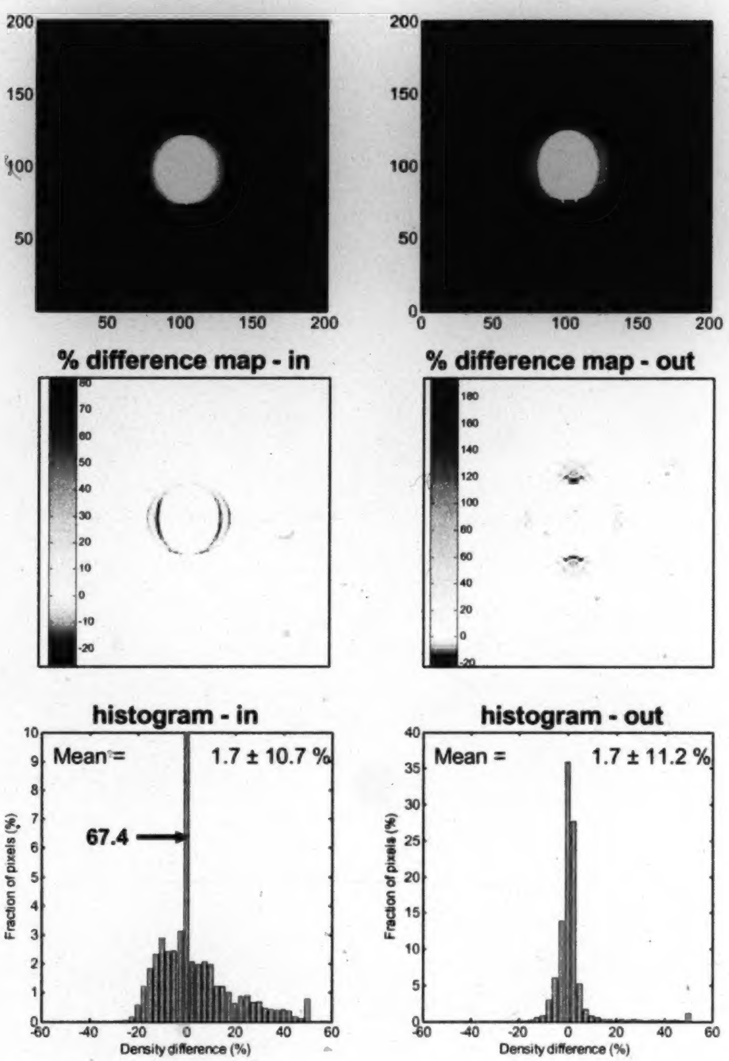

Figure 4.23 Time-averaged and CT reconstructed images along with TXO contours (dashed lines) for the medium sphere (diameter = 30 mm) undergoing a small SHM ($A_x = Az = 5$ mm) and imaged with a 'slow' 4 second acquisition time (alpha = 1). Also shown are the percent density difference maps within the TXO (% difference map – in) and within a 10 mm region surrounding the TXO (% difference map – out) along with their corresponding histograms (histogram – in, histogram – out).

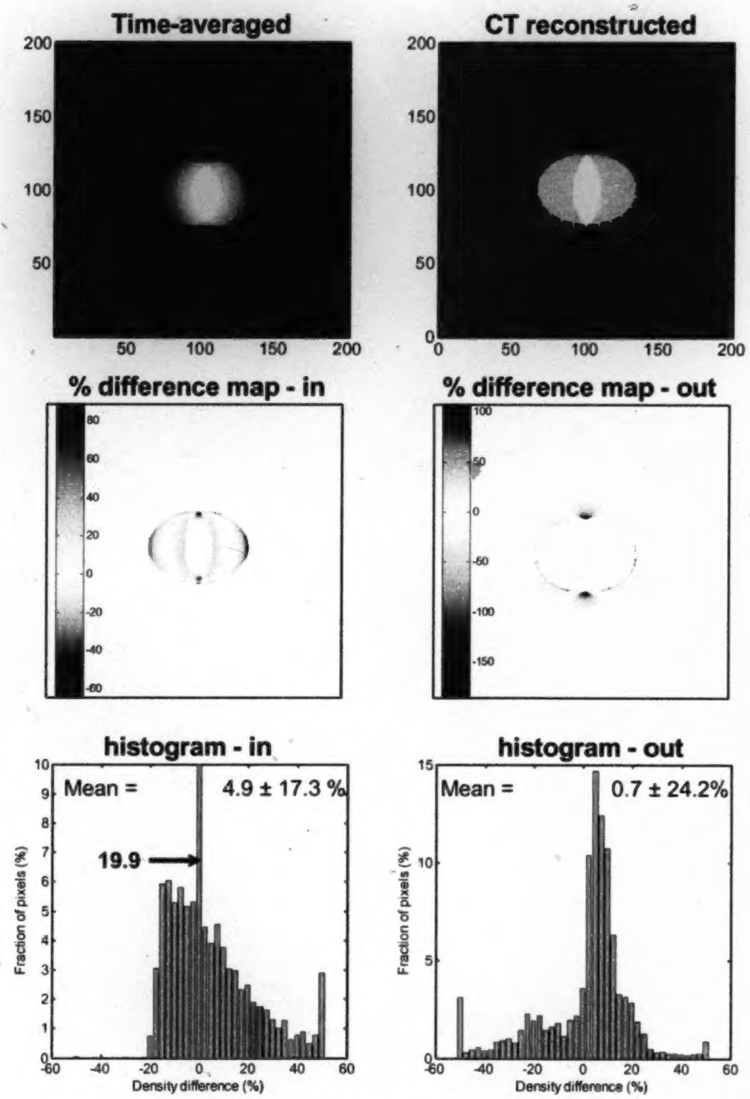

Figure 4.24 Time-averaged and CT reconstructed images along with TXO contours (dashed lines) for the medium sphere (diameter = 30 mm) undergoing an intermediate SHM ($A_x = Az = 15$ mm) and imaged with a 'slow' 4 second acquisition time (alpha = 1). Also shown are the percent density difference maps within the TXO (% difference map – in) and within a 10 mm region surrounding the TXO (% difference map – out) along with their corresponding histograms (histogram – in, histogram – out).

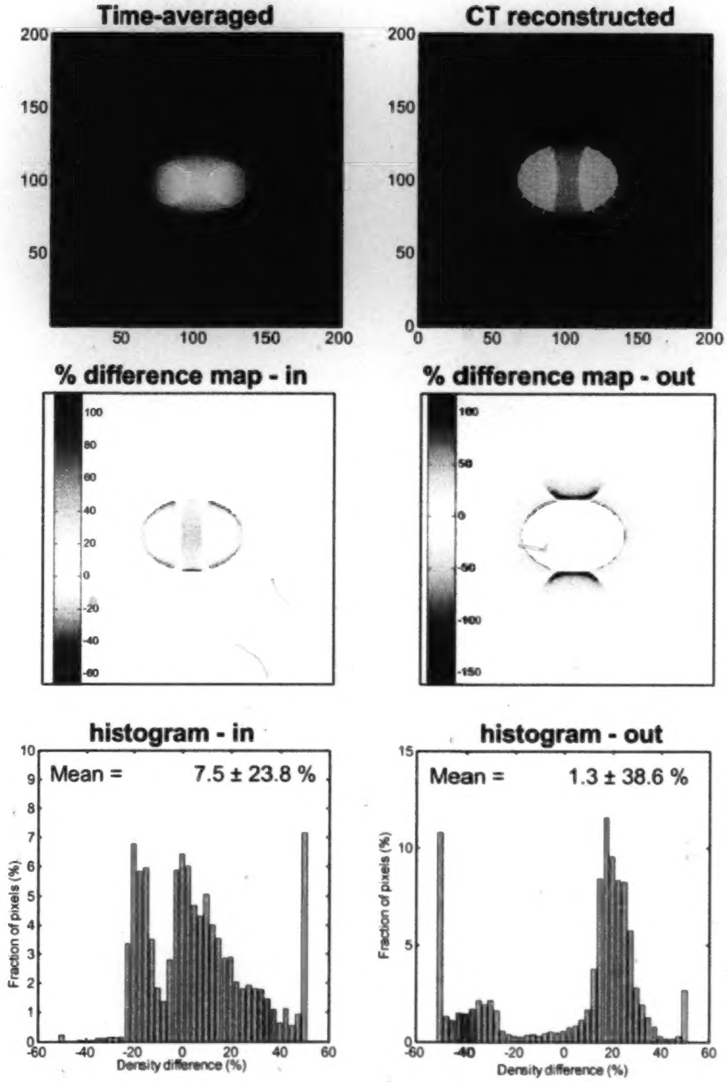

Figure 4.25 Time-averaged and CT reconstructed images along with TXO contours (dashed lines) for the medium sphere (diameter = 30 mm) undergoing a large SHM (A_x = Az = 25 mm) and imaged with a 'slow' 4 second acquisition time (alpha = 1). Also shown are the percent density difference maps within the TXO (% difference map – in) and within a 10 mm region surrounding the TXO (% difference map – out) along with their corresponding histograms (histogram – in, histogram – out).

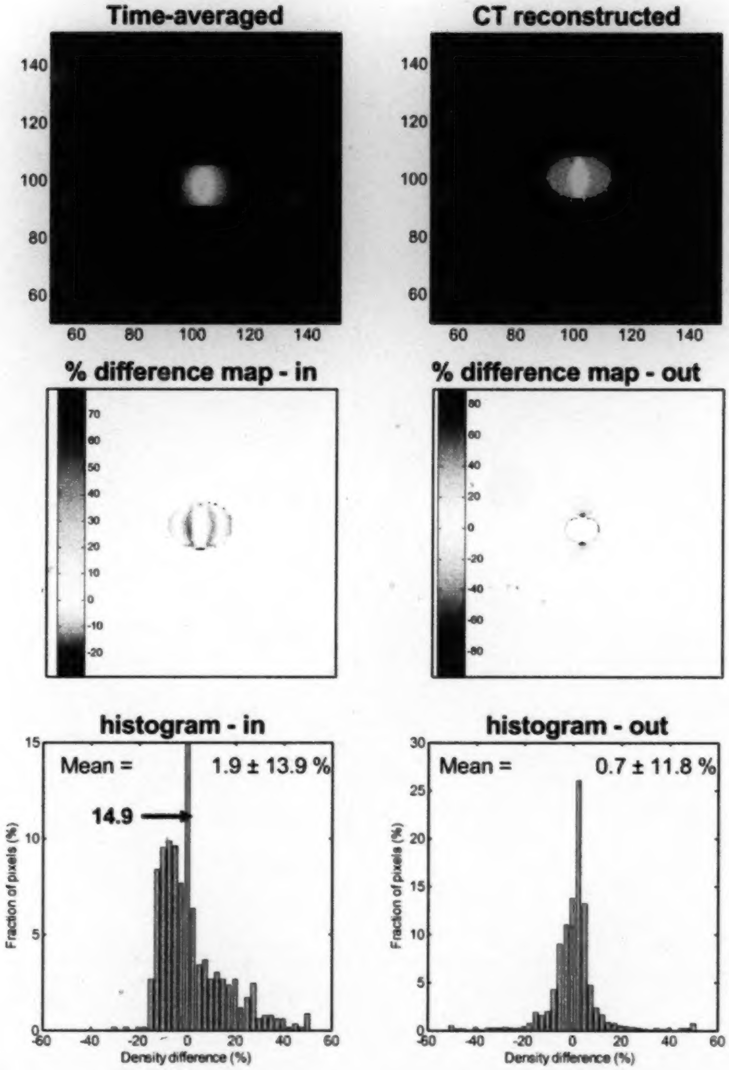

Figure 4.26 Time-averaged and CT reconstructed images along with TXO contours (dashed lines) for the small sphere (diameter = 10 mm) undergoing a small SHM (A_x = Az = 5 mm) and imaged with a 'slow' 4 second acquisition time (alpha = 1). Also shown are the percent density difference maps within the TXO (% difference map – in) and within a 10 mm region surrounding the TXO (% difference map – out) along with their corresponding histograms (histogram – in, histogram – out).

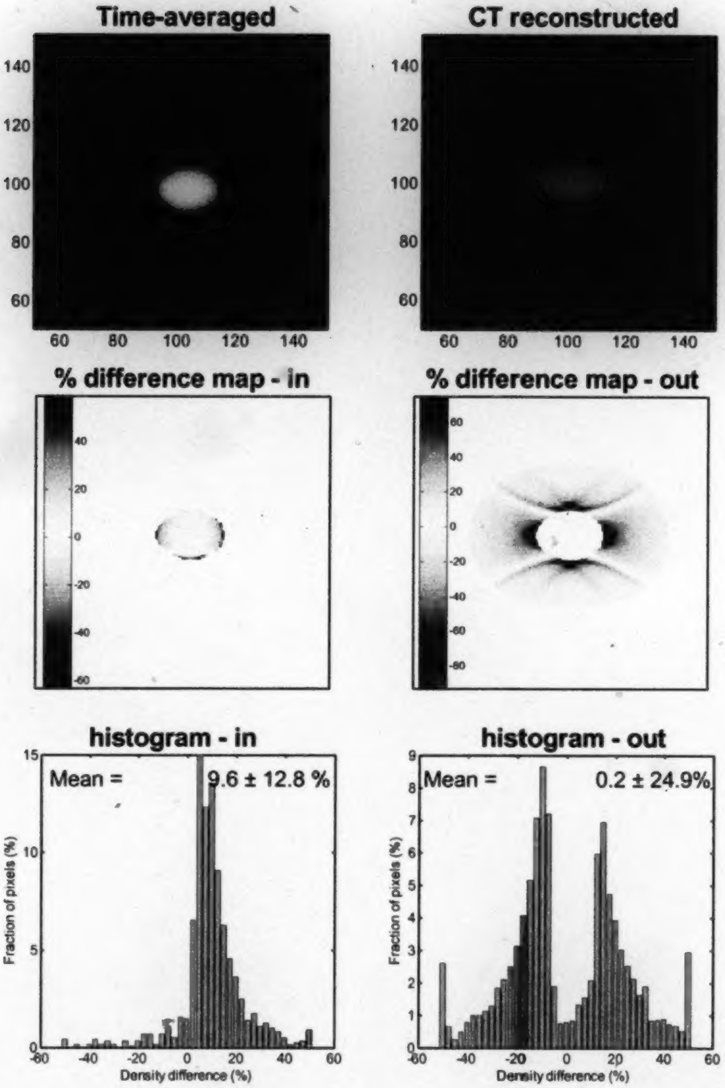

Figure 4.27 Time-averaged and CT reconstructed images along with TXO contours (dashed lines) for the small sphere (diameter = 10 mm) undergoing an intermediate SHM ($A_x = Az$ = 15 mm) and imaged with a 'slow' 4 second acquisition time (alpha = 1). Also shown are the percent density difference maps within the TXO (% difference map – in) and within a 10 mm region surrounding the TXO (% difference map – out) along with their corresponding histograms (histogram – in, histogram – out).

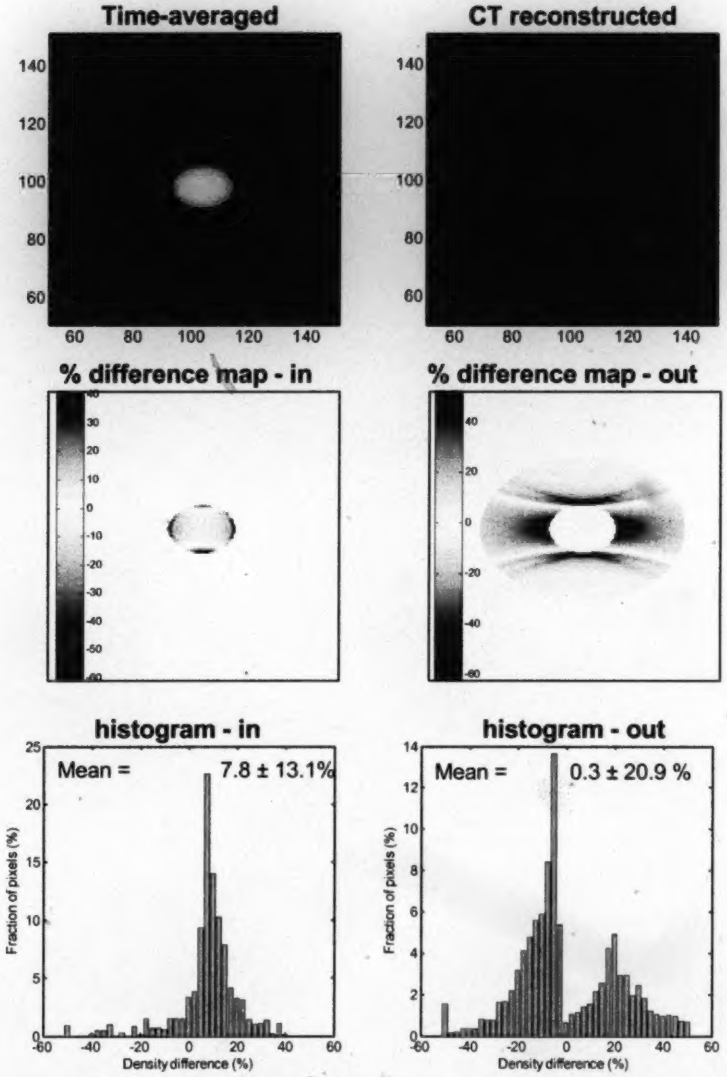

Figure 4.28 Time-averaged and CT reconstructed images along with TXO contours (dashed lines) for the small sphere (diameter = 10 mm) undergoing a large SHM (A_x = Az = 25 mm) and imaged with a 'slow' 4 second acquisition time (alpha = 1). Also shown are the percent density difference maps within the TXO (% difference map – in) and within a 10 mm region surrounding the TXO (% difference map – out) along with their corresponding histograms (histogram – in, histogram – out).

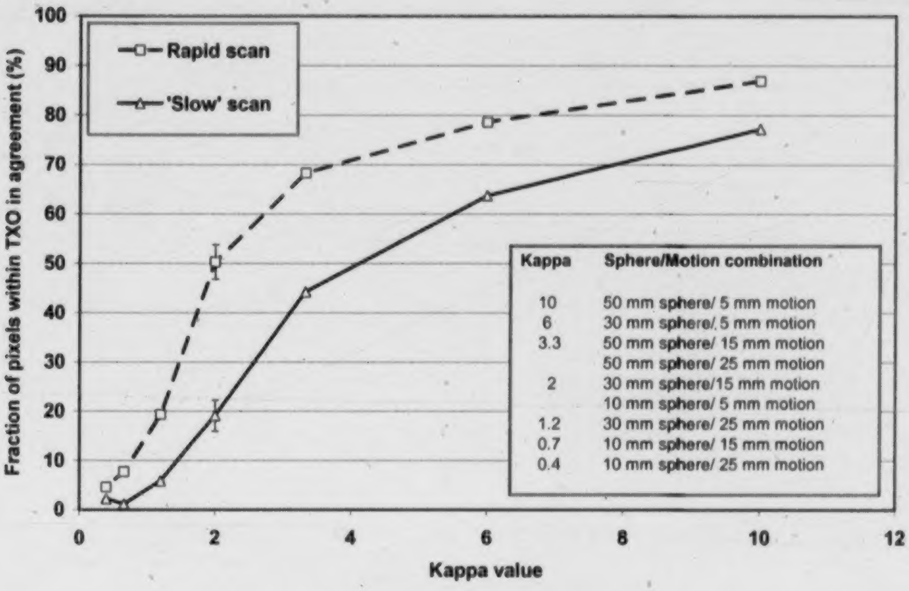

Figure 4.29 Fraction of pixels within the TXO in agreement. Agreement, in this case, is deemed to exist when CT pixel densities deviate by no more than 1 % from their corresponding time-average pixel densities.

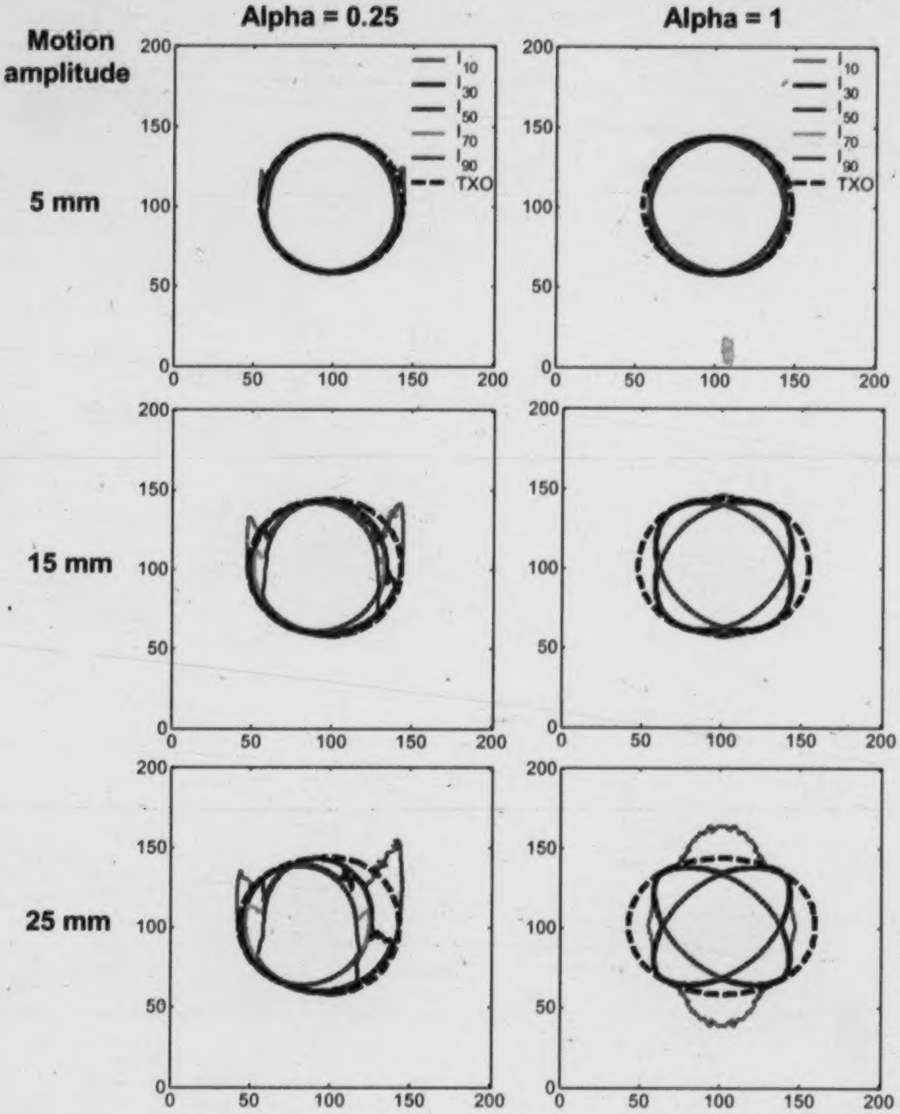

Figure 4.30 Segmentation results for the largest sphere (diameter = 50 mm) undergoing a SHM of various amplitudes during CT scanning. For visualization purposes, only five iso-intensity contours [I_{10}, I_{30}, I_{50}, I_{70}, I_{90}] are presented along with the TXO contour. (Note: I_{100} corresponds to the static lung tumor density (0.90 g/cm^3) while I_0 corresponds to the background density (0.25 g/cm^3)).

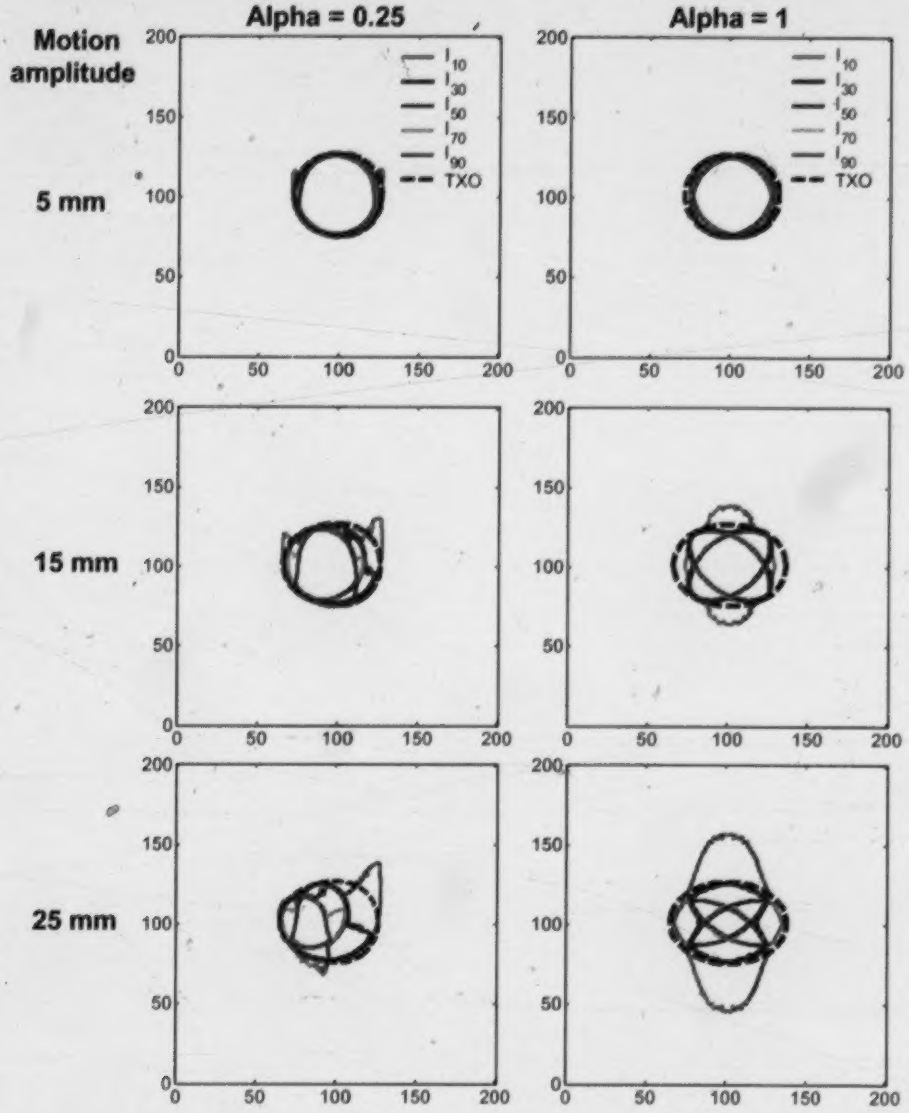

Figure 4.31 Segmentation results for the intermediate sphere (diameter = 30 mm) undergoing a SHM of various amplitudes during CT scanning. For visualization purposes, only five iso-intensity contours [I_{10}, I_{30}, I_{50}, I_{70}, I_{90}] are presented along with the TXO contour. (Note: I_{100} corresponds to the static lung tumor density (0.90 g/cm^3) while I_0 corresponds to the background density (0.25 g/cm^3)).

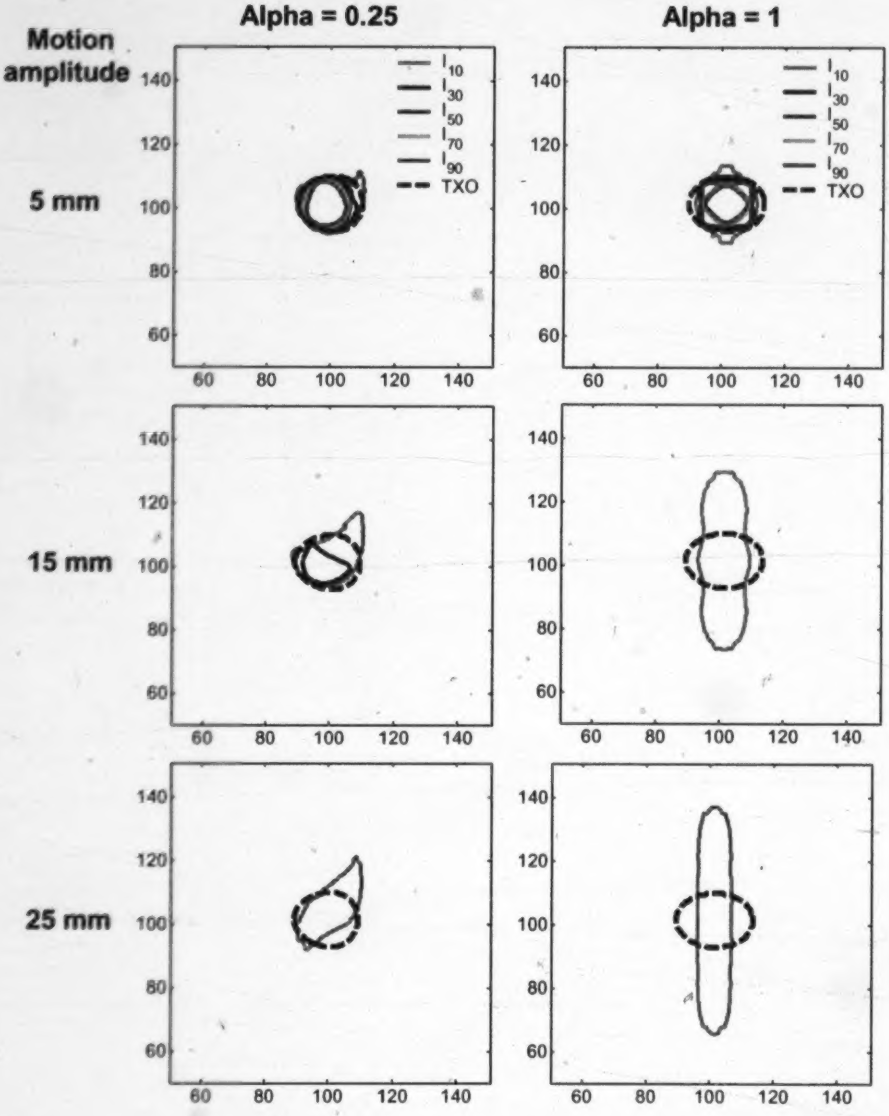

Figure 4.32 Segmentation results for the small sphere (diameter = 10 mm) undergoing a SHM of various amplitudes during CT scanning. For visualization purposes, only five iso-intensity contours [I_{10}, I_{30}, I_{50}, I_{70}, I_{90}] are presented along with the TXO contour. (Note: I_{100} corresponds to the static lung tumor density (0.90 g/cm^3) while I_0 corresponds to the background density (0.25 g/cm^3)).

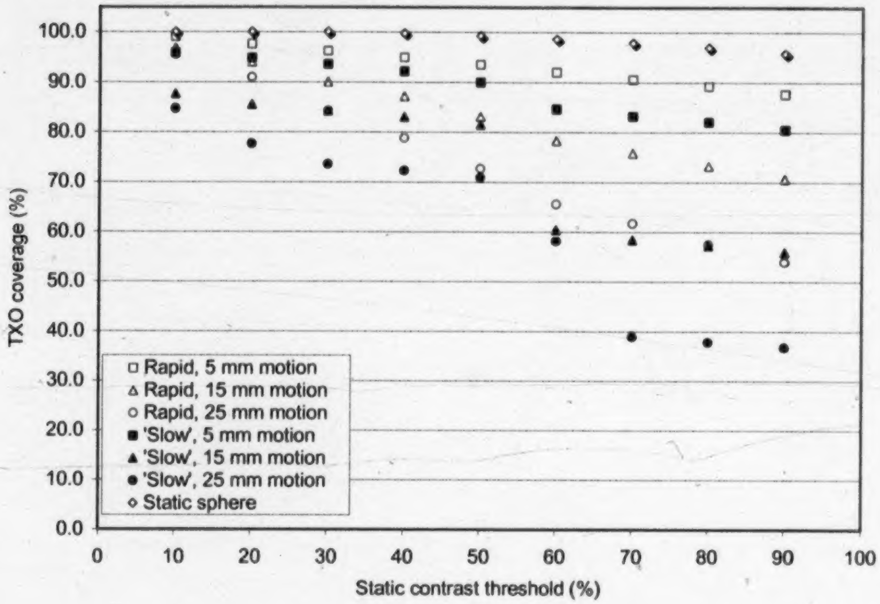

Figure 4.33 Percentage of TXO covered by the iso-intensity contours for the largest sphere (diameter = 50 mm) undergoing a SHM of various amplitudes during rapid and 'slow' CT scanning.

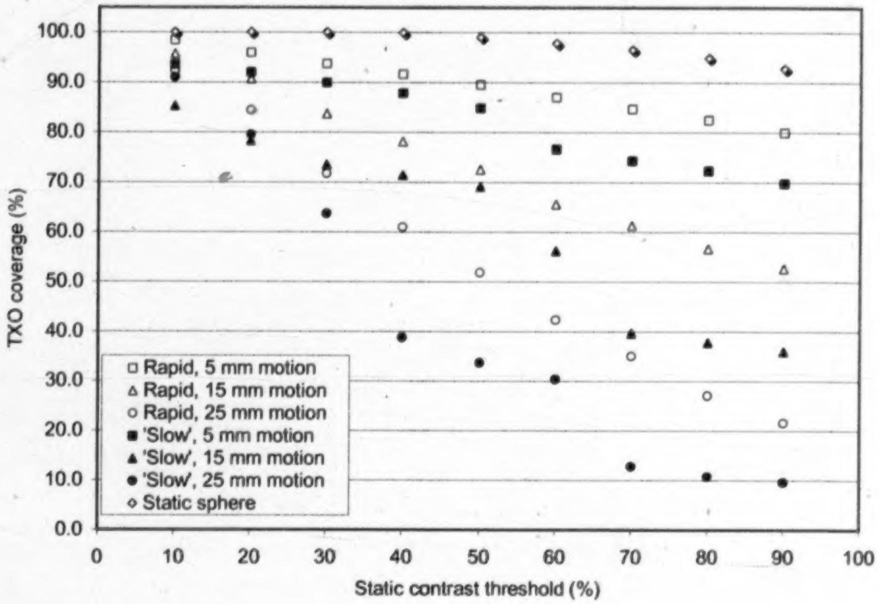

Figure 4.34 Percentage of TXO covered by the iso-intensity contours for the intermediate sphere (diameter = 30 mm) undergoing a SHM of various amplitudes during rapid and 'slow' CT scanning.

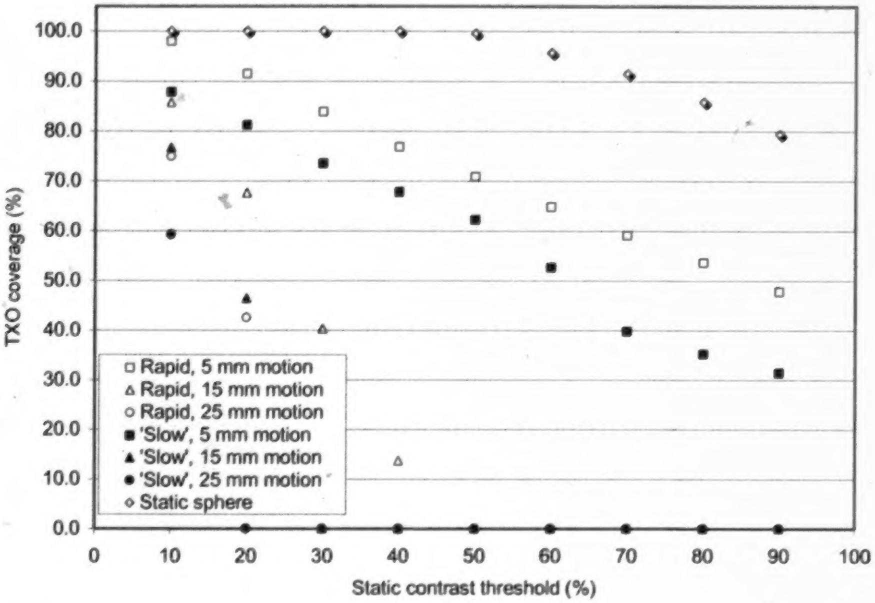

Figure 4.35 Percentage of TXO covered by the iso-intensity contours for the smallest sphere (diameter = 10 mm) undergoing a SHM of various amplitudes during rapid and 'slow' CT scanning.

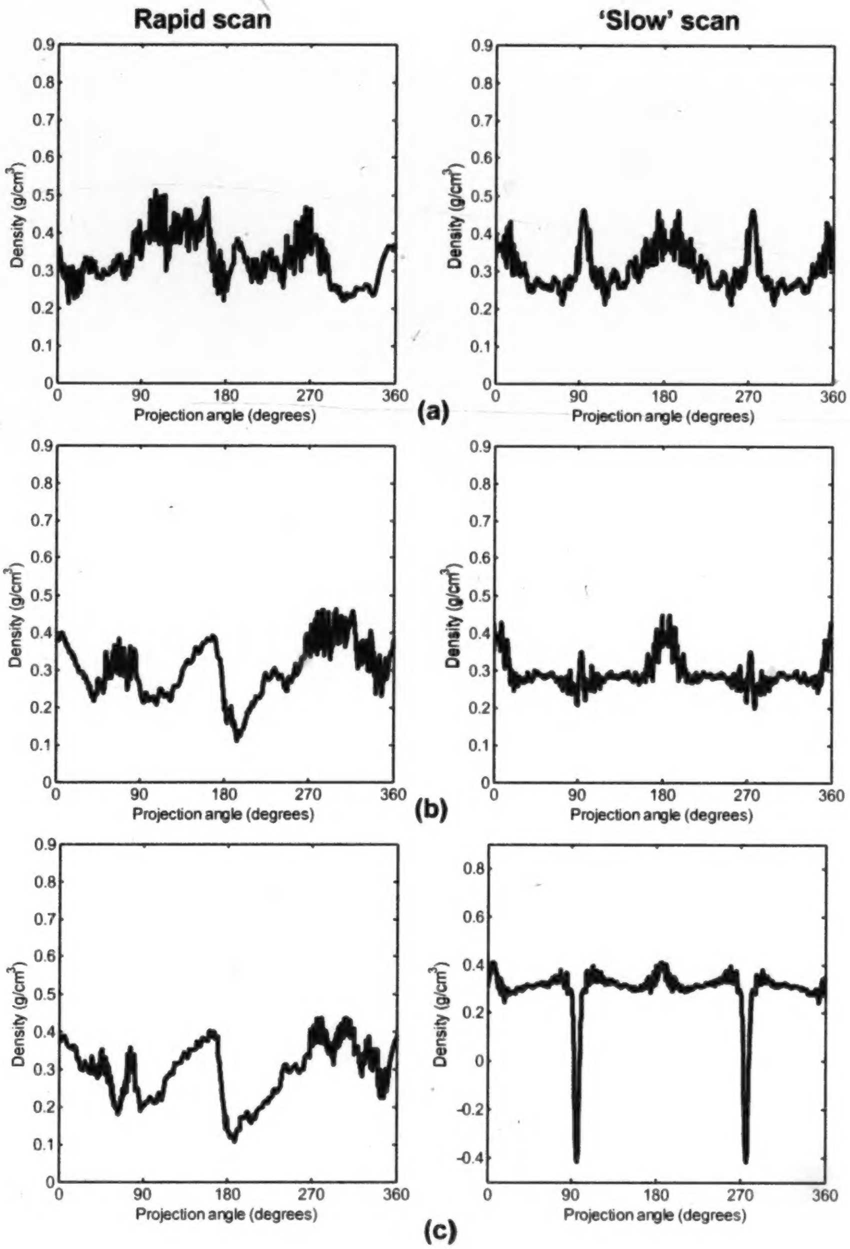

Figure 4.36 Density along the rapid and 'slow' TXO contours for the largest sphere (diameter = 50 mm) undergoing a SHM of various amplitudes during CT scanning: (a) 5 mm, (b) 15 mm, and (c) 25 mm.

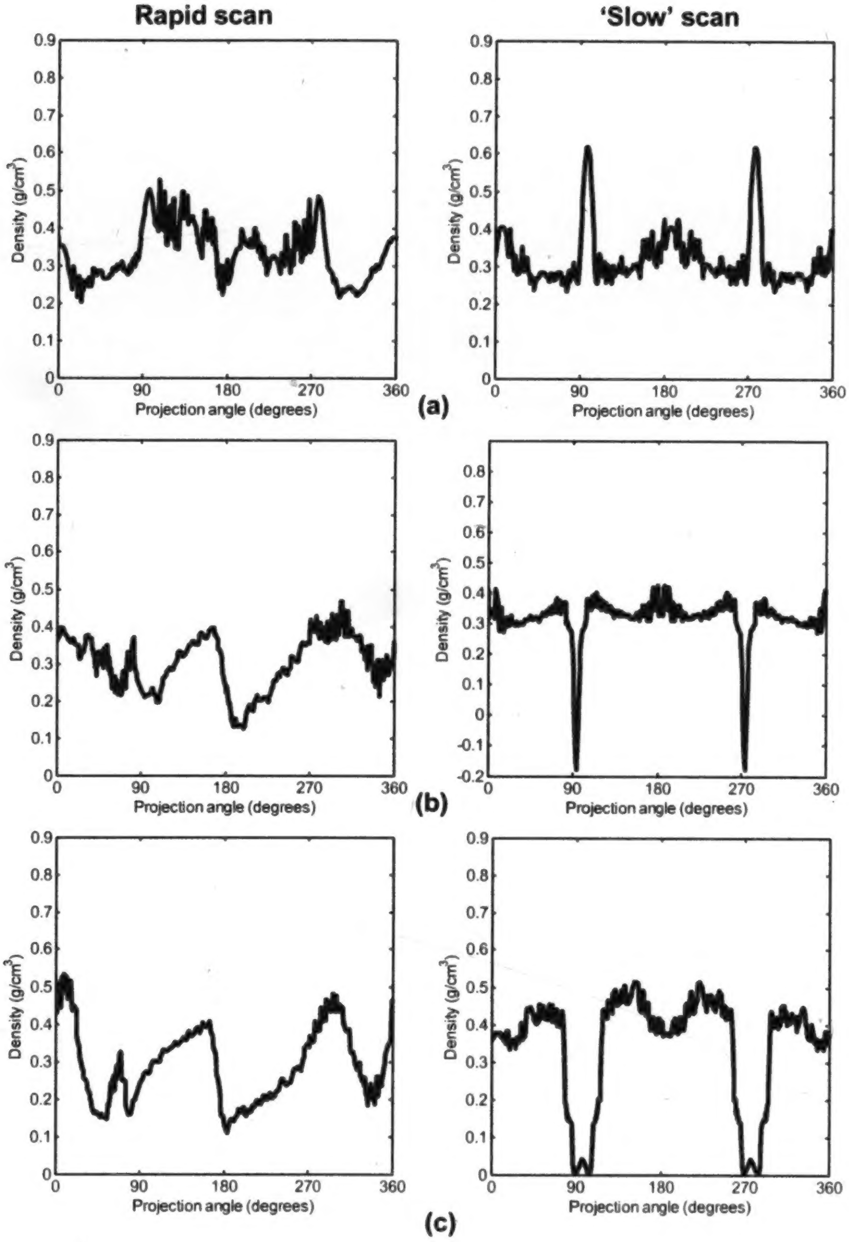

Figure 4.37 Density along the rapid and 'slow' TXO contours for the intermediate sphere (diameter = 30 mm) undergoing a SHM of various amplitudes during CT scanning: (a) 5 mm, (b) 15 mm, and (c) 25 mm.

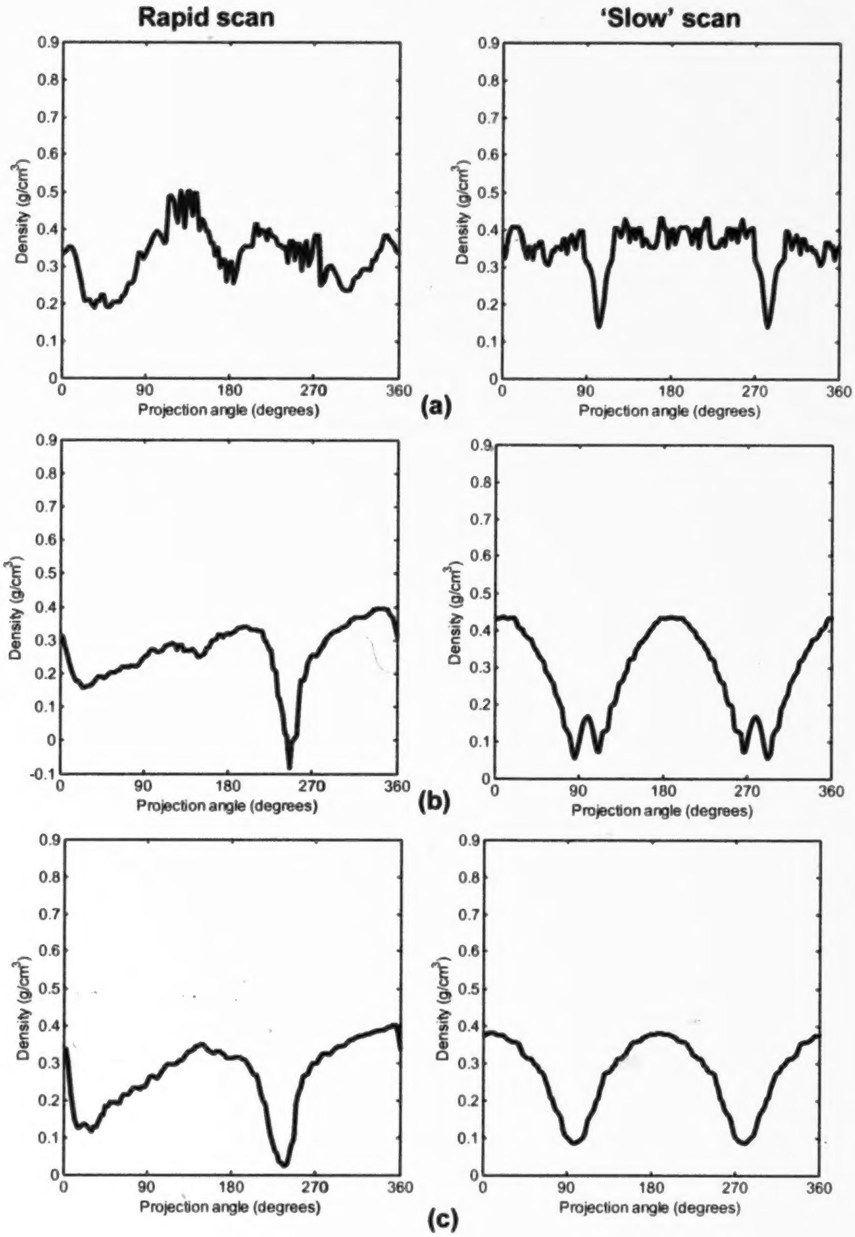

Figure 4.38 Density along the rapid and 'slow' TXO contours for the smallest sphere (diameter = 10 mm) undergoing a SHM of various amplitudes during CT scanning: (a) 5 mm, (b) 15 mm, and (c) 25 mm.

4.5 References

[Ba 1998] J. Balter, K. Lam, C. McGinn, *et al.*, "Improvement of CT-based treatment-planning models of abdominal targets using static exhale imaging," Int. J. Radiat. Oncol. Biol. Phys. **41**, 939 – 943 (1998)

[Ba 1996] J. Balter, R. Ten Haken, T. Lawrence, *et al.*, "Uncertainties in CT-based radiation therapy treatment planning associated with patient breathing," Int. J. Radiat. Oncol. Biol. Phys. **36**, 167 – 174 (1996)

[Bl 1981] S.M. Blumenfeld and G.H. Glover, "Spatial Resolution in Computed Tomography," in Radiology of the skull and brain: Technical aspects of computed tomography, edited by T.H. Newton and D.G. Potts, The C.V. Mosby Company, London (1981) pp. 3835 – 3849

[Ch 1998] E.L. Chaney, D.S. Fritsch and S.M. Pizer, "Objective GTV and normal structure segmentation," AAPM Monogr. No. 24, 271 – 290 (1998)

[Ch 1992] E. Chaney and S. Pizer "Defining anatomical structures from medical images," Semin. Radiat. Oncol. **2**, 215 – 255 (1992)

[Ch 2004] G.T.Y. Chen, J.H. Kung, and K.P. Beaudette, "Artifacts in computed tomography scanning of moving objects," Semin. Radiat. Oncol. **14**, 19 – 26 (2004)

[Go 1983] M. Goitein and M. Abrams, "Multi-dimensional treatment planning: I. Delineation of anatomy," Int. J. Radiat. Oncol. Biol. Phys. **9**, 777 – 787 (1983)

[Ha 1991] B.H. Hasegawa, *The physics of medical x-ray imaging*, 2nd Edition, Medical Physics Publishing, Madison, Wisconsin (1991)

[Ka 2000] W.A. Kalender, Computed tomography: fundamentals, system technology, image quality, applications, Publicis MCD Werbeagentur GmbH, Munich (2000)

[Ke 2004] P.J. Keall, "Acquiring 4D thoracic CT scans using a multislice helical method," Phys. Med. Biol. 49, 2053 – 2067 (2004)

[Ke 1991] P.J. Kelly, *Tumor Stereotaxis*, W.B. Saunders, Philadelphia (1991)

[Lu 2003] Q. Luo, "Artifacts in X-ray CT," http://ric.uthscsa.edu/personalpages/lancaste/DI2_Projects_2003/XrayCT_artifacts.pdf (2003)

[Mo 1983] C.L. Morgan, *Basic Principles of Computed Tomography*, University Park Press, Baltimore (1983)

[Pe 1992] D.J. Peck, J.P. Windham, H. Soltanian *et al.*, "A fast and accurate algorithm for volume determination in MRI," Med. Phys. 49, 599 – 605 (1992)

[Sp 1994] P. Sprawls, "X-ray imaging concepts: Basic considerations," AAPM Monogr. No. **20**, 41-74 (1994)

[Tr 1994] G. Tracton, E.L. Chaney, J.G. Rosenman, *et al.*, "MASK: Combining 2D and 3D segmentation methods to enhance functionality," SPIE Proc. 2299, 98 – 109 (1994)

Chapter 5: Phase sequence imaging to reveal the total volume occupied by mobile lung tumors

5.1 Introduction

As clearly indicated in Chapter 1, there is a pressing need for more accurate methods of determining field shapes which will provide adequate tumor coverage while sparing as much as possible surrounding critical structures for situations in which physiologic motion can neither be eliminated nor discounted and for which gating techniques are neither available nor applicable.

In this chapter, a slice-specific imaging technique is presented which provides a direct assessment of the extent of free-breathing tumor motion without recourse to gating techniques. This is accomplished by acquiring a phase sequence image (PSI) set, consisting of consecutive rapid CT images, at each slice location throughout the target volume during free-breathing. Each image constituting a PSI set thus captures the tumor at a different phase in its motion at a single cranio-caudal position. The phase relationship between the images of a given PSI set is provided by the duty cycle of the scanner. Sampling the motion phase space in this manner allows one to approximate the total volume occupied (TVO) by a tumor during the totality of its travel according to the following scheme. A clinical target volume (CTV) is defined for each image of a PSI set. Forming a composite clinical target volume (CCTV) contour from the union of CTV contours for a given a PSI set estimates the total cross-sectional area (TXO) presented by the tumor during the course of its motion at that slice location.

The CCTV approximates the total volume occupied (TVO) by the mobile tumor during the course of its travel and is constructed from the CCTV contours from all slice locations at which the tumor is present. By forming the union of contours provided by each element of a PSI set, the need to define phase relationships between images at different slice locations is eliminated. The CCTV defined in this manner yields a slice by slice determination of the total volume occupied by a mobile tumor.

5.2 Background

Consider an imaging sequence wherein acquisition begins at $t = t_i$ and requires a time interval δt to complete. This is followed by a non-imaging interval of ΔT prior to the onset of the next image acquisition. This pattern repeats until all images of the sequence are acquired. Each image in this PSI set spans a phase interval $\Delta\phi$ and is centered about the phase angle ϕ_n given by

$$\Delta\phi = 2\pi \frac{\delta t}{\tau_m} \tag{5.1}$$

and

$$\phi_n = \phi(t_i) + \frac{2\pi}{\tau_m}\left[\frac{\delta t}{2} + (n-1)(\Delta T + \delta t)\right] \tag{5.2}$$

where $n = 1, 2, 3, \ldots$, and τ_m = motion period of target (tumor). For example, let a tumor undergoing a simple harmonic motion with a free-breathing period of 4 seconds be imaged with a scanning sequence consisting of 10 full rotation acquisitions of duration $\delta t = 1$ sec, each separated by $\Delta T = 1.35$ sec (a standard default setting on the scanner used in this investigation). If the phase angle of the first image is ϕ_1, the subsequent 9 images of this PSI set will sample the motion phase space at $\phi_1 + 22.5^\circ$, $\phi_1 + 85.5^\circ$, $\phi_1 + 108.0^\circ$, $\phi_1 + 148.5^\circ$, $\phi_1 + 171.0^\circ$, $\phi_1 + 234.0^\circ$, $\phi_1 + 256.5^\circ$, $\phi_1 + 297.0^\circ$, and $\phi_1 + 319.5^\circ$. Each element of this PSI set will span a phase interval of $\pi/2$ or 90°. Care must be taken, however, to avoid sample clustering. For example, the above imaging sequence in combination with a motion period of 3.52 seconds produces a sampling yielding only three distinct elements, four of $\phi_1 + 51.064^\circ$, and three each of $\phi_1 + 171.064^\circ$ and $\phi_1 + 291.064^\circ$. This unfortunate circumstance can be easily avoided by choosing a different (δt, ΔT) combination. Patient respiration rate must thus be determined prior to imaging using fluoroscopy or some other means.

5.3 Methods and materials

5.3.1 Phantom study

The validity of the proposed CCTV approach is demonstrated by means of a phantom study employing simple geometric objects following well-defined trajectories. Doing so eliminates the uncertainties associated with a clinical assessment (e.g. uncertainties in both the physical extent of the tumor and its exact pattern of motion) and makes possible a rigorous comparison of the experimental CCTV to the actual or true total volume occupied (TVO) by the mobile target. For illustrative purposes, a simplified example, in which motion is constrained to the scanning plane, is initially presented. This is then followed by an assessment of more realistic motions for a more clinically relevant tumor shape and size. The investigation concludes with a demonstration of the practical application of the CCTV technique using clinical data.

A uniform cylinder constructed of POM (polyoxymethylene, an acetal homopolymer), with a 10 mm diameter, was used to illustrate the concept of the CCTV technique. The cylinder was oriented with its long axis orthogonal to the imaging plane and subjected to simple harmonic motion with a 25 mm amplitude along the horizontal *x*-axis.

In clinical situations, a large range of respiration-induced tumor motions is observed for tumors varying in size from the miniscule to the very large. For the purposes of this investigation, a 25 mm diameter POM sphere, representative of a medium sized tumor, served as a mobile target for the assessment of the CCTV technique. Three respiration-induced tumor motions were considered; small, intermediate and large simulating good, moderate and poor clinical scenarios, respectively. Simple harmonic motion along the *x*- (horizontal) and *z*- (longitudinal) axes, each with a period of 4 seconds and amplitudes of either 5, 15 or 25 mm, define the small, intermediate and large trajectories of the spherical test object.

Ten element PSI sets, obtained using full rotation acquisitions of $\delta t = 1$ s duration, each separated by $\Delta T = 1.35$ s, were acquired for each of the above (target, motion) combinations using a Picker PQ5000 CT scanner (Philips Medical Systems). Physical motion was provided by a set of tri-axial translation plates each actuated by cam follower drive mechanisms. Motion along each axis is governed by a separate cam. All three cams are driven by a single variable speed electric motor. The phase of motion along each axis is governed by the orientation of the individual cams with respect to one another.

All phantom studies are carried out in air for maximum contrast between mobile object and surrounding background. Individual CTV contours are defined according to iso-contrast threshold levels. A contrast level of 100 % corresponds to the density difference between the surrounding air medium and the static POM sphere or cylinder. All CT images are displayed using a level of –350 HU and a window of 1300 HU to reflect what one might expect to see under clinical viewing conditions. To aid visibility, all CT images are cropped to the central 201 X 201 pixels.

5.1.2 Clinical application

One patient was recruited and did consent to take part in a study of the clinical application of the CCTV technique. This patient presented with an intraparenchymal tumor fully circumscribed by lung. According to current institute clinical practice, this patient was initially examined using fluoroscopy in treatment position in order to estimate the superior-inferior (SI) boundaries of tumor motion. The location of these boundaries, as indicated by fluoroscopy, was marked on the patient's skin using external markers (wires). Definitive superior-inferior tumor motion boundaries were then identified using CT by first acquiring ten axial images in rapid succession (1 sec/rot, 2 mm slice thickness) at each boundary location as indicated by the skin markers. If any of the images revealed evidence of tumor, additional sets of 10 sequential images were acquired every 2 mm, moving outward from tumor center, until tumor was absent in all 10 scans. If the tumor was found to be absent in the initial set of CT images, the above procedure was carried out in an inward moving fashion. These boundary positions also serve to define the superior and inferior extents of the volume of interest. Once the superior and inferior tumor motion boundaries were accurately determined, the impact of internal tumor motion was evaluated by acquiring 10 element PSI sets (1 sec/rot, 4 mm slice thickness) for CCTV generation at every 4 mm throughout the volume of interest.

All CT images were transferred to a simulation workstation (AcQsim, Philips Medical System) and the gross tumor volume (GTV) was contoured on all images by a single clinician during a single session using a preset lung window setting according to standard clinical practice at this institute. GTV contour vertices were then extracted for further analysis using an in-house developed MATLAB (The MathWorks, Inc., version 6.5) program. It is common practice in radiotherapy planning to define a clinical target volume (CTV) by adding a safety margin around the GTV to account for subclinical involvement. For the purpose of this study, the CTV was equated to the GTV as per the RTOG 93-11 lung dose escalation protocol, which is also common practice in many centers, thus assuming the best case scenario for this investigation of internal tumor motion. CCTV contours were generated at each slice location throughout the volume of interest. Each cross-sectional area was then multiplied by the slice width to yield the CCTV. As the exact shape and path of motion of this tumor is not known, an accurate determination of the TVO is not possible. In the absence of a proper TVO, the CCTV is taken as the volume against which to compare for this clinical case. The use of uniform safety margins to account for tumor motion is contrasted with the CCTV technique by examining the following volumes at each slice location: (1) minimum internal target volume (MITV), defined as an individual CTV plus the minimum uniform internal margin (IM) required to ensure 100 % CCTV coverage at that slice location, and (2) internal target volume (ITV), generated by the addition of uniform internal motion margins to the CTV. For the purpose of this study, these volumes were defined for two distinct CTV cross-sections (the smallest and the largest) under the assumption that these cross-sections represent the worst and best case scenarios that may be encountered in radiotherapy planning.

5.4 Results and Discussion

5.4.1 Phantom Results

5.4.1.1 Cylindrical test object

The CCTV technique can best be demonstrated by considering a thin uniformly dense cylinder moving along the horizontal *x*-axis in a simple harmonic fashion, with amplitude greater than its diameter (see Figure 5.1). Experimentally, this is provided by the uniform 10 mm diameter POM cylinder, with its axis of rotation orientated orthogonal to the axis of motion, oscillating between $x = -12.5$ mm and $x = +12.5$ mm. This geometry insures that the cross-sectional area occupied by the mobile cylinder is, apart from end effects, invariant with slice location. Therefore, only one PSI set needs to be considered. Figure 5.2 illustrates the individual images of the PSI set for this experimental situation. The motion artifacts that distort these reconstructed images are clearly evident.

The cigar shaped area defined by the mobile cylinder during its entire course of travel is shown in Figure 5.3. The area delineated by the heavy black line represents the total cross-section occupied (TXO) by the mobile target and hence the contour of the TVO at that slice location. Adequate radiotherapy treatment of such a mobile target would require that the TVO be encompassed by the prescription dose if geometric miss is to be avoided. Individual images with acquisition times less than the period of motion cannot, by definition, represent the entire TVO. Increasing scan time in order to capture the full extent of the motion will result in images with a greater degree of motion related image distortion, the presence of which will further impede accurate TVO delineation [Ga 2004].

The effect of motion during image acquisition upon target delineation may be assessed by examining contours generated according to different contrast threshold levels. Figure 5.3 illustrates the contours for image #4, chosen at random from the 10 member PSI set. These contours correspond to contrast threshold levels of 10, 20, 30, 40, 50, 60, 70 and 80 % respectively. The TXO^{90}, resulting from the 90° phase interval captured in this image, is indicated by the dashed contour line. Significant sections of the 10 % and 20 % iso-contrast contours extend beyond the TXO^{90} boundary. The remaining iso-contours all reside within the TXO^{90} and thus fail to represent the TXO^{90} with any degree of accuracy. Evidently, no single iso-contrast contour can be associated with the TXO^{90}. Deriving the TXO^{90}, or any other clinically significant cross-sectional area such as that of the TXO, from a single image is clearly highly problematic. Clinical practice routinely includes the use of uniform margins to envelope the TVO. Unfortunately, this approach will result in either significant geographic miss or the inclusion of a substantial amount of uninvolved surrounding area. For example, 7.0 mm and 11.4 mm uniform margins are required with the 20 % and 50 % iso-contrast contours respectively to completely encompass the TXO at this slice location. Doing so, as seen in Figure 5.3, results in cross-sectional areas 2.0 and 3.0 times greater than the TXO.

CCTV cross-sectional areas formed by the union of iso-contrast contours from each individual image in the above PSI set are shown in Figure 5.4. Significant portions of the 10 % iso-contrast CCTV contour extend beyond the TXO. On the other hand, the 20 % iso-contrast CCTV cross-section presents only three small excursions beyond the TXO boundary. The remaining CCTV contours all reside within the TXO contour and encompass progressively less of the TXO as a function of increasing iso-contrast value. Of the nine iso-contrast contours, the 20 % iso-contrast CCTV best conforms to the TXO. Excluding excursions, this CCTV contour encompasses 92 % of the TXO cross-section. The contour defining this CCTV deviates by no more than −1 mm (interior) and +0.5 mm (exterior) from that of the TXO at any point. The excursions of this CCTV contour encompass an area external to the TXO which is only 0.8 % of the entire TXO. The information provided by this PSI set, in combination with a judicious choice of contour threshold, allows the TXO contour to be closely approximated. The addition of a small uniform margin is sufficient to completely encompass the TXO with a minimal involvement of external volumes. For this particular experimental situation, the addition of a 1 mm uniform margin to the 20 % CCTV contour is adequate to completely encompass the entire TXO cross-section and results in an area that is 1.2 times larger than the TXO. The CCTV approach thus yields a highly conformal match to the TVO while minimizing the inclusion of surrounding volumes.

5.4.1.2 Spherical test object

Now consider more realistic motions with components both in the imaging plane (x-axis) and orthogonal to it (z-axis) and to a spherical mobile target (see Figure 5.5). Since motion components along the y-axis serve only to yield more complex motion patterns but do not add further didactic value, they are left null. Figures 5.6, 5.7 and 5.8 respectively show the 10 element PSI sets for the 25 mm diameter POM sphere undergoing SHM ($n = 1$) with a period of 4 seconds and amplitudes of 5, 15 and 25 mm in both the lateral and superior-inferior directions. For each motion investigated, two PSI sets are shown. The first is located at the center of longitudinal motion ($z = 0$ mm). The second is situated 9 mm superior to this location ($z = 9$ mm). As one might expect, at each slice location greater image distortions are associated with increased amplitudes of motion. Furthermore, greater geometric distortions result at locations displaced from the center of longitudinal motion for a given motion. The distortions observed reflect the combination of both partial volume and motion artifact effects. For a constant period of motion, both effects increase with the amplitude of motion. Finally, partial volume effects are more pronounced near the limits of motion.

Composite clinical target volumes were constructed for iso-contrast thresholds ranging from 10 to 80 % at all slice locations throughout the volume of interest. Contours of these CCTVs at both the $z = 0$ and $z = 9$ mm locations for each motion amplitude are shown in Figures 5.9, 5.10 and 5.11 along with their corresponding TVO contours. Overall, all CCTV contours at a threshold of 10 % exhibit significant excursions beyond the TVO. Those derived at thresholds of 30 % and higher completely reside within it. As with the cylindrical object above, the 20 % iso-contrast CCTV contour is seen to conform closest to that of the TVO. Figure 5.12 shows the fraction (expressed as a percentage of the TVO) of the TVO encompassed by each iso-contrast CCTV. All iso-contrast CCTVs, with the exception of the 10 % CCTV in combination with the 5 and 15 mm motions, fall short of fully encompassing the TVO. As expected, the degree of conformity decreases with both increasing amplitude and with increasing contour delineation threshold value. The volumes (expressed as a percentage of the TVO) included within each CCTV which are external to the TVO are listed in Table 5.1. Iso-contrast CCTVs at thresholds 40 % and lower all extend outside the TVO. The remainder of CCTVs are completely circumscribed by it. Of those CCTV contours with excursions beyond the TVO, only the 10 % CCTV envelopes significant external volumes.

Complete circumscription of the TVO may be achieved by the addition of uniform margins. The minimum uniform margins required to encompass the TVO with the lower iso-contrast CCTVs (thresholds = 10, 20 ,30, 40 and 50 %) are listed in Table 5.2. As expected, these margins increase both with amplitude of motion and iso-contrast threshold. Inclusion of volumes external to the TVO always accompanies the addition of uniform margins which, without additional information, is the only reasonable approach when clinical application is contemplated. While the smallest required margins are associated with the 10 % CCTVs, the substantial volumes external to the TVO which they include renders them a poor choice for this endeavor.

With only small excursions beyond the TVO, the 20 % iso-contrast CCTVs prove the best choice for conformation to the TVO through the addition of uniform margins.

The utility of the CCTV approach may best be seen by comparison with individual CTVs associated with these motions. Iso-contrast CTV contours for image acquisition #7 (chosen at random) at both the z = 0 and z = 9 mm slice locations are shown in Figures 5.13, 5.14 and 5.15. While these CTV contours generally exhibit the same trend observed with CCTV contours of greater distortion at the same slice location as a function of motion amplitude, the exact pattern and magnitude of the variances observed is also dependent upon the particular phase of motion captured. The thick black contour in each image delineates the TXO at that slice location.

For a phantom study such as this, the TVO is well defined both in terms of its location and geometric extent. In the clinical setting, however, the TVO of a mobile tumor is rarely well known and, in the absence of gating, the exact phase of motion captured in any individual image is likewise uncertain. Given the uncertainties of tumor motion which abound in routine imaging, the prudent course of action is often to apply uniform margins to the CTV in order to account for the dynamic realities present. Based on considerations of target dynamics alone, a minimum uniform margin equal to the full range of motion is then required to ensure complete circumscription of the TVO for plans based on a single image at each slice location. This situation arises due to the fact that a single image may capture a mobile target at any position between and including its extrema of motion. If one uses the 50 % iso-contrast contours to represent the clinical CTV, then for the target-motion combinations contemplated here, the addition of such margins would result in cross-sectional areas (indicated by the thick dashed lines) at these slice locations ranging in size from 1.3 to 3.3 times that of the TXO. The internal target volume (ITV) contours created by the addition of these margins encompass areas external to the TVO from 26 % to 229 % that of the TXO at these slice locations. The minimum uniform margins required with the CCTV technique are 0.5, 1.5 and 3.1 mm for the 5, 15 and 25 mm motions, respectively. The substantially reduced margins required with the CCTV approach translate directly into increased conformity to the TVO with a concomitant decrease in the amount of surrounding volume enclosed.

5.4.2 Clinical Application

5.4.2.1 CTV cross-section variations

Significant CTV cross-sectional variations resulting from internal tumor motion were observed with the clinical data from the study patient at all slice locations throughout the volume of interest. Consistent with the phantom studies presented above, the largest variations in CTV contour are observed nearest the superior and inferior boundaries of tumor motion. Over all, CTV cross-sectional areas were seen to vary from the mean by less than ± 30 % at locations near the center of the volume of interest while significantly larger variations (range: -70.7 % to +132.0 %), including the occurrence of CTV absence, characterized the superior and inferior limits of motion. In addition, the difference between the largest and the smallest CTV cross-sections at any particular slice location varied by as much as a factor of 8.

5.4.2.2 Geographic failures resulting from application of a single IM

Figure 5.16 shows the CCTV contours generated, along with the smallest and largest observable CTV contours, at each slice location throughout the volume of interest. The CCTV generated from this data set has a volume of 57.5 cm^3. Lacking a well defined TVO, the utility of applying uniform margins to account for tumor mobility was assessed at all slice locations throughout the volume of interest by comparison to the CCTV. Various uniform internal motion margins ranging from 5 mm to 20 mm in increments of 5 mm were applied to both the smallest and largest CTV contours and the potential for geographic failure was assessed for these two limiting cases. Geographic failure was deemed possible when the internal target volume (ITV) contour associated with that margin failed to fully encompass the CCTV cross-section. Table 5.3 summarizes the occurrence of geographic failure observed with the use of these uniform internal margins. Since the superior and inferior boundaries of the tumor have already been well defined, the expansion to ITV was conducted in the slice plane only. When the smallest CTV contours were chosen throughout, a uniform margin of 20 mm is required to properly account for internal motion. A somewhat smaller margin of 15 mm is needed to ensure complete CCTV coverage when the largest CTV cross-sections were selected. The RTOG 93-11 lung dose escalation protocol proposed a minimum margin of 10 mm to account for both internal and external motions and daily patient setup variability. One half of this minimum RTOG margin may reasonably be assigned to account for patient motion and daily patient setup reproducibility [Ha 1999], leaving the remaining 5 mm to account for internal motion. Application throughout of a 5 mm internal motion margin to either the smallest or largest CTV cross-sections resulted in geographic failure at 100 % and 60 % of the slice locations, respectively.

5.4.2.3 Minimum IM necessary to encompass CCTV contour

Consider again a CTV composed entirely of either the smallest or largest cross-sections from each slice location. The ITV and volume of excess irradiated lung which would result in these two cases from the application of a single uniform margin throughout the entire volume of interest of a magnitude just sufficient to ensure complete CCTV coverage is summarized in Table 5.4. A 20 mm margin is required for the case in which the CTV is composed entirely of the smallest cross-sections at each slice location and a 15 mm margin must be applied when the largest cross-sections are used throughout. Application of the 20 mm margin to a CTV composed entirely of the smallest contours would result in an ITV of 150.3 cm^3 and the irradiation of 92.8 cm^3 excess lung volume corresponding to 5.4 % of total involved lung volume and 5.6 % of the remaining healthy lung tissue. On the other hand, the volume of excess irradiated lung associated with the application throughout of a 15 mm IM to a CTV comprised entirely of the largest cross-sections is 95.1 cm^3 resulting from an ITV which encompasses 152.6 cm^3. This corresponds to 5.6 % of the entire involved lung volume and 5.8 % of the remaining healthy lung. Overall, the ITVs created through the application of these single uniform margins throughout are approximately 2.6 times larger than the CCTV generated using the 10 element PSI CT image sets at each slice location. An actual planning scan for this patient would consist of a mixture of CTV contours ranging from the smallest to the largest at any given slice location and hence the application of a single uniform margin throughout would result in an amount of excess irradiated lung volume which would lie somewhere in the vicinity of the above values. The excess lung volumes irradiated would in reality be even larger as the addition of a small uniform margin to the CCTV is prudent, as evidenced by the phantom study above, in order to insure full internal motion tumor coverage.

5.4.2.4 Excess normal tissue volume in MITV

If the minimum IM required to fully encompass the CCTV contour could be clinically determined on a slice by slice basis, the volume of healthy lung tissue that would be unnecessarily irradiated would be smaller than from the application of a single uniform margin throughout. Table 5.5 summarizes the minimum IM needed with both the smallest and largest CTV cross-sections evaluated at each slice location in order to account for tumor dynamics. Also included is the resulting MITV and excess lung tissue volume that would be irradiated at each slice location. When the smallest CTV contours were selected throughout, the minimum internal uniform margins ranged from as small as 8.2 mm to as large as 19.2 mm and the total excess lung tissue volume associated with the use of these margins is 55.2 cm^3. This excess lung volume corresponds to an unnecessary irradiation of 3.2 % of the total involved lung volume and 3.4 % of the remaining healthy lung tissue. When the CT plan was composed entirely of the largest CTV cross-sections, the minimum uniform IM required at each slice location to encompass the CCTV ranged from 2.6 mm to 12.1 mm. Application of these minimum uniform IMs resulted in an excess irradiated lung volume of 44.5 cm^3, constituting 2.6 % of the total involved lung volume and 2.7 % of the remaining healthy lung tissue. The resulting MITVs are almost twice as large as the CCTV. Once again, the corresponding volumes for a clinical scan would exist somewhere in the vicinity of the above values.

5.5 Summary

In the absence of gating techniques, proper management of mobile tumors requires a slice-specific imaging technique which provides direct assessment of the motion involved. This may be accomplished by acquiring a phase sequence image (PSI) set, consisting of consecutive rapid CT images, at each slice location throughout the target volume during free breathing. Each image constituting a PSI set thus captures the tumor at a different phase in its motion. By forming a CCTV as the union of CTVs from each image of a PSI set, the total volume occupied by the tumor during the course of its travel may be approximated. Data gathered from a phantom study involving simple geometric objects undergoing well defined motions indicates that a CCTV constructed from 20 % isocontrast CTV contours provides a very good approximation to the true total volume occupied by the mobile target. The addition of small uniform margins to these 20 % isocontrast CCTVs proved sufficient to ensure complete TVO coverage. These margins ranged from 8 to 10 times smaller than those required with individual CTV contours such as one might encounter in a standard clinical CT scan. These smaller margins associated with the CCTV technique result in greater conformation to the TVO along with a substantial concomitant reduction in the inclusion of surrounding volumes external to the TVO.

The clinical data presented, even though limited to that from a single patient, clearly demonstrates the deficiency of a single CT scan to serve as the sole basis of tumor delineation for the RT planning of mobile lung tumors. The acquisition of PSI sets at each slice location throughout the VOI provides data essential to correct accounting for internal tumor motion. Circumventing the acquisition of this additional information by means of the application of uniform margins of presumed sizes will result in one of two undesirable consequences, both of which jeopardize curative outcome. The first, and most serious of these two, is an underestimation of the extent of tumor motion leading to inevitable geographic failure which threatens to nullify curative treatment intent. Alternatively, overestimation or even accurate selection of the margin required to provide complete tumor coverage will result in the irradiation of an unnecessary volume of healthy lung tissue which, in turn, limits the tolerable dose which may be safely delivered.

Table 5.1

Volume external to the TVO encompassed by different iso-contrast CCTVs. All volumes expressed as a percentage of the TVO.

Iso-contrast CCTV	Volume encompassed external to TVO (% of the TVO)		
	5 mm motion	15mm motion	25 mm motion
10 %	9.9	25.5	36.6
20 %	1.4	1.3	3.1
30 %	0.3	0.3	0.9
40 %	0.0	0.1	0.2
50 %	0.0	0.0	0.0
60 %	0.0	0.0	0.0
70 %	0.0	0.0	0.0
80 %	0.0	0.0	0.0
90 %	0.0	0.0	0.0

Table 5.2

Minimum uniform margin (mm) required with iso-contrast CCTVs of 10 % to 50 % to fully encompass the TVO.

Iso-contrast CCTV	Minimum uniform margin (mm)		
	5 mm motion	15 mm motion	25 mm motion
10 %	0.0	0.8	2.2
20 %	0.5	1.5	3.1
30 %	0.8	1.9	4.6
40 %	1.1	2.6	5.7
50 %	1.6	3.1	7.1

Table 5.3

Number of slice locations where geographic failure would occur from the application of common uniform margins to either the smallest or largest patient CTV cross-sections.

	Smallest CTV				Largest CTV			
Uniform margin (mm)	5	10	15	20	5	10	15	20
Slices with geographic failure	10	7	5	0	6	2	0	0

*Note: Total number of slices = 10

Table 5.4

ITV and excess irradiated lung volume, which would result at each slice location, from the application of an appropriate single uniform margin to either the smallest or largest CTV cross-sections. The appropriate margins for the smallest and largest CTV cross-sections are 15 mm and 20 mm, respectively. Total ITV and excess irradiated lung volumes are displayed in the last row.

Slice Location	CCTV (cm^3)	ITV (cm^3) Smallest CTV	ITV (cm^3) Largest CTV	Excess irradiated lung volume (cm^3) Smallest CTV	Excess irradiated lung volume (cm^3) Largest CTV
1	3.5	13.0	11.7	9.6	8.2
2	4.9	10.4	14.1	5.5	9.2
3	8.3	18.2	20.6	9.9	12.3
4	8.7	22.9	20.5	14.2	11.8
5	9.8	24.2	21.9	14.4	12.1
6	10.6	24.5	22.7	13.9	12.1
7	5.4	15.3	15.5	9.9	10.1
8	3.3	9.5	11.1	6.3	7.8
9	2.7	8.5	11.3	5.8	8.6
10	0.4	3.7	3.3	3.3	2.9
Total	**57.5**	**150.3**	**152.6**	**92.8**	**95.1**

Table 5.5

The size of the uniform margin required to completely encompass the CCTV for both the smallest and largest CTV cross-sections at each slice location throughout the volume of interest.

Slice Location	Minimum uniform internal margin (mm)		MITV (cm^3)		Excess irradiated lung volume (cm^3)	
	Smallest CTV	Largest CTV	Smallest CTV	Largest CTV	Smallest CTV	Largest CTV
1	12.5	5.4	7.6	5.4	4.2	1.9
2	19.2	5	9.8	6.7	4.9	1.8
3	14.9	10.6	15.3	16.1	7.0	7.8
4	11.6	7.8	14.3	13.3	5.6	4.6
5	12.9	14	16.7	20.8	6.9	11.0
6	14.7	12.1	18.7	19.5	8.1	8.9
7	18.9	7.6	14.4	9.3	9.0	3.9
8	17.5	8.1	7.9	6.4	4.6	3.2
9	17.9	2.9	7.2	3.9	4.5	1.2
10	8.2	2.6	0.9	0.7	0.5	0.3
Mean	**14.8 ± 3.6**	**7.6 ± 3.8**				
Total			**112.7**	**102.0**	**55.2**	**44.5**

Note: Total involved lung volume = 1701.5 cm^3

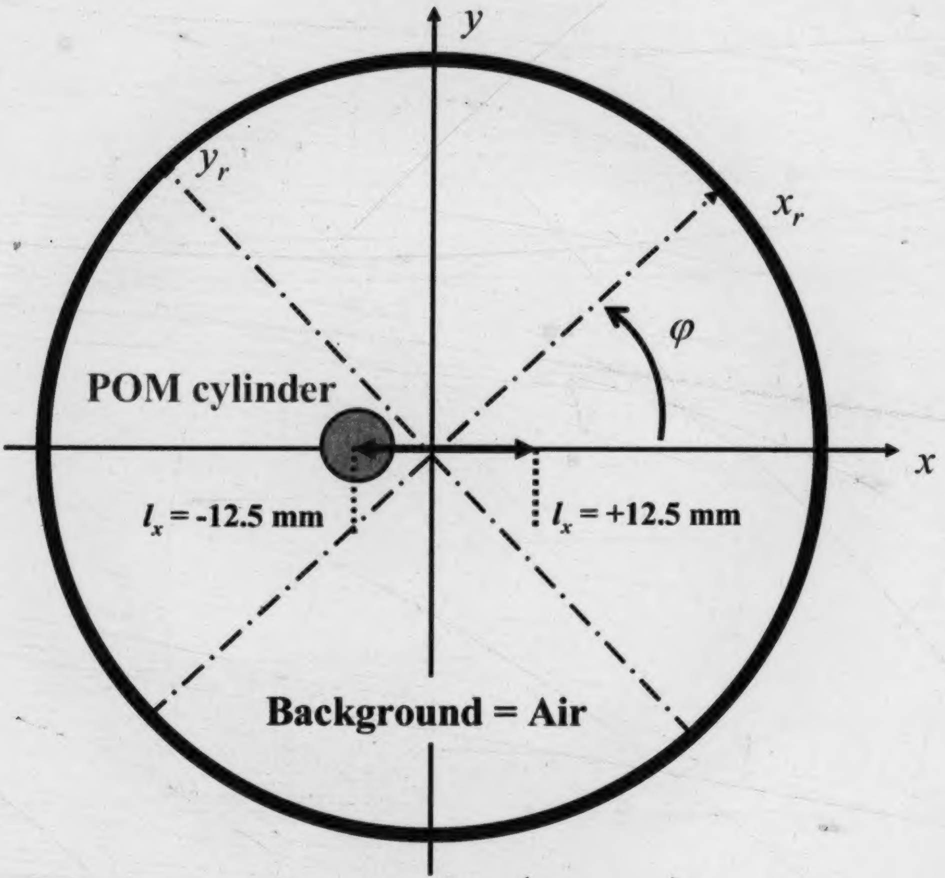
y
y_r
x_r
φ
POM cylinder
x
l_x = -12.5 mm
l_x = +12.5 mm
Background = Air

$$l_x(\varphi) = \frac{A_x}{2} - A_x \cdot \cos^2\left(\frac{\alpha}{2}\varphi - \phi_x\right)$$

$$A_x = 25\ \mathrm{mm}$$

Figure 5.1 Experimental setup for cylindrical phantom.

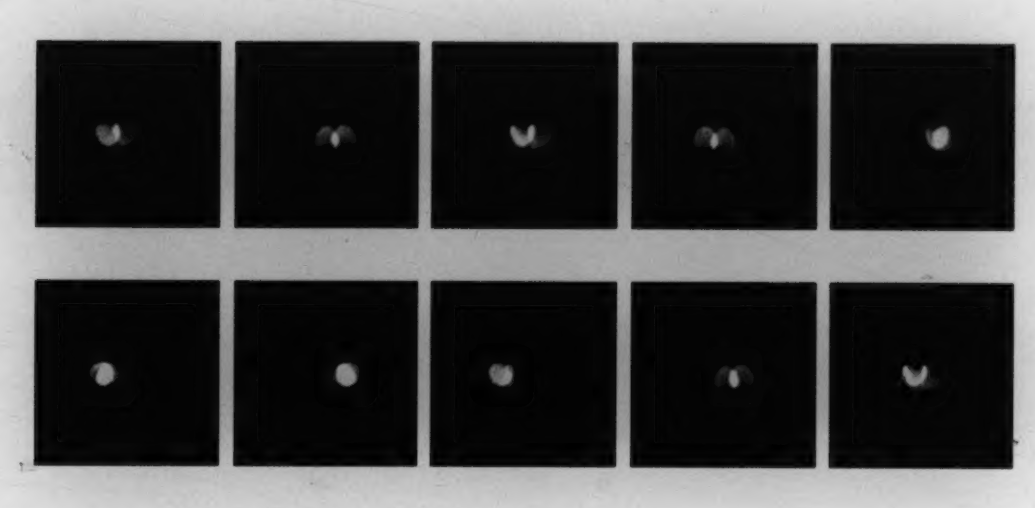

Figure 5.2 Phase sequence image (PSI) set for 10 mm diameter cylinder undergoing a simple harmonic motion along the horizontal axis of the scanner (A_x = 25 mm, rotation time = 1 sec, period of motion = 4 sec).

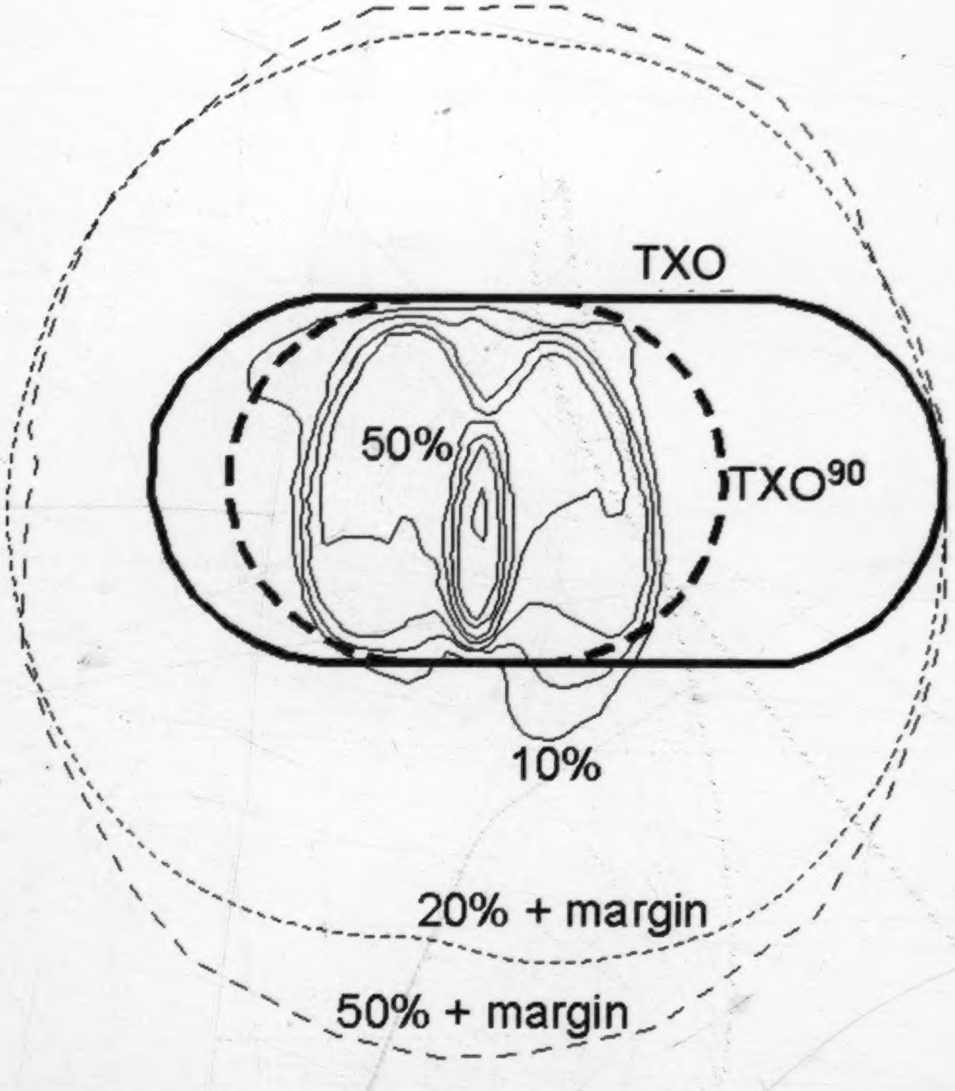
TXO
50%
TXO90
10%
20% + margin
50% + margin

Figure 5.3 TXO, TXO^{90} and individual iso-contrast contours for 10 mm diameter cylinder undergoing a simple harmonic motion along the horizontal axis of the scanner (A_x = 25 mm, rotation time = 1 sec, period of motion = 4 sec).

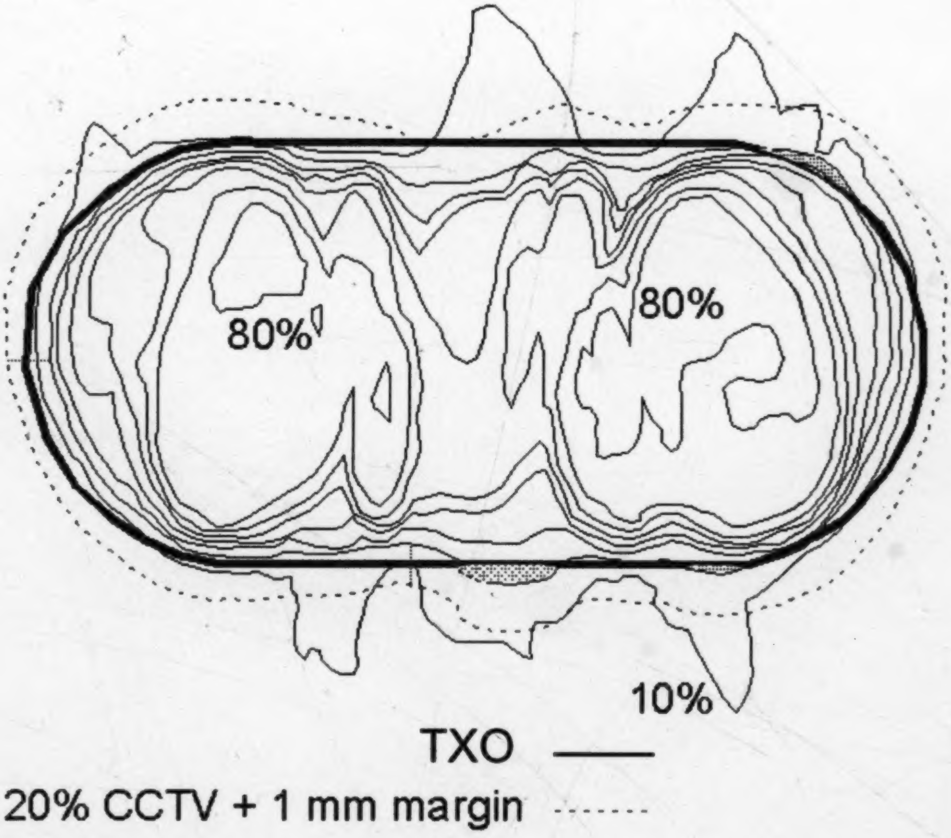

Figure 5.4 Iso-contrast CCTV contours for lateral cylinder motion in comparison to the TXO.

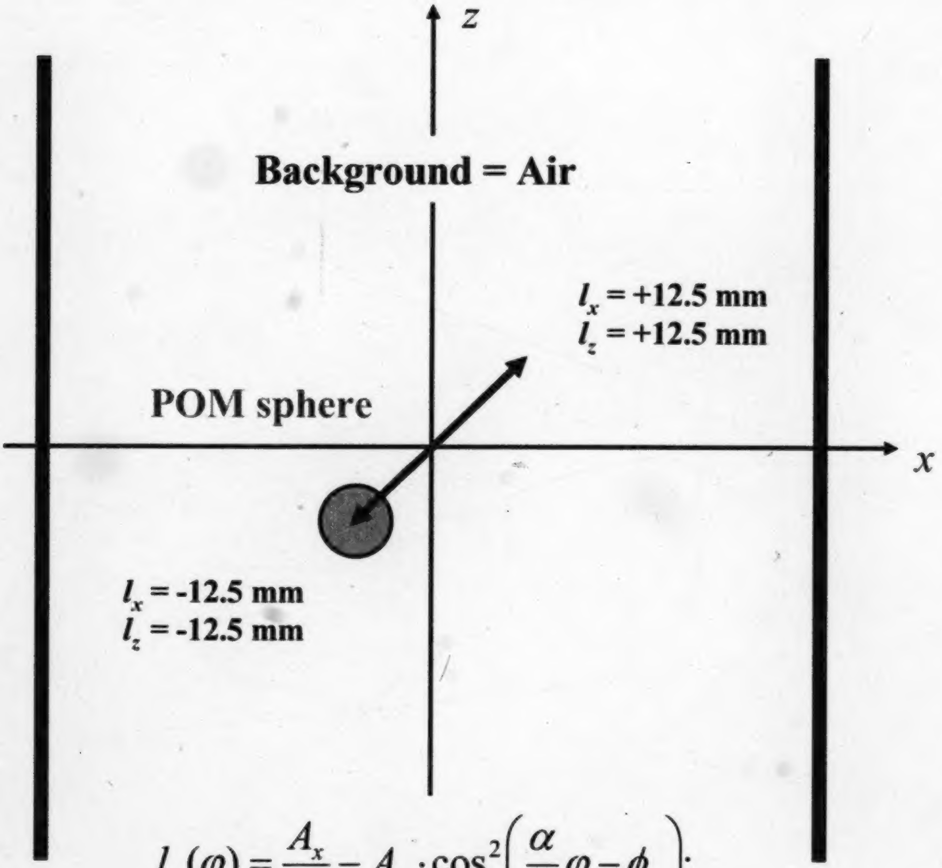
z
Background = Air
l_x = +12.5 mm
l_z = +12.5 mm
POM sphere
x
l_x = -12.5 mm
l_z = -12.5 mm

$$l_x(\varphi) = \frac{A_x}{2} - A_x \cdot \cos^2\left(\frac{\alpha}{2}\varphi - \phi_x\right);$$

$$l_z(\varphi) = \frac{A_z}{2} - A_z \cdot \cos^2\left(\frac{\alpha}{2}\varphi - \phi_z\right);$$

$$A_x = A_z = 25\,\text{mm}$$

Figure 5.5 Experimental set-up for spherical test phantom.

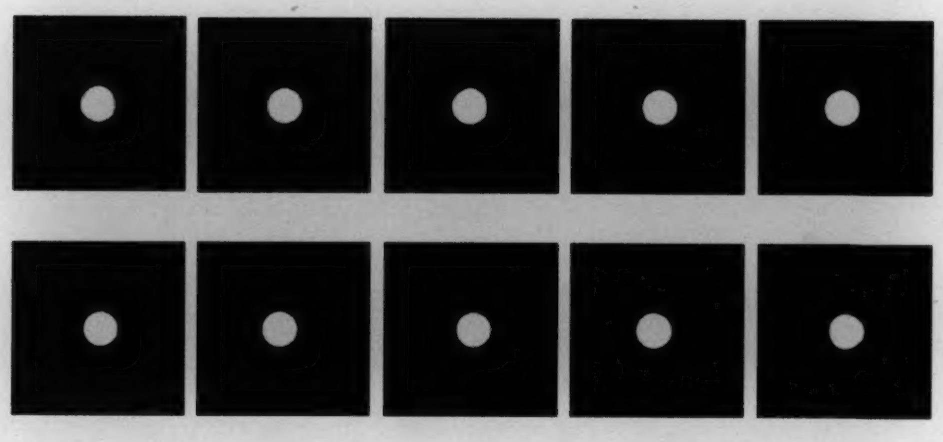

Figure 5.6a PSI set at z = 0 mm for 25 mm sphere undergoing a simple harmonic motion along the x- and z- axis of the scanner ($A_x = A_z = 5$ mm, rotation time = 1 sec, period of motion = 4 sec).

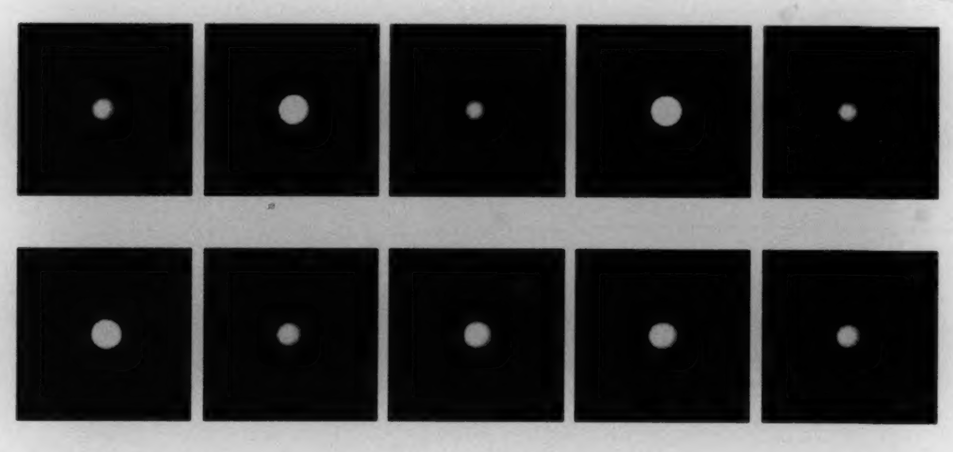

Figure 5.6b PSI set at z = 9 mm for 25 mm sphere undergoing a simple harmonic motion along the x- and z- axis of the scanner ($A_x = A_z = 5$ mm, rotation time = 1 sec, period of motion = 4 sec).

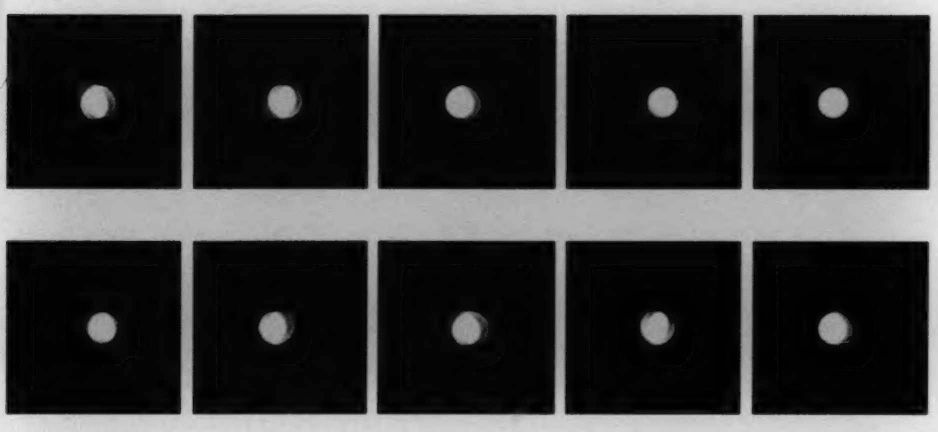

Figure 5.7a PSI set for 25 mm sphere at *z* = 0 mm undergoing a simple harmonic motion along the x- and z- axis of the scanner ($A_x = A_z = 15$ mm, rotation time = 1 sec, period of motion = 4 sec).

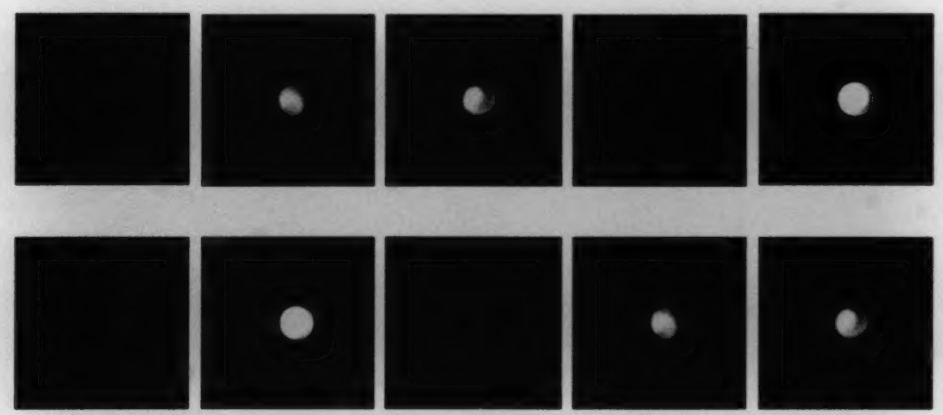

Figure 5.7b PSI set for 25 mm sphere at *z* = 9 mm undergoing a simple harmonic motion along the x- and z- axis of the scanner ($A_x = A_z = 15$ mm, rotation time = 1 sec, period of motion = 4 sec).

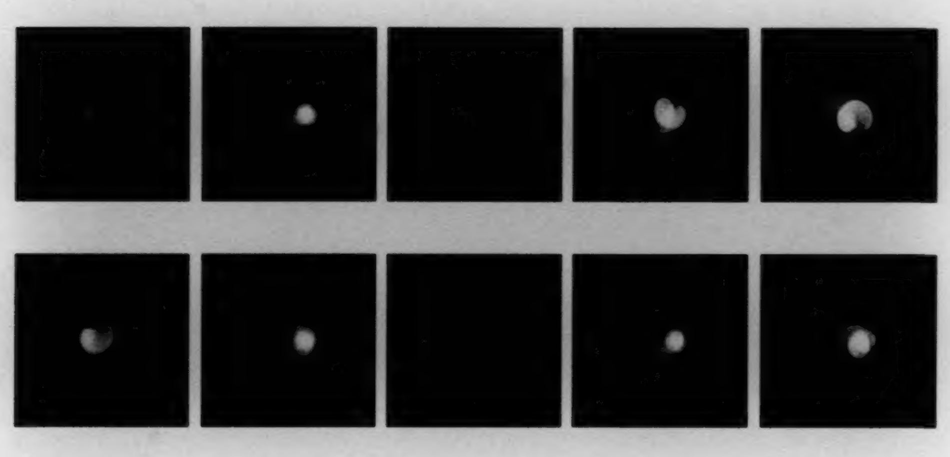

Figure 5.8a PSI set for 25 mm sphere at z = 0 mm undergoing a simple harmonic motion along the x- and z- axis of the scanner ($A_x = A_z = 25$ mm, rotation time = 1 sec, period of motion = 4 sec).

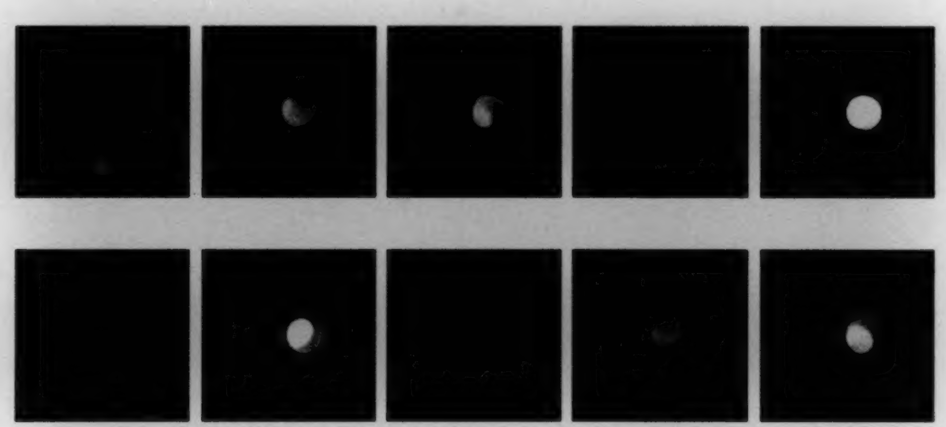

Figure 5.8b PSI set for 25 mm sphere at z = 9 mm undergoing a simple harmonic motion along the x- and z- axis of the scanner ($A_x = A_z = 25$ mm, rotation time = 1 sec, period of motion = 4 sec).

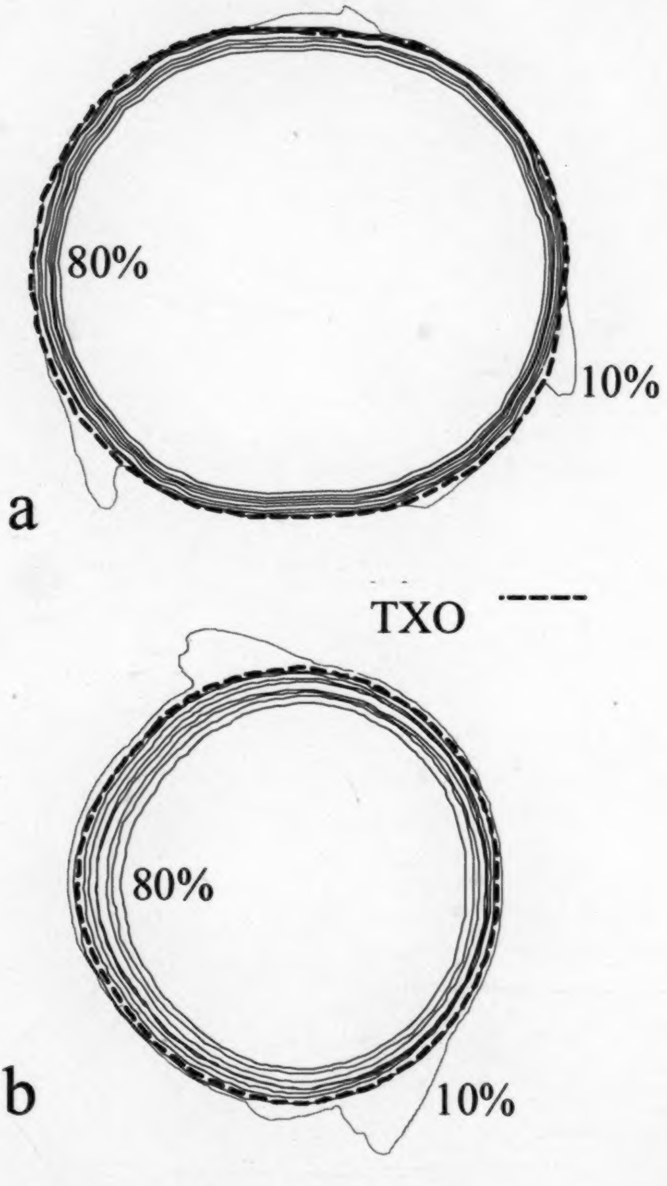

Figure 5.9 Iso-contrast CCTV contours for 25 mm sphere undergoing a simple harmonic motion along the x- and z- axis of the scanner ($A_x = A_z = 5$ mm, rotation time = 1 sec, period of motion = 4 sec) at a) $z = 0$ mm and b) $z = 9$ mm.

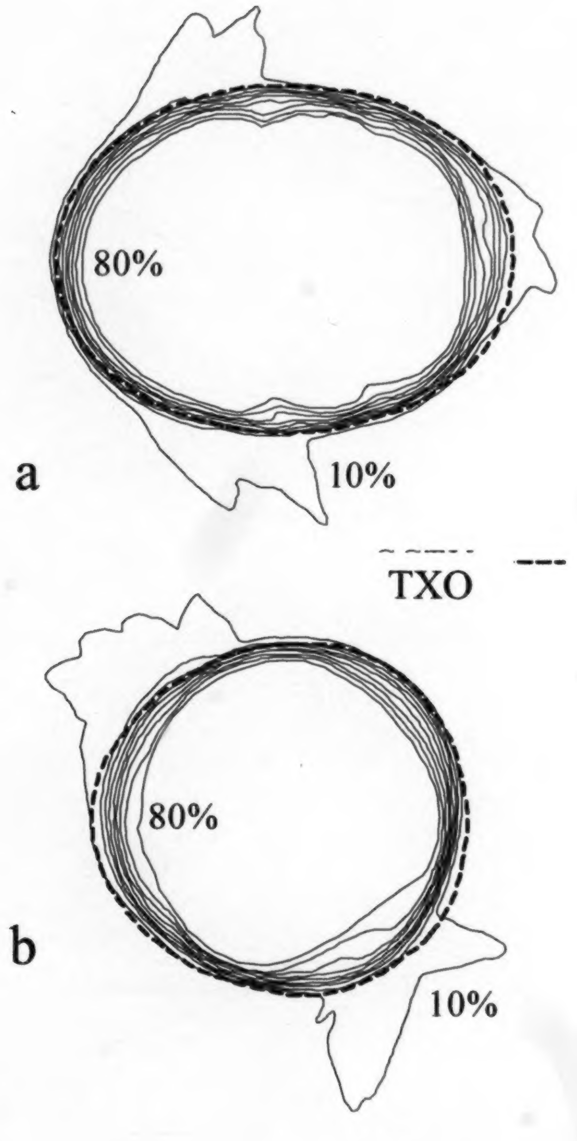

Figure 5.10 Iso-contrast CCTV contours for 25 mm sphere undergoing a simple harmonic motion along the x- and z- axis of the scanner ($A_x = A_z = 5$ mm, rotation time = 1 sec, period of motion = 4 sec) at a) $z = 0$ mm and b) $z = 9$ mm.

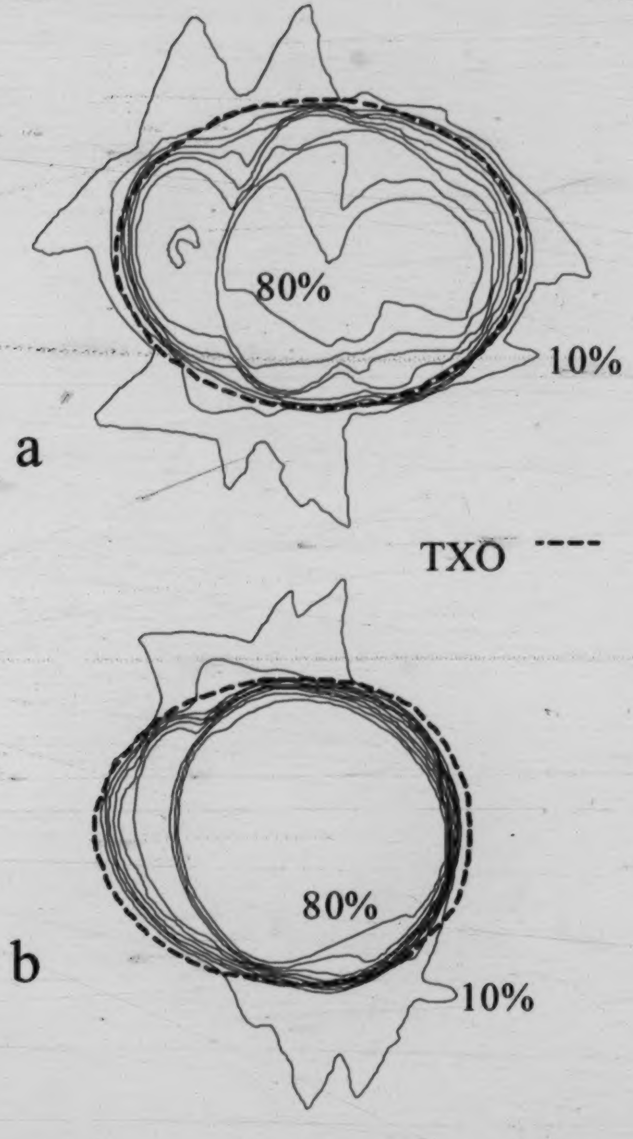

Figure 5.11 Iso-contrast CCTV contours for 25 mm sphere undergoing a simple harmonic motion along the x- and z- axis of the scanner ($A_x = A_z = 5$ mm, rotation time = 1 sec, period of motion = 4 sec) at a) $z = 0$ mm and b) $z = 9$ mm.

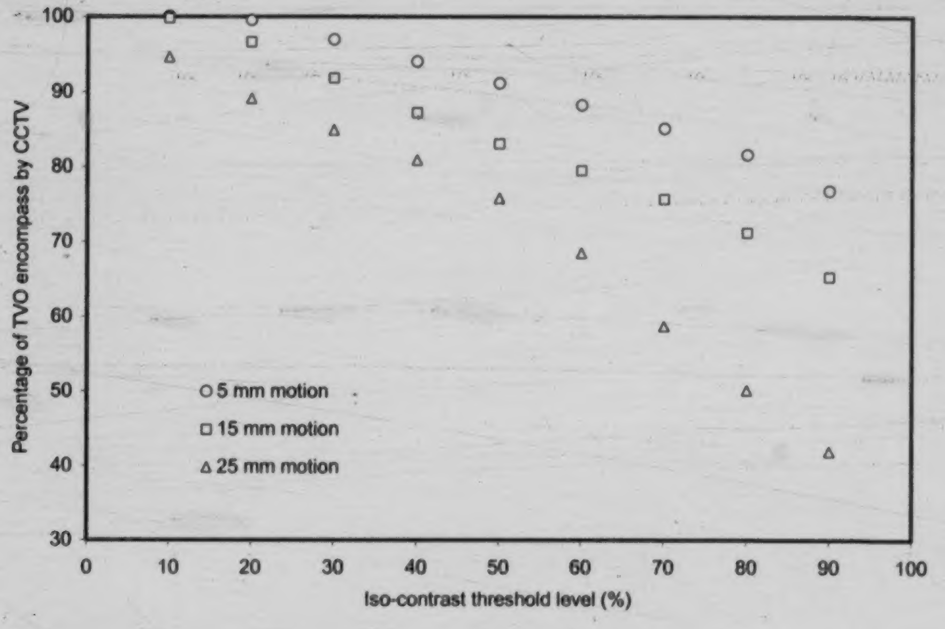

Figure 5.12 Plot of volume of TVO encompassed by CCTVs of various iso-contrast threshold levels.

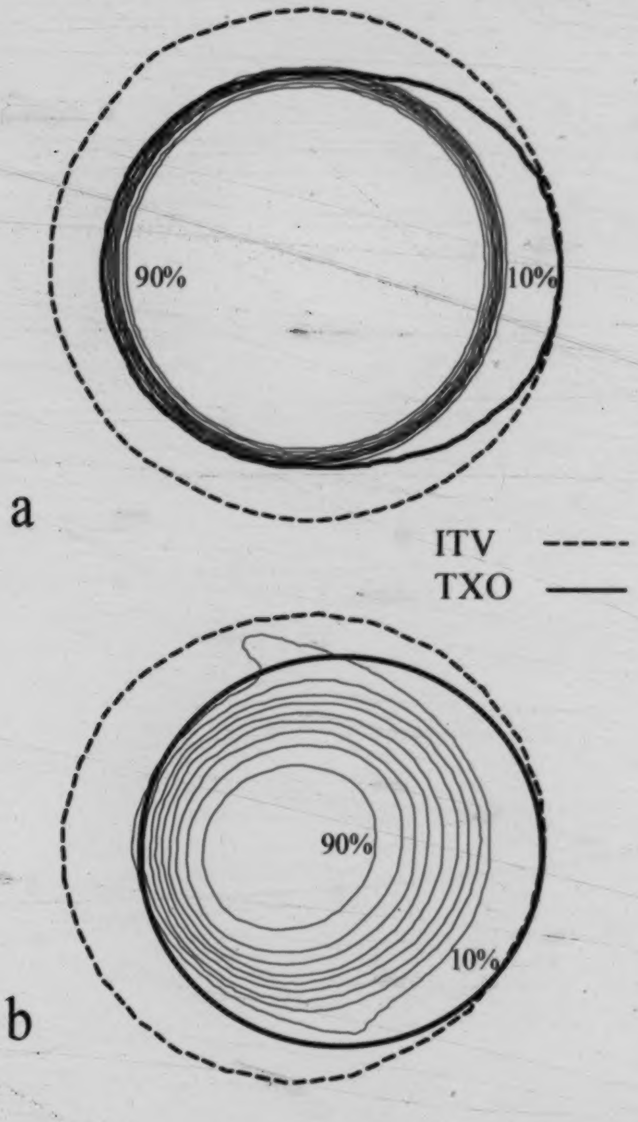

Figure 5.13 Iso-contrast contours for image #7 of the PSI set for the 25 mm sphere undergoing a simple harmonic motion along the x- and z- axis of the scanner ($A_x = A_z = 5$ mm, rotation time = 1 sec, period of motion = 4 sec) at a) $z = 0$ mm and b) $z = 9$ mm. TXO is denoted by the thick black contour and the ITV formed by the addition of a 5 mm uniform margin to the 50 % contour is revealed by the thick dashed line.

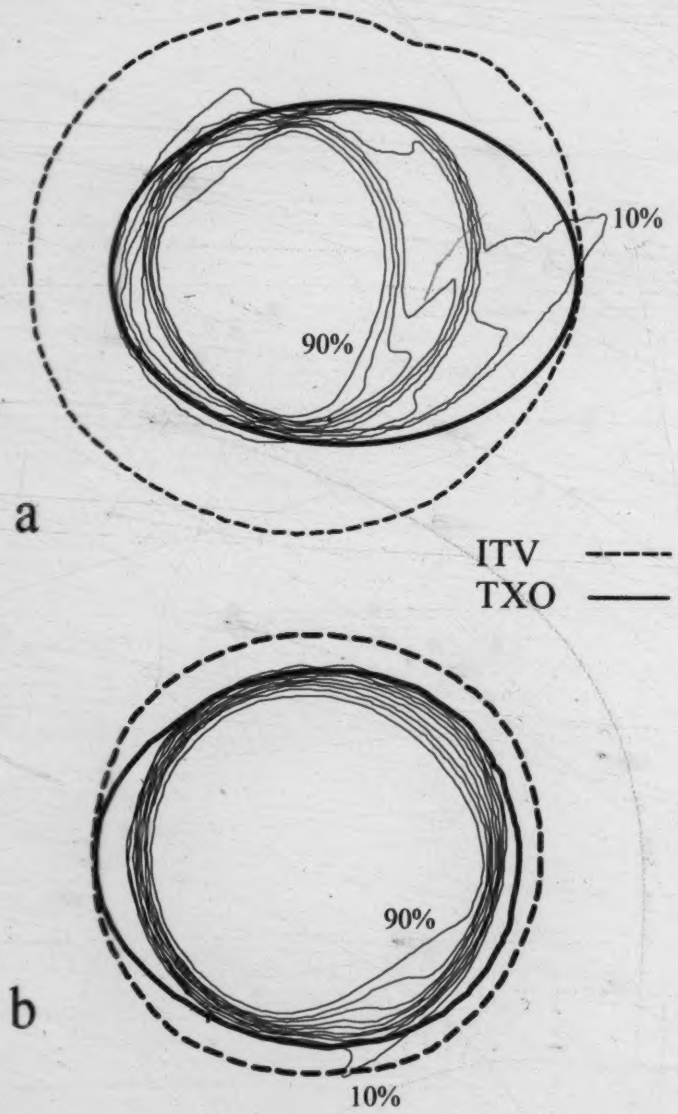

Figure 5.14 Iso-contrast contours for image #7 of the PSI set for the 25 mm sphere undergoing a simple harmonic motion along the x- and z- axis of the scanner ($A_x = A_z = 15$ mm, rotation time = 1 sec, period of motion = 4 sec) at a) $z = 0$ mm and b) $z = 9$ mm. TXO is denoted by the thick black contour and the ITV formed by the addition of a 15 mm uniform margin to the 50 % contour is revealed by the thick dashed line.

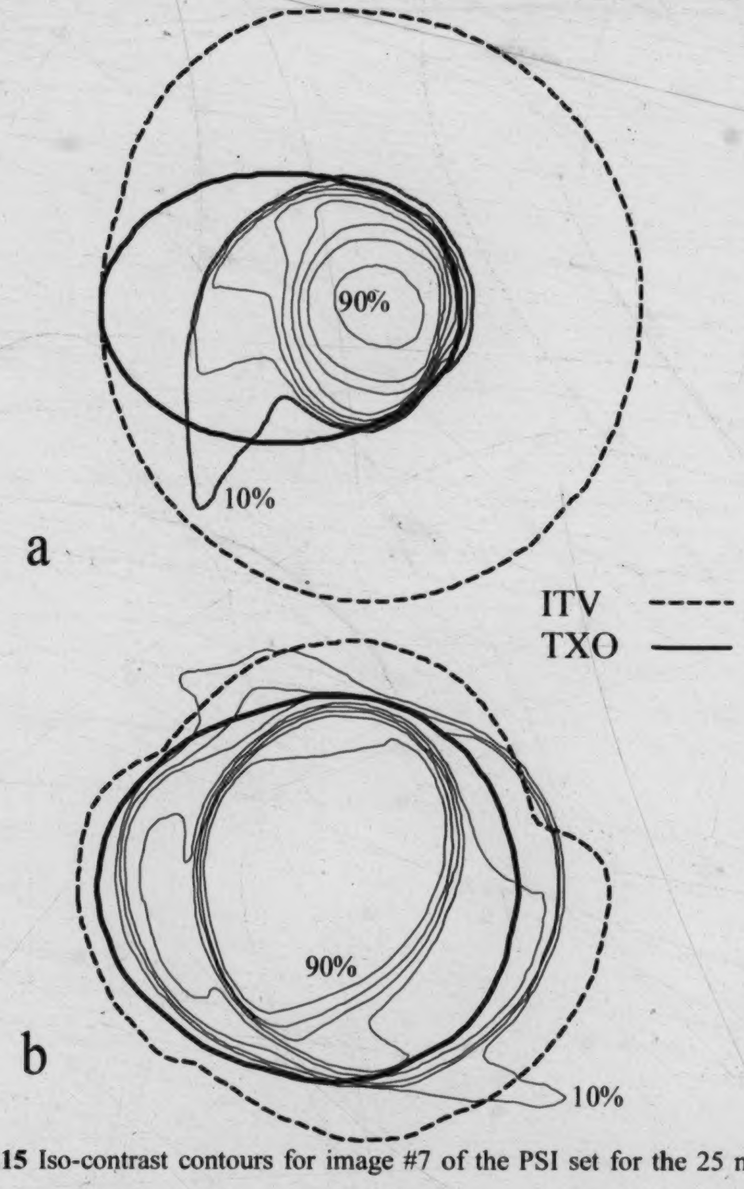

Figure 5.15 Iso-contrast contours for image #7 of the PSI set for the 25 mm sphere undergoing a simple harmonic motion along the x- and z- axis of the scanner ($A_x = A_z = 5$ mm, rotation time = 1 sec, period of motion = 4 sec) at a) $z = 0$ mm and b) $z = 9$ mm. TXO is denoted by the thick black contour and the ITV formed by the addition of a 25mm uniform margin to the 50 % contour is revealed by the thick dashed line.

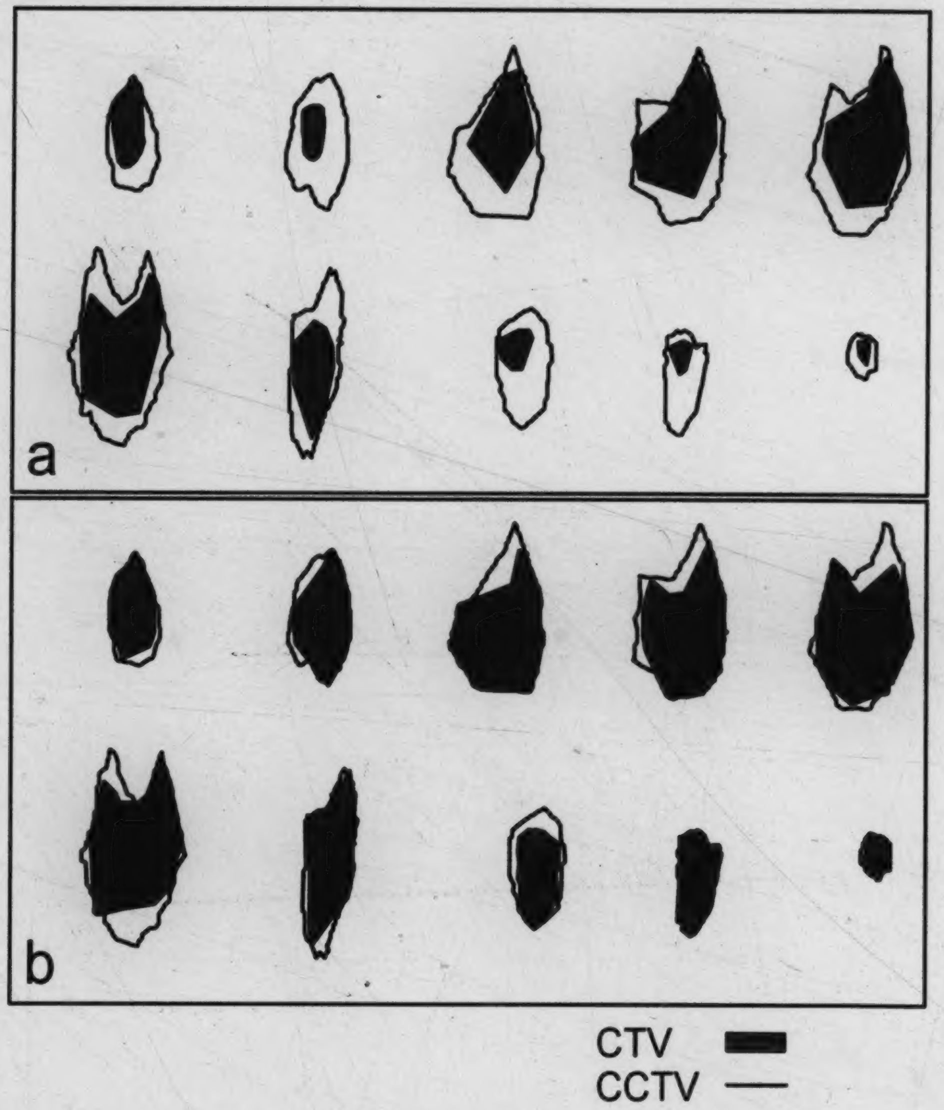

Figure 5.16 CCTV contours generated, along with the smallest (a) and largest (b) CTV contours, at each slice location throughout the volume of interest.

5.6 References

[Ga 2004] I.M. Gagné and D.M. Robinson, "The impact of tumor motion upon CT image integrity and target delineation," Med. Phys. **31**, 3378 – 3392 (2004)

[Ha 1999] R. Halperin, W. Roa, M. Field *et al.*, "Setup reproducibility in radiation therapy for lung cancer: A comparison between T-bar and expanded foam immobilization devices," Int. J. Radiat. Oncol. Biol. Phys. **43**,211 – 216 (1999)

Chapter 6: Conclusion

6.1 Thesis summary

An important factor in the success of conformal radiotherapy of lung tumors is the proper management of intra-fractional tumor motion. In the past few years, numerous explicit techniques to deal with the problem of lung tumor motion have arisen. These include breath-hold, respiratory gating and real-time tumor tracking [Ku 1996, Ba 1998, Ha 1999, Wo 1999, Ke 2004a, Ke 2004b]. While these techniques hold much promise, they are neither applicable to all patients nor are they universally available.

At present, most centers rely on the standard approach of using safety margins for lung radiotherapy even though numerous studies have shown it to be clearly inappropriate [Sh 2001, Ga 2004]. Some centers, however, currently employ implicit techniques such as 'slow' spiral, gated and 4-D CT to define patient-specific planning target volumes [La 2001, va 2001, Ri 2003, Ve 2003, Ke 2004a, Ke 2004b]. Regardless of the method of choice (explicit, implicit, standard), all planning CT data sets, with the exception of breath-hold acquisitions, are acquired while the target is non-stationary and are thus susceptible to motion artifacts. In the current pursuit to achieve better treatment outcomes in conformal lung radiotherapy, a better understanding must be gained of the detrimental effects of physiologically-induced tumor motion upon CT imaging [Bo 2004].

The main purpose of this thesis is an investigation into the fundamental nature of CT image artifacts associated with motion characteristic of lung tumors and the implications for target delineation. Also presented was an exploration of the feasibility of phase sequence imaging to reveal the total volume occupied by mobile tumors for clinical situations in which physiologic motion can neither be eliminated nor discounted and for which gating techniques are neither available nor applicable.

To aid in this investigation, a filtered backprojection algorithm was developed in MATLAB to reconstruct tomographic images. The ability of the computer model to properly reproduce experimental results under both static and dynamic conditions was experimentally established. For object geometries employed in all investigations (cylinder, sphere), the computer model was found to accurately reproduce experimental results (see Chapters 2, 3, and 4). Because of its ability to separate individual effects, computer modeling proved to be a powerful investigational tool with which to explore the principles of motion artifacts in CT (see Chapter 2), the functional dependence of motion artifacts associated with lung tumor motion (see Chapter 3) and the impact of respiration-induced tumor motion upon CT image integrity and target delineation (see Chapter 4). The investigations conducted using the computer model shed new light on the detrimental effects of internal tumor motion on CT imaging. Specifically, the following were observed:

- *The presence of motion during data acquisition produces inconsistencies in the projection data set*

- *CT reconstruction based upon such motion impacted projection data sets produces global effects on the resultant images*

- *Respiration-induced motion projects the reconstructed object in directions displaced from its velocity vector. This is in contrast to the smearing of mobile objects in planar radiography which is always along the line of motion*

- *The motion-induced artifact patterns were found to be functionally dependent upon the following parameters:*

- *the ratio of the image acquisition time to the time which characterizes the motion of the object*
- *the projection angle at the initiation of data acquisition*
- *the amplitude of object motion*
- *the phase of object motion*
- *the orientation of motion in the image plane*

✧ *The spatial extent of a mobile object is distorted from its true shape and location and does not accurately reflect the total volume occupied (TVO) during the extent of motion captured;*

✧ *The density distribution of a reconstructed mobile object is altered from its physical time-averaged density distribution;*

✧ *The densities of the surrounding structures (external to the TVO) are also altered from their true values; and*

The ability of phase sequence imaging to reveal the total volume occupied by mobile targets was investigated in Chapter 5. It was found that phase sequence imaging can yield accurate estimates of the internal target volume at a contrast threshold level of about 20 %.

6.2 Original contributions

While motion artifacts arising from physiological functions such as respiration and cardiac contraction have long been acknowledged as a problem in CT, very little quantitative material has appeared in the literature concerning the origin, nature, and effects of these image artifacts. To the best knowledge of the author of this thesis, having conducted an extensive review of the available literature, this work presents the first in depth analysis of respiration-induced motion artifacts in CT. Specifically, the following contributions of new knowledge are presented:

- *Identification of the parameters that govern both the pattern and magnitude of artifacts associated with continuous (periodic) motion characteristic of lung tumors*

- *An analysis of the functional dependence of respiration-induced motion artifact patterns*

- *An analysis of the impact of respiration-induced motion upon CT image integrity and contour delineation of the mobile object*

- *A novel approach (the PSI technique) to contour delineation of mobile lung tumors*

6.3 Future work

All results presented in this thesis relate specifically to axial imaging, a special form of spiral or helical CT imaging (pitch = 0). Since pitches > 0 are also routinely used in radiotherapy planning, further investigations are warranted. Some important questions that should be targeted in the future are:

- *What are the underlying principles of motion artifacts in helical imaging?*

- *How does varying the pitch affect the resultant reconstructed densities when motion is present during data acquisition?*

- *How sensitive are the reconstructed densities to the z-interpolation technique?*

- *How do object segmentation results in spiral CT compare to the true cross-section occupied by the mobile (TXO)?*

- *How does 'slow' spiral scanning compare to phase sequence imaging using rapid data acquisition for internal target volume delineation?*

- *How does 4D-CT imaging (spiral acquisition mode) compare to phase sequence imaging for internal target volume delineation?*

6.4 References

[Ba 1998] J. Balter, K. Lam, C. McGinn, *et al.*, "Improvement of CT-based treatment-planning models of abdominal targets using static exhale imaging," Int. J. Radiat. Oncol. Biol. Phys. **41**, 939 – 943 (1998)

[Bo 2004] T. Bortfeld and G.T.Y. Chen, "Introduction: Intrafractional organ motion and its management," Semin. Radiat. Oncol. **14**, 1 (2004)

[Ha 1999] J. Hanley, M.M. Debois, D. Mah *et al.*, "Deep inspiration breath-hold technique for lung tumors: the potential value of target immobilization and reduced lung density in dose escalation," Int. J. Radiat. Oncol. Biol. Phys. **45**, 603 – 611 (1999)

[Ke 2004a] P. Keall, "4-dimensional computed tomography imaging and treatment planning," Semin. Radiat. Oncol. **14**, 81 – 90 (2004)

[Ke 2004b] P.J. Keall., "Acquiring 4D thoracic CT scans using a multislice helical method," Phys. Med. Biol. **49**, 2053 – 2067 (2004)

[Ga 2004] I.M. Gagné and D.M. Robinson, "The impact of tumor motion upon CT image integrity and target delineation," Med. Phys. **31**, 3378 – 3392 (2004).

[Ku 1996] H.D. Kubo and B.C. Hill, "Respiration gated radiotherapy treatment: a technical study," Phys. Med. Biol. **41**, 83 – 91 (1996)

[La 2001] F.J. Lagerwaard, J.R. Van Sornsen de Koste, M.R. Nijssen-Visser, *et al.*, "Multiple "slow" CT scans for incorporating lung tumor mobility in radiotherapy planning," Int. J. Radiat. Oncol. Biol. Phys. **51**, 932 – 937 (2001)

[Ri 2003] E. Rietzel, G. T. Chen, K. P. Doppke, *et al.*, "4D computed tomography for treatment planning," Int. J. Radiat. Oncol. Biol. Phys. **57**, Supplement 0 (2003)

[Sh 2001] S. Shimizu, H. Shirato, S. Ogura, *et al.*, "Detection of lung tumor movement in real-time tumor-tracking radiotherapy," Int. J. Radiat. Oncol. Biol. Phys. **51**, 304 – 310 (2001)

[va 2001] J.R. van Sornsen de Koste, F. J. Lagerwaard, R. H. Schuchhard-Schipper, *et al.*, "Dosimetric consequences of tumor mobility in radiotherapy of stage I non-small cell lung cancer -- an analysis of data generated using 'slow' CT scans," Radiat. Oncol. **61**, 93 – 99 (2001)

[Ve 2003] S.S. Vedam, P.J. Keall, V.R. Kini, *et al.*, "Acquiring a four-dimensional computed tomography dataset using an external respiratory signal," Phys. Med. Biol. **48**, 45 – 62 (2003)

[Wo 1999] J.W. Wong, M.B. Sharpe, D.A. Jaffray, *et al.*, "The use of active breathing control (ABC) to reduce margin for breathing motion," Int. J. Radiat. Oncol. Biol. Phys. **44**, 911 – 919 (1999)